Proposed Guidelines of Using CFD and the Validity of the CFD Models in the Numerical Simulations of Wind Environments around Buildings

Cheng-Hu Hu

Thesis submitted for the Degree of
Doctor of Philosophy

School of the Built Environment
Heriot-Watt University

December 2003

Abstract

Using Computational Fluid Dynamics (CFD) to model the airflow around buildings has become one of its most important and challenging industrial applications in the CFD community. Applying CFD in the environmental design for the assessment of the outdoor environment is a relatively new approach and it is also currently being practised and developed in the consulting sectors of the building and construction industry. Owing to the nature of the turbulent winds and the intricacies of turbulent flow simulations, any CFD model pertaining to the winds contains a number of errors and uncertainties. Modelling the wind and studying the wind effects around buildings using CFD can be dangerous if an industrial practitioner is unfamiliar with the nature of the wind and the numerical algorithm of a CFD code. For a good and reliable numerical simulation, CFD users need to establish sufficient insight into the flow problems and identify the numerical errors and uncertainties. The guidelines proposed in this thesis aim to provide appropriate suggestions with regard to creating a relatively accurate and reliable CFD model for the simulations of wind environments around buildings using the existing numerical methods.

The research method consists of a series of validation studies. It was firstly to create a 2D CFD simulation of flows around a square cylinder and a 3D flow simulation around a cube. The simulations were compared with the available experimental data in order to contrast different computational approaches and suggest suitable computational parameters. The selected parameters were subsequently validated again with a number of more complicated cases. With all the results satisfied and the limitations of the CFD model unveiled, the final step was to apply the proposed numerical methods to an industrial case of environmental design.

All the important findings will be summarised and presented as proposed guidelines with the discussions of numerical errors. The methods of minimising the numerical errors will be also suggested in order to facilitate and promote good practice for a quality CFD simulation of the wind environment around buildings.

Acknowledgements

The research was a long and lonely journey in my academic life. Fortunately, I was not always alone. A number of people gave me lots of encouragement and advice while I was looking for a direction. I wish to express my most sincere appreciation to those who have helped me in this study: my supervisor Dr. Fan Wang for his critiques and supervision; Professor Ian Grant for his kind advice on the techniques of flow visualisation and PIV experiments; his PhD student Mr. Vladimir Fonov for his kind help in the experiments of flow visualisation and using PIV; my colleague Mr. Wei Li for his help in the wind tunnel experiments and his suggestions on the numerical aspects of CFD; the technical staff Mr. Peter Reid, Mr. James Maguire, Mr. Dave Murray and Mr. Tom Scott for their assistance in the supply of required instruments and facilities as well as for their efforts in crafting the models for a series of experiments carried out in the boundary layer wind tunnel.

Special thanks to Professor Ted Stathopoulos from the Concordia University in Canada for his constant support and advice on the wind tunnel experiments and CFD modelling of the wind environments around buildings. The research and the thesis would have not been possible to complete without the help from the people listed above.

Finally, to my parents and my brothers and sisters who have always wanted and encouraged me to the best for myself, I dedicate this thesis.

Table of Contents

Nomenclature

[L]	length
[T]	time
B(r)	flux limiter function in differencing scheme
$C_{\varepsilon 1}$	k-ε turbulence model constant
$C_{\varepsilon 2}$	k-ε turbulence model constant
C_{μ}	k-ε turbulence model constant
f_c	Coriolis parameter
f_{μ}	damping function of the two-layer k-ε model
g	gravity
I or $T.I.$	turbulence intensity
k	turbulent kinetic energy
l_m	length scale of the two-layer k-ε model
Ma	Mach number
p	static pressure
Re	Reynolds number
Re_y	local Reynolds number
T_{eqv}	equivalent temperature owing to windchill
T_{ij}	stress tensor
U_i	mean wind velocity component at x_i direction
V_{eff}	effective gust
V_G or U_G	wind velocity at the gradient height
V_r or U_r	reference wind velocity
y^+	dimensionless near-wall indicator, $y^+ = u_* y / \nu$
u, v, w	velocity components
u_i'	fluctuating velocity component at x_i direction
$\tilde{u}_i$	subgrid-scale velocity component at x_i direction
u_*	friction velocity, $u_* = (\tau_0/\rho)^{1/2}$
x, y, z	Cartesian co-ordinates
x_i	co-ordinates in tensor notation
z_0	roughness length (or height)
z_G	gradient height

α	exponent in the power-law model
δ	thickness of boundary layer
δ_{ij}	Kronecker delta, = 1 for $i = j$ and = 0 for $i \neq j$
ε	dissipation rate of k
κ	von Kámán constant
μ	dynamic viscosity of fluid
ν	kinetic viscosity of fluid (= μ/ρ)
ν_s	subgrid eddy viscosity
ν_t	eddy (or turbulent) viscosity
ρ	fluid density
τ_0	wall shear stress
τ_{ij}	turbulent stresses
$\sigma_{u,v,w}$	root-mean-square values of the fluctuating velocities in x, y, z direction respectively
div.	divergence (for vector), $\frac{\partial}{\partial x}\mathbf{i}+\frac{\partial}{\partial y}\mathbf{j}+\frac{\partial}{\partial z}\mathbf{k}$
grad.	gradient (for scalar), $\frac{\partial}{\partial x}\mathbf{i}+\frac{\partial}{\partial y}\mathbf{j}+\frac{\partial}{\partial z}\mathbf{k}$
$\int_{c.s.}$	surface integral
$\int_{c.v.}$	volume integral

Chapter 1 Introduction

Wind is one of the major and influential environmental factors in everyday life. Prediction and analysis of the external wind flows have been increasingly important to the building and construction industry as people are more aware of the potential environmental impact that may be raised by erecting the buildings or structures. Wind effects are versatile – they may affect structural responses, natural ventilation, energy consumption, cladding design, balcony design, snow accumulation, pollutant dispersion, pedestrian safety and comfort and so forth. Reducing adverse wind effects and making best use of wind resources have already become one of the agenda in "Sustainable Development" – the strategy seeking mutual benefits between the quality of life and the environment where we are living and working. The wind and building, which are closely connected with people's life, are certainly of principal concerns to policy makers or engineers. For instance, some cities in the United States and Australia have the ordinance that entails the study of wind environment around buildings to be part of project proposal before the development approval can be granted (Aynsley, 1989).

The study of wind effects upon or around buildings is mostly carried out at the stage of masterplanning or environmental design in which the design team can examine the proposal for possible wind issues. The investigation is usually a multi-disciplinary study involving the input from the architect, wind engineer and other professionals. The most common way to gather the information required is to create a model for assessment, either physically or numerically. Physical experiments mainly refer to wind tunnel tests, which have been well established in past few decades and a carefully controlled experiment in a sophisticated wind tunnel is probably the best way hitherto in the simulations of the natural wind and its effects upon structures and buildings (Plate, 1999). However, physical experiments are likely to be costly and time-consuming and usually the resources are not available in-house. This is a disadvantage when the modification of initial design is required, as the model will have to be reshaped or sometimes recreated and, the wind tunnel and instrumentation are also required to be tuned accordingly till all the results are satisfactory. It may also increase the difficulty in

terms of team collaboration, especially when the external resources have to be relied upon.

Numerical simulations take advantage of currently expanding computing power, which opens new possibilities in the calculations of airflow around a complex of buildings. Using numerical methods can also expedite the design process since all data have been digitised. The main tool – Computational Fluid Dynamics (CFD), which is a set of mathematical methods devised to solve the governing equations of flows and its role in the prediction and analysis of wind environments around buildings, is speculated to be more important in the foreseeable future.

1.1 Motivation and Background

The flow behaviours around buildings are complicated and they have considerable influences on a building itself and its surroundings. Traditionally, civil or structural engineers are more interested in the structural responses to strong winds since their priority is given to the design of a safe structure or building that can satisfy the requirements to resist adverse wind forces. Therefore the studies of wind forces acting upon buildings or structures are found extensively more than other wind issues in the literature. Since early 70s, however, the studies of wind environment around buildings became a new focus (Penwarden and Wise, 1975), as people need not only safe buildings for habitation but also comfortable environment around buildings for recreational purposes or for other outdoor activities.

Almost the same time, in early 70s, the era of CFD was launched (Anderson, 1995). The computing power and algorithm were not sophisticated enough to calculate flow problems in three dimensions but the studies using CFD to calculate flow problems were steadily emerging. Early CFD codes were developed particularly in the area of aeronautical or mechanical engineering and most of the codes were written by the researchers or engineers themselves for special purposes. In 1981, the first commercially available CFD code – PHOENICS was created as a general-purpose code (Spalding, 1981), which was becoming a tool of engineers and researchers other than code developers to study various flow problems. A number of researchers (e.g. Paterson and Apelt, 1986; Richards, 1989) applied this code to simulate the flows around a single building but the computing power at that time was still rather limited and therefore the

resolved flow fields were not of great details. The advancement of computer technology became very fast when the timeframe moved to 90s. Many other commercial CFD codes (e.g. Fluent, CFX, STARCD, FLOW3D) entered the market and some large consulting firms started using the commercial codes to model the airflow within a building for HVAC design (IMechE, 1991). Also, since the computing power had been largely increased, research into modelling the turbulent winds around buildings using more sophisticated turbulence models such as Large Eddy Simulation (LES) became very active. Many researchers (e.g. Werner and Wengle, 1991; Murakami, 1993; Frank, 1995) presented their achievements with their own codes in the last decade. More advanced industrial applications such as prediction of atmospheric dispersion and concentration of pollutants were also reported (Castro *et al.*, 1999).

Currently there are commercial codes and academic codes in the CFD community. Academic codes are usually not available to the users in the building and construction industry and those codes are, sometimes, not maintained. In addition, academic codes accentuate applying novel algorithms or newly developed mathematical models, which are not really of industrial users' interests. Therefore industrial practitioners mostly employ commercial codes to solve their problems and how to get the best of their commercial codes they have invested in to study the environmental flow problems is a realistic issue.

There have been many wind tunnel applications concerning the wind environment around buildings but applying CFD to simulate the external flows around buildings for the evaluation of pedestrian comfort is few. The main interests of these studies are no longer the wind pressures on the roof and main structure of a building but the flow pattern and the wind velocity at ground level in the vicinity of it. This type of winds is usually categorised into "pedestrian-level winds" as opposed to "high (speed) winds" that are mainly of concerns to civil and structural engineers. Pedestrian-level winds are affected by a number of factors such as the terrain, building forms and the local climate. The winds are more turbulent (or gusty) near the ground since the terrain roughness usually promotes turbulence. Turbulent winds with strong mean velocities may cause discomfort or potential danger to pedestrians since the wind forces received by a person are proportional to the square of the wind velocities. The studies of wind effects on people therefore have become an essential part in environmental design.

Since it is a relatively new application and practical guidelines with particular attention to this type of CFD simulations have not been found yet, there is a need to examine the existing numerical methods and make appropriate suggestions to the industrial users, especially for those users who are using a commercial code. Some users perhaps have already gained the experience in simulating the airflow within a building using their codes but the simulations of external flows can be a completely different story. The wind is highly turbulent and stochastic in nature and the governing equations depicting the airflow are non-linear and highly coupled. Consequently it produces a number of difficulties in this type of numerical simulations such as in the aspects of turbulence modelling and near-wall treatment (Murakami, 1998). Also, using a commercial code is certainly not easy, even for an experienced user because there are many physical and computational parameters required for a good simulation. In addition, most of the commercial codes are designed for general-purpose uses and many of them are not originally designed for the analysis of wind environments around buildings. Also, very often the problem is not of the code itself but of the user (Hall, 1996; Castro and Graham, 1999). Since users are likely to be puzzled when they are asked to choose the required parameters for their numerical simulations and sometimes, a computed result is far from the reality even though it looks reasonable because the problem solved is actually another flow problem. The need of appropriate guidelines is therefore indispensable and immediate. For instance, a professional institution such as BRE in the UK is also conducting a similar research (Cowlin and Westbury, 2002).

The research method is to examine a number of existing numerical methods in CFD using some representative cases and propose the guidelines that are relatively easy to be understood by industrial practitioners. The capabilities and limitations of the proposed methods will be discussed and a number of issues will be raised for further research. The main code employed for this study is PHOENICS, a commercially available code from CHAM Ltd. Another CFD code – CFX (from AEA Technology) is also applied in a small part of this study.

1.2 Scope of this Thesis

The thesis covers the background theories, wind tunnel experiments and numerical simulations. It consists of three interrelated parts – literature review, CFD simulations and validations and the proposed guidelines. There are two chapters dedicated for the

literature review because this study needs the knowledge of the wind, wind tunnel experiments and numerical simulations. Chapter 2 describes the structure of the wind, its formulation, characteristics and the lower part of the atmospheric boundary layer. Traditional wind tunnel studies were systematically reviewed, including the techniques of simulating the wind and their applications regarding the studies of pedestrian-level winds. The wind tunnel techniques reviewed there also laid a foundation for the experimental work presented in chapter 5. The essentials of CFD are presented in chapter 3. The derivation of the governing equations and the numerical methods employed by the CFD code were reviewed and discussed, including the types of computational grids, turbulence models, differencing schemes and the linear equation solvers. Chapter 2 and chapter 3 constitute the first part of this thesis.

The second part of this thesis consists of four chapters – Chapter 4 is composed of several numerical simulations around a 2D square cylinder and a 3D cube. The results were compared with the published experimental data for validations. The relatively better and appropriate computational parameters for the turbulent flow simulation around a bluff body were found from that chapter. Chapter 5 presents the flow simulations around a cube with wind tunnel experiments and CFD. In chapter 5, the flow fields around a cube orientated 0^{o} and 45^{o} were investigated with wind tunnel experiments and corresponding CFD simulations. Chapter 6 presents a series of CFD simulations of the flow fields around two and a group of buildings. The complexity of flow fields was much higher and the approaching winds with various directions (0^{o}, 15^{o}, 30^{o}, 45^{o}, 60^{o} and 90^{o}) were simulated. Chapter 7 describes an industrial case study using the proposed CFD approach for environmental design in which the pedestrian-level winds in the open space are of concerns. The effects of windchill were also simulated for a more comprehensive study of wind environment around buildings.

The last part of the thesis is the proposed guidelines of using a CFD code to model the wind environments around buildings. Chapter 8 summarises all the important findings from the previous chapters and the guidelines are composed specifically for the industrial users. Finally, the conclusions and the recommendations for further research are made in chapter 9.

Chapter 2 The Structure of the Wind and Wind Tunnel Studies of Wind Flows around Buildings – A Review

Wind is a phenomenon of air circulation caused by the pressure variations in the atmosphere. The lower part of the atmosphere is the atmospheric boundary layer within which the wind is highly turbulent due to the surface roughness and unstable thermal environments. This chapter briefly reviews the formulation of the wind, the atmospheric boundary layer, the turbulent wind near ground and the wind profiles over various terrain as well as the wind tunnel studies of wind environments around buildings. The main purpose of this chapter is to depict some theoretical background of wind studies and wind tunnel techniques that will be applied in the following chapters.

2.1 The Origin of the Wind

The solar radiation is far more intense at the equator than the poles; therefore it tends to create differential heating on the earth's surface, which in turn gives rise to gradients of pressure in the atmosphere. The pressure gradients dictate the air movements and they are represented by "isobars" in a weather map (figure 2.1).

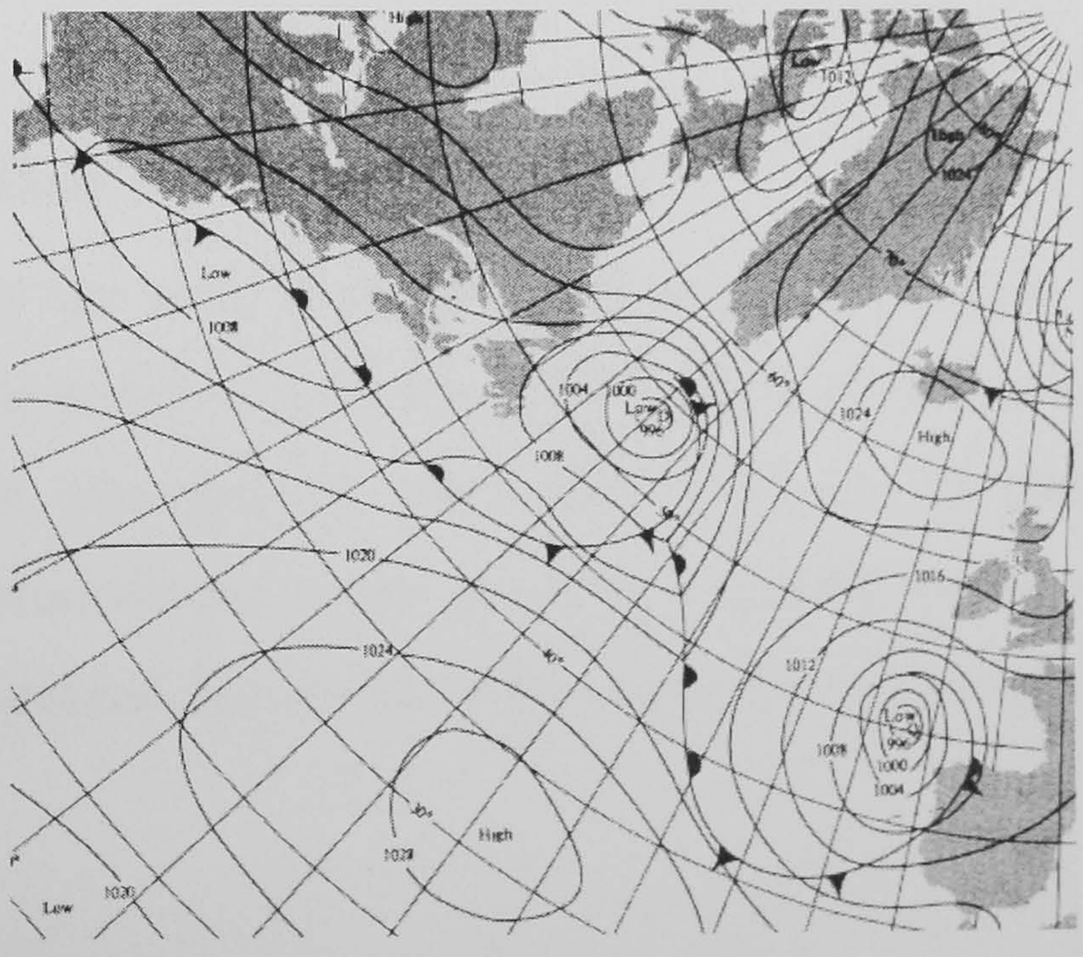

Figure 2.1 A weather map. The "isobars" are shown as contours. [From: Houghton and Carruthers (1976)]

In addition to the forces produced by these pressure differences, there are other forces due to the curvature and rotation of the earth. These forces acting together on a given mass of air result in various phenomena of wind (figure 2.2). At large heights above the ground level, the surface friction can be ignored and the resultant of these forces produces a steady motion that is parallel to the isobars. This atmospheric motion at that level is called *geostrophic wind* or *gradient wind* in meteorological terms. It is a macroscopic description of wind and the movement of the wind reported by weather forecast normally refers to the motion of gradient wind.

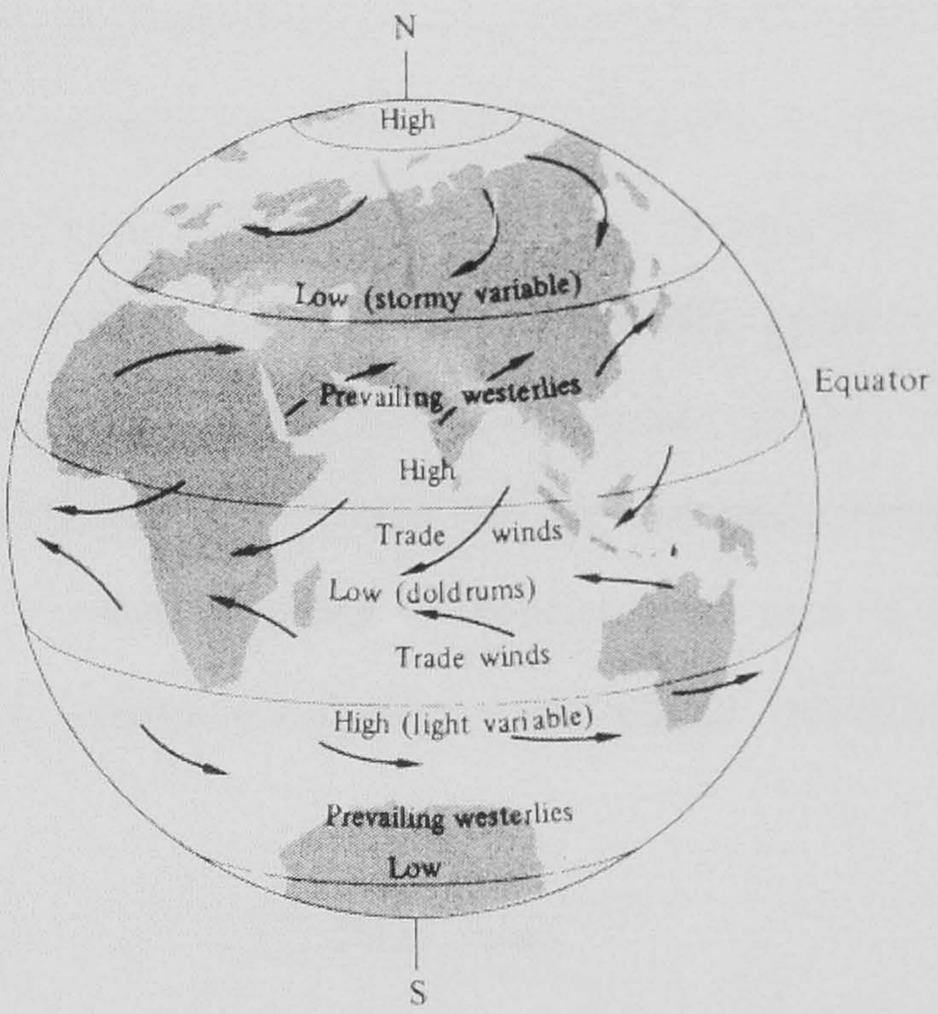

Figure 2.2 The general atmospheric circulation and the phenomena of wind. [From: Houghton and Carruthers (1976)]

2.2 The Gradient Wind

The gradient wind is the wind at the *gradient height* (z_G) where the wind velocity is purely affected by the pressure differences, the rotation of the earth (Coriolis force) and the earth's curvature. The gradient wind velocity V_G can be deduced with the same manner. In most circumstances where the effects caused by the earth's curvature are small enough to be ignored, Davenport (1967) suggests that the gradient velocity can be estimated by

$$V_G \approx \frac{\frac{dp}{dn}}{2\rho\omega\sin\lambda} = \frac{\frac{dp}{dn}}{\rho f_C} \tag{2.1}$$

where dp/dn is the pressure gradient between two isobars, ω the angular velocity of the earth, λ the latitude, ρ the air density and $f_C = 2\omega \sin\lambda = 1.458\times10^{-4} \sin\lambda \sec^{-1}$ is the Coriolis parameter. The estimates of the gradient height z_G are generally within the range of 300 ~ 600 m (Davenport, 1967; Harris, 1970; Counihan, 1974), subject to the terrain conditions but a later model proposed by Panofsky and Dutton (1983) suggests that the gradient height may be estimated by

$$z_G = 0.175 u_* / f_C \tag{2.2}$$

where u_* is a friction velocity defined as $u_* = (\tau_0 / \rho)^{1/2}$ in which τ_0 is the mean surface shear stress. In engineering practice, the gradient height is usually defined as the height at which the effects of surface shear become negligible and the wind speed V becomes a maximum or remains constant with height. Below the gradient height is identified as *planetary boundary layer* or *atmospheric boundary layer*, within which the wind velocity profile is significantly affected by the ground roughness and the thermal stability. This layer is closely related to human life and it is certainly of primary interests to the studies of various wind effects on people, buildings and structures.

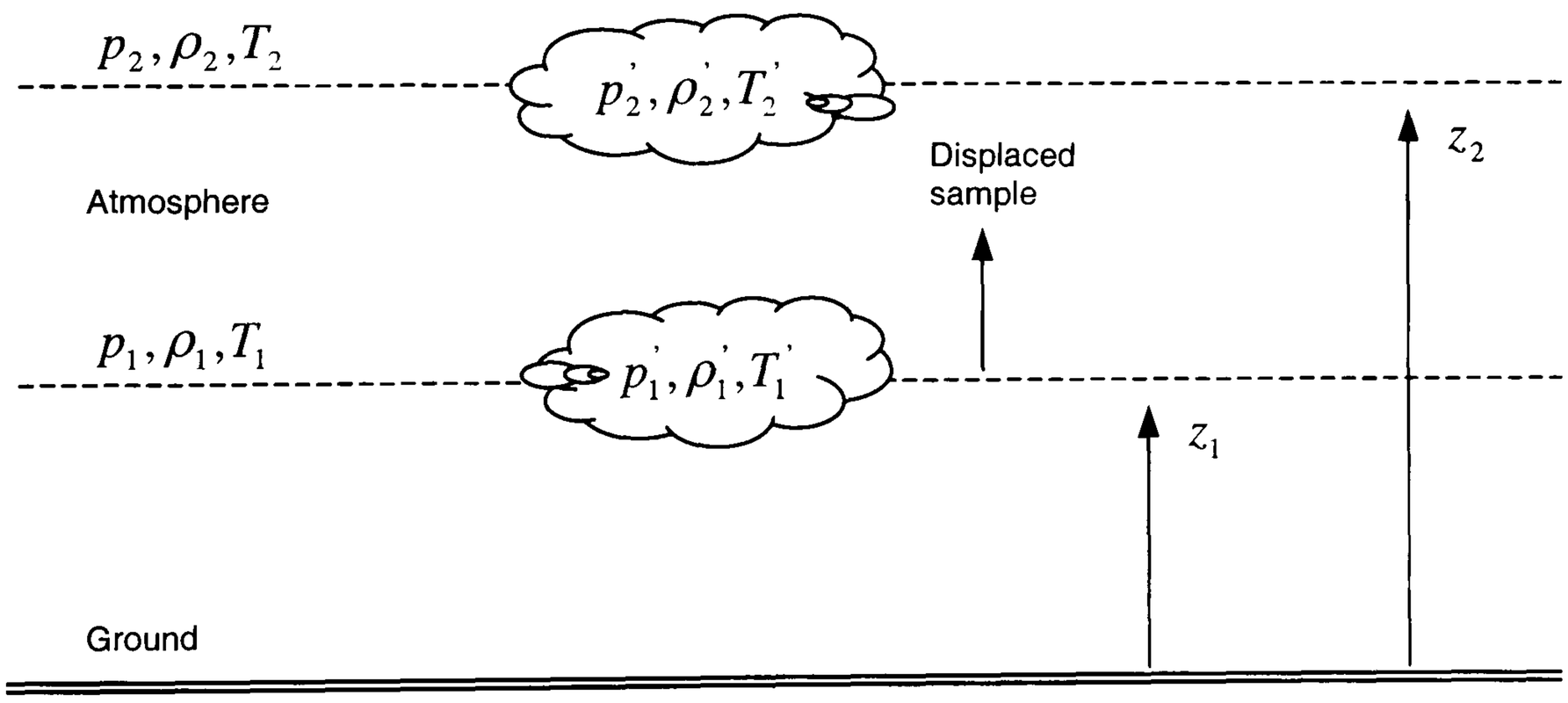

Figure 2.3 Illustrative description of atmospheric stability. [From: Houghton and Carruthers (1976)]

2.3 The Atmospheric Boundary Layer

In the boundary layer, the wind velocity is retarded by surface drag and friction. The surface friction also generates fluctuations in the flow (i.e. turbulence). The turbulent motions expedite the momentum exchange between air mass at different heights. Three

possibilities of air movement may arise due to the momentum exchange (figure 2.3). An element of air initially at level z_1 displaces upwards vertically to level z_2 in the atmosphere, the movement may change in three ways:

1) the displaced section may tend to return to its original position (if it becomes denser than the surrounding air);
2) it will tend to continue upwards (if it is less dense than the surroundings);
3) it will remain its new position (if its density becomes that of the air around it).

The three cases correspond to *positive stability*, *instability*, and *neutral stability* of the atmosphere, respectively. The state of stability profoundly affects the structure of the wind in the boundary layer. The main factor affecting the stability of the atmosphere is the gradient of temperature, i.e. the thermal stratification. In wind engineering practice, however, the atmosphere is generally assumed to be neutrally stable since the wind speed is usually strong enough to destroy the thermal stratification when the mechanical wind effects are of importance.

As the wind within the boundary layer is inherently turbulent, it is common to decompose the wind velocity into a mean quantity and a fluctuating component. In meteorological data, the mean wind velocity is usually taken from a mean value that is averaged from a period of one-hour observations. The mean wind speed is often called *hourly mean* wind speed. The fluctuating part of the wind velocity is the deviation from its mean value. With a mean value and a fluctuating component, the wind velocity in three dimensions can be expressed as

$$\tilde{\mathbf{V}}(x, y, z; t) = V(z) + \mathbf{v}(x, y, z; t) \tag{2.2}$$

where $\tilde{\mathbf{V}}$ is the instantaneous wind velocity and $\mathbf{v}$ is its fluctuating component above or below the mean value V. The scale of mean wind speed is proportional to the heights above ground level within the boundary layer.

Under the neutrally stable condition, the boundary layer can be divided at least into two sub-layers, one is the surface layer within which the shearing stress is approximately constant and the other one is a transient region in which the shearing stress changes its value gradually to zero at the gradient height. In the surface layer, which extends up to

100 m, the mean wind speed profile is accurately described by the well-established logarithmic profile:

$$V(z) = \frac{u_*}{\kappa} \ln\left(\frac{z}{z_0}\right) \tag{2.3}$$

where $V(z)$ is the mean wind speed at a height z, u_* is the friction velocity, z_0 the roughness height and κ is the von Kármán's constant (≈0.4). The value of z_0 can be determined by plotting the measured values of V against ln z or log z, and extrapolating the best-fitted straight line down to the axis where $V = 0$ (Arya, 1982).

Category	z_0 *(m)*	*Remark*
0	0.003	Corresponding to large expanses of water, mudflats, snow covered farmland and large flat areas of tarmac
1	0.01	Corresponding to flat grassland, parkland or bare soil, without hedges and with very few isolated obstructions
2	0.03	Meteorological standard, basic terrain roughness corresponding to typical UK farmland, nearly flat or gently undulating countryside, fields with corps, fences or low boundary hedges and few trees
3	0.1	Corresponding to farmland with frequent boundary hedges, occasional small farm structures, houses or trees
4	0.3	Corresponding to dense woodland, domestic housing typically between 10% and 20% plan-area density
5	0.8	Corresponding to city centres, comprising mostly four-storey buildings, or higher, typically between 30% and 50% plan-area density

Table 2.1 The categories of terrain and roughness parameters. [From: Cook (1985)]

Cook (1985) has suggested the values of z_0 with six easily recognisable terrain types (table 2.1) in the UK for design of wind load on buildings and structures.

To develop a velocity profile in equilibrium, a long upstream *fetch* (distance upwind of the site from the building) of uniform terrain roughness is required. Typically the distance of the fetch is 10 to 20 times the height of the building (ASCE, 1999).

From equation (2.3) the fluctuating components can also be determined with the value of u_*. Lumley and Panofsky (1964) suggest that

$$\sigma_u = 2.5u_* \quad \sigma_v = 2.0u_* \quad \sigma_w = 1.25u_* \tag{2.4}$$

where σ_u, σ_v and σ_w are the root-mean-square (r.m.s.) values of the three fluctuating components at streamwise, spanwise and vertical directions respectively. The scale of turbulence – *turbulence intensity* is defined by

$$I_i(z) = \frac{\sigma_i}{V(z)} \tag{2.5}$$

where I_i is the turbulence intensity, $i = u$, v, or w. Substitute σ_i and $V(z)$ with equation (2.3) and (2.4), the equation (2.5) becomes

$$I_u(z) = \frac{1.0}{\ln(z/z_0)} \qquad I_v(z) = \frac{0.8}{\ln(z/z_0)} \qquad I_w(z) = \frac{0.5}{\ln(z/z_0)} \tag{2.6}$$

For a moderately rough terrain, $z_0 = 0.03$ m, the turbulence intensity I_u at ground level is approximately 30%, indicating that the nature of the wind at ground level is highly turbulent. It is one of the major challenges in numerical simulations of the turbulent wind. The other expressions I_v and I_z are of less use if the main concerns are not of the directionality of the turbulence. The turbulence intensity referred in this study is equivalent to I_u unless specified.

Above the surface layer, the effects of the Coriolis force increases and the influence of surface roughness decreases; therefore the wind velocity profile departs significantly from the basic logarithmic form. Based on the universal velocity defect law and with experimental observations, Harris and Deaves (1981) have proposed a mean wind velocity profile throughout the entire atmospheric boundary layer as follows:

$$\frac{V(z)}{u_*} = \frac{1}{\kappa}\left[\ln(z/z_0) + a_1(z/z_G) + a_2(z/z_G)^2 + a_3(z/z_G)^3 + a_4(z/z_G)^4\right] \tag{2.7}$$

where $a_1 = 5.75$, $a_2 = -1.875$, $a_3 = -1.33$ and $a_4 = 0.25$ are constants. Equation (2.7) is an accurate expression of mean wind speed profile derived from boundary-layer theory and experimental data. It takes the roughness and the gradient height into account and it rectifies the inadequacy of the commonly used logarithmic profile that is only valid in the surface layer. In addition, Harris and Deaves (1981) also have proposed an estimation of σ_u / u_* throughout the entire atmospheric boundary layer as a measure of turbulence by the following equation:

$$\sigma_u / u_* = 2.63(1-6f_c / u_*)[0.538+0.09\ln(z/z_0)]^{16(1-6f_c/u_*)} \quad (2.8)$$

Although equations (2.7-8) are good representations of the wind velocity profiles in a naturally stable atmospheric boundary layer, they have not been widely used in engineering applications. Probably because their lengthy mathematical expressions and the uncertainties of natural wind make them less favourable to engineers.

Conventionally, a simple empirical formulation often used for the atmospheric boundary layers (not just the surface layers) is the well-known *power law* formula, which takes the form of

$$\frac{V(z)}{Vz_r} = \left(\frac{z}{z_r}\right)^{\alpha} \quad (2.9)$$

where z_r is a reference height and Vz_r is the mean velocity at that height. If z_r is taken as 10 m, which is a meteorological standard height, equation (2.9) becomes

$$V(z) = V_{10}\left(\frac{z}{10}\right)^{\alpha} \quad (2.10)$$

and, similarly if z_r is a gradient height, then the equation is written as

$$V(z) = V_G\left(\frac{z}{z_G}\right)^{\alpha} \quad (2.11)$$

where $V(z)$ is the wind velocity (m/s) at a height z (m), α is the exponent dependent on terrain conditions, V_{10} is the wind velocity at a height of 10 m above ground level and V_G is the wind velocity at the gradient height. Some typical values for different terrain conditions have been summarised in table 2.2. These types of terrain can be roughly classified as "rural", "suburban" and "urban" exposures (figure 2.4). The "power law" type of model has the advantage of simplicity and is of sufficient accuracy for most wind-engineering applications (ASCE, 1999). Consequently many wind simulations in wind tunnels tend to model the wind against a power-law profile, especially when modelling a full-depth of atmospheric boundary layer (Farell and Iyengar, 1999). The "power law" models are, however, purely empirical, lacking the support of proven theory and they do not consider the surface roughness as a scaling parameter. Therefore

it has been criticised that the power law models are not a good representation of velocity profile near the ground.

Type of terrain	z_G, *gradient height (m)*	α
(a) Open terrain with very few obstacles e.g. open grass or farmland with few trees, hedgerows and other barriers etc; prairie, tundra shores and low islands of inland lakes; deserts.	300	0.16
(b) Terrain uniformly covered with obstacles 10 to 15 m in height; e.g. residential suburbs; small towns; woodland and shrub, small fields with bushes, trees and hedges.	430	0.28
(c) Terrain with large and irregular objects; e.g. centres of large cities, very broken country with many windbreaks of tall trees, etc.	560	0.40

Table 2.2 Values of z_G and $1/\alpha$. [From: Davenport (1965), Harris (1970)]

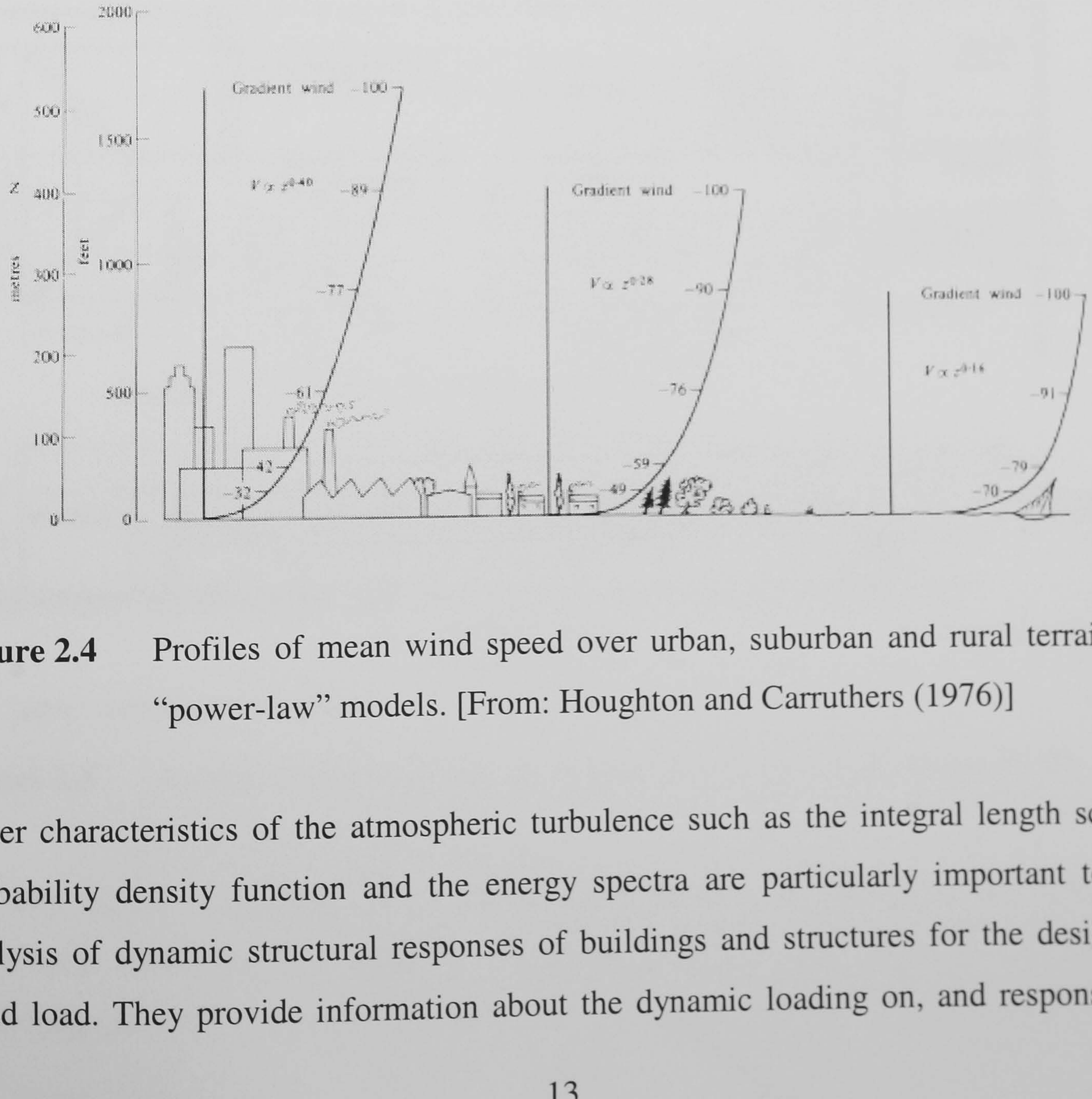

Figure 2.4 Profiles of mean wind speed over urban, suburban and rural terrain by "power-law" models. [From: Houghton and Carruthers (1976)]

Other characteristics of the atmospheric turbulence such as the integral length scales, probability density function and the energy spectra are particularly important to the analysis of dynamic structural responses of buildings and structures for the design of wind load. They provide information about the dynamic loading on, and response of,

building and aircraft structures in the atmospheric wind (ESDU, 1974). These are, however, not to be discussed for this study, as the scope is limited to the wind flows around buildings and the associated wind effects on people, rather than the wind forces upon buildings or structures.

2.4 Wind Tunnel Simulations of the Wind

A wind tunnel designed particularly for the simulations of the atmospheric boundary layers is called *boundary layer wind tunnel* (BLWT). Two types of BLWT are currently employed for wind studies, one is the closed-circuit tunnel (figure 2.5), and the other one is the open-circuit tunnel (figure 2.6). The closed-circuit tunnels are capable of modelling the thermal stratification of the atmosphere (Ogawa *et al.*, 1981) and they are ideal for the study of the atmospheric dispersion when the buoyancy and convection effects are of concerns (Cermak, 1970). In contrast, the open-circuit tunnels are usually applied in modelling the neutrally stable wind, as it is difficult to produce and maintain the temperature gradients in this type of tunnels.

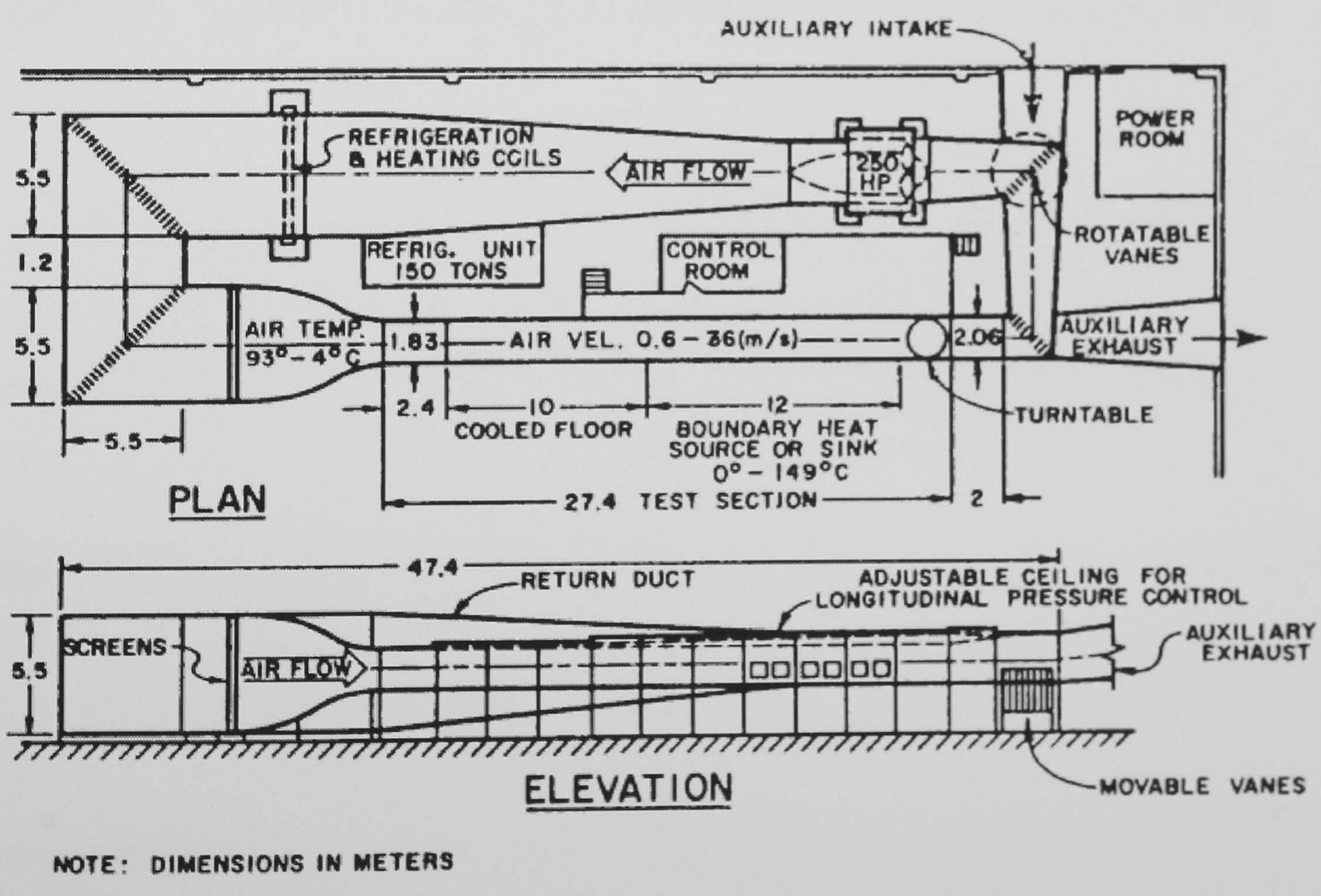

Figure 2.5 A close-circuit boundary layer wind tunnel. [From: Cermak (1979)]

The key feature of a BLWT is the test section length L. A fully developed boundary layer with scaled gradient heights z_G from 0.5 to 1.5 m are usually required for modelling the wind effects on building models in the common scale range from 1:200 to

1:600. This requires L to be in the range between 15 m and 30 m without the use of boundary-layer argumentation devices at the test-section entrance (figure 2.7).

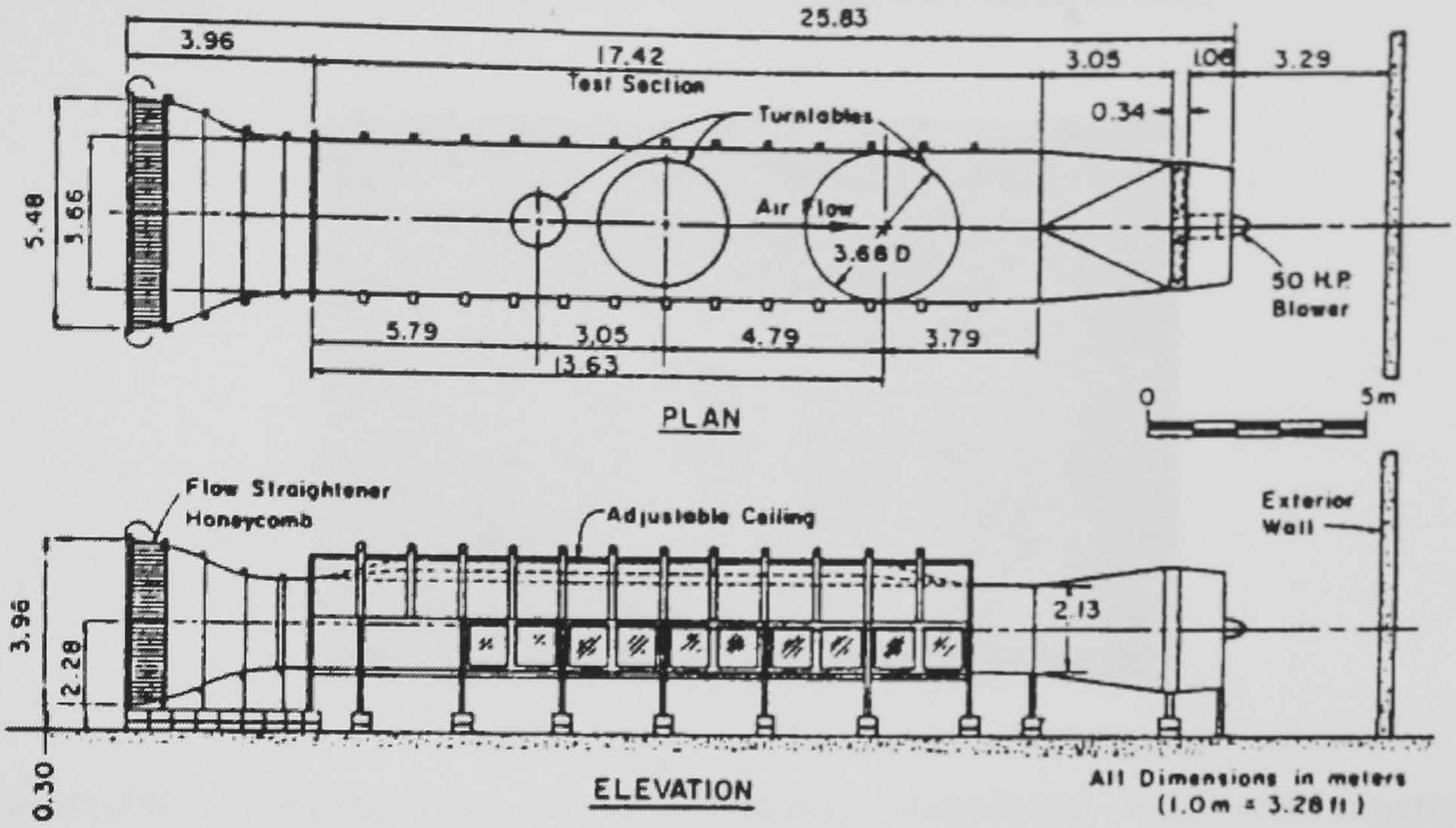

Figure 2.6 An open-circuit boundary layer wind tunnel. [From: Cermak (1979)]

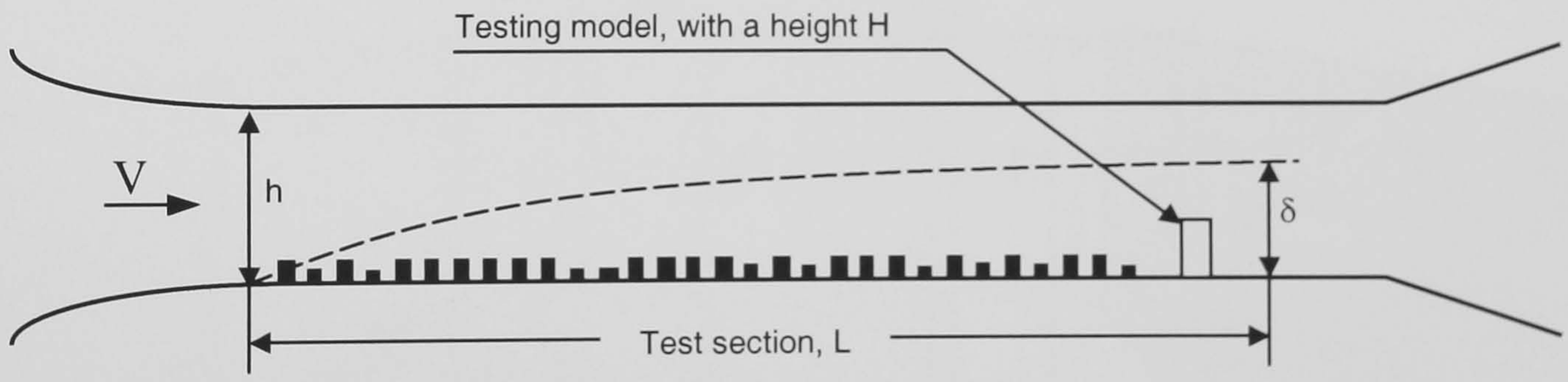

Figure 2.7 The simulated boundary layer developed naturally in a long-test-section wind tunnel (L / h >12), where δ is the thickness of the boundary layer and the δ should be greater than 1 ~ 2H. [From: Cermak (1979)]

If using the argumentation devices, the thickness of ABL can be increased from 0.5 m at L = 15 m without argumentation devices to 1.5 m by appropriately setting some turbulence generators at the entrance in an open-circuit wind tunnel (Cermak, 1981). Cermak (1982) has also presented a simulation of the atmospheric boundary layer (ABL) in a long test section tunnel with and without argumentation devices for comparison and he concludes that there is no significant loss of similarity by

introducing these devices to increase the thickness of ABL. These argumentation devices such as turbulence generators, roughness elements and barrier walls are therefore deemed necessary in those tunnels with a shorter test section. Currently there are two categories of ABL simulations using the argumentation devices.

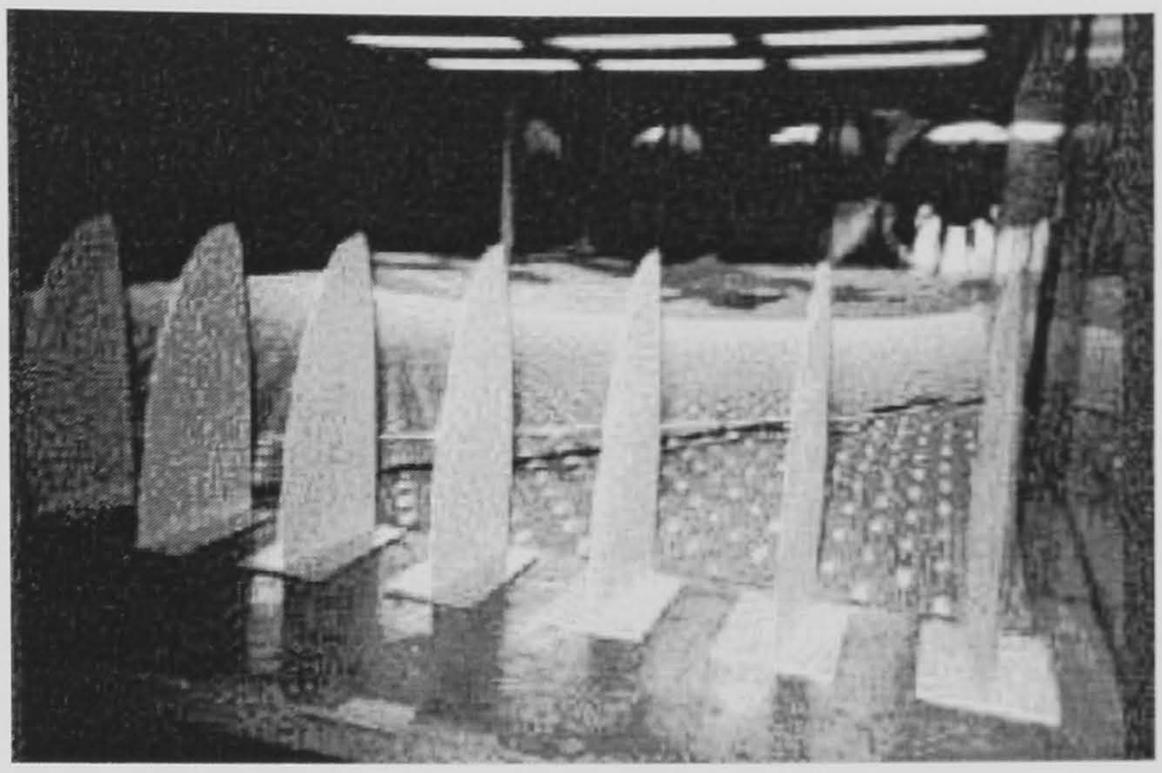

Figure 2.8 Counihan-type vortex generators, castellated wall and roughness elements for a full-depth simulation of the ABL. [From: Flow Science (2002)]

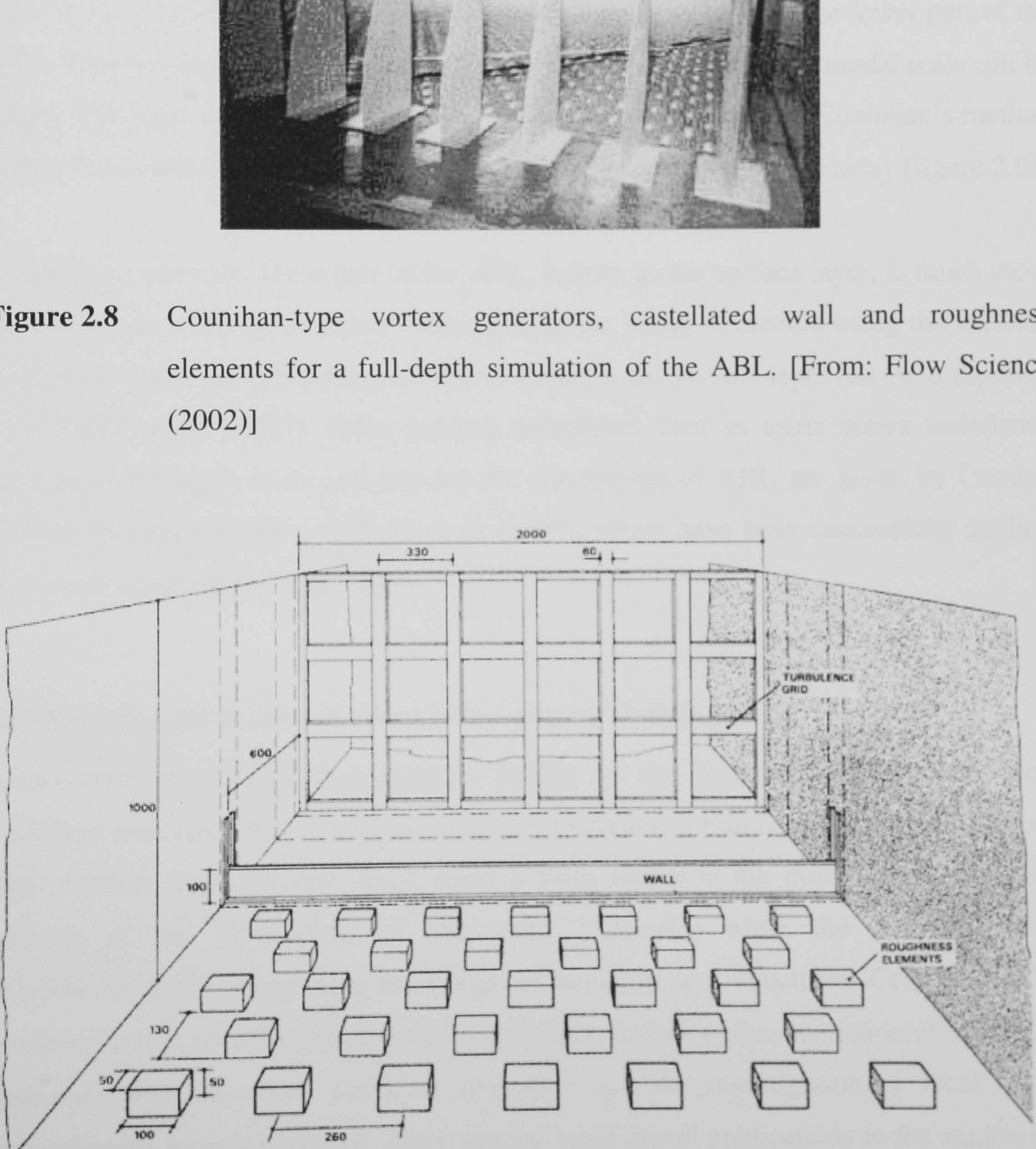

Figure 2.9 Cook's method for a part-depth simulation of the ABL [From: Cook 1982]

The two categories are the full-depth simulation and the part-depth simulation. For a full-depth simulation, the method proposed by Counihan (1969) has been applied in many tunnels. He uses an array of elliptical vortex generators, a castellated wall and roughness elements (figure 2.8) to simulate the ABL up to the gradient height. A shortcoming of his method is that the model scale is likely to be small, typically in the range between 1/400 and 1/600 in a medium-size wind tunnel.

In contrast to Counihan's method, Cook (1973, 1978, 1982) suggests a method using a grid frame, a barrier wall and roughness elements to simulate only the lower part of the ABL. This is a preferable way of testing low-rise buildings since the model scale can be larger. The most significant difference between Cook's method and Counihan's method is that Cook makes use of a grid frame instead of the vortex-generator array (figure 2.9).

In addition, since the lower part of the ABL, known as the surface layer, is much more relevant to the built environment where people are living, a method using the inclined horizontal vanes and oscillating airfoils to simulate the surface layer has been reported by Cermak *et al.* (1995). Other modern techniques such as using active turbulence generators (multiple fans) and jets for the simulations of ABL are given by Cermak (1987), Marshall (1984) and Nishi *et al.* (1999), which have been successfully applied to various wind engineering studies.

2.5 Wind Tunnel Studies of Wind Flows around Buildings

Traditionally the BLWT is a desirable facility for the studies of wind effects upon buildings and structures. Numerous wind tunnel studies of buildings and structures have been conducted in the past, since using a wind tunnel is the most appropriate way hitherto in the simulations of the wind, especially when the accurate wind characteristics are essential to the design of buildings and structures. Cermak (1977) presented a typical wind tunnel study of structures, including the simulation of the ABL, instrumentation, dynamic structural responses and the investigation of local wind environments around buildings. More general wind tunnel applications to the studies of a wide range of wind engineering problems have been addressed by Cermak (1975). The modelling criteria, as discussed by Tieleman (1982), Cermak (1984), Simiu and Scanlan (1996), need to be considered for similarity requirements. The requirements in

general are the dynamic similarity, geometric similarity as well as other important properties. The minimum requirements proposed by ASCE (1999) are

1) vertical distributions of the mean wind speed and the intensity of the longitudinal turbulence component shall be modelled;
2) important properties of atmospheric turbulence, in particular the relevant length scale of the longitudinal turbulence component, shall be modelled to approximately the same scale as that used to model buildings or structures; and
3) the longitudinal pressure gradient in the wind tunnel test section should be sufficiently small as not to significantly affect the results.

The scale factors involved in a wind tunnel testing of wind flows around buildings are the length scale $\mathscr{L}$, the velocity scale $\mathscr{V}$ and the frequency or time scale $\mathscr{T}$. The selection of a proper length scale is essential, as the model can neither be too small to present required details for observation, nor be too large for the simulation of a proper ABL to be developed. This puts the scale limits for the average size of wind tunnel between 1/100 and 1/500. This raises a problem for wind tunnel testing, as the scaled model is hundreds times smaller than the prototype; therefore the wind velocity in a wind tunnel has to be hundreds times larger than the normal wind velocity in full scale if the Reynolds number similarity needs to be fulfilled. Fortunately, the equality of model and full-scale Reynolds number, based on the mean wind speed V_h and a characteristic dimension of the structure L_b is not necessary for sharp-edged structures, provided that the model Reynolds number $L_b V_h / \nu$ is not less than 10^4 (ASCE, 1999). Since the kinetic viscosity of air at 20°C is very small ($\nu = 1.51\times10^{-5}$), the Reynolds number in either wind tunnel testing or the full scale measurement is normally greater than 10^4. As a result, certain wind tunnel testing of buildings and structures can be seen as independent of Reynolds number. Thus the velocity scale is free of choice. The choice is made so that a good response to instrumentation can be obtained. The scales now can be determined by

$$\text{Length scale } \mathscr{L} = L_m / L_p \tag{2.12}$$

$$\text{Velocity scale } \mathscr{V} = V_m / V_p \tag{2.13}$$

The suffixes *m* and *p* refer to the model and prototype respectively. Once the two scales are chosen, the time scale is automatically given by

$$\text{Time scale } \mathcal{T} = T_m / T_p = \mathcal{L} / \mathcal{V} \tag{2.14}$$

The choice of the wind speed in a wind tunnel test is usually the normal operating fan speed. The time scale is consequently affected by the length scale and the minimum response of instrumentation. The sampling rate can be set equivalent to one hour in full scale for the hourly-mean values and the turbulence statistics.

There are many wind tunnel studies of wind environment around buildings presented in the literature. The variations of wind speeds in the vicinity of buildings and the effects on people are of the primary concerns in these studies. Isyumov and Davenport (1977) presented a methodology for predicting the wind environment around buildings using a BLWT. Lawson and Penwarden (1977) carried out their studies with and without a wind tunnel and found that the mechanical wind effects would be of greater influences on people's comfort. In addition, Hunt *et al.* (1976) and Murakami *et al.* (1980) also completed a number of studies for suggesting wind comfort criteria based on various wind tunnel experiments. Arens *et al.* (1989) and Durgin (1989) also presented a number of case studies to propose wind ordinance and comfort criteria for two US cities with wind tunnels. At a larger scale, wind tunnels have been used to study the wind over a city (Flay and Andrews, 1995).

Researches of the wind tunnel techniques for the studies of ground-level winds or pedestrian-level winds have been fruitful. Durgin and Chock (1982) presented a brief review of past studies about pedestrian-level winds, including the typical procedures, wind tunnel techniques and their limitations for making estimates in the assessment of pedestrian winds. Wu and Stathopoulos (1993) discussed various widely used methods (hot-wires, hot-films and pressure sensors) for the wind tunnel studies of pedestrian-level winds and assessed some newly developed techniques such as Laser-Doppler Anemomentry, Particle-Image Velocimetry, and Infrared Thermography for suchlike wind studies. In addition, a surface sensor devised by Irwin (1981) and was further investigated by Wu and Stathopoulos (1994) also became an option in the measurement of pedestrian-level winds.

The studies of pedestrian-level winds (PLW) are to evaluate the wind conditions along streets, pedestrian ways and in the vicinity of buildings. The objectives of PLW studies are normally to identify the areas where the wind conditions may be potentially adverse and to propose viable solutions to the original design. A typical approach of PLW study using a BLWT is illustrated as figure 2.10. The criteria of wind comfort, however, are not universally agreed and it has been proven difficult to establish a set of criteria that are generally accepted (Bottema, 2000). The unsteadiness of PLW is a major difficulty in this aspect because the parameters (mean values, root-mean-square variations and peak values) involved are in different relationships when wind direction varies (ASCE, 1999).

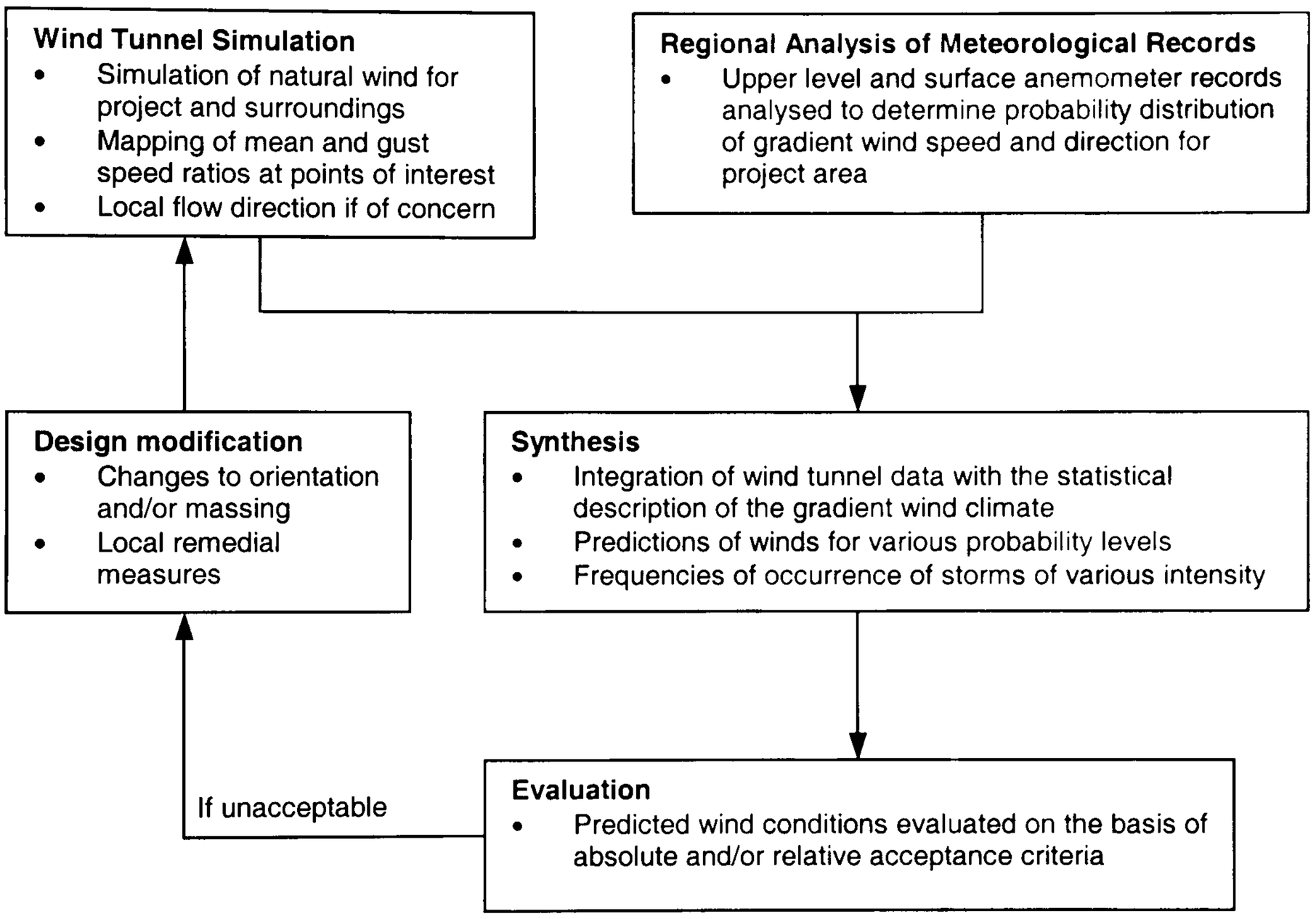

Figure 2.10 Outline of typical study of the pedestrian-level wind environment. [From: Isyumov (1978)]

Most of the existing criteria are based on mean wind velocities and gusts. The studies of Hunt *et al.* (1976) and Murakami *et al.* (1980) indicate that the gusting wind component is significant in determining what people perceive as windy. Further, both found that gusts lasting less than 2 or 3 seconds do not affect people's balance. The term *effective gust* proposed by them becomes a preferred parameter to evaluate the pedestrian comfort. The effective gust is defined by

$$V_{eff} = \overline{V} + gV_{rms} \tag{2.15}$$

where $\overline{V}$ is the mean wind speed, V_{rms} the root-mean-square (r.m.s.) value and g is a constant. From field measurements and observations, the peak gust wind speeds are between 1.5 and 2.0 times the mean, and with a knowledge of the standard deviation from the mean (i.e. the r.m.s. value), it is possible to deduce the mean gust speed (Melbourne, 1978). If the distribution of gusts were Gaussian, then for g = 3.5, V_{eff} would be approximately equal to the 2 or 3 second peak gust and lower values of g represent gusts lasting longer (ASCE, 1999). Hunt *et al.* (1976) chose g = 3.0 and Murakami *et al.* (1980) chose 3.5. Other values have also been used, such as Isyumov (1978) chose g = 1.5. An acceptable wind speed determined by (2.15) for sitting may be $V_{eff} < 6.0$ m/s and a speed of $V_{eff} < 7.2$ m/s may be acceptable for walking. Higher values 6.0 m/s $\leq V_{eff} \leq$ 9.0 m/s may be tolerable for various outdoor activities. When $V_{eff} \geq 20$ m/s it is normally considered dangerous for pedestrians. Arens (1982) has summarised a general guidance to apply the wind comfort criteria on considering pedestrian winds during building design and more general discussions about the study of wind environment around buildings have been given by Penwarden and Wise (1975).

2.6 Full-Scale Measurements of Wind Flows around Buildings

Full-scale investigations are expensive, difficult and time-consuming, and depend on the uncertainties of the weather (Lawson, 1980). Consequently the full-scale measurements are rarely attempted and the data available to public is scarce. Most of the full-scale measurements are concerned with the surface pressure or the aeroelastic characteristics of a building or structure, such as the works done by Dalgliesh (1982), Lee (1982), and Holmes (1982). Their wind tunnel data are generally in good agreements with their full-scale measurements. More recent full-scale measurements have been reported by Richards and Hoxey (1993), Visser and Cleijine (1994), and Flay and Andrews (1995). The paper by Visser and Cleijine (1994) is directly related to wind comfort studies and they have observed that their wind tunnel data agree well with the full scale measurements when a longer term (yearly) average is taken, whereas the agreement is less satisfactory if the averaging time is shorter. As the simulated wind in a wind tunnel is normally in neutrally stable conditions but suchlike circumstances are infrequent in real life. Therefore some discrepancies can exist if comparing wind tunnel studies with full-scale measurements. Usually wind tunnel models tend to give conservative results when some local details such as the landscaping, trees and windbreaks are omitted in the wind tunnel test.

Another difficulty to obtain the full-scale measurement of ground-level winds is that the assessment of wind comfort is usually carried out at the stage of masterplanning where the new buildings have not been constructed yet. Using wind tunnel or other numerical methods is the only solution at this stage. After all, the wind environment around buildings is more complicated, unlike the indoor environment in which the environmental parameters such as the humidity and air exchange rate can be controlled and monitored properly for a full-scale test. As a result, most of the experimental data about external flows around buildings are generated in wind tunnels because the simulated winds are relatively easier to be controlled and the uncertainties of weather can be excluded. In general, wind tunnel experiments are comparable with full-scale measurements, provided that the similarity requirements of importance can be satisfied.

2.7 Summary

This chapter has reviewed the wind, the structure of atmospheric boundary layer and some wind tunnel techniques and applications. The turbulent nature of the wind makes it difficult to be correctly modelled and the best way of modelling the fluctuating wind hitherto is using the boundary layer wind tunnel. Wind tunnel studies of pedestrian-level winds have been well established and two main parameters influencing pedestrian comfort are the mean wind speed and its r.m.s. value.

Some wind tunnel techniques presented in this chapter will be applied in chapter 5. Another important part of this study – Computational Fluid Dynamics (CFD), is to be depicted and discussed in next chapter.

Chapter 3 Wind Simulations Using Computational Fluid Dynamics – Fundamentals and Theoretical Framework

Computational Fluid Dynamics (CFD) is a scientific tool using computational methods to study a wide variety of flows for academic research or engineering applications. Applying CFD to simulate and analyse various wind flows around or upon buildings is a relatively new discipline and it has been increasingly important in the industry. In company with the advancement of computer technologies, the techniques of CFD may have the potential to provide an alternative way that is less time-consuming and more cost-effective for wind studies (Rodi, 1995). This chapter is to glimpse the underlying theories and elucidate some techniques that are currently employed by CFD codes.

3.1 Governing Equations

The wind is subject to a number of externally applied forces, including pressure, gravity and shear. These forces can be classified into surface forces and body forces. There are a number of ways to derive the governing equations and the most common method is the *control volume approach*.

3.1.1 Conservation of Mass

The law of conservation of mass states that mass can be neither created nor destroyed. Consider a control volume of fluid as illustrated in figure 3.1, the net mass flow through the surface of the control volume is

$$\int_{c.s.} \rho(\mathbf{v}\cdot\mathbf{n})dS \tag{3.1}$$

and the rate of change of the mass within the control volume is

$$\frac{\partial}{\partial t}\int_{c.v.} \rho dV \tag{3.2}$$

where ρ is the density, **v** the flow velocity vector, and **n** is the unit vector normal to the surface of the control volume.

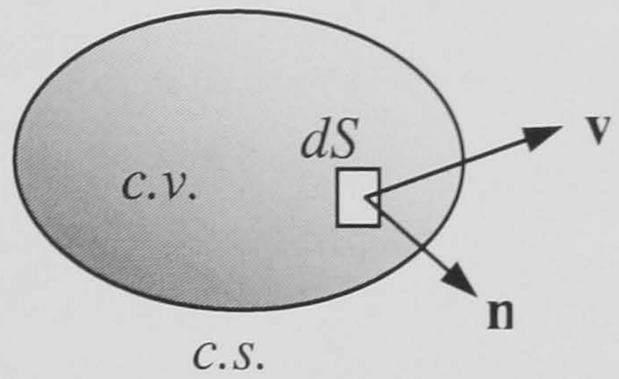

Figure 3.1 A control volume (CV) of fluid with a control surface (CS).

The plus (+) sign can be assigned to the mass flow through the control surface if the net mass flow is out of the control surface and the minus (-) sign is assigned to the rate of change of the mass if the mass decreases within the control volume. Since the mass is conserved, the net mass flow must be equal to the rate of change of the mass and, the sum of the net mass flow through the control surface and the rate of change of the mass within the control volume must equal to zero, therefore

$$\int_{c.s} \rho(\mathbf{v}\cdot\mathbf{n})dS + \frac{\partial}{\partial t}\int_{c.v.} \rho dV = 0 \tag{3.3}$$

By applying Gauss's divergence theorem, equation (3.3) can be rewritten as

$$\int_{c.v.} \rho \mathrm{div}(\mathbf{v})dV + \frac{\partial}{\partial t}\int_{c.v.} \rho dV = 0 \tag{3.4}$$

Integrating equation (3.4) leads to the differential form of equation and it becomes

$$\frac{\partial \rho}{\partial t} + \mathrm{div}(\rho\mathbf{v}) = 0 \tag{3.5}$$

Equation (3.4) or (3.5) is also identified as *continuity equation*.

3.1.2 Conservation of Momentum

The second set of equations is the momentum equations, which are also known as "Navier-Stokes equations" (N-S equations). Newton's second law of motion states that the momentum is conserved and the time rate of change of momentum of a system is equal to the resultant force acting upon that system, i.e.

$$\frac{d(m\mathbf{v})}{dt} = \sum \mathbf{F} \tag{3.6}$$

Mass (m) and momentum ($m\mathbf{v}$) are considered as two of the principal *extensive* properties of fluid. The extensive property denotes that the property is dependent on the amount of matter considered. Conversely, the *intensive* properties such as density ρ (mass per unit volume) and velocity $\mathbf{v}$ (momentum per unit mass) are independent of the amount of matter considered. For a given quantity of matter or control mass (CM), the relationship between the extensive property Φ and the intensive property ϕ is

$$\Phi = \int_{\Omega_{CM}} \rho\phi d\Omega \tag{3.7}$$

where Ω_{CM} stands for the volume occupied by the CM. The Ω_{CM} is not necessarily equal to a CV, as illustrated in figure 3.2.

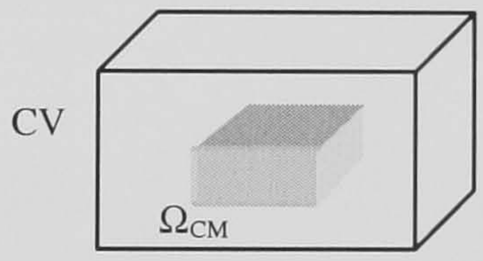

Figure 3.2 An illustration of Ω_{CM} and CV. The Ω_{CM} is the volume occupied by the mass and the CV is a defined region where the governing equations of flows are derived from.

In equation (3.7), $\phi = 1$ for the mass and $\phi = \mathbf{v}$ for the momentum. The rate of change of a given property Φ in the control mass is made by two contributions, as following:

$$\frac{d\Phi}{dt} = \frac{d}{dt}\int_{\Omega_{CM}} \rho\phi d\Omega = \underbrace{\frac{d}{dt}\int_{c.v.} \rho\phi dV}_{\substack{\text{rate of change} \\ \text{of } \phi \text{ within a CV}}} + \underbrace{\int_{c.s.} \rho\phi(\mathbf{v}-\mathbf{v}_b)\cdot\mathbf{n}dS}_{\substack{\text{net flux through} \\ \text{the surface of the CV}}} \tag{3.8}$$

where $\mathbf{v_b}$ is the velocity with which the control surface is moving. When $\phi = \mathbf{v}$, the left hand side of equation (3.8) becomes

$$\frac{d(m\mathbf{v})}{dt} = \int_{c.s.} \rho\mathbf{v}(\mathbf{v}-\mathbf{v}_b)\cdot\mathbf{n}dS + \frac{d}{dt}\int_{c.v.} \rho\mathbf{v}dV \tag{3.9}$$

Since the momentum is possessed by a given amount of matter when it is in motion, a mass flow through the control surface therefore produces momentum which is equal to the product of the mass flow through the surface and its velocity, i.e. the *momentum flux*. Equation (3.9) states that the rate of change of momentum of a given quantity of mass is equal to the sum of the momentum flux through the control surface and the rate of change of the momentum within the control volume. For a fixed CV, the control surface is not moving, i.e. $\mathbf{v_b} = 0$ and the first derivative of the second term on the right hand side of equation (3.9) becomes a local (partial) derivative. The time rate of change of momentum is equal to the externally applied forces; therefore equation (3.9) can be rewritten as

$$\frac{\partial}{\partial t}\int_{c.v.}\rho\mathbf{v}dV + \int_{c.s.}\rho\mathbf{v}\mathbf{v}\cdot\mathbf{n}dS = \sum\mathbf{F} \tag{3.10}$$

The externally applied forces – body forces and surface forces are the resultant forces acting upon the control volume. Gravity is a body force and the surface forces refer to pressure, normal and shearing stresses. Equation (3.10) becomes

$$\frac{\partial}{\partial t}\int_{c.v.}\rho\mathbf{v}dV + \int_{c.s.}\rho\mathbf{v}\mathbf{v}\cdot\mathbf{n}dS = \underbrace{\int_{c.s.}\mathbf{T}\cdot\mathbf{n}dS}_{\text{Surface forces}} + \underbrace{\int_{c.v.}\rho\mathbf{g}dV}_{\text{Body force}} \tag{3.11}$$

where $\mathbf{g}$ is the acceleration of gravity, $\mathbf{T}$ is the stress tensor. Since momentum is a vector quantity, the momentum (convective and diffusive) fluxes through a CV boundary are the scalar products of second rank tensors ($\rho\mathbf{v}\mathbf{v}$ and $\mathbf{T}$) with the surface vector $\mathbf{n}dS$. Ferziger and Peric (1999) write the stress tensor $\mathbf{T}$ in the form of

$$\mathbf{T} = -\left(p + \frac{2}{3}\mu\mathrm{div}(\mathbf{v})\right)\mathbf{I} + 2\mu\mathbf{D} \tag{3.12}$$

$$\mathbf{D} = \frac{1}{2}[\mathrm{grad}\mathbf{v} + (\mathrm{grad}\mathbf{v})^{\mathrm{T}}] \tag{3.13}$$

where $\mathbf{I}$ is the unit tensor, p the static pressure, $\mathbf{D}$ the rate of strain tensor and μ is the dynamic viscosity of fluid. The above equations can be written, in index notation in Cartesian coordinates, as follows:

$$T_{ij} = -\left(p + \frac{2}{3}\mu \frac{\partial u_j}{\partial x_j} \right)\delta_{ij} + 2\mu D_{ij} \tag{3.14}$$

$$D_{ij} = \frac{1}{2}\left(\frac{\partial u_i}{\partial x_j} + \frac{\partial u_j}{\partial x_i} \right) \tag{3.15}$$

where δ_{ij} is the Kronecker symbol ($\delta_{ij} = 1$ if $i = j$ and $\delta_{ij} = 0$ for $i \neq j$). Applying the Gauss's divergence theorem again with respect to equation (3.11), the differential form of the momentum conservation equation reads

$$\frac{\partial(\rho \mathbf{v})}{\partial t} + \mathrm{div}(\rho \mathbf{v}\mathbf{v}) = \mathrm{div}\mathbf{T} + \rho \mathbf{g} \tag{3.16}$$

The continuity equation (3.5) and the momentum equation (3.16) are written in a coordinate-free form. Their corresponding expressions using index notation in Cartesian coordinate are

$$\frac{\partial \rho}{\partial t} + \frac{\partial(\rho u_i)}{\partial x_i} = 0 \tag{3.17}$$

$$\frac{\partial(\rho u_i)}{\partial t} + \frac{\partial(\rho u_i u_j)}{\partial x_j} = -\frac{\partial p}{\partial x_i} + \frac{\partial}{\partial x_j}\left[\mu\left(\frac{\partial u_i}{\partial x_j} + \frac{\partial u_j}{\partial x_i} \right) - \frac{2}{3}\delta_{ij}\frac{\partial u_k}{\partial x_k} \right] + g_i \tag{3.18}$$

In addition to the momentum equations and continuity equation, there are energy equations and state (of gas) equation constructing a complete set of equations to describe the flows involving heat and other thermodynamic process. These equations, however, not to be derived because the wind flows have been assumed to be adiabatic and the wind speed is high enough to destroy usual thermal stratifications. Therefore only the continuity and momentum equations are of primary concerns at this stage. Moreover, a further simplification can be made when the winds are treated as incompressible flows.

3.1.3 Equations of Incompressible Flows

The generic momentum equations and continuity equation derived above are rather complicated since the variations of density have to be considered. If the density is a constant, then the fluid is said to be incompressible and the above equations can be largely simplified. The condition to determine whether a flow is incompressible is the

ratio of its velocity to the speed of sound. The ratio is known as "Mach number", defined as

$$\mathrm{Ma} = \frac{v}{c} \tag{3.19}$$

where v is the velocity of flow and c is the speed of sound. At low Mach numbers ($\mathrm{Ma} \leq 0.3$), the flow is generally considered as incompressible (Ferziger and Peric, 1999; White, 1999). In most of the practical engineering applications concerning the wind, the wind speed considered for environmental design is normally not greater than 20 m/s and therefore the Mach number is much less than 0.3. Consequently using the incompressible flow equations is sufficient for the numerical simulations of suchlike flows. The incompressible flow equations can be written as follows:

$$\frac{\partial u_i}{\partial x_i} = 0 \tag{3.20}$$

$$\frac{\partial u_i}{\partial t} + \frac{\partial (u_i u_j)}{\partial x_j} = -\frac{1}{\rho}\frac{\partial p}{\partial x_i} + \frac{\mu}{\rho}\frac{\partial}{\partial x_j}\left(\frac{\partial u_i}{\partial x_j} + \frac{\partial u_j}{\partial x_i}\right) \tag{3.21}$$

The body forces have been neglected since the atmosphere has been assumed to be neutrally stable and those forces are important only in cases when there is a free surface or when the density distribution is inhomogeneous (Schlichting, 1968). There are four variables; p, u, v and w in equations (3.20-21) and these equations also form a set of closed equations to solve the four unknowns. Theoretically all the variables are solvable. Nevertheless, equations (3.20-21) are non-linear partial differential equations and due to the insurmountable difficulties in mathematics, an analytical and exact solution to the equations is still not known yet, except for the simplest flows. A way to solve the primitive equations numerically is using Direct Numerical Simulation (DNS) but it is currently limited to academic interests for research.

3.2 Turbulence Modelling

Direct Numerical Simulation solves the governing equations without any "turbulence model" since it resolves the flow field from the smallest eddies to the largest ones and their variations at each time step are also resolved. It is certainly not suitable for highly turbulent flows because their wide range of length, velocity and time scales will result in enormous computation that requires huge computing power and time. For these

flows, an alternative is to devise a "turbulence model" for the (modified) governing equations. A considerable amount of the models have been proposed in the field of fluid dynamics but the majority of which can be classified by the following categories:

- Space-filtered models
- Time-averaged models

The representative of the first category is Large Eddy Simulation (LES), which is to simulate the large (low frequency, energy-containing) eddies directly whereas the small (high frequency, energy-dissipating) eddies are modelled with some assumptions. It still needs to resolve the flow field at each time step but the number of grids required for spatial resolution can be less than DNS because it is not necessary to resolve the smaller eddies which are not influential to the mean flows. The models employed in LES are known as "subgrid models".

In contrast, the time-averaged models are devised for the closure of the Reynolds Averaged Navier-Stokes (RANS) equations, which are essentially mean flow equations but there are additional terms representing turbulence contributions that cannot be eliminated from the averaging process. These additional terms need be determined by modelled equations and these models are generally termed as RANS models. The most widely used RANS models in industry are two-equation models, one of which is the most well-known k-ε model.

3.2.1 Large Eddy Simulation

LES employs a "filter function" to determine the spatially resolvable eddies and leaves the unresolved eddies to be modelled. The filter function is to resolve the flow properties (velocity, pressure, etc.) of a large eddy within a specified volume. A general spatial, volume averaged function can be expressed as

$$\overline{f}(\mathbf{r}) = \int_{-\infty}^{\infty}\int\int G(\mathbf{r}-\mathbf{r}')\cdot f(\mathbf{r}')\,\mathrm{d}\mathbf{r}' \tag{3.22}$$

where $\mathbf{r}$ is a space vector $(\mathbf{r} = x_1\mathbf{i} + x_2\mathbf{j} + x_3\mathbf{k})$, $G(\mathbf{r}-\mathbf{r}')$ is a filter function and $\int_{-\infty}^{\infty}\int\int G(\mathbf{r}-\mathbf{r}')\,\mathrm{d}\mathbf{r}' = 1$. The one-dimensional "box" or "top hat" filter is given as

$$G(x-x') = \begin{cases} \dfrac{1}{\Delta} & \text{for } |x-x'| \le \dfrac{\Delta}{2} \\ \\ 0 & \text{elsewhere} \end{cases} \tag{3.23}$$

where the Δ is the characteristic filter width. Therefore a three-dimensional filter can be written as

$$G(x_i - x_i') = \begin{cases} \dfrac{1}{\Delta^3} & \text{for } \left|x_i - x_i'\right| \le \dfrac{\Delta}{2} \\ \\ 0 & \text{elsewhere} \end{cases} \tag{3.24}$$

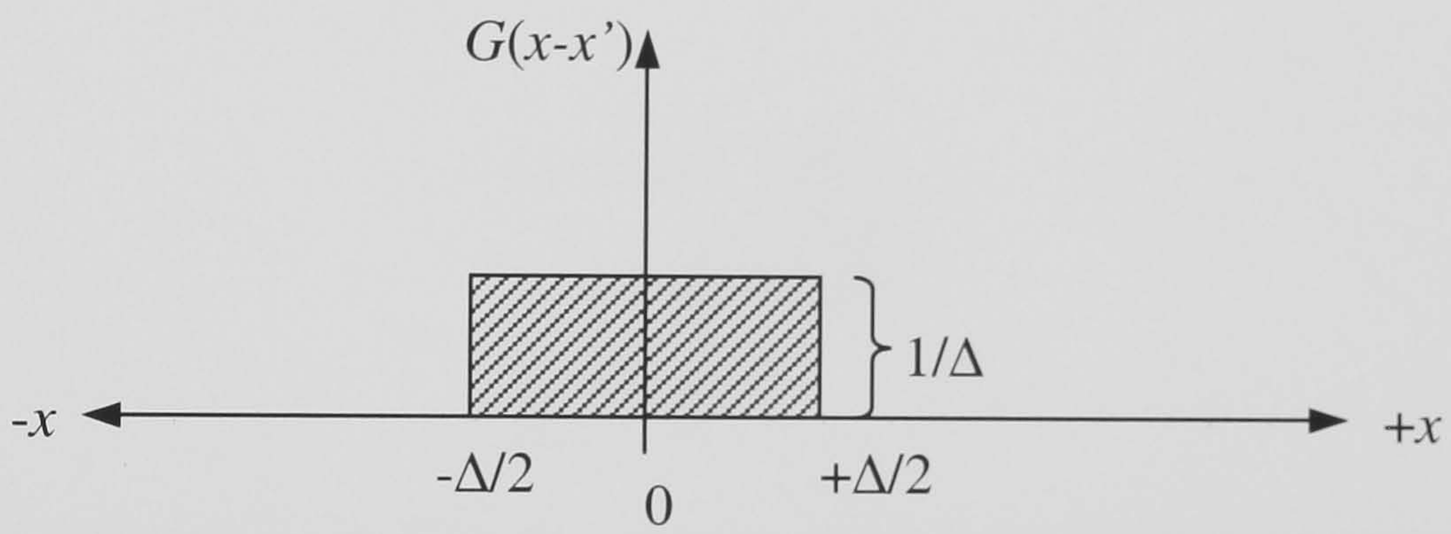

Another filter is the *Gaussian filter* favoured by Stanford group (Ferziger, 1977), which, however, involves more complicated mathematical operations. There are many filter functions available but the one proposed by Schumann (1975) is preferred by some commercial CFD codes (e.g. PHOENICS) employing finite volume methods. It replaces the explicit filtering (prefiltering) by volume average on each grid cell so that the large scales, marked by $\overline{Q}$, can be separated by following operation:

$$\overline{Q}(x_1, x_2, x_3) = \frac{1}{\Delta x_1 \Delta x_2 \Delta x_3} \int_{x_1-\frac{\Delta}{2}}^{x_1+\frac{\Delta}{2}} \int_{x_2-\frac{\Delta}{2}}^{x_2+\frac{\Delta}{2}} \int_{x_3-\frac{\Delta}{2}}^{x_3+\frac{\Delta}{2}} Q(x_1', x_2', x_3')\, dx_3' dx_2' dx_1' \tag{3.25}$$

where x_1, x_2, and x_3 are the coordinates of the meshgrid centre and Δx_j are the mesh size lengths in the x_j direction. In this way the physical properties (e.g. the velocity, the pressure) is split up into resolvable and subgrid components, i.e. $Q = \overline{Q} + \tilde{Q}$, where $\tilde{Q}$ is

the subgrid scale of Q. The filtered N-S equation for incompressible flows now can be written as

$$\frac{\partial \bar{u}_i}{\partial t} + \frac{\partial (\overline{u_i u_j})}{\partial x_j} = -\frac{1}{\rho}\frac{\partial \bar{p}}{\partial x_i} + \frac{\mu}{\rho}\frac{\partial}{\partial x_j}\left(\frac{\partial \bar{u}_i}{\partial x_j} + \frac{\partial \bar{u}_j}{\partial x_i}\right) \tag{3.26}$$

The second term on the left-hand side of (3.26) needs to be investigated further as the product $\overline{u_i u_j}$ has not been determined yet. Considering that $u_i = \bar{u}_i + \tilde{u}_i$ and $u_j = \bar{u}_j + \tilde{u}_j$, the product $\overline{u_i u_j}$ can be obtained by

$$\overline{u_i u_j} = \overline{(\bar{u}_i + \tilde{u}_i)(\bar{u}_j + \tilde{u}_j)} = \overline{\bar{u}_i \bar{u}_j} + \overline{\bar{u}_i \tilde{u}_j} + \overline{\tilde{u}_i \bar{u}_j} + \overline{\tilde{u}_i \tilde{u}_j} \tag{3.27}$$

Let

$$\tau_{ij} \equiv \rho(\overline{u_i u_j} - \bar{u}_i \bar{u}_j) = \rho(L_{ij} + C_{ij} + R_{ij}) \tag{3.28}$$

where

$$L_{ij} = \overline{\bar{u}_i \bar{u}_j} - \bar{u}_i \bar{u}_j$$

$$C_{ij} = \overline{\bar{u}_i \tilde{u}_j} + \overline{\tilde{u}_i \bar{u}_j}$$

$$R_{ij} = \overline{\tilde{u}_i \tilde{u}_j}$$

Both of the terms L_{ij} (Leonard term) and C_{ij} (Cross term) can be determined by a filtering procedure, therefore the only term required to be modelled in equation (3.28) is R_{ij}. The filtering procedure given by equation (3.25) can obtain very favourable results for L_{ij} and C_{ij}, in which

$$\overline{\bar{u}_i \bar{u}_j} = \bar{u}_i \bar{u}_j \tag{3.29}$$

and

$$\overline{\bar{u}_i \tilde{u}_j} = \overline{\tilde{u}_i \bar{u}_j} = 0 \tag{3.30}$$

since $\bar{u}_i$ is a constant within each control volume and $\overline{\tilde{u}_i} \equiv 0$, as illustrated in figure 3.3. With equation (3.28), the filtered N-S equation (3.26) can be written as

$$\frac{\partial \bar{u}_i}{\partial t} + \frac{\partial (\bar{u}_i \bar{u}_j)}{\partial x_j} = -\frac{1}{\rho}\frac{\partial \bar{p}}{\partial x_i} + \frac{\mu}{\rho}\frac{\partial}{\partial x_j}\left(\frac{\partial \bar{u}_i}{\partial x_j} + \frac{\partial \bar{u}_j}{\partial x_i}\right) - \frac{1}{\rho}\frac{\partial \tau_{ij}}{\partial x_j} \tag{3.31}$$

where the subgrid stresses $\tau_{ij} \equiv \rho(\overline{u_i u_j} - \bar{u}_i \bar{u}_j) = \rho R_{ij}$ by the virtue of equations (3.29-30). The τ_{ij} become additional variables or residual stresses that are required to be determined by a closure model, i.e. the "subgrid model".

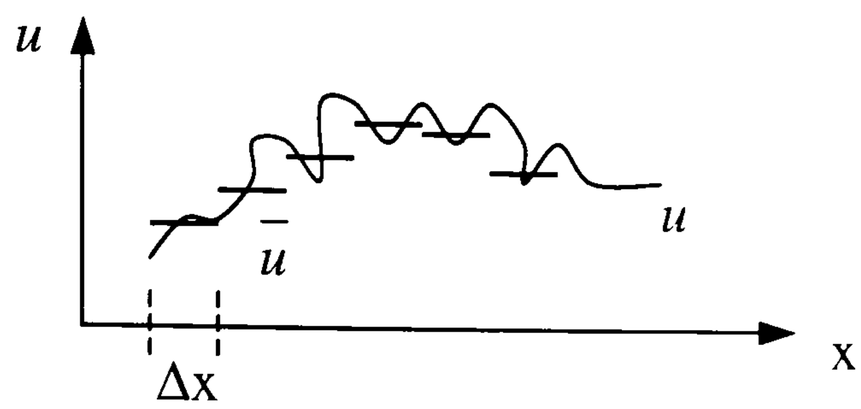

Figure 3.3 Filtered u, in which $\bar{u}$ is a constant over a filter width. [From: Abbott and Basco (1989)]

A subgrid model usually consists of assuming the anistropic part of the residual stress tensor τ_{ij} to be proportional to the resolved (large-scale) strain rate tensor $\bar{S}_{ij}$; therefore

$$\tau_{ij} = \rho\overline{\tilde{u}_i \tilde{u}_j} = -2\mu_s \bar{S}_{ij} \tag{3.32}$$

and

$$\bar{S}_{ij} = \frac{1}{2}\left(\frac{\partial \bar{u}_i}{\partial x_j} + \frac{\partial \bar{u}_j}{\partial x_i}\right) \tag{3.33}$$

Equation (3.32) can be written as

$$\overline{\tilde{u}_i \tilde{u}_j} = -2\nu_s \bar{S}_{ij} \tag{3.34}$$

where $\nu_s = \mu_s/\rho$ is the subgrid eddy viscosity which dimensionally equals to $[L^2][T^{-1}]$; therefore ν_s is assumed to be proportional to some physical quantity with a dimension of $[L^2][T^{-1}]$. One of the most well-known models is the Smagorinsky (1963) model in which ν_s is expressed as

$$\nu_s = (C_s \Delta)^2 (2\bar{S}_{ij} \bar{S}_{ij})^{\frac{1}{2}} \tag{3.35}$$

where C_s is the Smagorinsky constant and $\Delta = \sqrt{(\Delta_1^2 + \Delta_2^2 + \Delta_3^2)/3}$ is the characteristic filter width, which may be given by the meshgrid lengths. The value of C_s lies in the range between 0.065 and 0.23, depending on local flow conditions (Ciofalo, 1994). PHOENICS employs a value of 0.17 for this constant.

LES has been attempted by some authors to study the flows over a bluff body and buildings. Ciofalo (1995) demonstrated using a commercial CFD code "Harwell Flow3D" to model the flows in a smooth channel and in a ribbed channel respectively but his studies were limited to modest Reynolds number (Re = 1,000 – 7,000) flows. Shah and Ferziger (1997) presented a LES study of flow past a cube and the flow was simulated at Re = 40,000 using approximately 1.1 million grids in a computing domain with a size of $10\delta \times 7\delta \times 2\delta$ (δ is the cube height). The minimum grid spacing was 0.006δ since the flow was at high Reynolds number and therefore the rapid-transition eddies near solid walls were required to be resolved. In addition, small time steps were required to resolve the rapid transition process. LES was also attempted at much higher Reynolds number flow ($Re = 10^5$) by Yu and Kareem (1997, 1998) in which they investigated the flow around a rectangular prism and the number of grids was substantially increased to 3.5 – 4.0 million. A more complicated case study of wind flows around buildings was presented by Song and He (1999) in which they applied LES to investigate pedestrian winds in an urban area but the computing costs were about 3 weeks with a supercomputer!

Another difficulty of using LES to model engineering flows is that the boundary conditions have to be time-dependent and how small the time step is required can be a question. This imposes a difficulty in wind simulations because the fluctuating wind velocities at the inlet will have to be simulated with a probability distribution function or other artificial methods (Thomas and Williams, 1999). These techniques are, however, also very difficult to be carried out in the industry without modifying their codes and it is more difficult if the industrial users are using commercial codes because a commercial code is already complicated enough and it is usually not easy for users to implement their additional coding. Some other difficulties associated with using LES to study industrial flows are given by Gosman (1999). Therefore, although LES has been proven superior to other classical RANS models (Murakami, 1998), it has not been widely accepted for routine simulations in the industry.

3.2.2 RANS Models

RANS models are additional "modelled" equations devised for the closure of Reynolds Averaged N-S equations. The averaging process is with respect to time. For each time-dependent variable, it can be decomposed into a mean value, which is statistically

stationary (time-independent) and a fluctuating component, such as $u = U + u'$, where U is the mean velocity taken over a sufficient long period of time and u' is its fluctuating deviation from the mean (figure 3.4). The average of the fluctuating component $\overline{u'}$ is zero but the value of $\overline{u'u'}$ is a nonzero (> 0) value (figure 3.5).

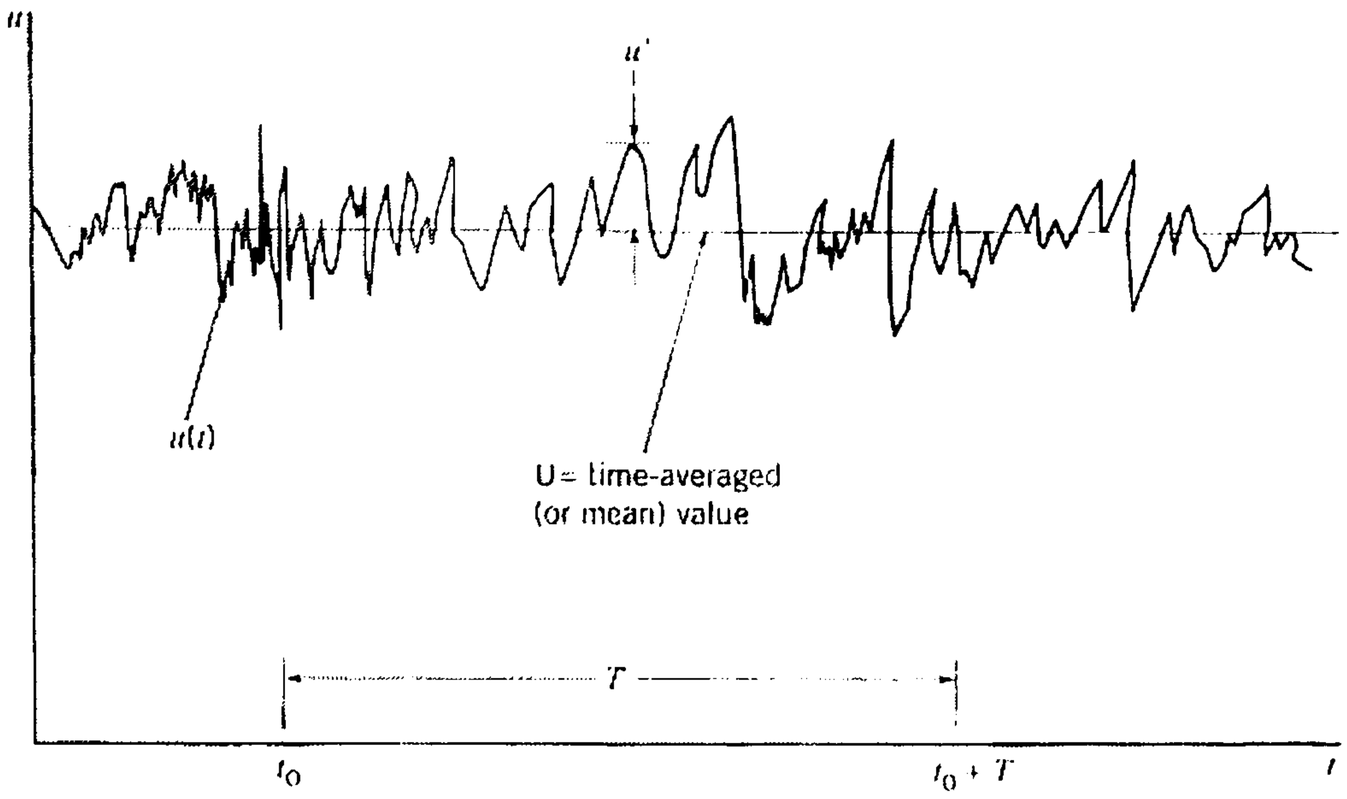

Figure 3.4 The decomposition of $u(t) = U + u'(t)$ [From: Munson *et al.* (1998)]

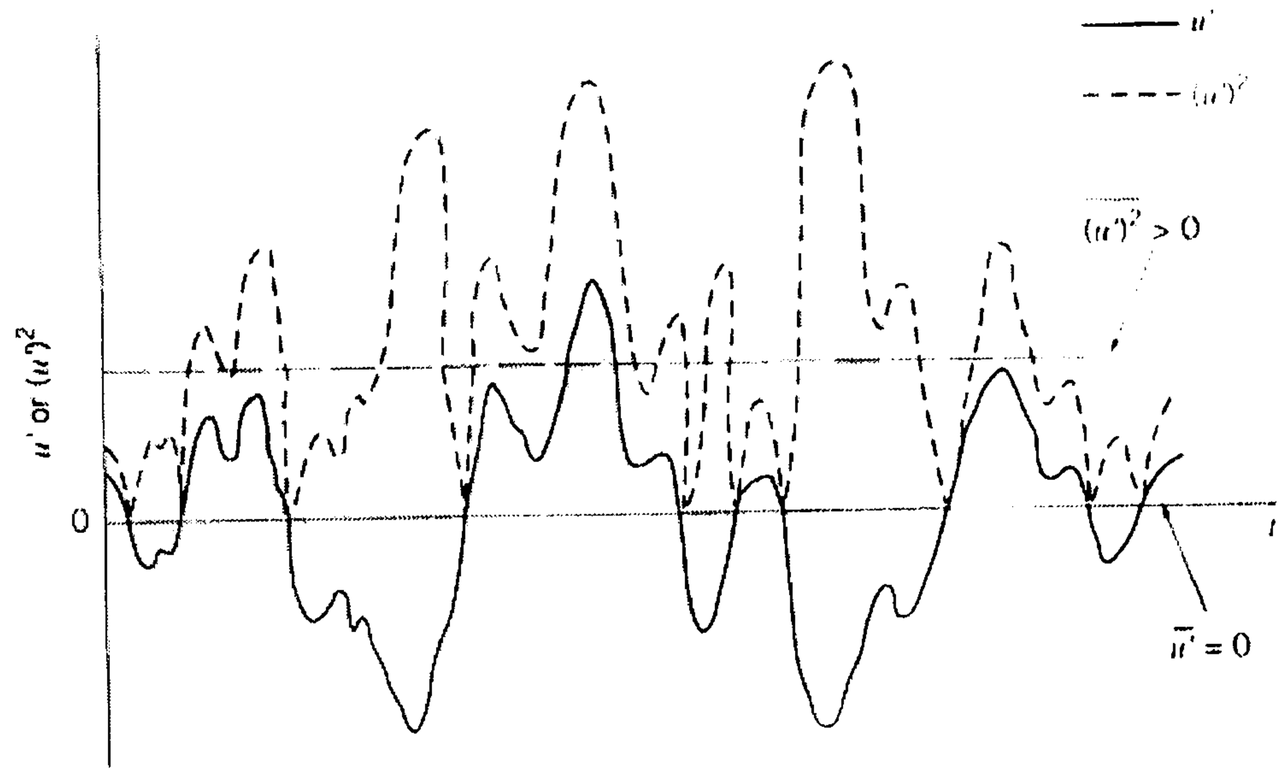

Figure 3.5 Average of the fluctuations and average of the square of the fluctuations. [From: Munson *et al.* (1998)]

Substituting u_i and p with the same notation ($u_i = U_i + u_i'$; $p = P + p'$) into the primitive continuity (3.20) and N-S equations (3.21) and take averages of individual terms with respect to time, the Reynolds Averaged N-S equations can be obtained:

$$\frac{\partial U_i}{\partial t} + U_i \frac{\partial U_i}{\partial x_j} = -\frac{1}{\rho}\frac{\partial P}{\partial x_i} + \frac{\mu}{\rho}\frac{\partial}{\partial x_j}\left(\frac{\partial U_i}{\partial x_j} - \rho\overline{u_i' u_j'}\right) \tag{3.36}$$

and the continuity equation becomes

$$\frac{\partial U_i}{\partial x_i} = 0 \tag{3.37}$$

where U_i are the mean velocities, P is the mean static pressure and $-\rho\overline{u_i' u_j'}$ are turbulent or Reynolds stresses ($\tau_{ij} \equiv -\rho\overline{u_i' u_j'}$), which are the stresses contributed by turbulent fluctuations. In equations (3.36-37) the terms $\partial U_i/\partial t$ are all equal to zero, as the mean values are independent of time. After the time-averaging process, there are additional six unknowns ($-\rho\overline{u_i' u_j'}$) found but only four equations (3.36-37) are available. The additional unknowns need to be determined. The oldest proposal for modelling the Reynolds stress is Boussinesq's eddy-viscosity concept, which assumes that, in analogy to the viscous stress in laminar flows, the turbulent stresses are proportional to the mean-velocity gradients. The eddy-viscosity concept (or hypothesis) is expressed by

$$-\rho\overline{u_i' u_j'} = \mu_t\left(\frac{\partial U_i}{\partial x_j} + \frac{\partial U_j}{\partial x_i}\right) - \frac{2}{3}\rho\delta_{ij}k \tag{3.38}$$

or more commonly

$$-\overline{u_i' u_j'} = \nu_t\left(\frac{\partial U_i}{\partial x_j} + \frac{\partial U_j}{\partial x_i}\right) - \frac{2}{3}\delta_{ij}k \tag{3.39}$$

where $\nu_t = \mu_t/\rho$ is the turbulent eddy viscosity, $\delta_{ij} = 1$ when $i = j$ and $\delta_{ij} = 0$ otherwise. The turbulent kinetic energy k is defined as

$$k \equiv \frac{1}{2}\overline{(u_i')^2} = \frac{1}{2}(\overline{u'^2} + \overline{v'^2} + \overline{w'^2}) \tag{3.40}$$

The kinetic energy is always a positive value. The turbulent eddy viscosity ν_t is with a dimension of [$L^2 T^{-1}$]; therefore the eddy viscosity is considered to be proportional to a velocity scale (V_s with the dimension of [LT^{-1}]) and a length scale (L_s with the dimension of [L]). There are many conventional models devised to calculate ν_t for different flows and they can be classified by

- Zero-equation models – V_s and L_s are calculated directly from local mean flow quantities.

- One-equation models – V_s is calculated from a suitable transport equation, usually the turbulent kinetic energy (k), whereas L_s is prescribed empirically.
- Two-equation models – V_s and L_s are both calculated from transport equations, usually the turbulent kinetic energy (k) and its dissipation rate (ε).

The simplest models are the zero-equation models in which there is no transport equation involved. They determine the turbulent eddy viscosity either directly from experiments or through empirical formula. Prandtl's mixing-length model proposed in 1925 is the representative one (Schlichting, 1968; Welty *et al.*, 1969; Tennekes and Lumley, 1972). The drawback of the mixing-length model is that there is no account for the processes of convective or diffusive transport, which are important for some flows like rapid developing flows and recirculating flows. It is certainly not suitable for complex flows like the winds around buildings.

One-equation models, by its definition, involve a transport equation to model the velocity scale. Physically the most meaningful velocity scale to be modelled is $\sqrt{k}$ because k is the turbulent kinetic energy contributed by turbulent quantities (per unit mass) and $\sqrt{k}$ is with a dimension of velocity [LT^{-1}]. Therefore the modelled eddy viscosity equation becomes

$$\nu_t = c_\mu' \sqrt{k}\, L \tag{3.41}$$

where L is a prescribed length scale and c_μ' is an empirical constant. The modelled k equation is a transport equation in which the processes of convective and diffusive transport of k have been accounted for. For most of the one-equation models, the transport equation of k at high Reynolds number without buoyancy considered is:

$$\underbrace{\frac{\partial k}{\partial t}}_{\text{rate of change of } k} + \underbrace{U_i \frac{\partial k}{\partial x_i}}_{\text{convective transport of } k} = \underbrace{\frac{\partial}{\partial x_i}\left(\frac{\nu_t}{\sigma_k}\frac{\partial k}{\partial x_i}\right)}_{\text{transport of } k \text{ by diffusion}} + \underbrace{\nu_t\left(\frac{\partial U_i}{\partial x_j}+\frac{\partial U_j}{\partial x_i}\right)\frac{\partial U_i}{\partial x_j} - C_D\frac{k^{3/2}}{L}}_{\text{rate of production of } k \text{ - rate of destruction of } k} \tag{3.42}$$

where σ_k and C_D are constants. Although one-equation models are superior to the zero-equation models, they have not been widely applied in general flow problems mainly because it is difficult to specify the distribution of length scales in more complex flows. As a result, the one-equation models are not recommended for the numerical simulations of wind flows around buildings.

Since one-equation models cannot satisfy general flow problems, the development of RANS models therefore has to move on to two-equation models which also determine the length scale with a transport equation. The concept of modelling the length scale is that the length scale L_s characterising the size of the large, energy-containing eddies is subject to transport process in a similar manner to the energy k. The eddy size can be very much dependent on its initial size in the transport process and the length scale is also affected by dissipation (ε), which destroys the small eddies and thus effectively increases the eddy size and, vortex stretching connected with energy cascade, which reduces eddy size (Rodi, 1993). The dissipation rate $\varepsilon = dk / dt$ is approximately equal to k / t_s, where t_s is a characteristic time scale of the most energetic turbulent eddies. It can be estimated by $t_s = L_s / k^{1/2}$ and therefore ε is proportional to $k^{3/2} / L_s$. The balance of all these processes can be expressed in the modelled transport equations of k and ε. Among two-equation models, the standard k-ε model by Lauder and Spalding (1974) has been proven most popular and it has been successfully applied in various flows. The k-ε model uses k and ε to define V_s and L_s by

$$V_s = k^{1/2} \qquad L_s \approx \frac{k^{3/2}}{\varepsilon} \tag{3.43}$$

Since ν_t is proportional to the product of V_s and L_s, therefore

$$\nu_t \propto (k^{1/2}) \times \left(\frac{k^{3/2}}{\varepsilon} \right) \tag{3.44}$$

or

$$\nu_t = C_\mu \frac{k^2}{\varepsilon} \tag{3.45}$$

where C_μ is a constant that makes the left-hand side of equation (3.44) equal to its right-hand side. At high Reynolds numbers, the k-ε model without considering buoyancy is in the form of

$$\underbrace{\frac{\partial k}{\partial t} + U_i \frac{\partial k}{\partial x_i}}_{\text{transport of } k} = \underbrace{\frac{\partial}{\partial x_i}\left(\frac{\nu_t}{\sigma_k} \frac{\partial k}{\partial x_i} \right)}_{\text{transport of } k \text{ by diffusion}} + \underbrace{\nu_t \left(\frac{\partial U_i}{\partial x_j} + \frac{\partial U_j}{\partial x_i} \right) \frac{\partial U_i}{\partial x_j} - \varepsilon}_{\text{rate of production of } k \text{ - rate of destruction of } k} \tag{3.46}$$

$$\underbrace{\frac{\partial \varepsilon}{\partial t} + U_i \frac{\partial \varepsilon}{\partial x_i}}_{\text{transport of } \varepsilon} = \underbrace{\frac{\partial}{\partial x_i}\left(\frac{\nu_t}{\sigma_\varepsilon} \frac{\partial \varepsilon}{\partial x_i} \right)}_{\text{transport of } \varepsilon \text{ by diffusion}} + \underbrace{C_{1\varepsilon} \frac{\varepsilon}{k} \left(\frac{\partial U_i}{\partial x_j} + \frac{\partial U_j}{\partial x_i} \right) \frac{\partial U_i}{\partial x_j} - C_{2\varepsilon} \frac{\varepsilon^2}{k}}_{\text{rate of production of } \varepsilon \text{ - destruction of } \varepsilon} \tag{3.47}$$

where $\sigma_k, \sigma_\varepsilon, C_{1\varepsilon}$ and $C_{2\varepsilon}$ are empirical constants. The transport equations of k and ε are based on the mathematical interpretations of the physics involved in the transport process. A comprehensive discussion about the physics involved can be found in Bradshaw *et al.* (1981). The values for these constants in the standard k-ε model are obtained from experimental data fitting a wide range of flows such as free turbulent flows and wall flows. The values of the constants determined are

$$C_\mu = 0.09, \sigma_k = 1.00, \sigma_\varepsilon = 1.30, C_{1\varepsilon} = 1.44, \text{and } C_{2\varepsilon} = 1.92 \tag{3.48}$$

The above high Reynolds number k-ε model needs additional functions to account for the flow near walls where the velocities are affected by the "law of the wall". The most common approach is using "wall function" to describe the flow behaviour near walls. The velocity in the turbulent region close to a smooth wall can be described by a log-law as

$$u^+ = \frac{1}{\kappa}\ln(y^+) + B = \frac{1}{\kappa}\ln(Ey^+) \tag{3.49}$$

where $u^+ = u/u_*$ and $y^+ = u_* y/\nu$, y is the distance away from the wall; u_* is the friction velocity and ν is the kinetic viscosity of fluid; κ is the von Kármán's constant (κ = 0.41); B and E are constants (B = 5.5 or E = 9.8 for smooth wall). By adjusting the constants, the log-law wall function can be applied to rough walls (Schlichting, 1968). The log-law is valid when $30 < y^+ < 500$. If the nearest point is at a distance y_p from the wall, the mean velocity at the point y_p with $30 < y_p^+ < 500$ satisfies the log-law. Also, from experimental measurements, the rate of production of turbulent energy is equal to its dissipation rate (i.e. equilibrium); therefore the following wall function is used in many CFD codes when the k-ε model is available:

$$u^+ = \frac{1}{\kappa}\ln(Ey_p^+); \quad k = \frac{u_*^2}{\sqrt{C_\mu}}; \quad \varepsilon = \frac{u_*^3}{ky} \tag{3.50}$$

One advantage of using wall function is that the velocity field in near wall regions is resolved with some simple algebraic equations instead of integrating the model equations right through to the wall and therefore it is economical for computation. The wall function may be generalised for walls involving heat transfer, as it has been postulated by Lauder and Spalding (1974). The generalised wall function, however, is

of less use for the simulations of airflow around buildings because the wind structure has been generally assumed to be adiabatic.

Since the standard k-ε model has been widely used to predict various industrial or engineering flows, its limitations are also well documented. For instance, use of the standard k-ε model with wall function may not be able to predict swirling flows and separated flows correctly in some regions where pressure gradients are steep and local anisotropy prevails (Rodi, 1993). Also, the standard k-ε model is based on the assumption that the eddy viscosity is the same for all Reynolds stresses, as stated in equation (3.39) and (3.45). This probably is too crude for some complicated flows and particular attentions may have to be taken when using the k-ε model to simulate certain industrial flows (Casey and Wintergerste, 2000).

Over past few decades, some other refined turbulence models have been proposed to improve this deficiency. One of the most sophisticated RANS models is the Reynolds stress model, also called the second-order or second-moment closure model. It is to solve each Reynolds stress ($\overline{u_i' u_j'}$, per unit mass) directly with a transport equation and the eddy viscosity concept is not employed in its computation. Therefore there are six additional partial differential equations presented in this model. These six additional equations are solved with another transport equation of ε to form a complete set of equations for all Reynolds stresses. The computing cost is much higher and therefore this model has not been generally applied to engineering flows. This model is still under development because its performance varies, sometimes it is better than two-equation models but sometimes not, mainly due to the inadequacy of modelled ε equation (Bradshaw, 1997). The turbulence models selected for this study are the k-ε family models and they will be discussed further in later chapters.

3.3 Numerical Grid

There are a number of ways to solve the partial differential equations numerically. For example, finite difference (FD) methods, finite volume methods (FV) and finite element (FE) methods are the most popular approaches applied in the field of solid or fluid mechanics. Currently FV methods are used in most of the commercial CFD codes. The computing domain needs to be discretised before one of these methods applied to solve

the differential equations and therefore the role of the numerical grid is essential at this stage. The numerical grid is to define the discrete locations at which the variables (pressure, velocities, etc) are to be calculated and stored. The grids are in fact a discrete representation of the geometric domain since it is composed of a finite number of "control volumes" or "elements". The numerical grids can be classified by "structured" and "unstructured" grids.

3.3.1 Structured Grid

Structured grids allow the grid lines to be numbered consecutively and the position of any grid point (or control volume) within the domain is uniquely identified by a set of two (in 2D) or three (in 3D) indics, e.g. (i, j, k). The Cartesian grid is of this type and it is the simplest grid structure. One example of using Cartesian grids to simulate the wind flow around a cube is shown as figure 3.7.

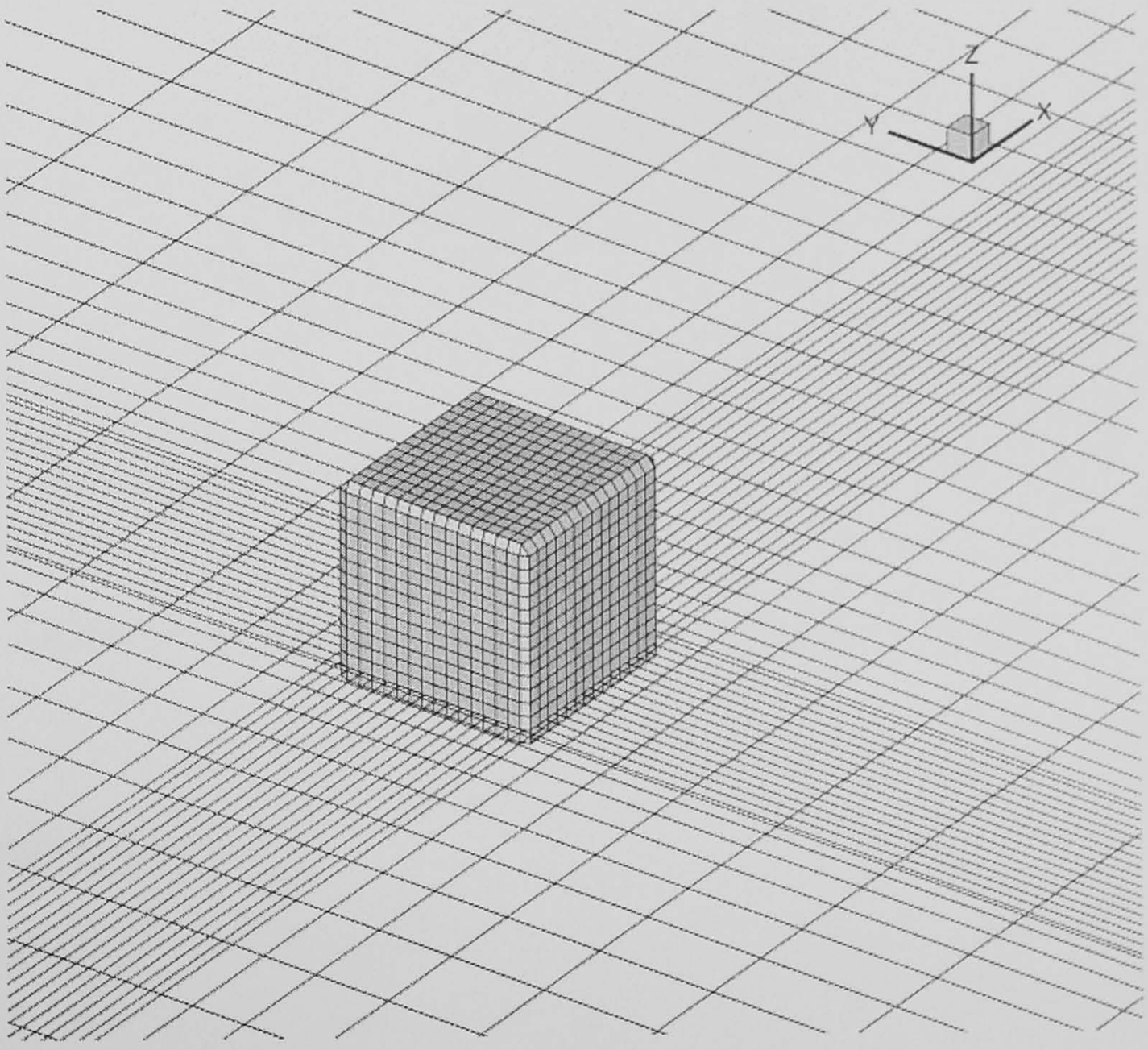

Figure 3.7 Cartesian grids.

In Cartesian grids or structured grids, each point P has four nearest neighbours in two dimensions and six in three dimensions. The indices of neighbouring points of P differs by ±1 from the corresponding index of P. Normally the structured grids are body-fitted if the grids are not of Cartesian type. An example of structured and body-fitted 3D grid for the simulation of airflow around a L-shape building is shown as figure 3.8. One of

the advantages using structured grids is that the neighbour connectivity simplifies the programming task and the matrix of the algebraic equation system has a regular structure, which can best be exploited by some linear equation solvers. Some commercial CFD codes (e.g. PHOENICS) can only accept structured grids for this reason. The disadvantage of structured grids is that they are ideal only for geometrically simple domains because it becomes very difficult to create structured and body-fitted grids if the geometry is complicated, such as a building with irregular shapes. On the other hand, the unstructured grids are more flexible because they can fit in any shape of geometry and solution domain.

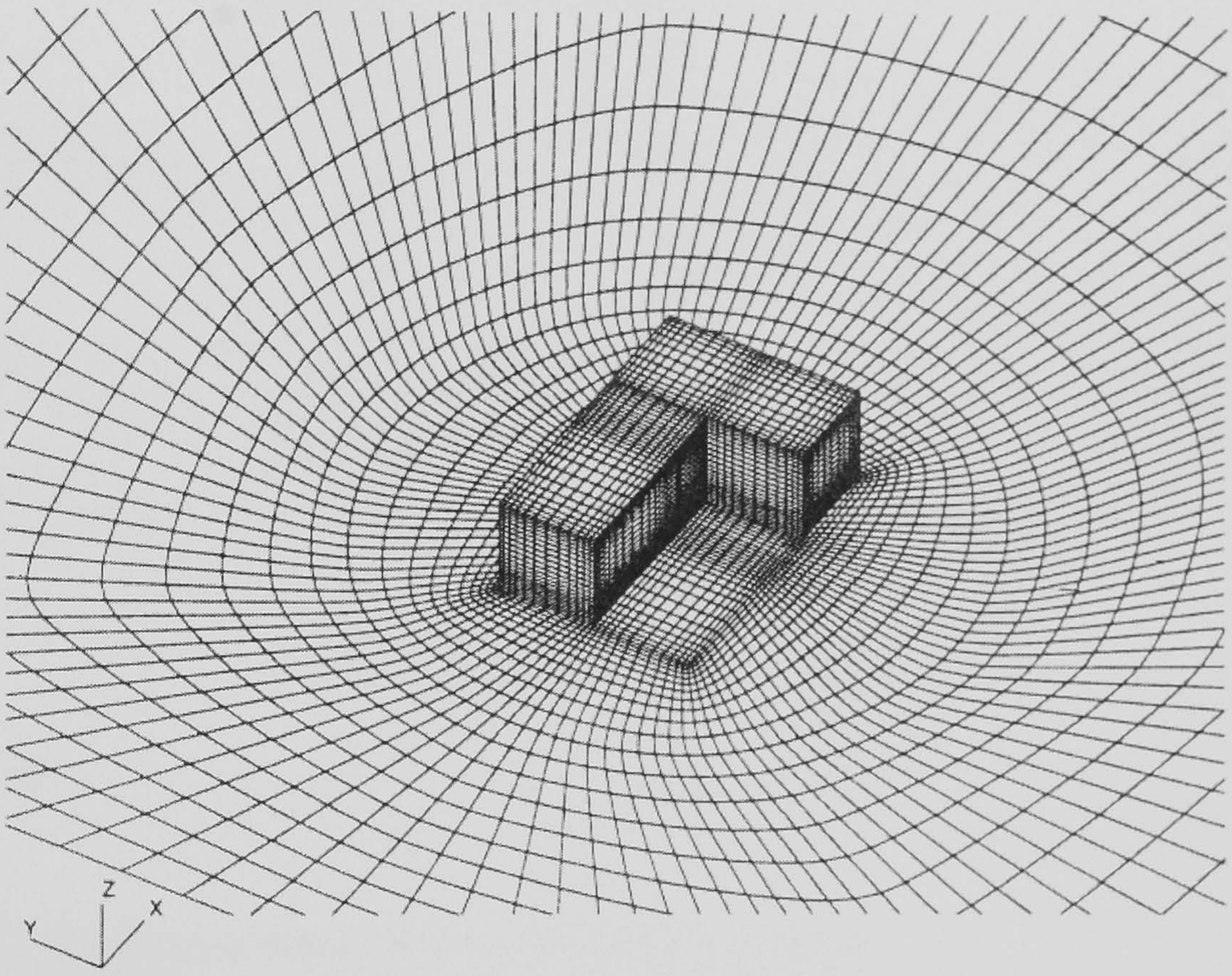

Figure 3.8 Structured and body-fitted grids [From: Hall (1996)]

3.3.2 Unstructured grid

Unstructured grids are usually made of triangles or quadrilaterals in 2D and tetrahedra or hexahedra in 3D. These grids can be generated automatically by existing algorithm, such as some techniques summarised by Thompson *et al.* (1985). The unstructured grids are easy to be controlled and refined locally for some regions where higher resolutions are required. The advantage of unstructured grids is, however, offset by the disadvantage of the irregularity of the data structure. Node locations and neighbour connections need to be specified explicitly using a "connectivity matrix" and the matrix of the algebraic equation system is no longer in a form of regular, diagonal structure. Therefore the solvers for those irregular matrix systems need more time and storage to

calculate each variable. Unstructured grids are mostly used in FE methods but it has been increasingly embraced by FV methods in commercial CFD codes. Probably because most of the industrial practitioners often need to solve problems where a complex geometry is involved and the users prefer a quick method that can generate the numerical grids for computation easily. The code – CFX 5 employs an unstructured grid system with automatic meshing capability. An example of unstructured grids generated for a building complex is shown in figure 3.9.

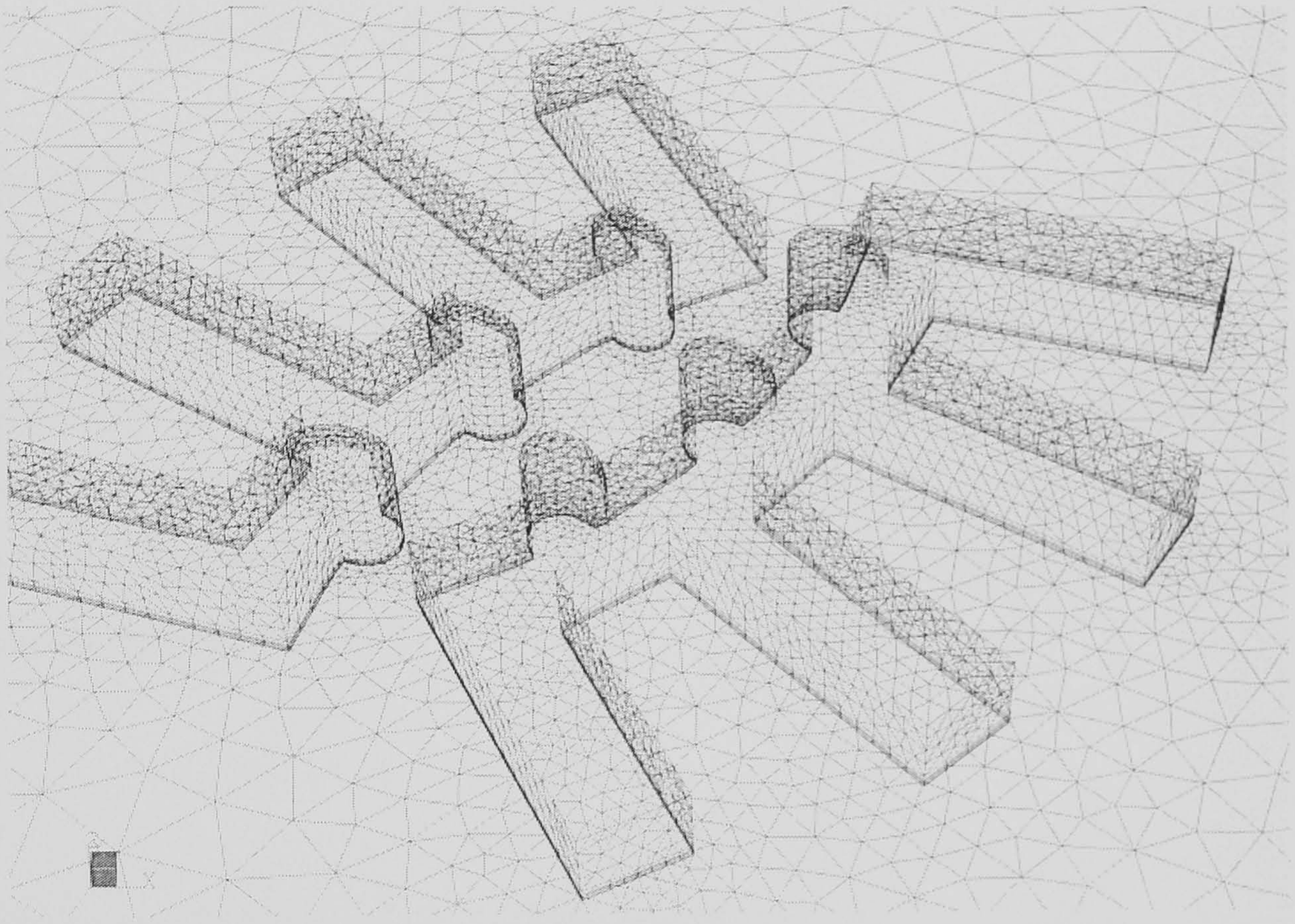

Figure 3.9 Unstructured grids for a building complex.

3.4 Finite Volume Equations

The step of grid generation is a prerequisite for the FV method. Once the grids have been generated, the computing domain is said to be "discretised" and the following task is to integrate the conservation equations over each control volume. A generic form of the steady convection-diffusion equation is

$$\underbrace{\int_{c.s.} \rho\phi\mathbf{v}\cdot\mathbf{n}dS}_{\text{convection}} = \underbrace{\int_{c.s.} \Gamma \text{grad}\phi\cdot\mathbf{n}dS}_{\text{diffusion}} + \underbrace{\int_{c.v.} S_\phi dV}_{\text{source}} \tag{3.51}$$

where Γ is the diffusion coefficient (e.g. fluid viscosity) and S_ϕ is the source term (e.g. pressure gradient). Equation (3.51) states the flux balance over a control volume. The left hand side gives the net convective flux and the right hand side contains the net

diffusive flux and the generation or destruction of the property ϕ within a CV. The grids form the CVs and the CV centre (node) stores the value of ϕ (figure 3.10).

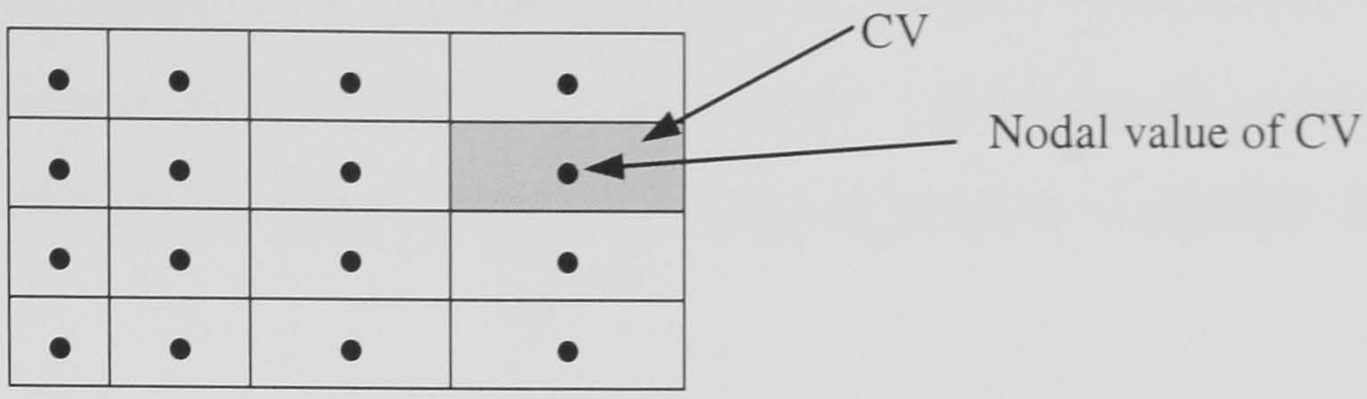

Figure 3.10 Nodes centred CV, the value at a node-centred CV represents the mean over the CV volume.

Equation (3.51) applies to each CV as well as the solution domain as a whole. The summations of all CVs are the global equations of the solution domain, since surface integrals over inner CV faces cancel out. To obtain an algebraic equation for each CV, the surface and volume integrals need be approximated using interpolation or other mathematical methods. Consider a 2D control volume in Cartesian grids (figure 3.11), The CV faces can be subdivided into four plane faces, denoted by "*e*, *w*, *n*, *s*" with respect to the central node P.

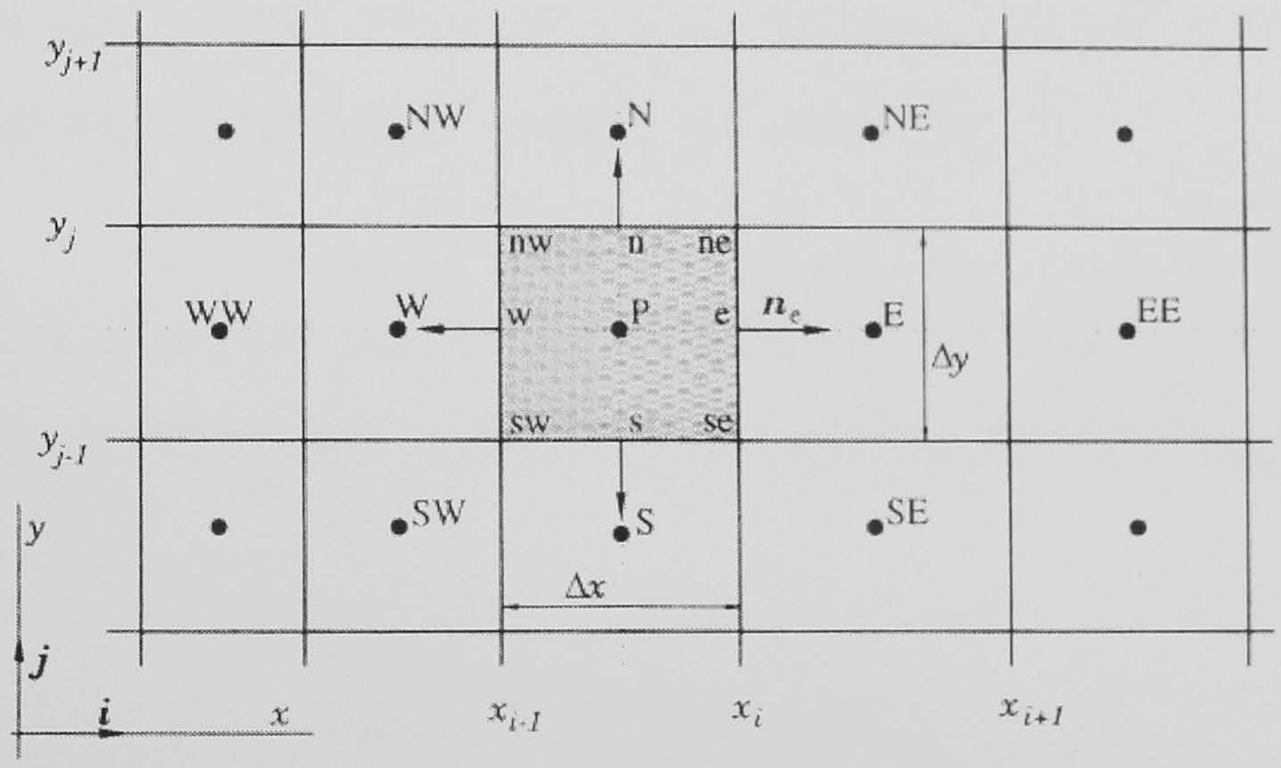

Figure 3.11 Typical CV and notation used in 2D Cartesian grid. [From: Ferziger and Peric (1999)]

The net flux through the CV boundary is the sum of integrals over four CV faces, therefore

$$\int_S f dS = \sum_i \int_{S_i} f dS \tag{3.52}$$

where S means surface integral, f is the component of the convective ($\rho\phi\,\mathbf{v}\cdot\mathbf{n}$) or diffusive ($\Gamma \text{grad}\phi\cdot\mathbf{n}$) vector in the direction normal to CV face. To calculate the surface integral in equation (3.52) exactly, the integrand f must be known everywhere on the surface (S_e, S_w, S_s, S_n) but it is not available, as only nodal values are calculated and stored so that an approximation must be made. The approximation is usually done at two levels:

- the integral is approximated in terms of the variable values at one or more locations on the cell face;
- the cell face values are approximated in terms of the nodal (CV centre) values.

A simple approximation to get the face value (e.g. f_e) is using interpolation, so

$$f_e = \frac{1}{2}(\phi_P + \phi_E) \tag{3.53}$$

where ϕ_P and ϕ_E are the CV-centred values of ϕ at P and E. The accuracy is of second order in terms of its Taylor series expansion of ϕ at e. Equation (3.53) is the "Central Differencing Scheme" (CDS). There are other different methods to determine the face value and some of the methods will be discussed in section 3.5.

The source term is also required to be approximated in equation (3.51). The simplest method is to replace the volume integral by the product of the mean value and the CV volume as

$$(S_\phi)_P = \int_{C.V.} S_\phi dV = \overline{S_\phi}\Delta V \approx S_P \Delta V \tag{3.54}$$

where $\overline{S_\phi}$ is the mean value over the CV and S_P is the value of ϕ at the CV centre P. The quantity S_P can be easily obtained since all variables are available at node P and no interpolation is required. The approximation becomes an exact value if S_ϕ is either constant or varies linearly within the CV. If S_ϕ is not a constant over the CV, it will have to be linearised. Pantakar (1980) suggests using the following expression:

$$\overline{S_\phi} = S_C + mS_P \tag{3.55}$$

where S_C is the constant part of $\overline{S_\phi}$, m is the slope or coefficient of S_p. Once all the surface integrals and volume integrals are determined, the equation (3.51) becomes an algebraic equation with the form of

$$a_P\phi_P = a_E\phi_E + a_W\phi_W + a_S\phi_S + a_N\phi_N + b \tag{3.56}$$

or more generally

$$a_P\phi_P = \sum_i a_i\phi_i + b \tag{3.57}$$

where a_P is the coefficient of ϕ_P, a_i are the coefficients of neighbouring cell-centred values ϕ_i, b is the source term. There are four coefficients on the right hand side of equation (3.56) for a 2D case, whereas there are six coefficients for a 3D case. Each control volume has its own equation like (3.57) and these equations will be solved numerically with a linear equation solver. The linear equation solvers will be discussed in section 3.7.

3.5 Differencing Schemes

Differencing schemes (or discretisation schemes) are numerical interpolations applied to the convection and diffusion terms of a transport equation (e.g. equation (3.51)). The CDS is usually applied to diffusion terms since it has been examined and concluded that it is accurate and suitable for diffusion terms. However, it is not suitable for convection terms because it is unbounded and it may produce unphysical oscillations (i.e. unboundedness, the computed result may present unphysical values that are well beyond the upper or lower limit of ϕ) in regions of strong convection and in the presence of discontinuities (Patankar, 1980). Consequently, the convection terms need other better interpolation methods.

3.5.1 Upwind Differencing and Central Differencing Schemes

A well-established differencing scheme is the "Upwind Differencing Scheme" (UDS). UDS defines the cell face value ϕ_F (figure 3.12) by

$$\phi_F = \begin{cases} \phi_C & \text{if the convective flux is from } \phi_C \text{ to } \phi_D \\ \phi_D & \text{if the convective flux is from } \phi_D \text{ to } \phi_C \end{cases} \tag{3.58}$$

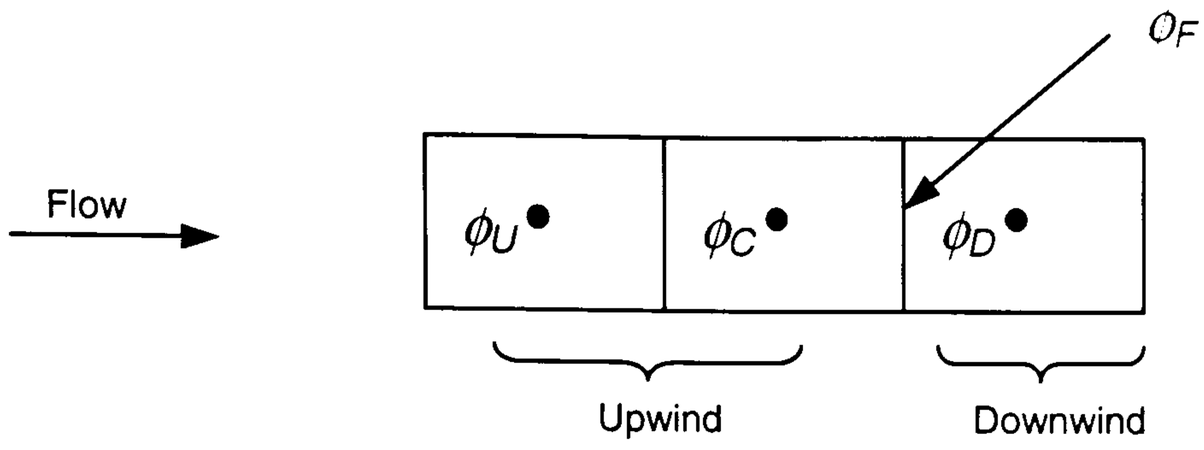

Figure 3.12 Upwind and downwind cells. ϕ_U, ϕ_C and ϕ_D are cell-centred values.

UDS is unconditionally stable and bounded but it is only a first-order accurate scheme. Therefore it is numerically diffusive, especially when the flow direction is diagonal or oblique to the grid lines (Malin and Waterson, 1999). It appears that UDS and CDS are somewhat complementary in their advantages and disadvantages: the stability and boundedness of UDS versus the accuracy of CDS. A Hybrid Scheme proposed by Spalding (1972) is a combination of UDS and CDS. The hybrid scheme can switch itself to UDS or CDS, depending on whether convection or diffusion effects are dominant; therefore the face value is determined by

$$\phi_F = \begin{cases} \phi_F^{CDS} & \text{if } P_e < 2 \\ \\ \phi_F^{UDS} & \text{if } P_e > 2 \end{cases} \tag{3.59}$$

where P_e is the Peclet number ($P_e = \rho|u|L / \Gamma$, u is the flow velocity in the local cell, L is a characteristic length of the local cell face and Γ is the diffusion coefficient). P_e is a ratio of convection and diffusion. The Hybrid Scheme is the default scheme in PHOENICS. It is relatively stable but it is diffusive in certain flow simulations. For example, in the simulations of airflow around buildings, P_e is usually much greater than 2, except some regions near solid walls where the Peclet number is small. Therefore, most of the time the computation is actually using UDS.

3.5.2 Higher-Order Differencing Schemes

Since UDS and CDS are not satisfactory for the discretisation of convection terms in certain numerical simulations, other methods such as higher-order schemes are therefore devised. A popular higher-order scheme "QUICK" by Leonard (1979) is an answer to the perceived falling of UDS and CDS. The QUICK scheme uses two upwind and one downwind cell-centred values:

$$\phi_F = \phi_C + \frac{1}{8}(3\phi_D - 2\phi_C - \phi_U) \tag{3.60}$$

It is third-order accurate and this scheme retains the accuracy of CDS and the stability of UDS. Consequently it has become a popular choice for modelling of incompressible flows (Waterson, 1994). Nevertheless, it still may suffer from unboundedness and may yield negative values to turbulent kinetic energy (Malin and Waterson, 1999). It is unfavourable for modelling turbulent flows. As a result, the requirement invokes the development of non-linear higher order schemes.

3.5.3 Non-Linear Higher-Order Schemes

The schemes (UDS, CDS, QUICK) are linear schemes in terms of its flux limiter expression. The flux limiter expression is written as

$$\phi_F = \phi_C + 0.5\mathrm{B(r)}(\phi_C - \phi_D) \tag{3.61}$$

where B(r) is a limiter function, and the gradient ratio is defined as

$$\mathrm{r} = (\phi_D - \phi_C) / (\phi_C - \phi_U) \tag{3.62}$$

Therefore B(r) = 0 gives UDS and B(r) = r implies CDS. The limiter function can be generalised as

$$\mathrm{B(r)} = 0.5\{(1 + \mathrm{K})\mathrm{r} + (1 - \mathrm{K})\} \tag{3.63}$$

where K = 1 for CDS and K = 1/2 for QUICK. The equation (3.59) can also be written in the following form:

$$\phi_F = \phi_C + \{0.25(1+\mathrm{K})(\phi_D - \phi_C) + 0.25(1-\mathrm{K})(\phi_C - \phi_D)\} \tag{3.64}$$

which is known as the Kappa formulation in which $-1 \leq \mathrm{K} \leq 1$. Non-linear higher-order schemes are mostly based on the Kappa formulation to secure accuracy but they incorporate some functions to adjust themselves in order to fulfil some specific criterion such as maintaining positive coefficients or total-variation-diminishing (TVD) property (Waterson, 1994). As an example, the SMART scheme proposed by Gaskell and Lau (1988), determines the face value ϕ_F by

$$\phi_F = \phi_C + 0.5\mathrm{B(r)}(\phi_C - \phi_D) \text{ with } \mathrm{B(r)} = \max(0, \min(2\mathrm{r}, 0.75\mathrm{r} + 0.25, 4)) \tag{3.65}$$

Hence the face value ϕ_F is determined completely according to the local flow conditions and the value of B(r) is always positive, as it is flux-limited. The scheme secures boundedness to avoid some unwanted behaviour that may produce spurious oscillations or negative values to k and ε. A drawback of non-linear schemes is that they may be less accurate than the linear higher-order schemes (CDS, QUICK, etc.) because the adjustment made in the mechanism sometimes may omit the higher-order correction terms. For example, the SMART scheme can switch itself to ordinary UDS when B(r) = 0 in equation (3.65). Other non-linear schemes possess similar behaviour. The differencing schemes will be tested and discussed further in chapter 4.

3.6 Solution of the Pressure-Linked Equations

The Navier-Stokes equations (3.21) for incompressible flows are not a simple convection-diffusion equation (3.51) because there is a pressure term ($\partial p/\partial x_i$) involved. The N-S equations are pressure-linked equations and the N-S equations must be solved simultaneously with the continuity equation (3.20) to determine all the unknowns. When turbulence is considered, the additional modelled equations are required to be solved as well and the solution procedure becomes more complicated. If the pressure term is known, the process of obtaining discretised equations for velocities from the momentum equations is similar to that of the convection-diffusion equations. Therefore a thought was that why not guess a pressure field and then apply some corrections during the iterative solution procedure. This thought has been realised by a method "SIMPLE" (Semi-Implict Method for Pressure-Linked Equations) and a revised version "SIMPLER" proposed by Patankar (1980).

3.6.1 SIMPLE Algorithm

SIMPLE is essentially a trial-and-error approach to get correct values that satisfy both of the N-S equations and continuity equation. The important steps of execution are:

1. Guess a pressure field.
2. Solve the momentum equations to obtain velocities which may satisfy the momentum equations but not necessarily continuity.
3. Construct continuity errors for each cell.

4. Solve the pressure-correction equation and the continuity error becomes the source term.
5. Adjust the pressure and velocity fields to get the velocities that satisfy continuity but not momentum.
6. Go back to step 2, and repeat with the new pressure field until continuity and momentum errors are acceptably small.

A variant of SIMPLE, known as SIMPLEST is the algorithm employed by PHOENICS to solve the pressure-linked equations (Spalding, 1981). The solution procedure of SIMPLEST is similar to SIMPLE but it has been enhanced to accelerate the rate of convergence by separating convection and diffusion terms for individual treatment. One of the advantages using SIMPLEST algorithm is that the pressure correction does not require under-relaxation during iteration and this is favourable because there is no certain way to determine an optimum under-relaxation factor (see section 3.7).

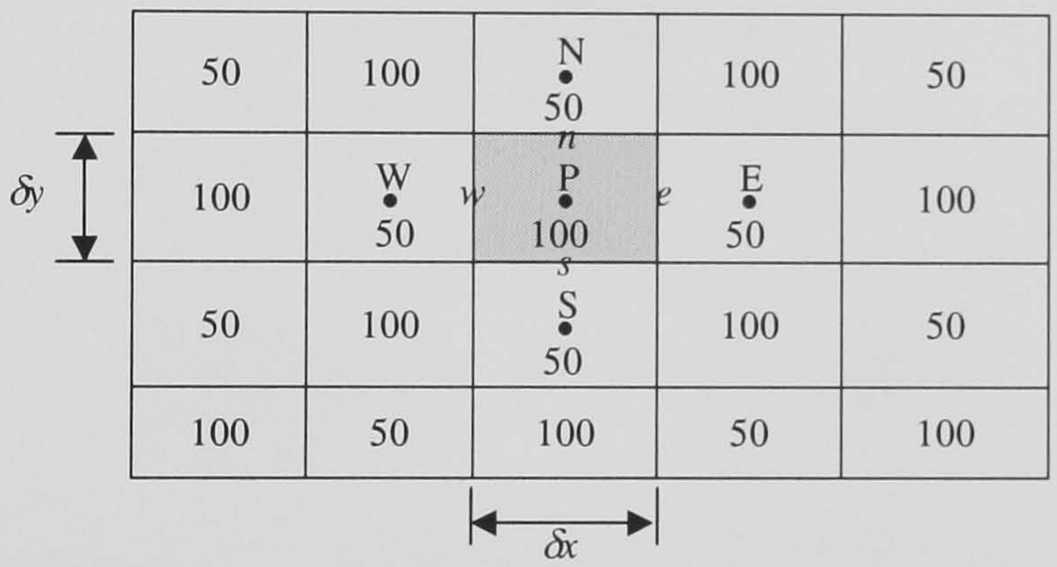

Figure 3.13 "Checker-board" pressure distribution. The values shown are the pressures stored in cell centres (e.g. $P_P = 100$, $P_E = 50$, $P_W = 50$, etc.)

Another difficulty regarding the pressure term in the momentum equation is the formulation of finite-volume equations. If the pressure distribution is like "checker-board" pressure field (figure 3.13), the cells for pressure and velocities need to be considered separately.

3.6.2 Staggered Grid Arrangement

Staggered grid arrangement is devised to avoid eliminating the pressure term in the formulation of the momentum equation. Consider a pressure field shown as figure 3.13, the pressure field is known and the pressure distribution is in "checker-board" form. The pressure term in the u and v momentum equations is

$$\frac{\partial p}{\partial x} = \frac{P_e - P_w}{\delta x} = \frac{(P_E + P_P)/2 - (P_P + P_W)/2}{\delta x} = \frac{(P_E - P_W)/2}{\delta x} = 0 \qquad (3.66)$$

and

$$\frac{\partial p}{\partial y} = \frac{P_n - P_s}{\delta y} = \frac{(P_N + P_P)/2 - (P_P + P_S)/2}{\delta y} = \frac{(P_N - P_S)/2}{\delta y} = 0 \qquad (3.67)$$

If the velocity cells are defined in the same position as pressure, the contribution of the pressure term will be zero in the momentum equation. To avoid this, the velocity cells and pressure cells have to be defined differently. The "staggered grid" is to evaluate scalar variables, such as pressure, density, temperature, etc. at the usual cell-centred nodes and to calculate velocity components on staggered grids centred around the cell faces. An illustration of the 2-D flow calculation with the staggered grids is shown in figure 3.14.

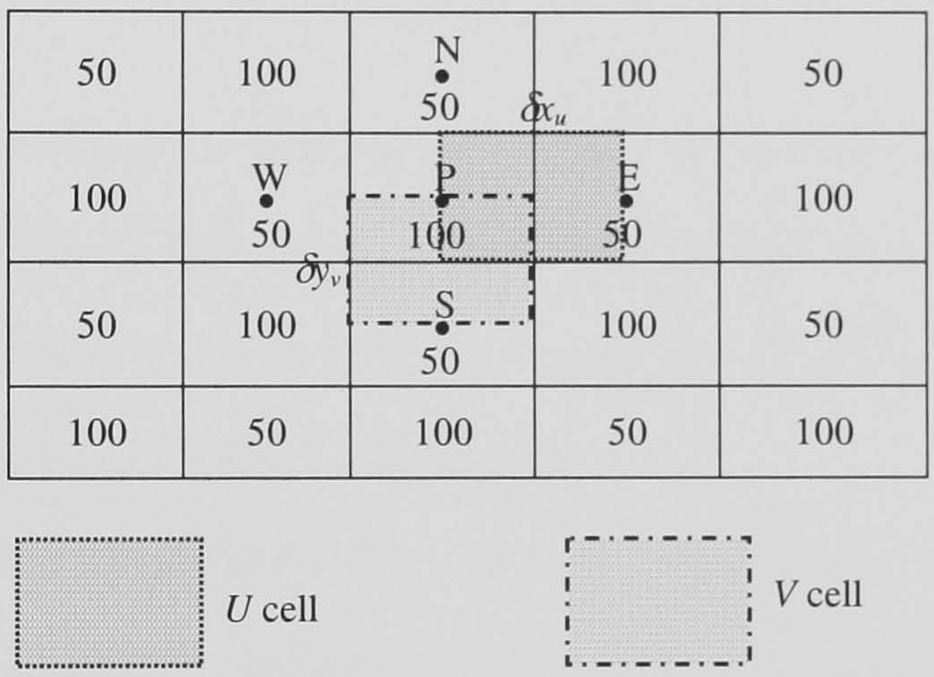

Figure 3.14 Staggered grid arrangement. The scalar cell centre is P and the velocity cells are around the scalar cell centre; each velocity cell centre coincides with the centre of the scalar cell face. Therefore the velocities are stored in the cell-face centres of the scalar cell.

With the staggered grids, the pressure term calculated for *U*-momentum equation is

$$\frac{\partial p}{\partial x} = \frac{P_E - P_P}{\delta x_u} \qquad (3.68)$$

and for *V*-momentum equation is

$$\frac{\partial p}{\partial y} = \frac{P_P - P_S}{\delta y_v} \qquad (3.69)$$

where δx_u and δy_v are the width of *U* cell and *V* cell respectively. Now the pressure term is a non-zero value calculated from equations (3.68-69) if using the same pressure field (figure 3.13). One advantage of applying the staggered grids is that the momentum equations need not be modified and the velocities and pressure remain strongly coupled.

The staggered-grid arrangement is the default formulation of finite-volume equations in PHOENICS and it is ideal with Cartesian coordinate system. Nevertheless, it is perhaps unsuitable if using curvilinear coordinates or unstructured grids because it is difficult to define staggered grids in those coordinate systems. There are other methods dictating all the variables (including velocities) to be solved and stored in the cell centre or cell corner but the numerical algorithm are rather complicated, usually involving Rhie-Chow (1983) interpolation and some special treatment. CFX 5 solves and stores the fluid variables at cell corners as it employs an unstructured grid system.

3.6.3 Elliptical Equation and Boundary Conditions

Parabolic, *elliptical*, or *hyperbolic* are mathematical terms in classifying the nature of differential equations. The characteristics of flows described by these equations are:

- *Parabolic*: a flow that the previous event cannot be affected by its following event, i.e. the *one-way* behaviour exists. For example, the developing boundary-layer-type flow in which the flow is consistent in direction and the flow in a later position does not affect the flow in its previous position.
- *Elliptical*: opposite to parabolic flows, the elliptical flow exhibits a sort of *two-way* behaviour, i.e. the flow conditions at a given location can be influenced by the changes on either side of that location. For example, the recirculating flows.
- *Hyperbolic*: it has a kind of one-way behaviour but not along coordinate directions. This kind of flow problem can be classified as generalised elliptical flow problems.

The steady N-S or RANS equations are elliptical equations (Bradshaw *et al.*, 1981) and the flows described by the equations are likely to generate recirculating flows at some locations of the computing domain. Most of the CFD codes initially assume the flow simulation is elliptical. The implications of elliptical or parabolic flows in computation are the formulation of equations, storage consumption and the requirement of boundary conditions. If the flow is parabolic, the storage for variables can be much less because only the latest flow variables are stored. It is also unnecessary to specify a down-stream boundary condition because the flow is along a one-way coordinate. Elliptical flows need more storage for flow variables and the down-stream boundary conditions are required. Therefore it is necessary to specify all the boundary conditions surrounding the computing domain in an elliptical flow simulation. Some commercial CFD codes may have their default boundary condition (BC) if unspecified. PHOENICS

automatically sets a symmetry boundary condition if users do not specify a BC at any side of the computing domain. This may affect the size of computing domain because the symmetry BC poses an impermeable boundary of the domain and the gradient of ϕ (e.g. pressure gradient $\partial p/\partial x_i$, velocity gradient $\partial u_i/\partial x_i$, etc.) normal to that boundary is zero. If the computing domain is too small, the pressure gradient (for example) normal to the boundary may not be zero, consequently a symmetry BC may not be appropriate at that boundary and consequently the calculated flow field may be affected by the incorrect BC.

There are many computational parameters required in the numerical simulations of turbulent flows such as the turbulence models, grid structures, differencing schemes, boundary conditions and domain size. When a CFD model has been created, the next step is to solve those equations.

3.7 Linear Equation Solvers

The finite volume equations are algebraic equations, which may be linear or non-linear, depending on the nature of the partial differential equations. There are two different categories of solutions: direct methods and iterative methods. Direct methods are based on a finite number of arithmetic operations leading to the exact solution of a set of linear algebraic equations. Iterative methods, on the other hand, are based on a succession of approximate solutions, leading to the correct solution with minimum or acceptable error after a finite number of steps. In the non-linear case, the algebraic equations are usually solved by an iterative technique that involves guessing a solution, linearising the equations about that solution and improving the solution. The process is repeated until a converged result is obtained. Another reason to use iterative methods is that the number of equations in FV methods is normally large. For example, each CV has a linear equation like (3.57) for each variable ϕ and there are at least six variables (p, u, v, w, k, ε) in a CV if using the k-ε model to simulate a turbulent flow. Therefore each CV contains six equations for an incompressible and turbulent flow. A system of algebraic equations can be written in a matrix form:

$$[A]\{\phi\} = \{Q\} \tag{3.70}$$

where [A] is the matrix containing coefficients of $\{\phi\}$ and. $\{Q\}$ is the matrix of known values (usually are boundary values). The direct method such as Gaussian elimination is to let [A] be a unity matrix, (i.e. the diagonal elements are all equal to one) and the unknowns $\{\phi\}$ can be determined once [A] becomes a unity matrix. The number of arithmetic operations required will be very large if the matrix [A] is large. If the number of grids or cells is 100,000 in the domain, the total number of equations need to be solved is 600,000, which is a huge amount of computation and using Gauss elimination is rather inefficient. It is not a common method employed in CFD. An iterative method to solve ϕ is by trial-and-error:

$$[A]\{\phi^n\} = \{Q\} - \{\omega^n\} \tag{3.71}$$

where ϕ^n is an approximate solution of ϕ and ω^n is a non-zero residual at nth iteration. The convergence error (e^n) can be estimated by

$$e^n = \phi - \phi^n \tag{3.72}$$

where ϕ is the converged solution. The purpose of the iteration is to drive the residual ω to zero as far as possible. Many methods are available and a small collection of which are listed as below:

- Jacobi method
- Gauss-Seidel method with successive over-relaxation
- Stone's method
- Conjugate gradient methods
- Multigrid methods

These methods have been described in many standard textbooks concerning numerical methods (e.g. Hirsch, 1988; Versteeg and Malalasekera, 1995; Ferziger and Peric, 1999). The default linear equation solver in PHOENICS is the Stone's method, known as SIP (strongly implicit procedure) solver. The conjugate gradient solvers and the multigrid solvers are also available to incompressible flow problems in PHOENICS. When these solvers are applied to the coupled equations (e.g. N-S equations or RANS equations), the solution procedure in PHOENICS is sequential. The sequential solution is to treat each equation as if it has only one unknown and the other terms are temporarily regarded as known variables using the best currently available values. The

current values at the first iteration may be obtained from the initial values given by users. Carefully selected initial values may accelerate the rate of convergence. These equations then are solved in turn, repeating the cycle until all equations are satisfied. The procedure usually requires

- *inner iterations* – iteration performed in each equation to get a current value for the unknown that can satisfy this equation, and
- *outer iteration* – iteration performed for all equations as a cycle to update the values determined by inner iteration so that these values may be improved to satisfy all equations.

It is also necessary to limit the change in each variable from one outer iteration to the next because sometimes a radical change to the value determined in previous cycle may result in an unstable circumstance (i.e. divergence). The technique of limiting the change is called *under-relaxation*. If a value ϕ determined at nth outer iterations is ϕ^{new} and the modified ϕ by under-relaxation is ϕ^n, thus

$$\phi^n = \phi^{n-1} + \alpha_\phi(\phi^{new} - \phi^{n-1}) \tag{3.73}$$

where ϕ^{n-1} is the ϕ determined in previous outer iteration, α_ϕ is the under-relaxation factor satisfies $0 < \alpha_\phi < 1$. The optimum under-relaxation factor is problem-dependent and the selection is usually by experience. The under-relaxation factor cannot affect the final converged solution but it does influence the behaviour of convergence.

With respect to velocities (u, v, w), the under-relaxation factor is usually replaced by the *false time step*, which is a pseudo time step used in the momentum equations for steady-state solution. It is to contrast that the time step used in a time-dependent flow simulation is a *real time step*, which is the temporal discretisation for the transient terms. Also the term of under-relaxation applied in the momentum equation for a steady-state solution is analogous to the transient term in the momentum equation (Versteeg and Malalasekera, 1995). In PHOENICS, usually the false time step for strong convection flows (e.g. wind flows around bluff bodies) is determined by the "cell residence time", which can be calculated from

$$DT_f = \frac{XULAST}{U_{in} \times NX} \tag{3.74}$$

where DT_f is the false time step; U_{in} is the X-direction velocity in the inlet; XULAST is the domain length at the X-direction and NX is the number of cells within it. Equation (3.74) assumes the dominant flow direction is at X direction. Sometimes a smaller value may be required for higher-order schemes because they need strong under-relaxation (small DT_f) to yield convergence. CFX 5 employs a multi-grid solver, which improves the rate of convergence by a process called "multigridding". It involves carrying out early iterations on a fine mesh and later iterations on progressively coarser virtual ones. The results are then transferred back from the coarsest mesh to the original fine mesh. It is a preferable method if the number of grids is large.

3.8 Summary

The fundamentals and some technical content of CFD have been presented in this chapter. CFD comprises a number of essential components for a successful flow simulation. A good flow simulation inevitably entails sufficient understanding of fluid dynamics and mathematical methods. Users cannot entirely rely on computer if they are not aware of the functions of those computational parameters. Many commercial CFD codes have their default values for those parameters but they are usually not optimal for some flow simulations, since the CFD developers cannot take care of all of the conceivable flow problems. For example, their default values may be sometimes good for internal flows but not necessarily for external flows. The selection of computational parameters therefore becomes CFD users' responsibilities.

The following chapters will present a series of case studies to suggest good practice for the simulations of wind environments around buildings.

Chapter 4 Numerical Simulations of Flows around a 2-D Square Cylinder and a 3-D Cube

Flow around a 2-D square cylinder is a fundamental case in the studies of bluff body aerodynamics. Although the geometry is simple, there are still many complicated flow phenomena such as vortex shedding, recirculation and flow separation around the cylinder. These phenomena are important to the understanding of wind environment around buildings. Among many similar physical experiments that have been reported in the literature, the investigation of flow field around a square cylinder made by Lyn *et al.* (1995) probably is the most prominent one in this field. They applied LDA (Laser-Doppler anemometry) to investigate the unsteady flow field around a square cylinder in a water tunnel and their data were quoted by many other authors (e.g. Murakami and Mochida, 1995; Mohammadi and Medic, 1996; Rodi, 1997) for various comparisons of CFD studies. Their CFD simulations focus on the comparison of turbulence model, including LES for the investigation of unsteady flow field. The experimental data for the flow field around a 3-D cube are from Martinuzzi and Tropea (1993). Lakehal and Rodi (1997) have simulated this case with CFD but they still accentuate the comparison of turbulence models. However, more comparisons regarding other computational parameters such as differencing schemes have not been discussed in their studies. This chapter firstly describes a 2-D numerical simulation using different computational parameters (turbulence models and differencing schemes) for comparison with Lyn's data. The main objectives are to discover a better turbulence model and a relatively accurate differencing scheme. The relatively better computational parameters will be subsequently applied to the 3-D case for more examinations.

4.1 Method

The experiment by Lyn *et al.* (1995) is an investigation of the vortex shedding phenomena induced by a square cylinder. The unsteady flow field, however, was not simulated because the main concerns of this study were of their mean values – the time-averaged velocities behind the 2D square cylinder and the mean turbulent kinetic energy in the vicinity of it. The Reynolds number of the flow was about 21,400, based on the

characteristic width of the cylinder. The boundary conditions such as the dimensions of the computing domain, the velocity of approaching flow and the intensity of turbulence were set as close as possible to the experiment described in their paper. The computed results will be compared with experimental data in respect of mean velocity profile and the profile of mean turbulent kinetic energy.

4.1.1 The Computing Domain and Grids

The dimensions of computing domain were determined by the size of the testing section of their water tunnel. The grids were of Cartesian type as the geometry of this simulation was simple. Also, it was easy to control the expansion ratios with the Cartesian grids around the square cylinder. The grids (figure 4.1) were refined in succession to get the grid-independent computation. The grid-independent solution was obtained when there was no significant change to flow field as grid density increased. The minimum spacing of grids was 0.05D (D is the width of the square cylinder). Therefore the numerical errors due to the mesh structure were minimised and the other computational parameters – turbulence models and differencing schemes were not affected by the grids.

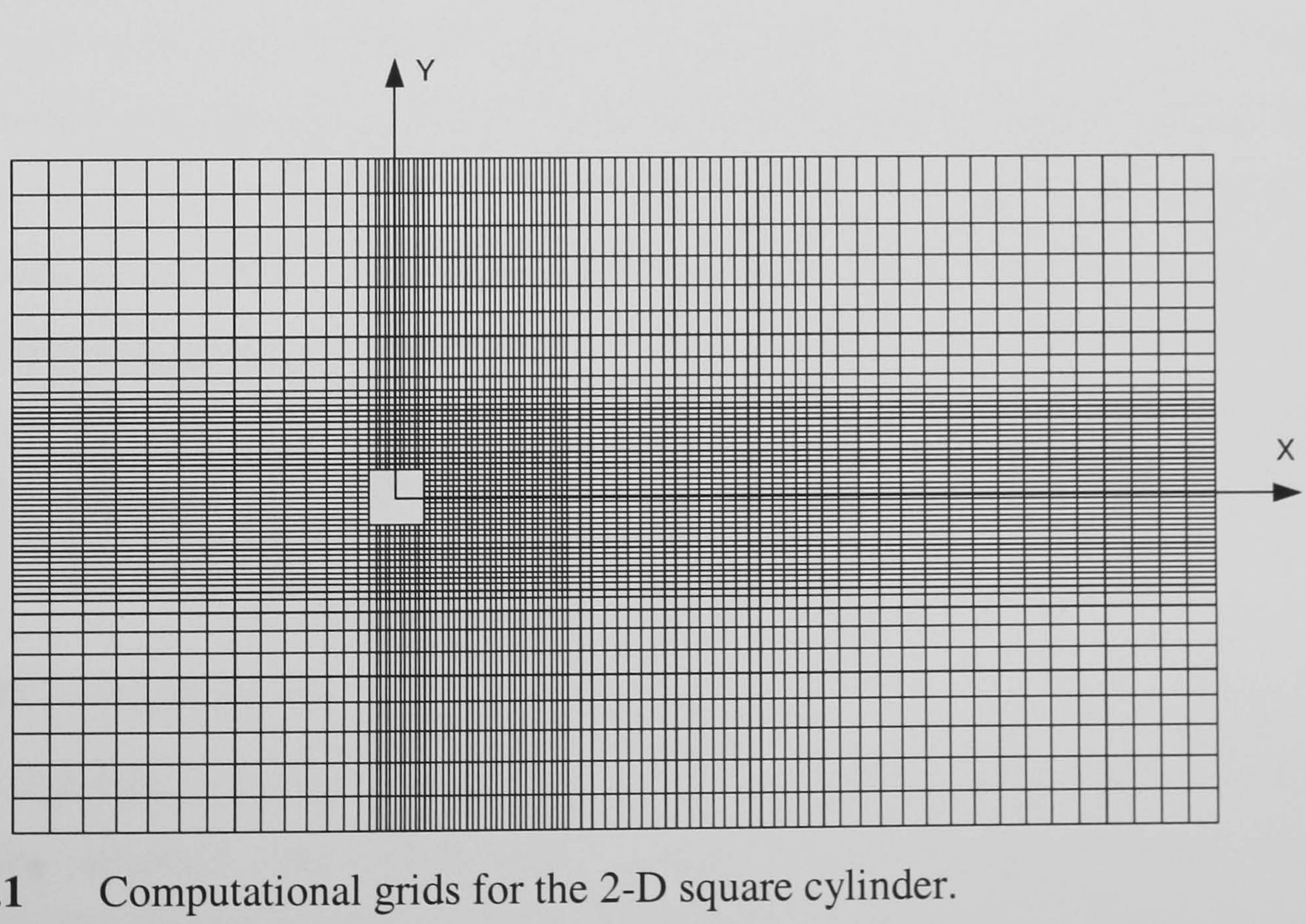

Figure 4.1 Computational grids for the 2-D square cylinder.

4.1.2 Turbulence Models

Since the main interests of this study was the time-averaged flow field and a time-dependent flow simulation was not intended, therefore the conventional two-equation RANS models were chosen for their popularity in the industry. Large eddy simulation

(LES) was not attempted since it need much more computing resources. The selected models, based on their popularity in the industry, were the standard k-ε model (Lauder and Spalding, 1974), the RNG k-ε model (Yakhot and Smith, 1992) and the two-layer k-ε model (Rodi, 1991). Other two-equation models are also available in PHOENICS but those less popular models have been excluded in this study because their applications regarding the wind flow simulations are few.

The above three k-ε family models have been applied in various simulations of flows past bluff bodies. Applying the two-layer k-ε model in a flow simulation around a cube has been reported by Zhou and Stathopoulos (1997). Using the RNG k-ε model in modelling flows around bluff bodies has been presented by Chang and Meroney (2001). Applications of the standard k-ε model in flow simulations around buildings are found plentiful in the literature, such as Paterson and Apelt (1986), Murakami and Mochida (1989), Murakami *et al.* (1990), Richards and Wanigaratne (1993), etc. The RNG model is a modified version of the standard k-ε model in which the constants of the standard k-ε model have been replaced with different values and a source term is added to the transport equation of ε. The two-layer k-ε model uses the standard k-ε model only away from the wall in the fully-turbulent region, and the near-wall viscosity-affected layer is resolved with a one-equation model involving a length-scale prescription. These models have their own merits reported in previous studies under various circumstances for different flow simulations. Nevertheless, these models have not been compared together using an identical computing domain and geometry for a bluff-body flow simulation. Through the comparison, this may be of help to acquire more understanding of their performance in predicting the flow field around a bluff body.

4.1.3 Differencing Schemes

Another important computing parameter in the flow simulation is the choice of differencing scheme. The differencing scheme possesses an important role in discretisation of the finite-volume equations. It is also a source of error in numerics, as the discretisation procedure is actually an approximation to the exact equation. A plethora of differencing schemes can be found in the literature and many of them have been built into PHOENICS. There are five linear higher-order schemes and twelve non-linear higher-order schemes available in PHOENICS for staggered grids, in addition to the default scheme – Hybrid differencing scheme. Malin and Waterson (1999) have

given a review of these higher-order schemes and some suggestions in choosing a differencing scheme have also been reported. They do not recommend using linear higher-order schemes (e.g. CDS, QUICK) in any flow simulation involving transport of scalars (e.g. mass concentration or species) because those schemes are likely to give unphysical values (unboundedness). For incompressible flows where no transport of scalars are involved, applying linear higher-order schemes to velocity variables (u, v, w), however, may be recommended according to their studies. In contrast, non-linear higher-order schemes (e.g. SMART) are highly recommended except VANALB and OSPRE schemes because they also present some unbounded behaviour. However, the flow simulations in their testing cases are mainly about laminar flows and the cases regarding turbulent flows are rare. The present study will further examine the higher-order schemes with turbulent flow simulations. Since it has learned that many of the higher-order schemes have similar performance, it becomes clear that to test each scheme is unnecessary. Therefore the selected differencing schemes for this study were:

- Hybrid – default scheme.
- QUICK – 3rd order accurate linear higher-order scheme.
- SMART – 3rd order accurate non-linear higher-order scheme.
- VANL2 – Van Leer harmonic scheme, also known as HLPA (hybrid linear / parabolic approximation) proposed by Zhu (1992), which is a 2nd order accurate non-linear higher-order scheme and it also complies with TVD (Total variation diminishing) criteria (c.f. Hirsch, 1990).

The selected schemes were applied to velocities (u, v, w) as well as k and ε and all the schemes were employed with above selected turbulence models. It is also possible to apply a linear higher-order scheme to velocities and a non-linear higher-order scheme to k and ε. The combination of a linear higher-order scheme and a non-linear higher-order scheme was therefore also tested.

4.2 Results – 2D Square Cylinder

The 2-D computation was investigated first. All the data were non-dimensionalised by the characteristic length D of the cylinder and the freestream velocity U_r. The first set of data to be compared was the mean velocities at the wake of the cylinder. In Lyn's experiment, the velocity field comprises a number of components as following:

$$u(t) =< u(\phi(t)) > + u'(t)$$
$$= U + \tilde{u}(t) + u'(t) \tag{4.1}$$

where U is the long-time-averaged velocity, $\tilde{u}(t)$ the periodic component with zero mean and $u'(t)$ is the turbulent component. Since the flow field of vortex shedding is periodic, therefore the periodic motion can be defined by a number of phases, i.e. $\phi(t)$. The component $< u(\phi(t)) >$ denotes the ensemble-averaged velocity obtained from the periodic and unsteady motion of the fluid. The ensemble-averaged velocity is not statistical-stationary as it contains the periodic component $\tilde{u}(t)$ but the long-time-averaged velocity U is a statistical-stationary (time-independent) value. The velocity component to be compared is the time-independent velocity U.

4.2.1 Comparison of Mean Velocity Profile

From figure 4.2, the experimental data shows the recirculation zone is within a range about X/D = 1.4 and the streamwise velocities at the wake are soon recovered from the momentum loss within a short distance, around X/D = 4 where the velocities are about 60% of the freestream velocity.

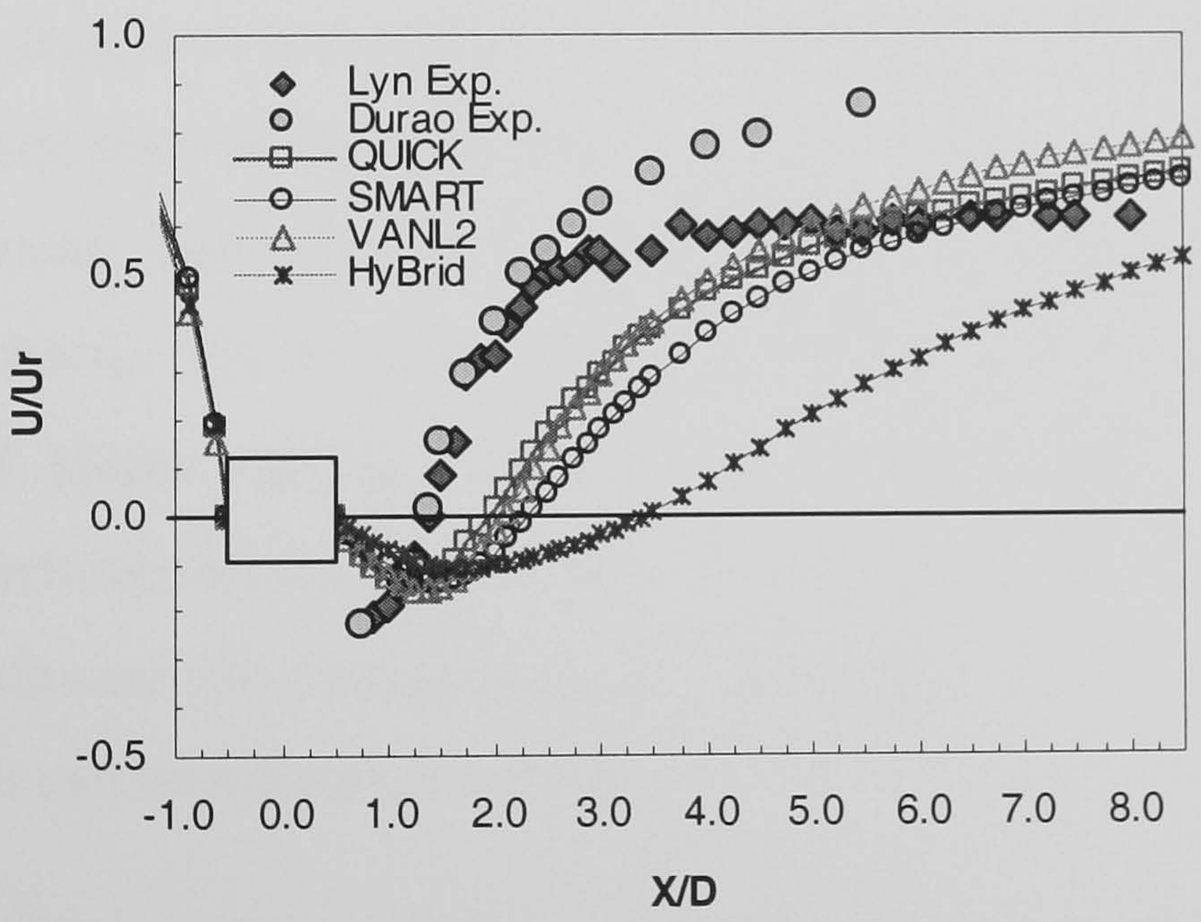

Figure 4.2 Velocity profiles calculated by the standard k-ε model with various differencing schemes.

The computed results exhibited the same trend but the length of recirculation zone predicted by the standard k-ε model was unanimously larger, around X/D = 2.2. Figure 4.2 also shows that the Hybrid scheme, which is a combination of the first-order upwind differencing scheme (UDS) and the second-order central differencing scheme (CDS), results in the worst agreement with the experimental data. It is mainly because the first-

order UDS is numerically diffusive and the advantage of CDS cannot be exploited when the local Peclet number is greater than 2 (c.f. chapter 3). In contrast, the values calculated by other higher-order schemes, QUICK, SMART and VANL2 were better.

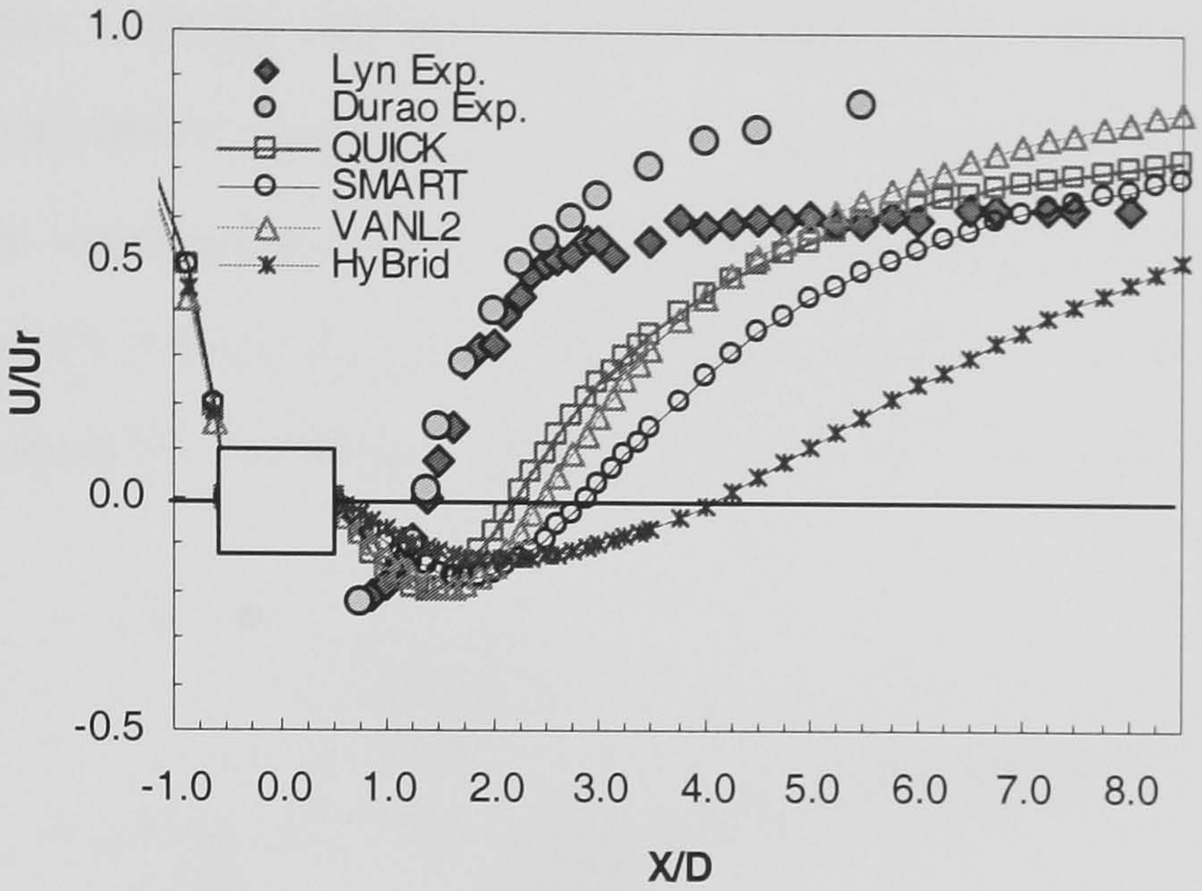

Figure 4.3 Velocity profiles calculated by RNG modified k-ε model with various differencing schemes.

The RNG modified k-ε model was subsequently tested with the same differencing schemes. The length of recirculation zone calculated by the RNG model was larger and less satisfactory than the performance of standard k-ε model. Figure 4.3 shows that using higher-order schemes with the RNG model still yield better results compared to the Hybrid scheme. The RNG modified k-ε model attempts to eliminate the excessive production of kinetic energy (k) calculated by the standard k-ε model in order to improve its performance for the calculation of separated flows but this modification also renders an unfavourable consequence, i.e. slow recovery of momentum at the wake of the cylinder. It can be inferred from that

$$\nu_t = C_\mu \frac{k^2}{\varepsilon} \tag{4.2}$$

so ν_t (eddy viscosity) is smaller if k becomes smaller. Since the production of k calculated by the RNG model was reduced by its modification, therefore the eddy viscosity became smaller in its calculation. As the eddy viscosity calculated by the RNG model was smaller, the length of recirculation zone predicted by the RNG model was generally larger regardless of which differencing scheme was used.

Figure 4.4 presents the performance of the two-layer k-ε model with the selected differencing schemes. The predictions made by this model agreed favourably with the experimental data using any differencing scheme tested here. The length of the recirculation zone and the trend of velocity profile were all predicted very well. The model introduces a fairly well-established length scale distribution near the wall and employs a one-equation model to resolve the near-wall layer, whereas the outer layer is resolved by the standard k-ε model approach. The near-wall layer and the outer layer join at the regions where the local Reynolds number is equal to 350. The two-layer approach employed by this model exhibited excellent performance in this case.

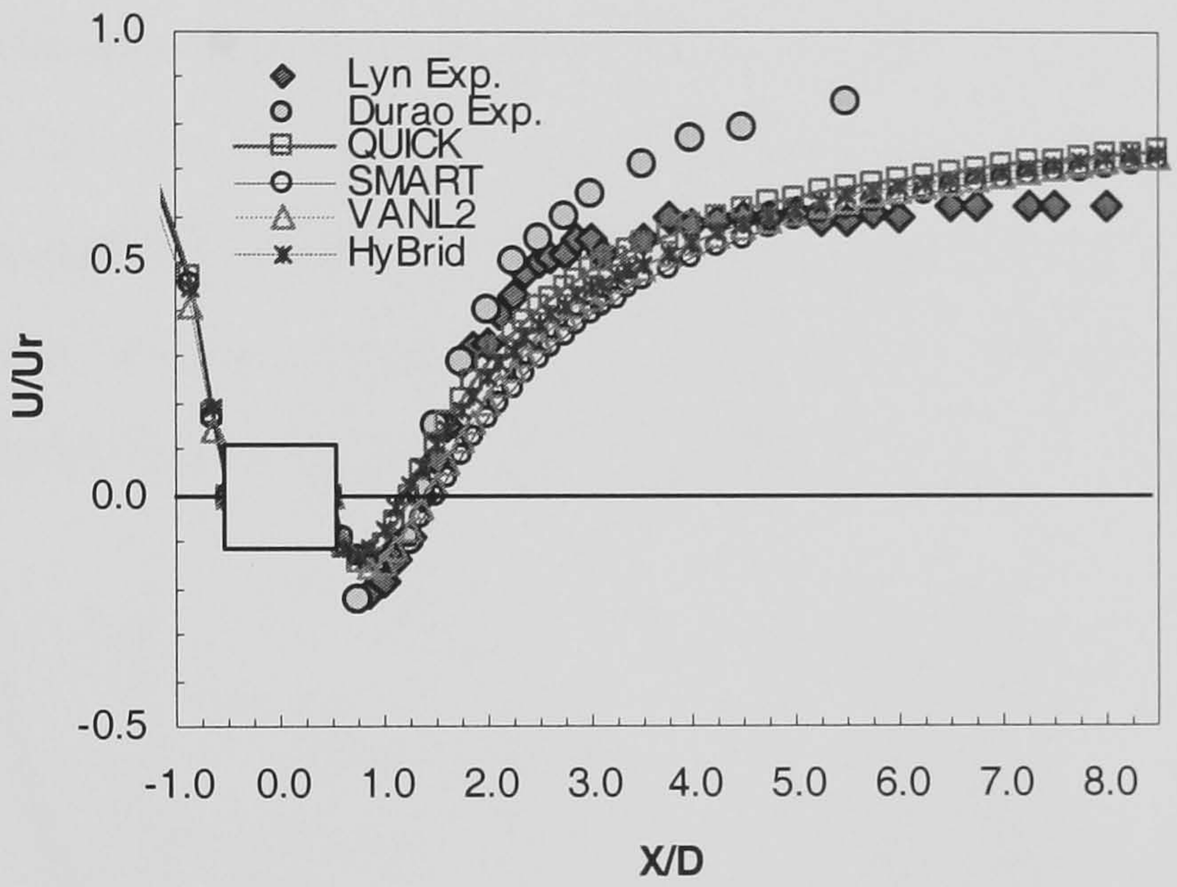

Figure 4.4 Velocity profiles calculated by the two-layer k-ε model with various differencing schemes.

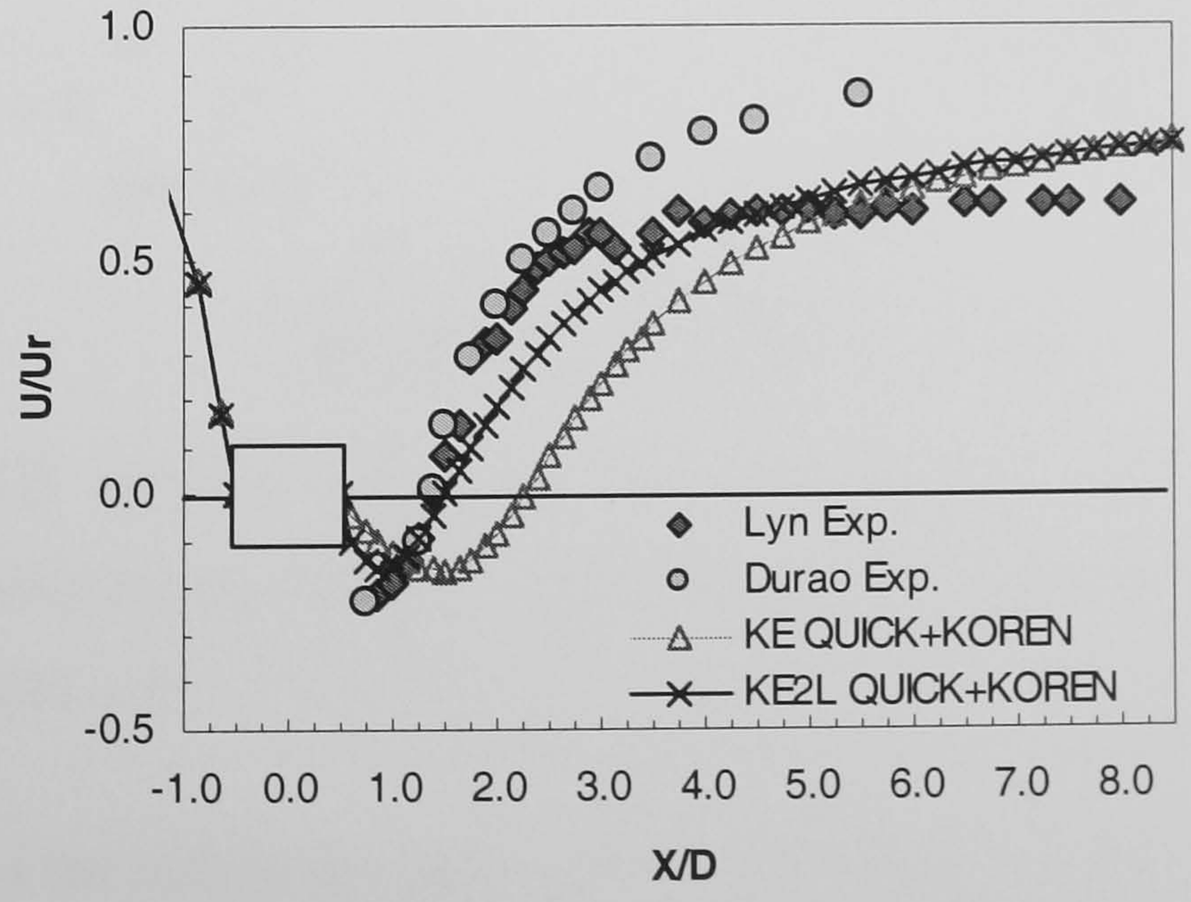

Figure 4.5 Velocity profiles calculated by the two-layer k-ε model and the standard k-ε model with the combined differencing schemes.

Figure 4.5 shows the velocity profile by applying the linear higher-order scheme QUICK to the velocities (u, v, w) and using another non-linear higher-order scheme KOREN with respect to k and ε. It presents similar results compared with previous calculations and still, the two-layer model makes a better prediction of the velocity profile.

4.2.2 Comparison of Mean Turbulent Kinetic Energy Profile

The second set of data to be examined is the averaged turbulent kinetic energy (KE), since the turbulence contributions are also of importance to the evaluation of pedestrian comfort. The available data for comparison are at the locations X/D = 2 and X/D = 6 laterally from Y/D = 0 to Y/D = 2. As the flows at the wake in the experiment were periodically changed due to the phenomenon of vortex shedding, the observed turbulent kinetic energy also varied periodically. The primitive periodically varied values were averaged in order to obtain the long-time-averaged values for comparison.

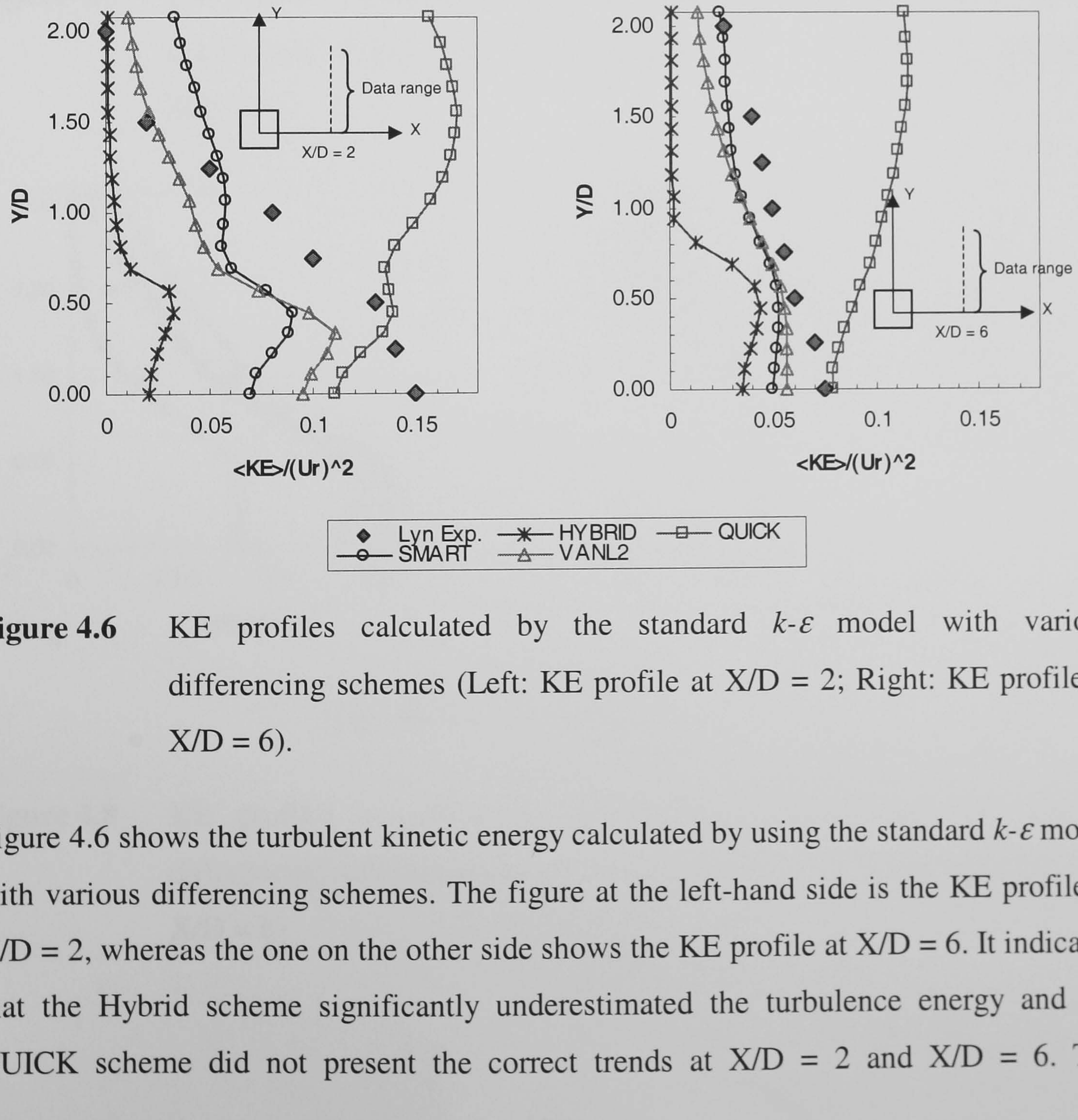

Figure 4.6 KE profiles calculated by the standard k-ε model with various differencing schemes (Left: KE profile at X/D = 2; Right: KE profile at X/D = 6).

Figure 4.6 shows the turbulent kinetic energy calculated by using the standard k-ε model with various differencing schemes. The figure at the left-hand side is the KE profile at X/D = 2, whereas the one on the other side shows the KE profile at X/D = 6. It indicated that the Hybrid scheme significantly underestimated the turbulence energy and the QUICK scheme did not present the correct trends at X/D = 2 and X/D = 6. The

predictions made by the other two non-linear schemes were improved, either for KE at X/D = 2 or KE at X/D = 6. The calculations made by QUICK scheme and the standard k-ε model obtained too much turbulent kinetic energy at these two locations.

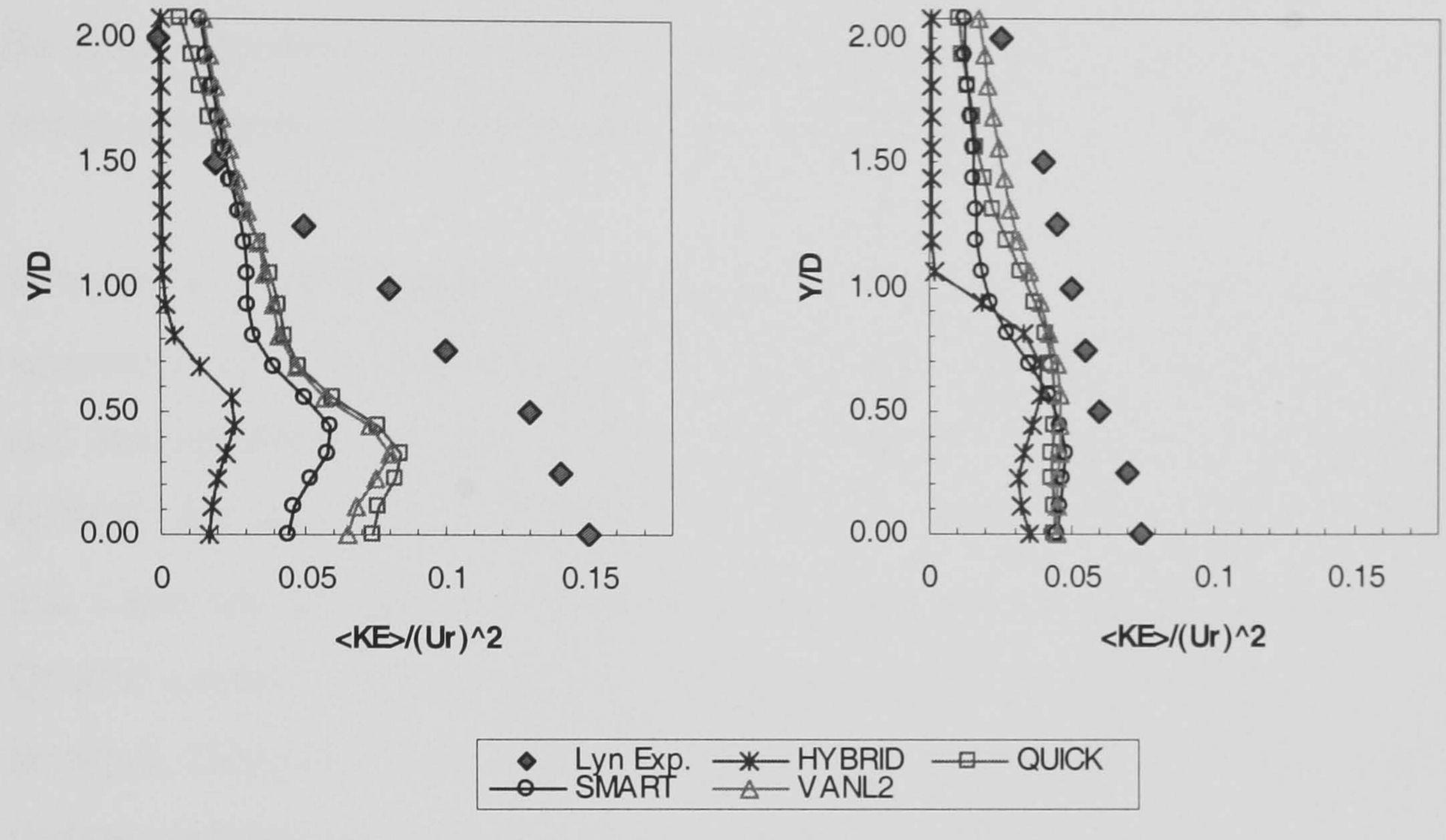

Figure 4.7 KE profiles calculated by the RNG modified k-ε model with various differencing schemes (Left: KE profile at X/D = 2; Right: KE profile at X/D = 6).

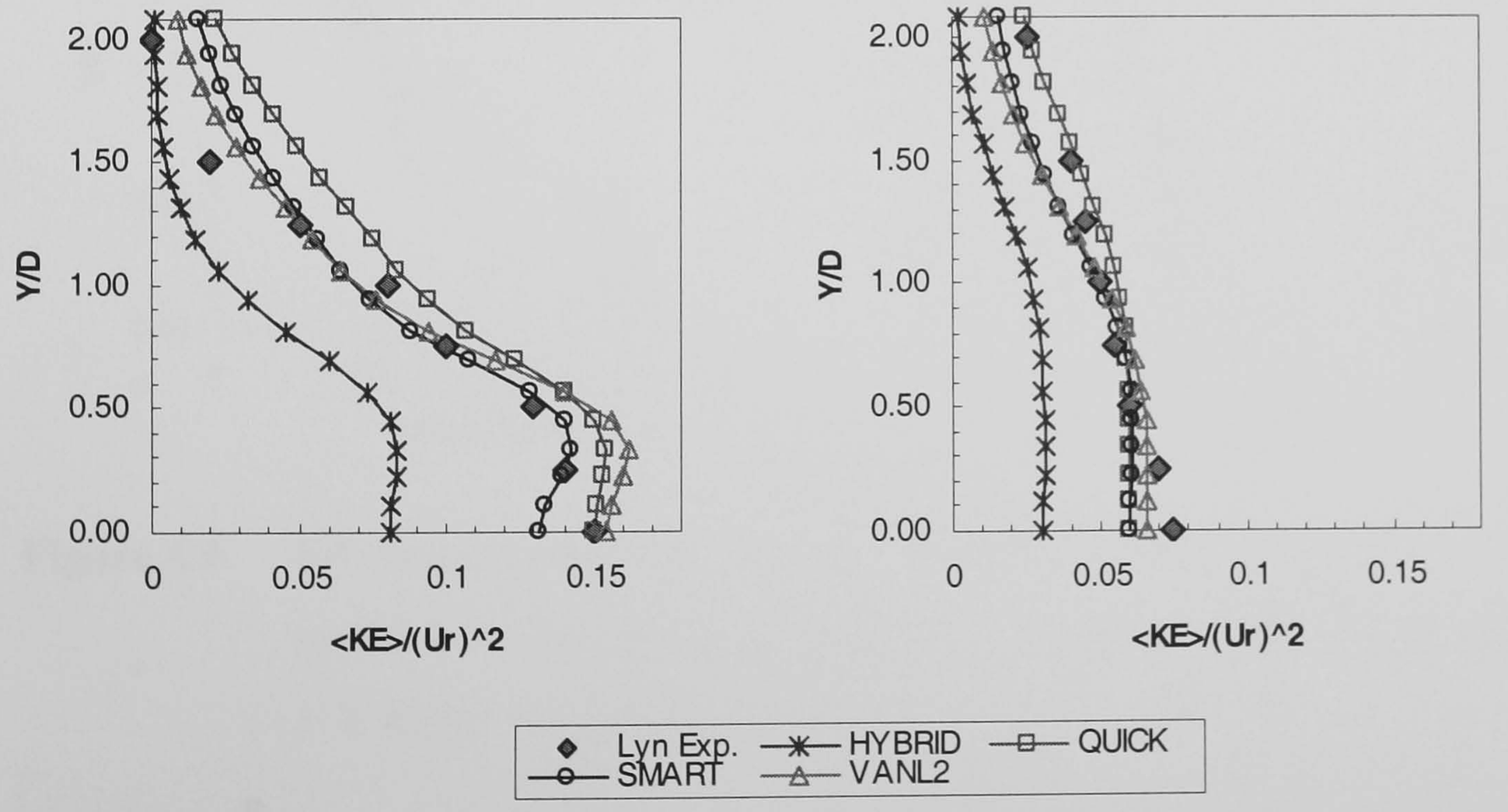

Figure 4.8 KE profiles calculated by the two-layer k-ε model with various differencing schemes (Left: KE profile at X/D = 2; Right: KE profile at X/D = 6).

When the RNG modified k-ε model was used, the prediction made by Hybrid scheme was still worse and although the other higher-order schemes obtained better results, the computed KE values were much lower than the experimental data at X/D = 2 and the calculated KE values at X/D = 6 were all lower than the measured values (figure 4.7). By observing these two graphs in figure 4.7, it also proved that the turbulent kinetic energy calculated by the RNG model was indeed smaller in the wake region.

In figure 4.8, the KE profile calculated by the two-layer k-ε model was in much better agreement with the experimental data but the performance of the Hybrid scheme was still less satisfactory. Figure 4.9 shows the computed values using the combination of QUICK (for velocities) and KOREN (for k and ε) differencing schemes. It was noticed that when the standard k-ε model was used with this combination, the deficiency of QUICK scheme – presenting an incorrect trend of KE values (figure 4.6), was fairly rectified. Using this combination did not affect the performance of the two-layer model and the performance of the two-layer k-ε model was still better.

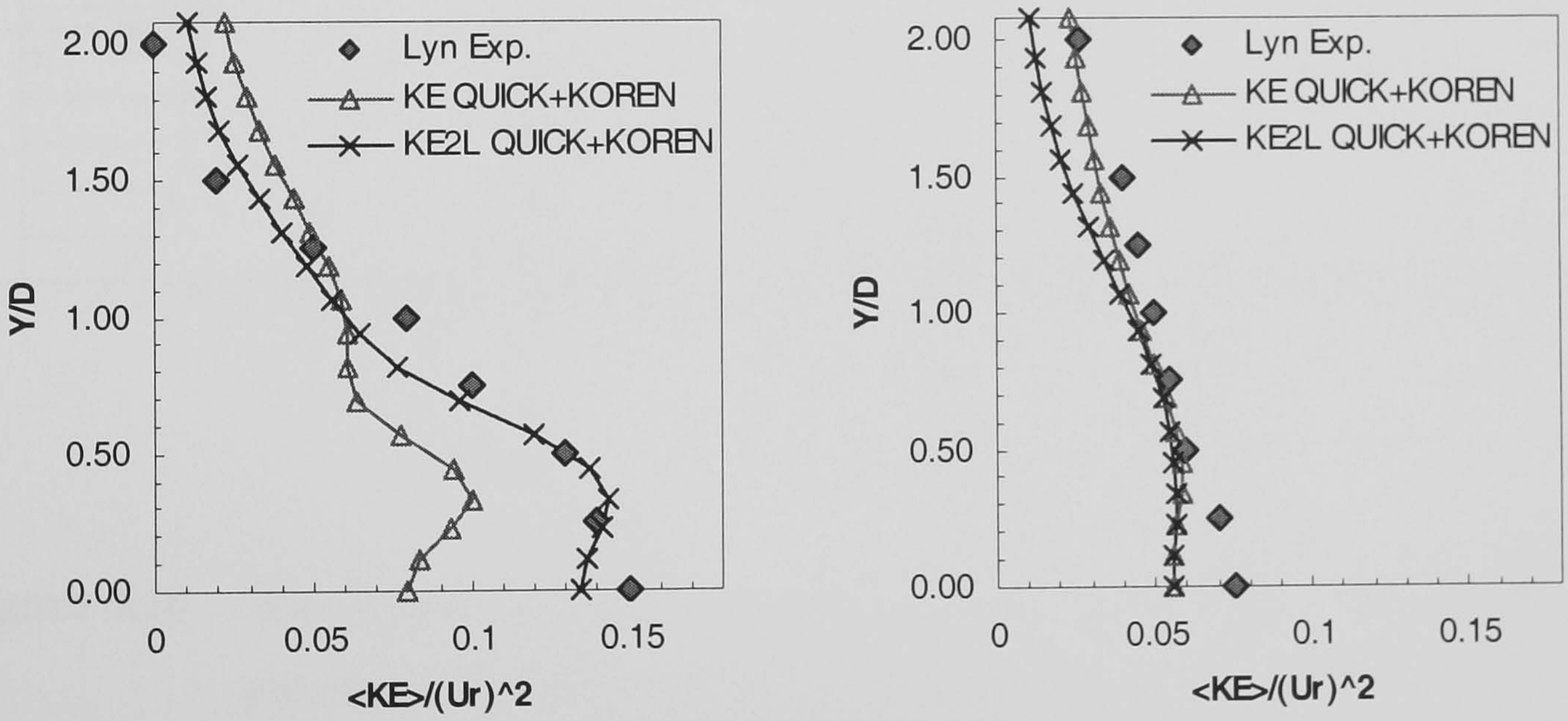

Figure 4.9 KE profiles calculated by the two-layer k-ε model and the standard k-ε model with the combined differencing schemes (Left: KE profile at X/D = 2; Right: KE profile at X/D = 6).

From these comparisons, it became clear that the two-layer k-ε model generally performed favourably when it was applied with one of the higher-order differencing schemes. In addition, the performance of the standard k-ε model with non-linear higher order schemes was also relatively satisfactory. The two non-linear higher-order schemes – SMART and VANL2 were able to obtain higher level of accuracy in this 2-D case. Therefore the preliminary conclusion can be made – *Either using the two-layer k-ε*

model or the standard k-ε model with non-linear higher-order differencing schemes is likely to obtain better predictions of the flow field around a bluff body. This statement will be examined further in the following section.

4.3 Flow Simulation around a 3-D Cube

The 3-D simulations were carried out by using the two-layer k-ε model and the standard k-ε model with a non-linear higher-order differencing scheme. The experimental data are available from Martinuzzi and Tropea (1993). In their experiment, a cube was placed in a tunnel with fully developed channel flows and the measurements were made with respect to the flow velocities and the distributions of turbulence energy at the (vertical) symmetric plane of the cube (figure 4.10).

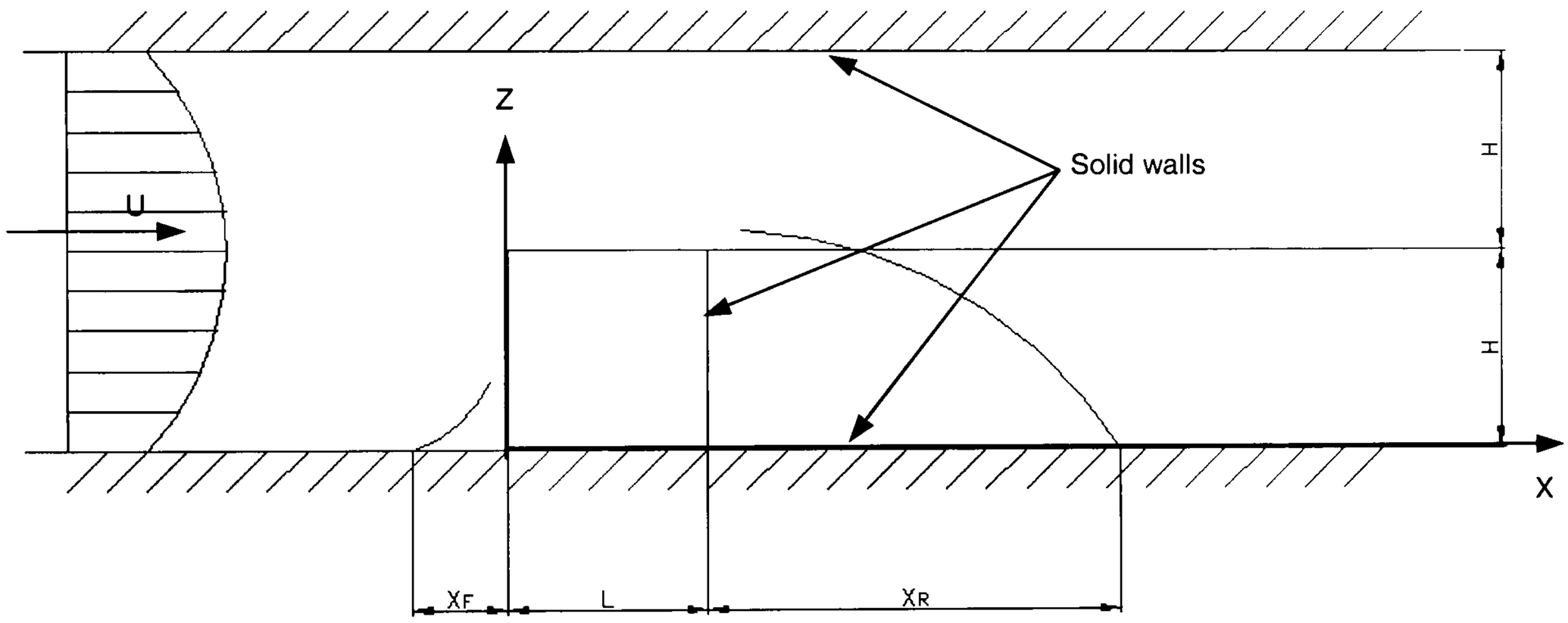

Figure 4.10 The layout of Martinuzzi and Tropea's experiment. The height of the channel is 2H (H is the height of the cube); U is the bulk velocity in the inlet. X_F is the length of flow separation in the front of the cube and X_R is the length of flow reattachment at the leeward side of the cube.

This case has been studied numerically by Lakehal and Rodi (1997) in which they employ several variants of the k-ε model to simulate the flow field around the cube. Their results indicate that a good prediction of X_R is difficult. Another study by Shah and Ferziger (1997) is a numerical simulation using LES and their results agree very well with the experimental data but the computing costs have been very high since the number of grids is over 1.1 million. Since this is also a standard case for validation of numerical models, the preliminary conclusions made in the previous section will be further examined using this case.

4.3.1 Geometry and Computational Grids

The dimensions of the channel were 3.9 m × 0.6 m × 0.05 m (length × width × height) and the cube height was 0.025 m. The leading edge of the cube was placed 52 channel heights downstream of the inlet in order to obtain fully developed flows at least 5 channel heights upstream of the front face of the cube. The computational grids were also of Cartesian type and the grids were refined in the vicinity of the cube to enhance the resolution of the velocity field for comparison with the experimental data. The minimum spacing was 0.01H (H is the cube height) near the walls. The number of grids was 159 × 67 × 26 (streamwise × spanwise × vertical) for the k-ε model and 164 × 67 × 31 for the two-layer model (figure 4.11). The solutions were grid-independent in both CFD simulations.

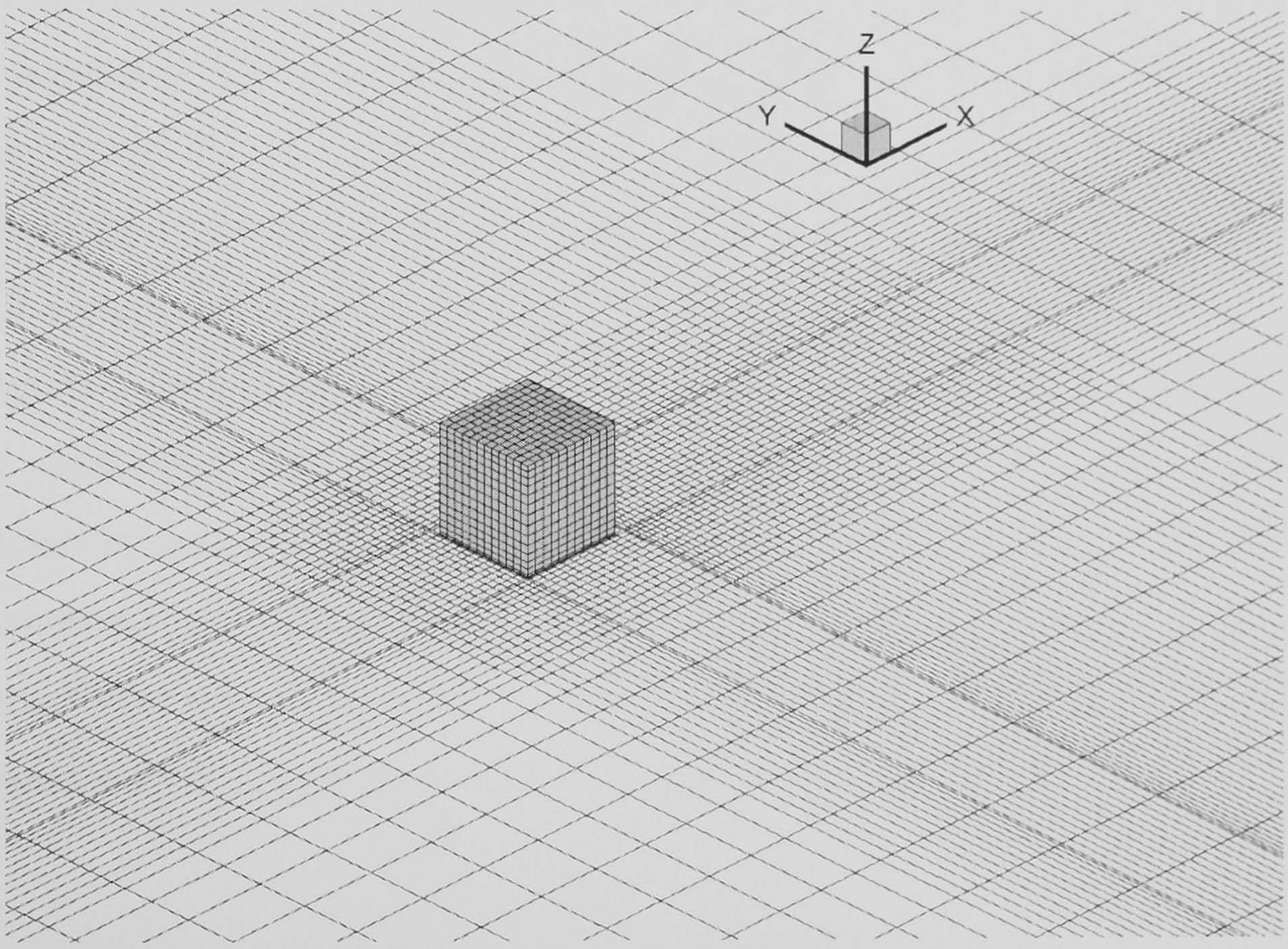

Figure 4.11 The computational grids for the 3D cube. The flow is approaching along the X-axis direction.

4.3.2 Turbulence Model and Differencing Scheme

Two turbulence models were applied in this computation – the standard k-ε and the two-layer k-ε models. The differencing scheme – SMART was used for the convection terms of the RANS equations and the transport equations of k and ε. Using the SMART scheme was in favour of its accuracy of 3rd order. As the SMART scheme requires stronger under-relaxation to control the behaviour of convergence during iteration, the

value of false time step suggested by equation (3.74) was not strong enough to secure convergence in previous tentative runs. From trial-and-error, a 10 times smaller value was found adequate for this computation. Since the under-relaxation factor was "tight", the values would not change much at each outer iteration, therefore the number of iterations required need be larger to get the final steady solution. The conjugate-gradient solver was used and after 3,000 iterations, the residual for the mass of air was less than 10^{-6}, thus the mass was conserved and the computation was sufficiently converged.

4.4 Results – 3D Cube

The available data for comparison are the mean velocity profiles and the turbulent kinetic energies along the streamwise axis (X-axis) at the plane of symmetry. The flow pattern is also available for comparison. Therefore some interesting flow characteristics such as separation and recirculation can be compared qualitatively and quantitatively. The experimental data is from Martinuzzi and Tropea (1993) in which they use oil film to visualise the flow field around the cube and several flow characteristics such as vortex, flow separation and reattachment have been identified (figure 4.12). They also have measured the profiles of mean flow velocities (U) and turbulent kinetic energies along the centre line of the cube on the plane of symmetry. The computed flow pattern was depicted by the streamlines (figures 4.13-14). Although the oil streaks are different from streamlines but they are still comparable to certain extent, such as the approximate locations of flow separation, recirculation and reattachment. The computed results will be compared with the experiment of Martinuzzi and Tropea (1993).

4.4.1 Comparison of Flow Pattern

Figure 4.12 shows the picture of oil streaks; the reattachment region is marked by "R" and the well-known horse-shoe vortex is depicted by the line "A" and "B". The "D" corresponds to the outer limits of the cube wake. The distance between the two ends of this line "D" decreases (converging) up to approximately the reattachment point and then increases (diverging) again. The computed streamlines using the two-layer k-ε model and the standard k-ε model are shown in figure 4.13 and 4.14 respectively. In figure 4.13, the zone between "A" and "B" was slightly larger than figure 4.14. The dissimilarities in the wake flows calculated by these two models were very few.

Comparing figures 4.12-14, the location of flow reattachment "R" calculated was unanimously farther than the experiment.

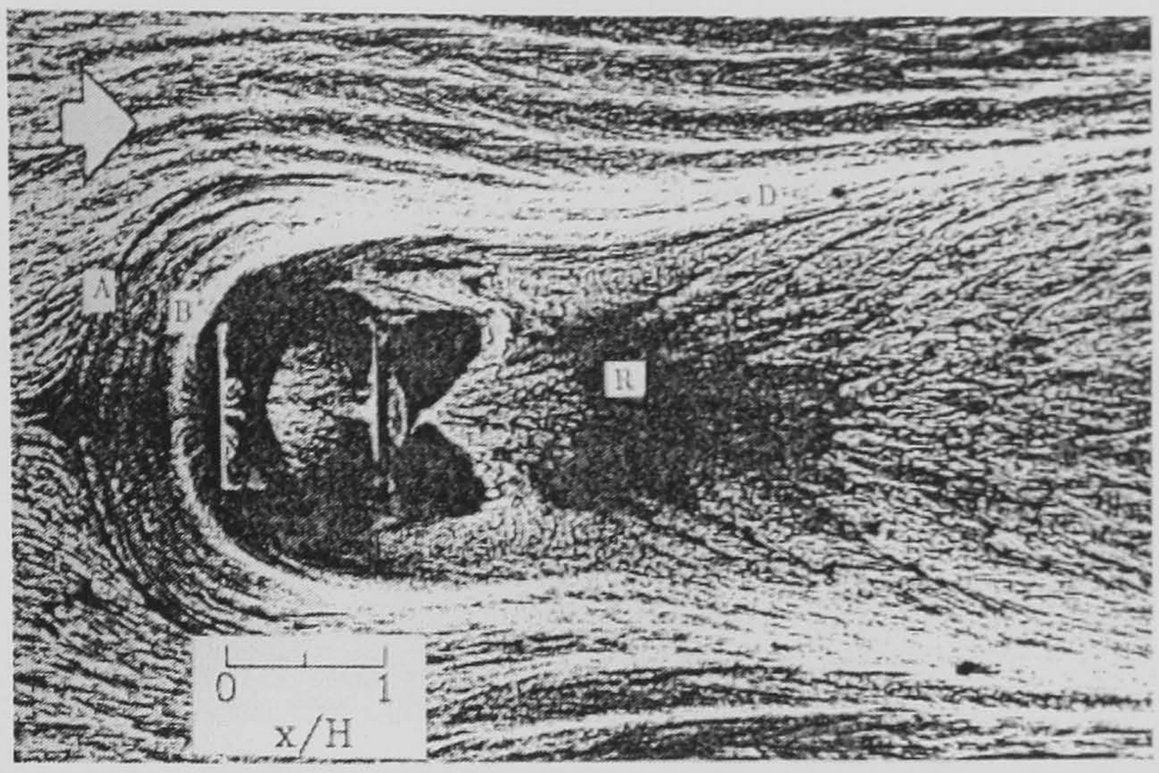

Figure 4.12 The flow field around the cube [Martinuzzi and Tropea (1993)].

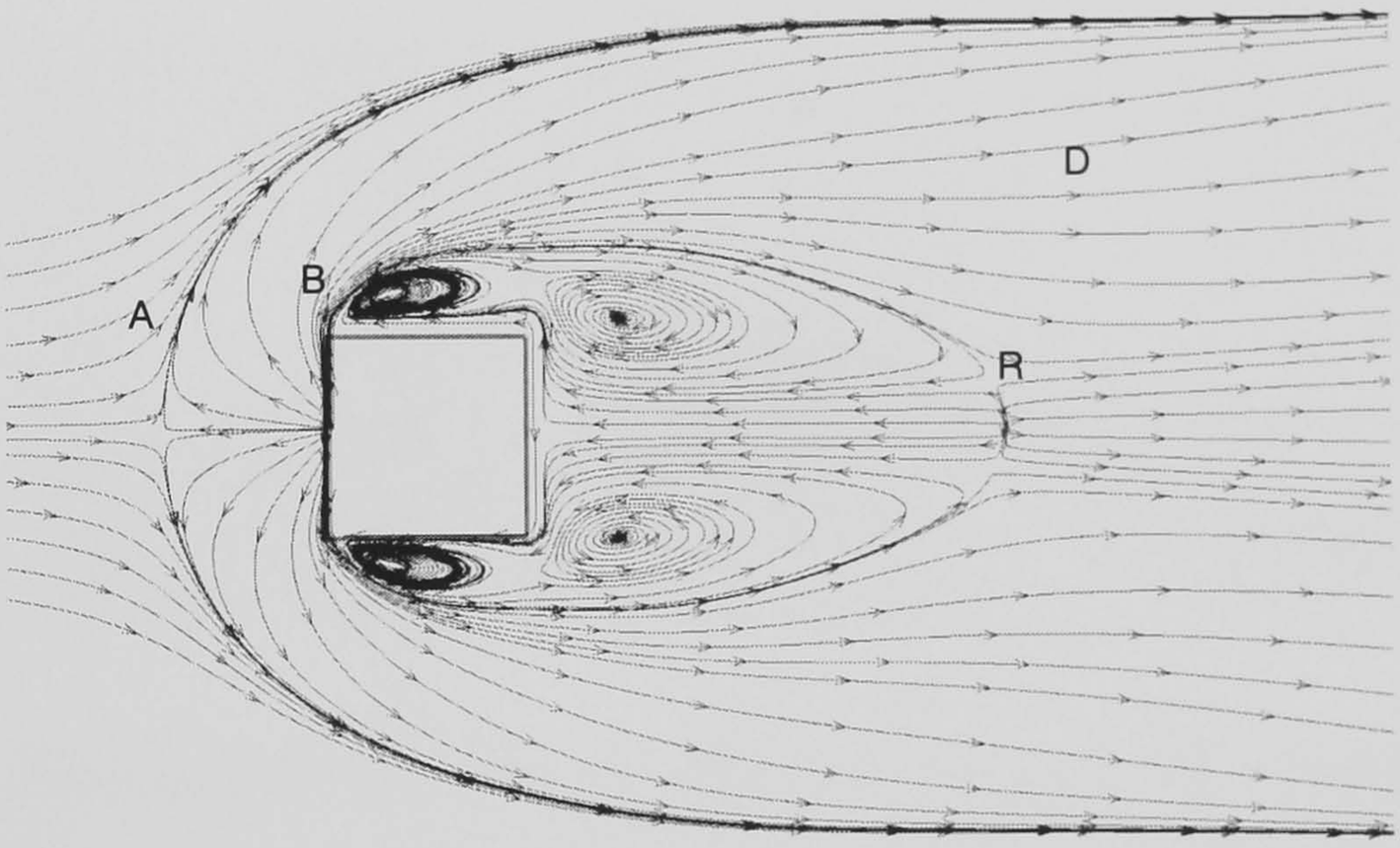

Figure 4.13 The (horizontal) streamlines computed by the two-layer k-ε model.

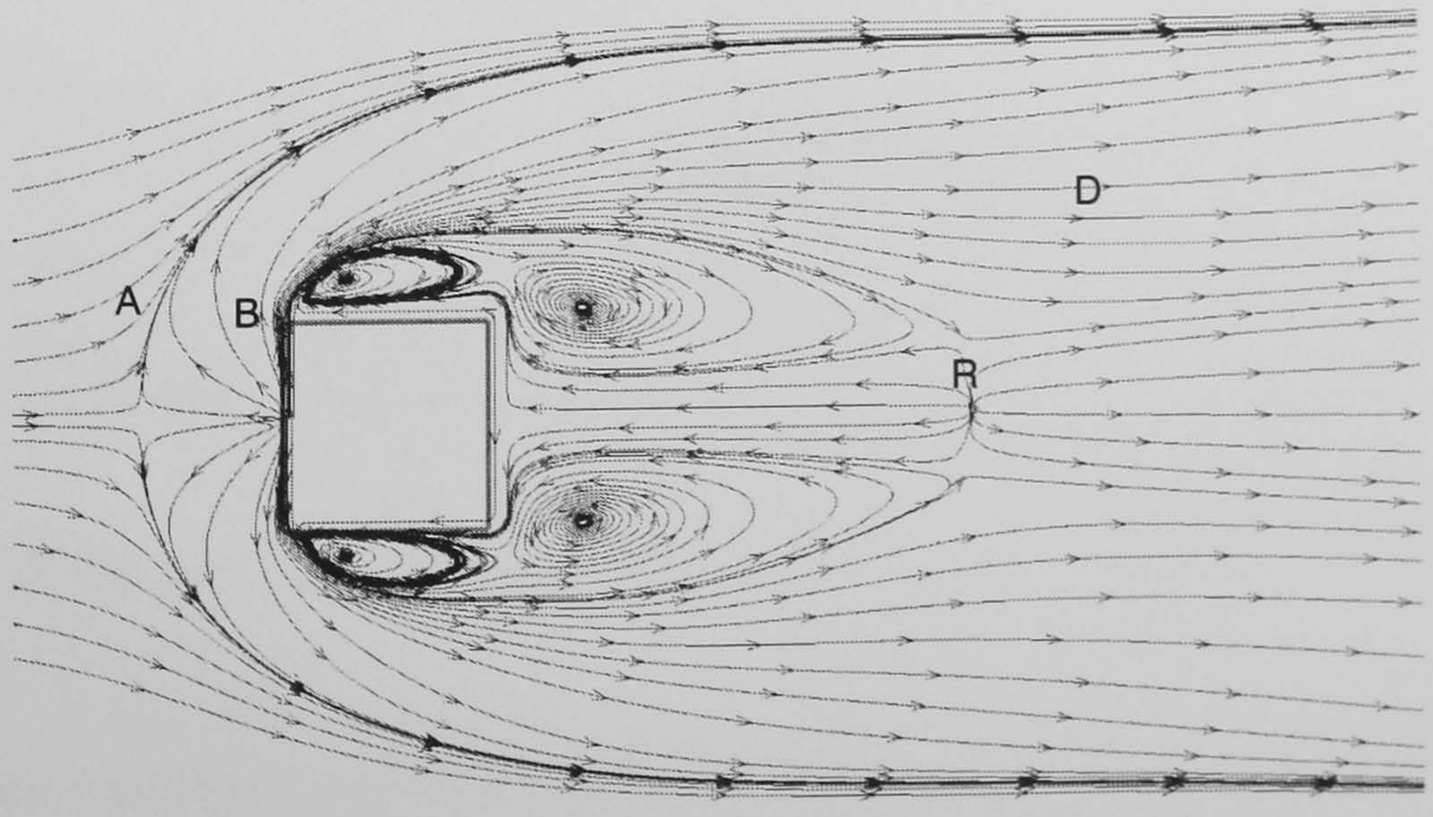

Figure 4.14 The (horizontal) streamlines computed by the standard k-ε model.

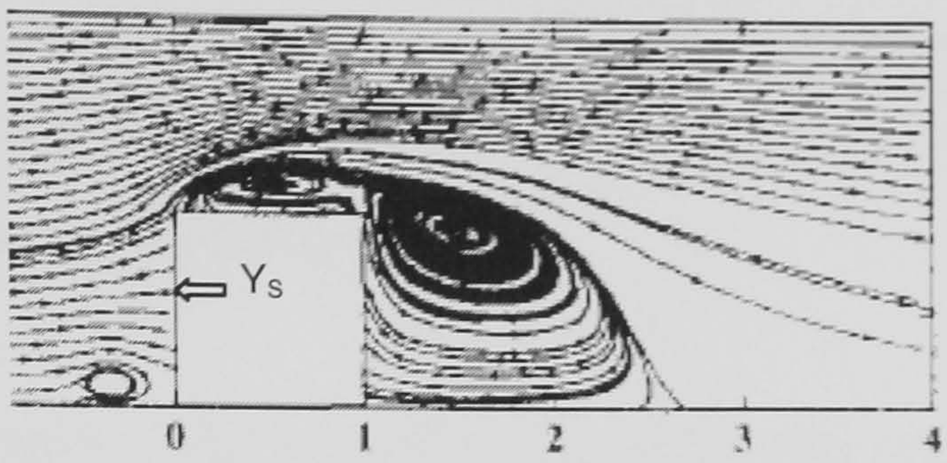

Figure 4.15 The flow past the vertical pane of the 3D cube in the experiment [From: Lakehal and Rodi (1997)].

Figure 4.15 shows the flow field on the vertical plane of symmetry. It depicts the standing shoe vortex (or "bubble") in front of the cube, the flow separation at the top and the major flow recirculation zone at the leeward side. The stagnation point Y_S / H is about 0.7 observed from the figure.

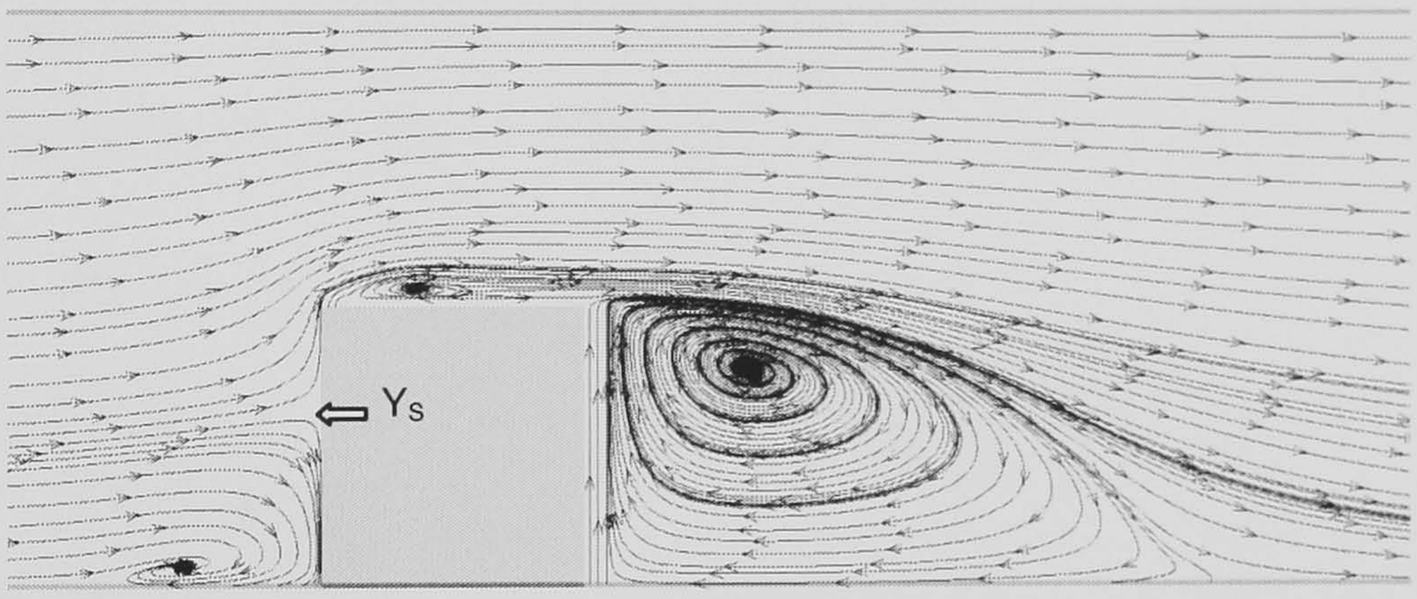

Figure 4.16 Flow past the 3D cube, calculated by the two-layer k-ε model.

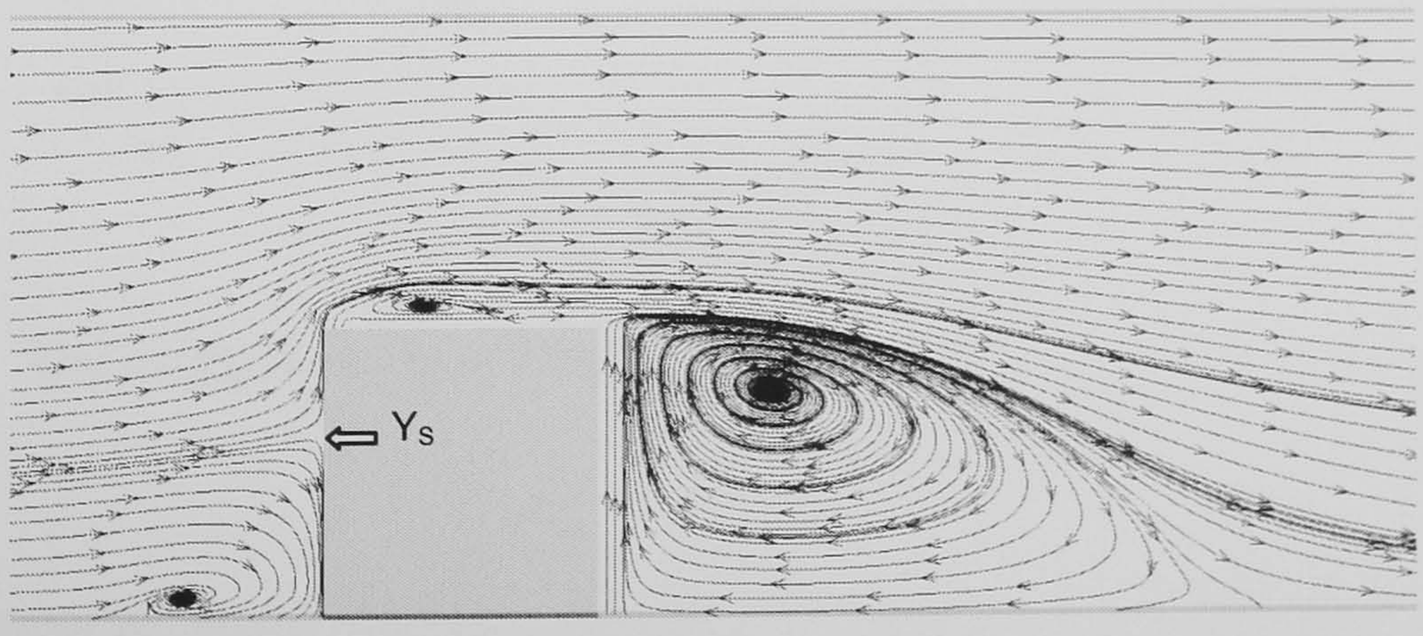

Figure 4.17 Flow past the 3D cube, calculated by the standard k-ε model.

The streamlines calculated by the two-layer k-ε model and the standard k-ε model are shown in figure 4.16 and 4.17 respectively. Very few differences were found between these two figures but the curvatures of the streamlines on the top of the cube were relatively "flat" compared with figure 4.15. Consequently the zone of flow separation

on the top of the cube was not as thick as shown in the experiment. The predicted stagnation point Y_S was clearly present at the location Y_S / H = 0.7, which was in very good agreement with the experimental result.

The length of reattachment – X_R is another flow feature concerned. The experiment (figure 4.15) shows that X_R is about 1.6 – 1.7H. The calculated X_R by the two-layer model and the standard k-ε model was almost the same, which was X_R = 2.16H (figure 4.18). The X_R calculated by Lakehal and Rodi (1997) is 2.68H and 2.18H using the two-layer k-ε model and the standard k-ε model respectively. With reference to their calculations, the present study was slightly better. However, they used another CFD code employing different algorithm, which probably was one of the possible reasons that they did not get a similar result. Another comparison is regarding the zone of standing vortex – X_F. The X_F was 0.76H and 0.65H by the two-layer k-ε model and the standard k-ε model respectively, whereas the measured value X_F = 0.9H. The calculation of X_F made by the two-layer model was also better.

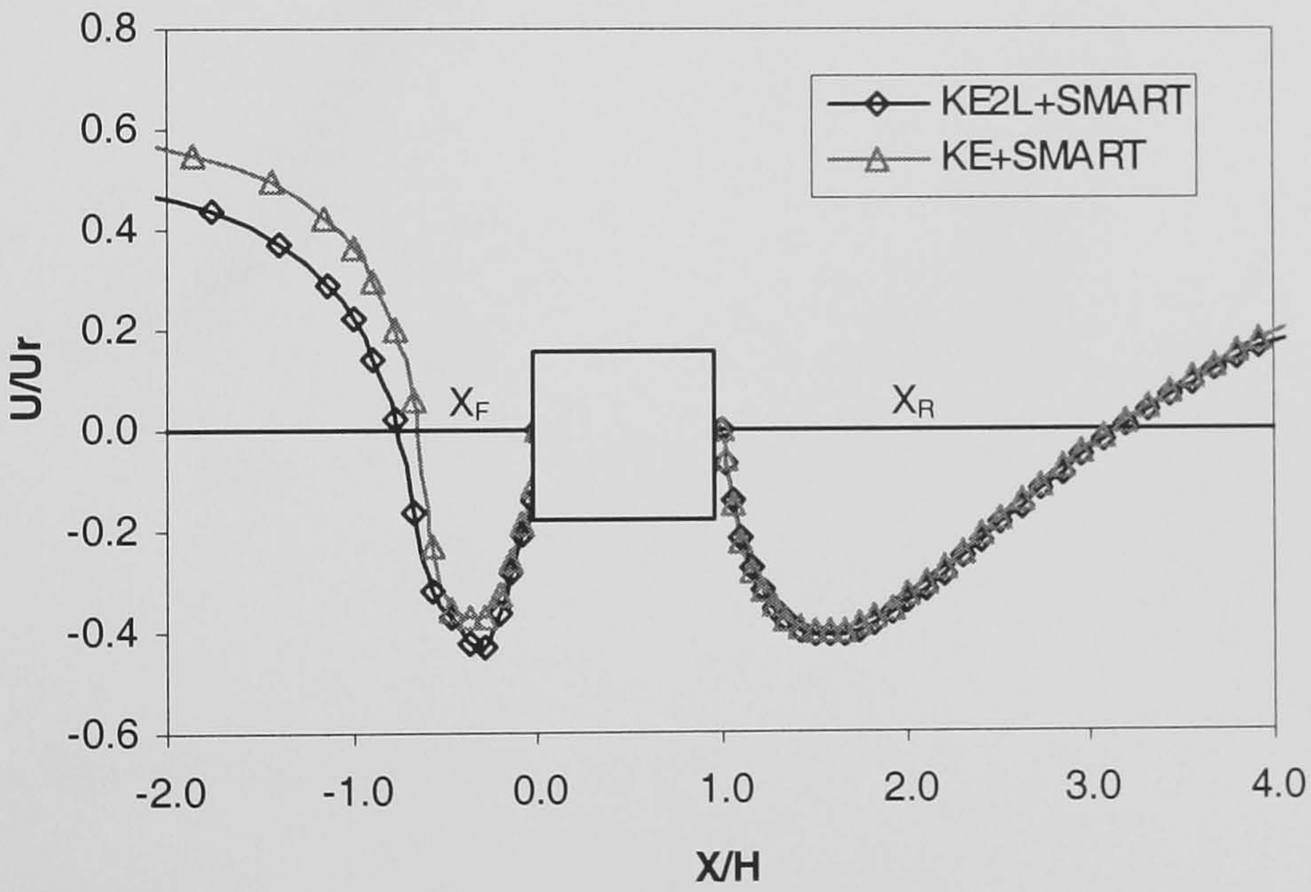

Figure 4.18 The computed X_F and X_R.

4.4.2 Comparison of Mean Velocity Profile

The mean velocity profiles and the distributions of KE along the centre line (symmetric plane) of the cube were subsequently compared. The velocity profiles were compared at X/H = -1.0, 1.5, 2.5 and 4.0, whereas the KE profiles were compared at X/H = 0.5, 1.0 and 2.0. The available data for comparisons is illustrated in figure 4.19.

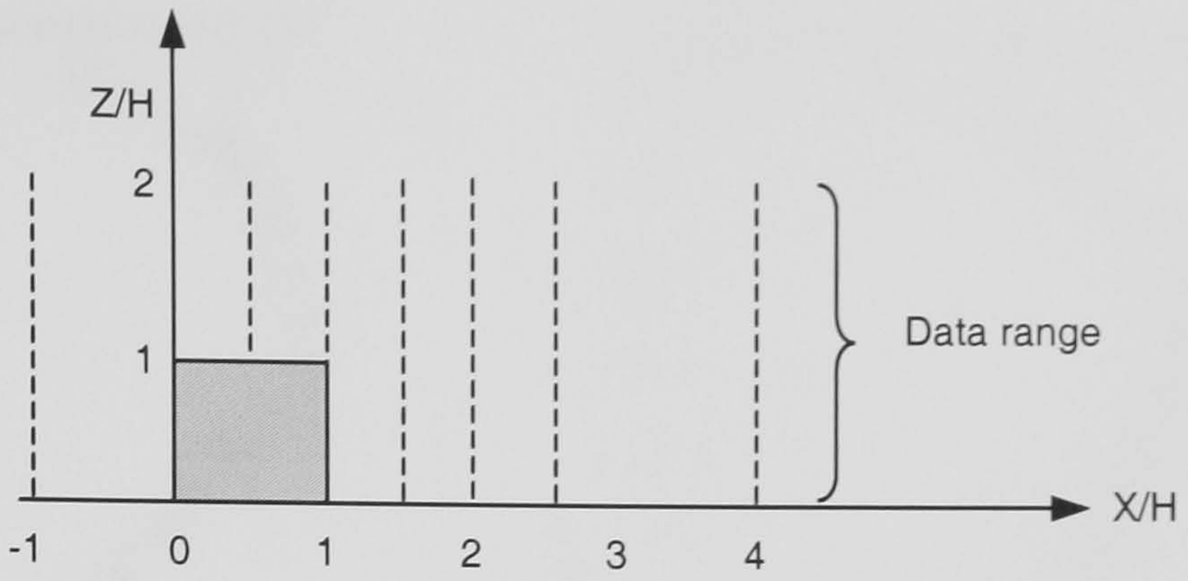

Figure 4.19 The locations of velocity profiles and KE profiles for comparisons.

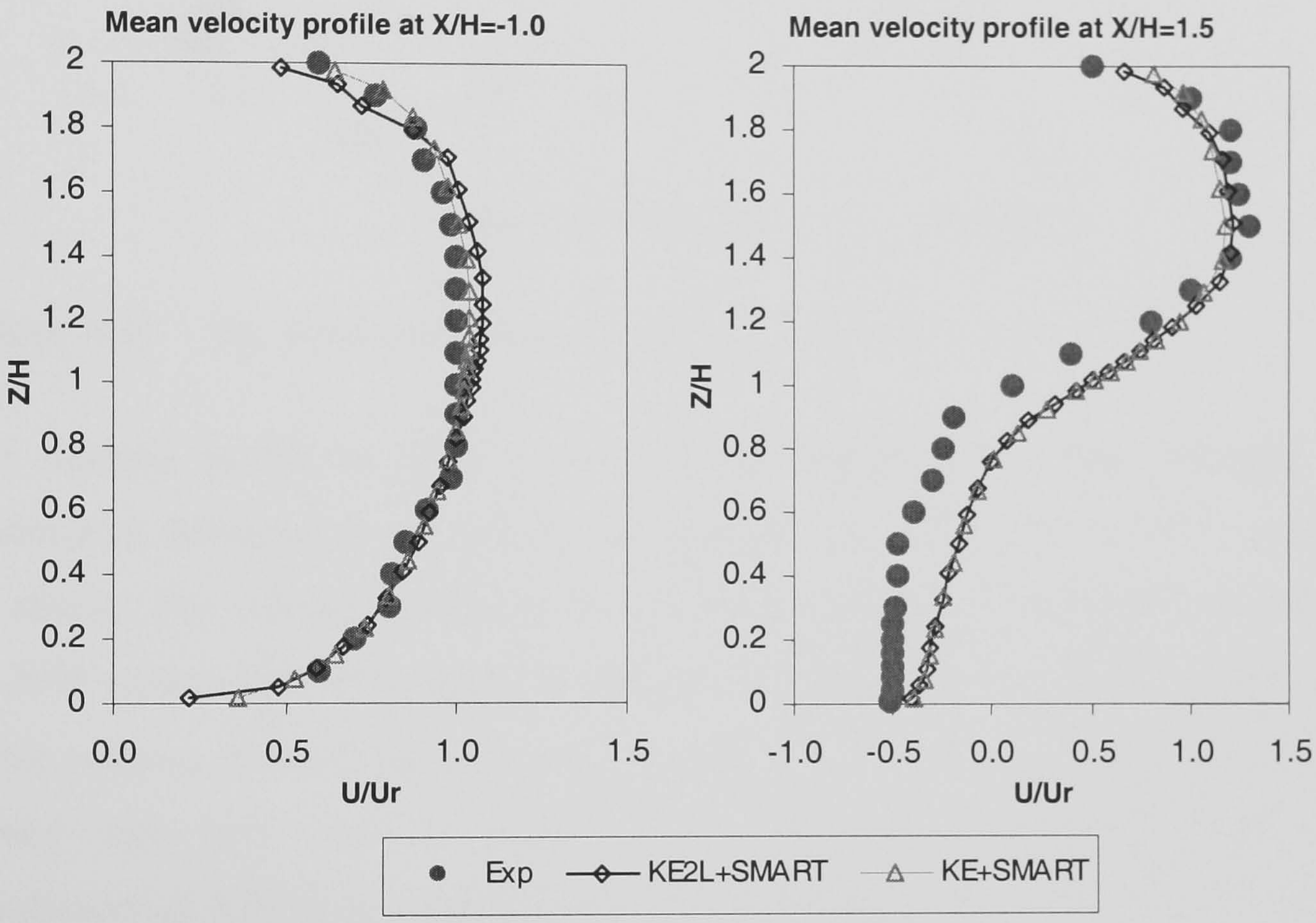

Figure 4.20 The velocity profiles at X/H = -1.0 and X/H = 1.5

The velocity component for comparison was the streamwise velocity U and all the measured values and computed values were normalised by the bulk velocity (U_r) in the free stream. The KE values were also normalised by the square of the free stream velocity $(U_r)^2$. The experimental data shows that the freestream velocity profile in front of the cube is a fully developed channel flow (figure 4.20). The calculated velocity profile at X/H = -1.0 was in very good agreement with the measured values, either using the standard k-ε model or the two-layer k-ε model with the higher-order scheme.

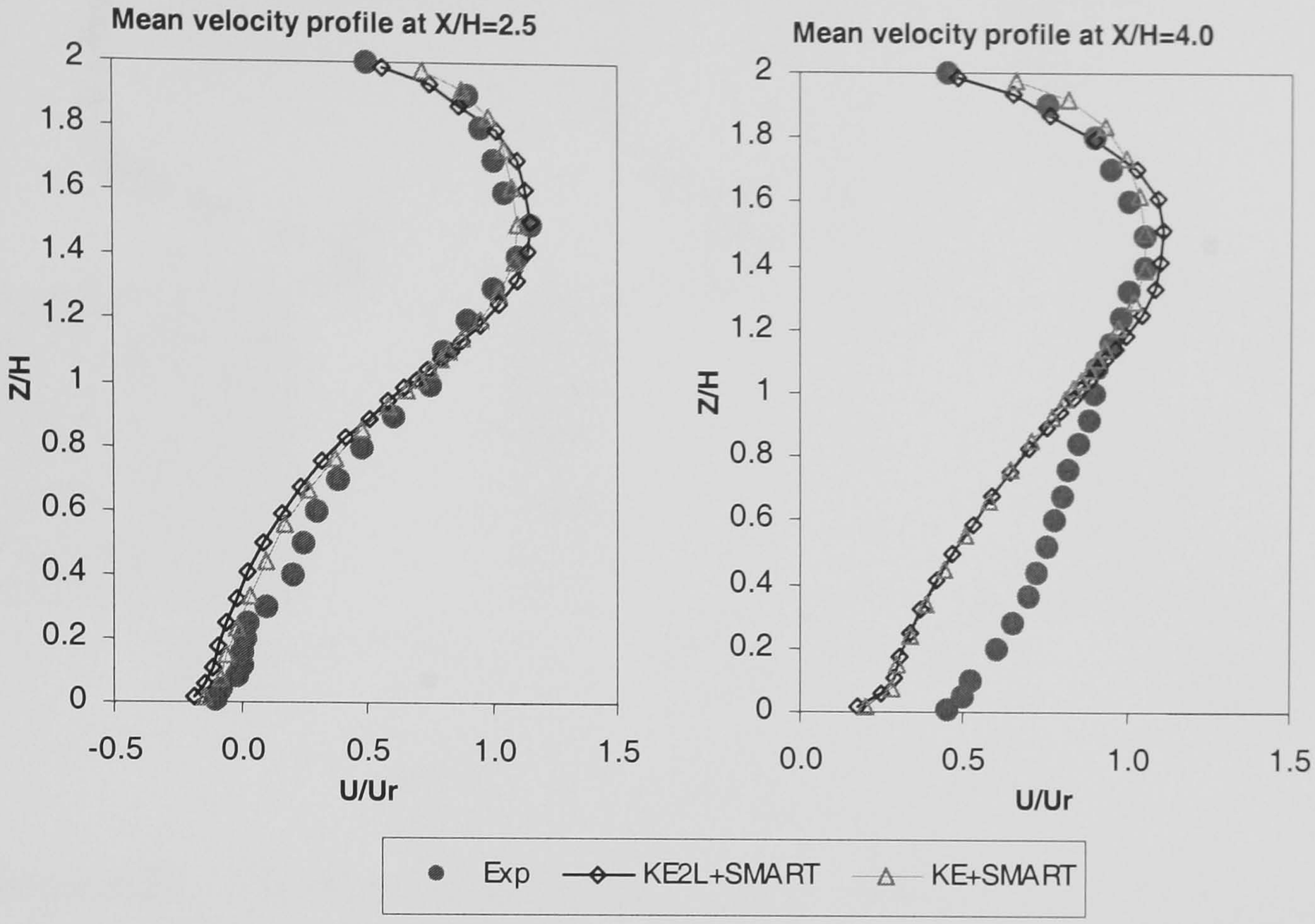

Figure 4.21 The velocity profiles at X/H = 2.5 and X/H = 4.0

The velocity profile at X/H = 1.5 from the experimental data indicates that the momentum deficiency is obvious at the leeward side of the cube and the reverse flows are strong. The velocity profile of the reverse flows depicted by computation was about 10-20% weaker than the measured values within the range $0 \leq Z/H \leq 1.0$ but the trend of the velocity distributions was correct. At X/H = 2.5, the computed velocity profiles agreed very well with the experimental data, whereas the agreement was less satisfactory at X/H = 4.0 (figure 4.21). The computed values at X/H = 4.0 were about 50% weaker than the measured values within the range $0 \leq Z/H \leq 0.2$ and it also revealed that the momentum recovery was slower due to the calculated reattachment length X_R was longer. From this comparison, the calculated velocity profiles using the two layer k-ε and the standard k-ε models were likely to underestimate the streamwise velocities at X/H = 1.5 and X/H = 4.0. Apart from these locations, the mean velocity profiles predicted using the above turbulence models were likely to be correct.

4.4.3 Comparison of Mean Turbulent Kinetic Energy Profile

The KE profiles at X/H = 0.5 and 1.0 are available within the range $1 \leq Z/H \leq 2$, i.e. above the cube. The experimental data indicate that the productions of KE are significant in the range $1 \leq Z/H \leq 1.3$ (figure 4.22), where is the region characterised by separated flows.

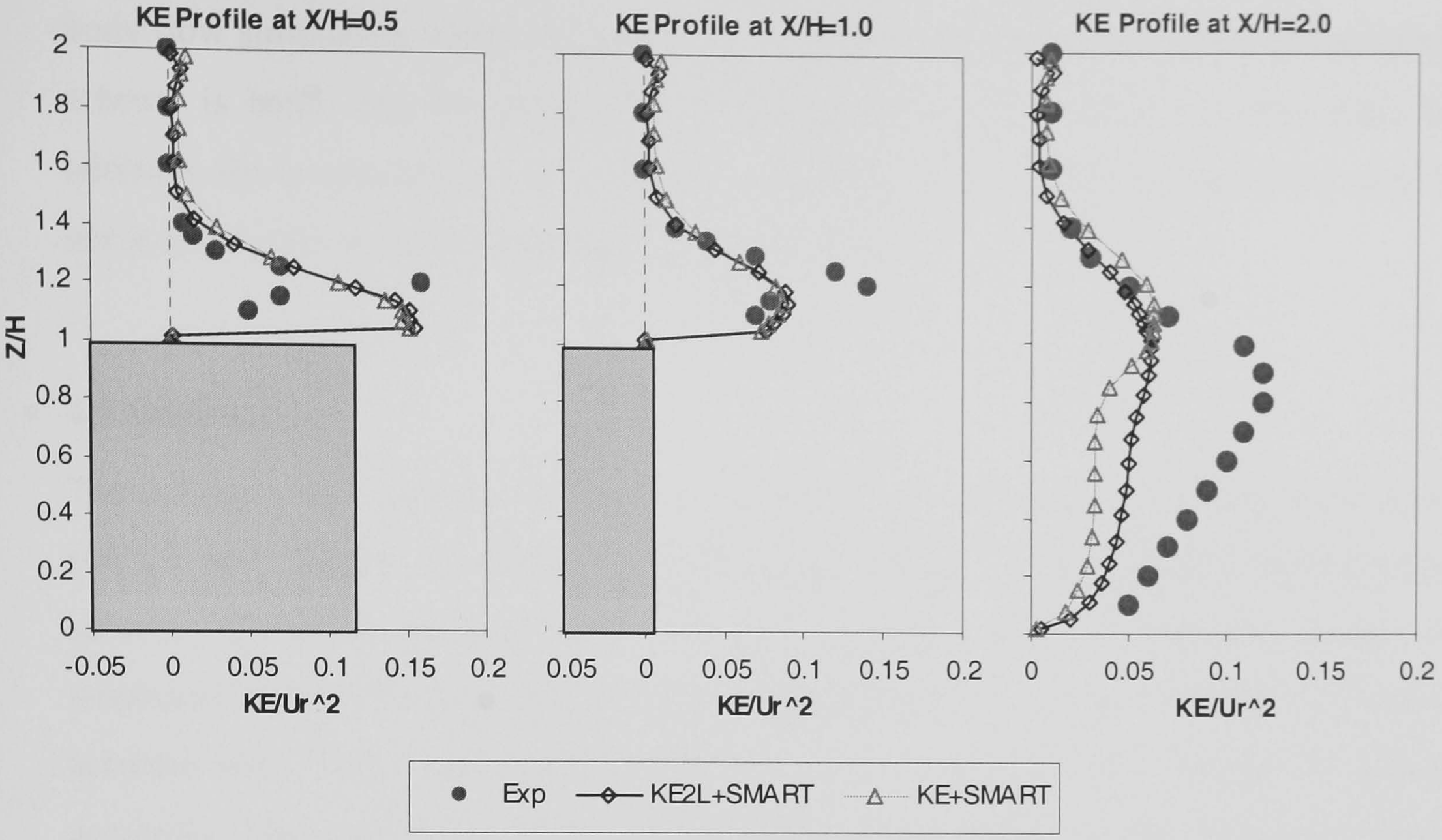

Figure 4.22 The calculated KE profiles vs. measured data

Figure 4.22 also shows that the productions of KE decrease sharply above Z/H = 1.4 at X/H = 0.5 and 1.0. At X/H = 0.5, the calculated KE distributions were significantly larger in the range $1 \leq Z/H \leq 1.2$ but the calculated values agreed very well with the experimental data in the range $1.3 \leq Z/H \leq 2$. The productions of KE calculated by these two turbulence models were of very few differences. At X/H = 1.0, the calculated values were in good agreement with the experimental data, except the values at Z/H = 1.2, where the calculated values were about 30% lower. It was lower because the overproduction of KE at X/H = 0.5 decreased the size of the separation zone (c.f. figures 4.15-17) and therefore the production of KE was weaker at this location. The experimental data at X/H = 2.0 reveal that the production of KE is significant, though the flow velocities are likely to be low at the leeward side of the cube. The calculated values at this location, however, were generally lower than the measured data in the range $0 \leq Z/H \leq 1$. The predicted values calculated by the two-layer k-ε model were slightly better and the calculated values were in fairly good agreement within the range $0 \leq Z/H \leq 0.2$. Since the KE profiles calculated by these two turbulence models were lower, it consequently explained that the reattachment length X_R predicted by them was generally longer than the experimental observation.

From these comparisons, it is fairly adequate to conclude that using the standard k-ε model with the higher-order differencing scheme is relatively satisfactory for a bluff

body flow simulation. Using the two-layer k-ε model with the higher-order differencing scheme is better but the improvement may not be very significant in this case. In addition, the computing cost of using the two-layer model is slightly higher because it needs finer grids to resolve the regions near the walls.

4.5 Summary

The turbulent flow simulations past a 2-D square cylinder and a 3-D cube have been studied with various computational parameters. Using the higher-order differencing schemes generally produces better results regardless which turbulence model is employed in the 2-D case. Noticeably, the performance of VANL2 scheme (2^{nd} order accurate with TVD condition) is almost as good as the SMART scheme (3^{rd} order accurate). The preliminary investigations indicate that using the two-layer k-ε model and the standard k-ε model is relatively satisfactory. With further examinations using the two-layer k-ε model and the standard k-ε model for the flow simulation past the 3-D cube, the two-layer model still yield better results but using the standard k-ε model with the non-linear higher-order differencing scheme also yields good performance.

Since the accuracy is of primary concern in this study, the suggested computational parameters for bluff-body flow simulations are the two-layer k-ε model with the non-linear higher-order scheme – SMART. This approach will be further validated with more complicated cases in the following chapters.

Chapter 5 Flows around a Single Cube by Experimental Investigation and Numerical Simulation

Although the flow field around a cube has been intensively studied, either experimentally or numerically, most of the data available to the public are about the variations of wind pressures *on* the surfaces of a cube or the velocity profiles at the (vertically) symmetric plane. Since this study is more concerned with the *velocity* field (horizontally) *around* a building, experimental data pertaining to the velocity distributions at the ground level in the vicinity of it is more favourable. The first part of this chapter is composed of the experiments conducted for the measurements of the wind velocities at the ground level around a cube. The experiments also include the observations of the flow fields using a flow visualisation technique. The data obtained will be compared with CFD simulations.

The CFD simulations are presented in the second part of this chapter. The suggested computational parameters will be applied again in creating the CFD models.

5.1 Experiment Set Up

The boundary layer wind tunnel (BLWT) in the School of the Built Environment at Heriot-Watt University was used for this experiment. The tunnel is of an open-circuit type (figure 5.1). The length of test section is 17.5 m and the cross section of the working area is 3.2 m × 1.5 m (width × height). It was not a boundary layer wind tunnel since there was no appropriate configuration for simulating the natural wind. The preparation of the wind tunnel applied some techniques described in chapter 2. As the ratio of the test section length to the height of the working section is less than 12, the test section is not long enough to generate adequate thickness of the boundary layer spontaneously. Hence, it was necessary to employ some augmentation devices for this tunnel in order to accelerate the growth of the simulated atmospheric boundary layer. Two options were considered – Counihan's approach and Cook's method. As the most interesting part regarding the atmospheric boundary layer was the lower part of it near ground, Cook's method was therefore chosen for this study. The grid frame (turbulence

generator), barrier wall (for momentum deficit) and carpet (roughness element) were designed for and deployed in this tunnel.

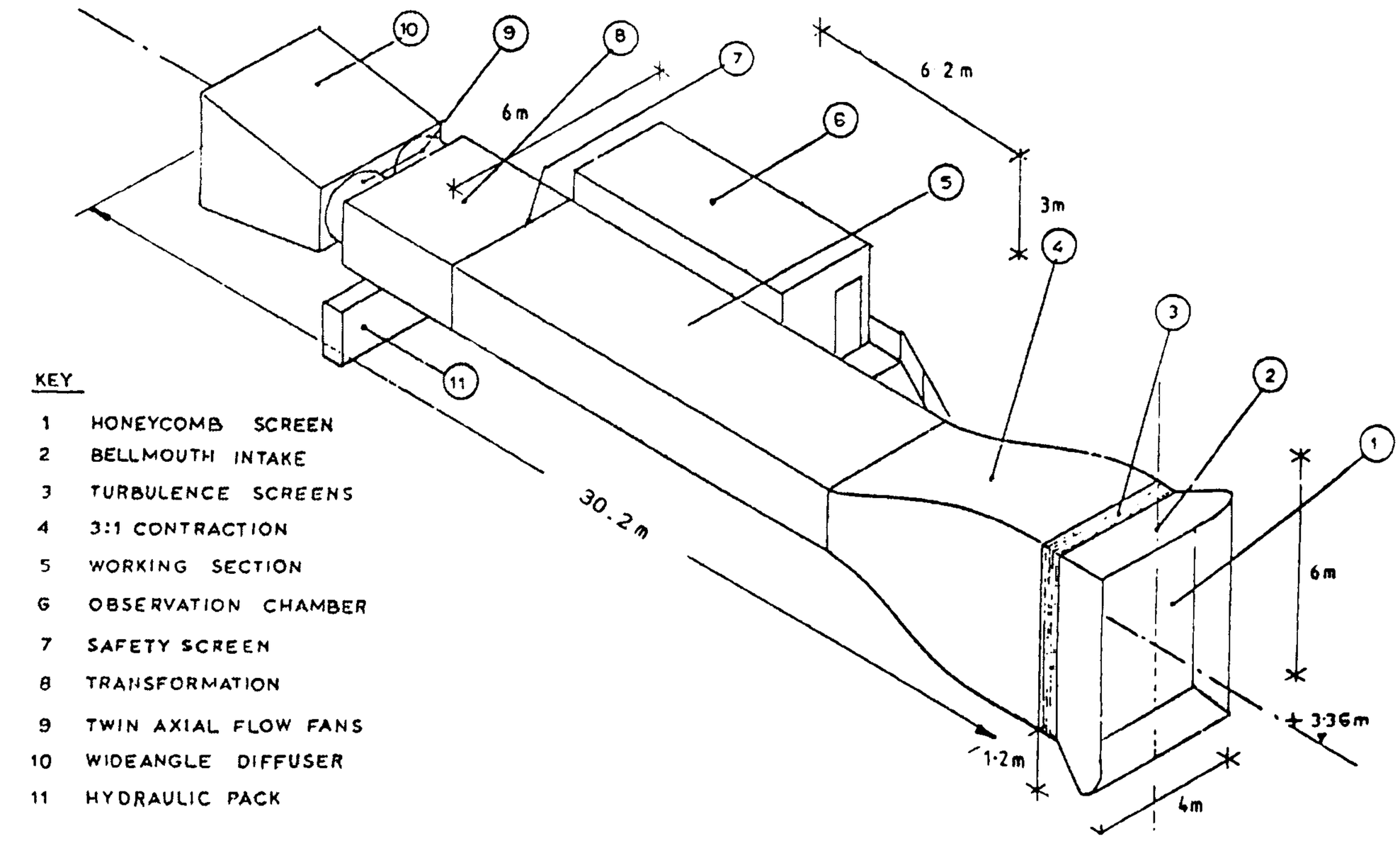

Figure 5.1 The BLWT at the School of the Built Environment, Heriot-Watt University. [From: Saeid (1991)]

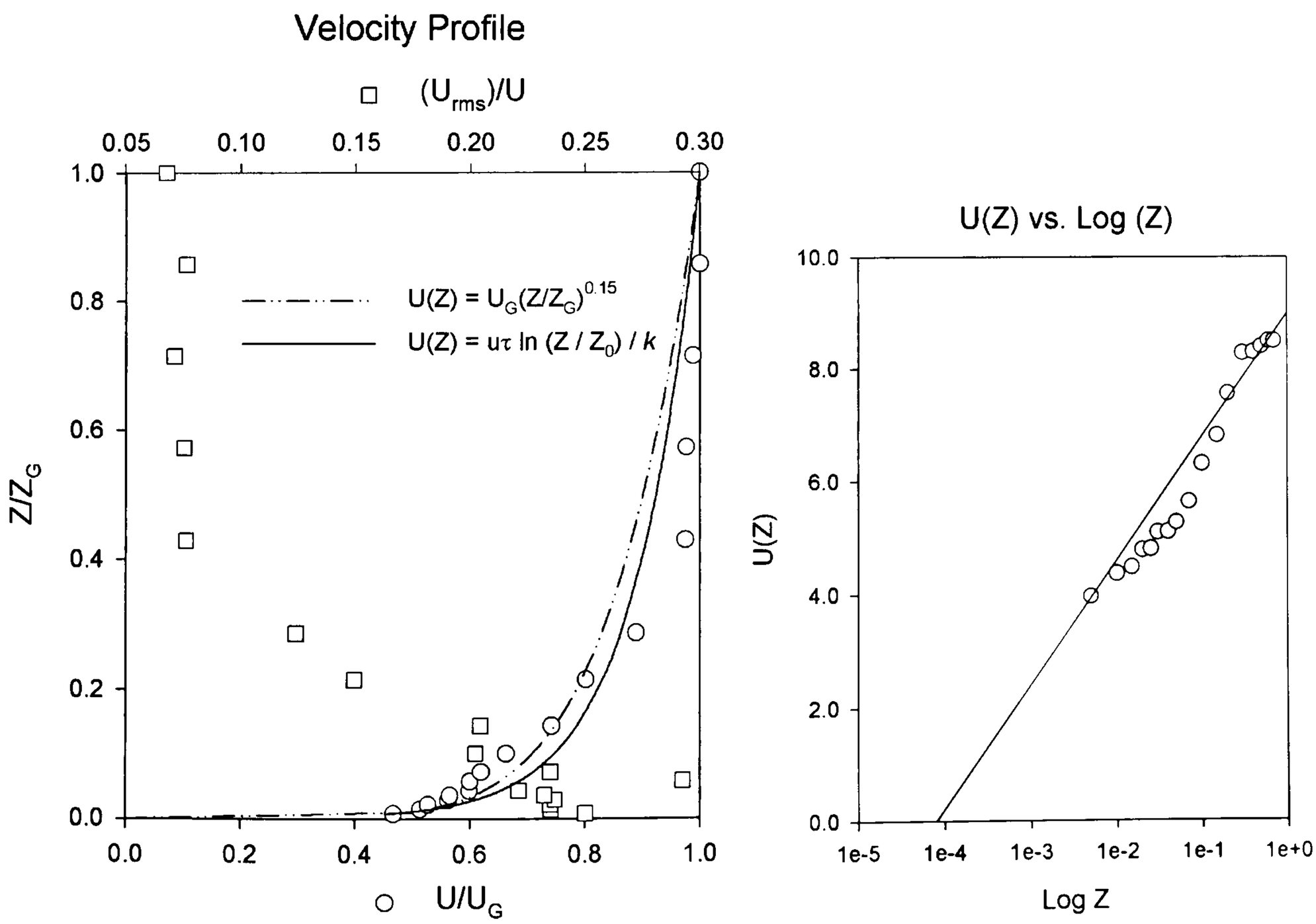

Figure 5.2 The measured mean wind velocity profile and the extrapolated z_0.

The hot-wire probe (single wire, 55P11) manufactured by Dantec was used to measure the velocity profile of the approaching wind. The requisition of data was through a CTA (constant temperature anemometer) module and a signal converter connected to a PC with a software package "Streamware" (from Dantec) installed. The thickness of the boundary layer was about 0.7 m since the measured mean velocity did not change noticeably beyond that height. The value of the roughness height z_0 was 0.08 mm, extrapolated from the plot of measured velocities against Log Z (figure 5.2). With z_0 determined, the friction velocity u_* (or u_τ) can be deduced from the log-law model by equation (2.3). In addition to the log-law model presented, figure 5.2 also shows that the profile of the mean wind velocity (U) is approximately equal to a power-law model with an exponent of 0.15 and the intensity of turbulence (U_{rms} / U) is about 25% near the ground and it decreases to about 5% at the gradient level.

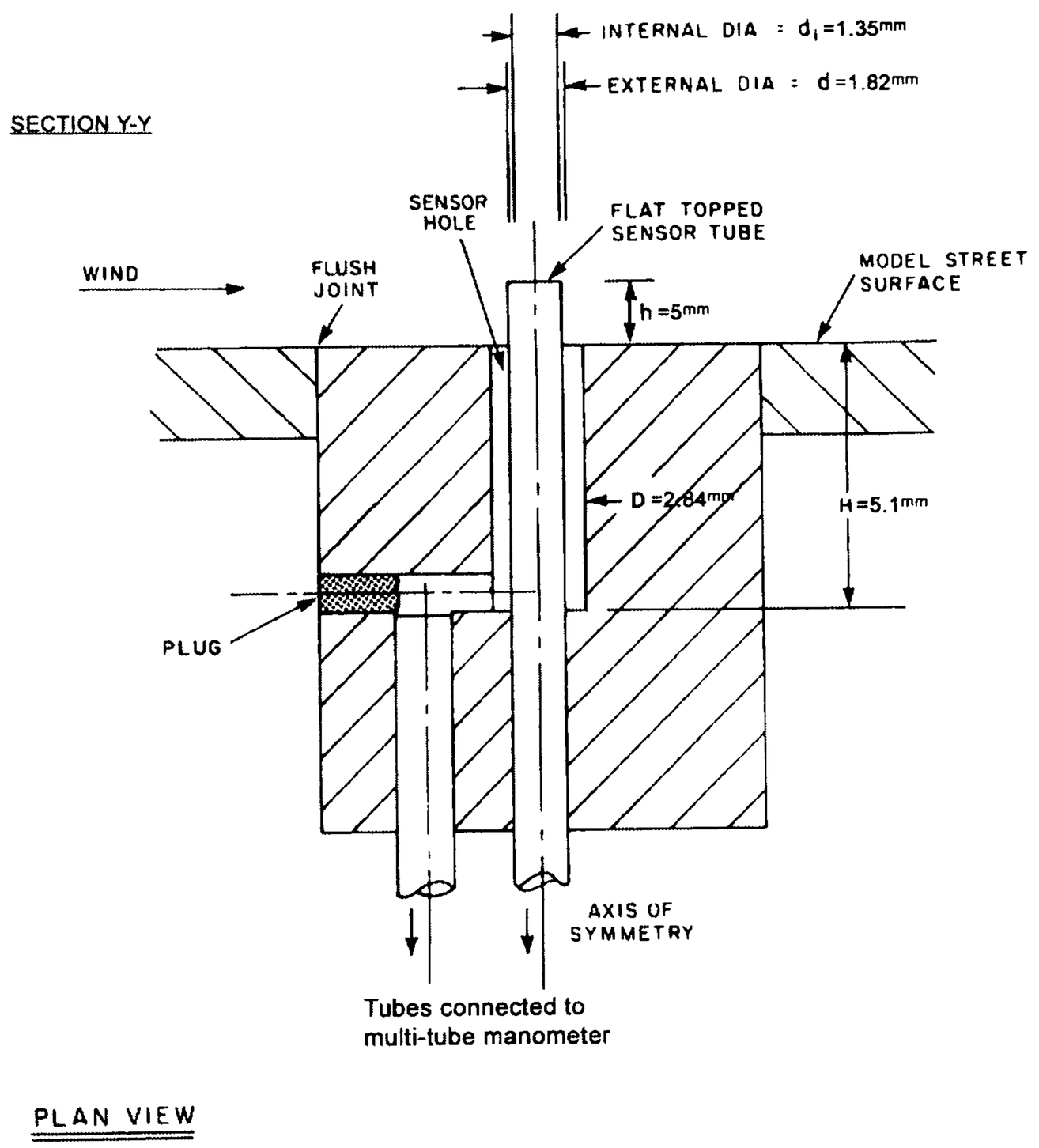

Figure 5.3 The Irwin sensor (dimensions are shown in the drawing).

The log-law profile and the power-law model almost overlapped near the ground and the power-law model seemed to be already sufficient to describe the mean wind velocity profile. The ground-level winds were measured with Irwin sensors (figure 5.3). Irwin (1981) derives an empirical formula to calculate the wind velocity from the pressure difference measured by the sensor, as following:

$$Q_h = A(\nu / h) + B(\Delta p / \rho)^{1/2} \tag{5.1}$$

where Q_h is the mean velocity ($=\sqrt{(U^2 + V^2)}$) , Δp is the pressure difference, A and B are calibration constants. Equation (6.1) is valid for $\Delta p h^2/\rho\nu^2 > 10^4$. Irwin suggests A = 85 and B = 1.74 when $h/d > 0.5$, $d_i/d = 0.72$, $D/d = 1.56$ and $H/d > 1.5$. The dimensions of the Irwin sensor made for this experiment were $h/d = 2.75 > 0.5$; $d_i/d = 0.74$; D/d = 1.56 and $H/d = 2.8 > 1.5$. Since the sensor was not made exactly as the same as it was presented in Irwin's paper due to the availability of materials, it was required to calibrate the sensor. The calibration was done by connecting the sensor to a manometer and applying Irwin's formula to calculate the velocities from the pressure differences reported by the manometer and then to compare the velocities measured by hot-wire. The hot-wire probe was orientated vertically so that the velocity detected was the horizontal velocity Q_h.

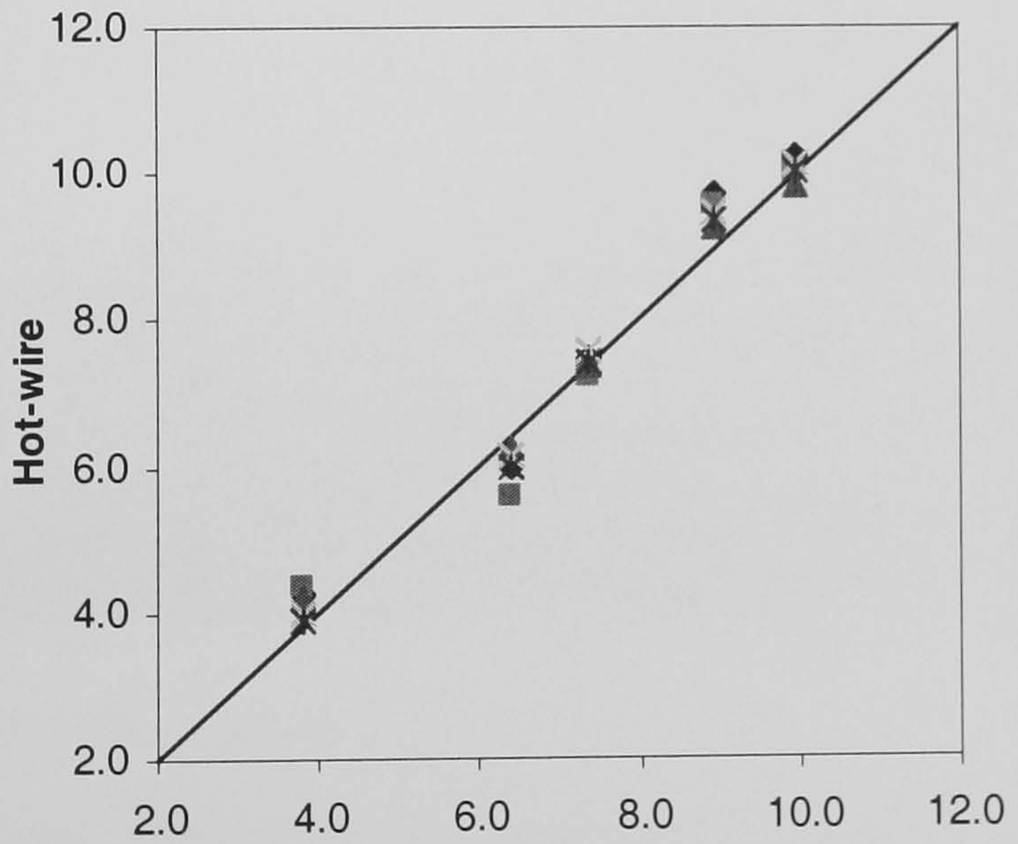

Figure 5.4 Calibration of the Irwin sensor. The horizontal axis shows the velocities calculated from equation (5.1), whereas the vertical axis exhibits the velocities detected by hot-wire.

The velocity range for the calibration was between 3.8 m/s and 10.2 m/s. The suggested values for A and B appeared to be working well for these newly made sensors, as the

velocities agreed well with the velocities detected by the hot-wire (figure 5.4). Therefore these sensors and the empirical formula were employed for the measurements of the ground-level wind velocities.

The sensors were deployed around the cube (figure 5.5) and the minimum distance between two sensors was 50 mm in order to eliminate the interference between each sensor. All the sensors were flush-mounted on the turntable and the pressure differences were obtained from the readings shown on the multi-tube manometer (figure 5.6).

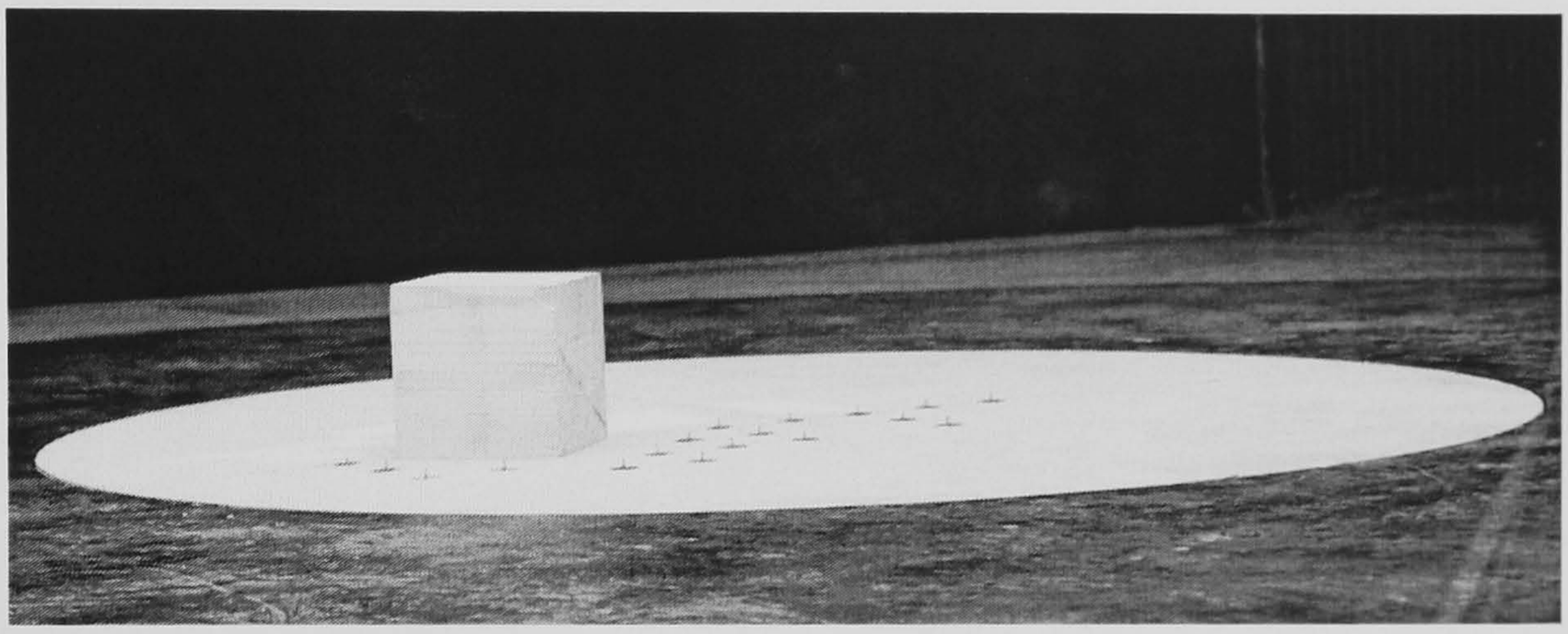

Figure 5.5 The experiment setup – the cube and the Irwin sensors. The number of sensors is 18.

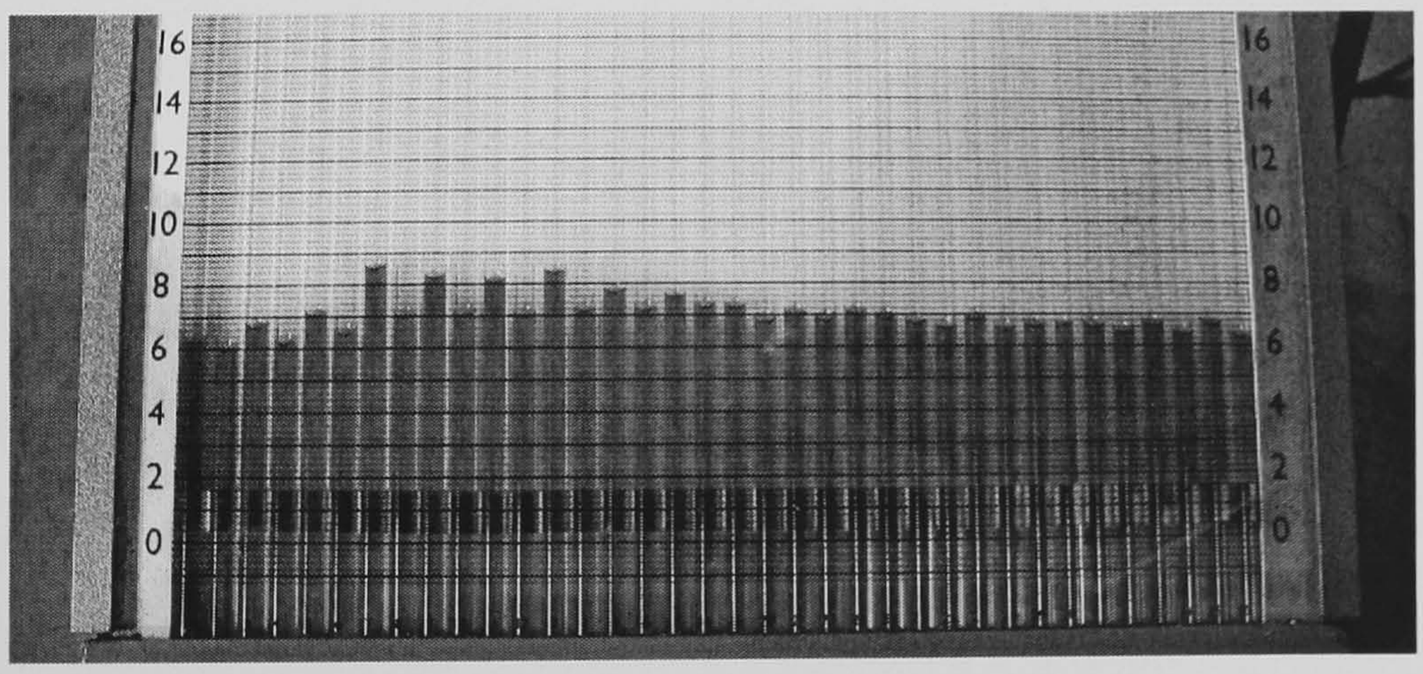

Figure 5.6 The multi-tube manometer. As each Irwin sensor has two connections, the pressure difference Δp can be obtained by the different readings between each set of two tubes. The Δp is then converted into velocity using equation (5.1).

The multi-tube manometer was not very sensitive to the fluctuating pressures but it was adequate to get the average readings for the calculations of mean velocities. The operating wind speed in the tunnel was set to maximum (12 m/s) to enhance the response of the sensor so that the pressure differences could be more discernible by

eyes. The orientation of the cube was firstly normal to the wind direction and the second orientation was 45° to the approaching wind. The size of the cube was 100 mm × 100 mm × 100 mm and the blockage ratios were 0.2% and 0.28% when the cube orientated 0° and 45° respectively. The effects of blockage may influence the measured values if the blockage ratio is larger than 5% (ASCE, 1999). Since the blockage ratio was small, there was no correction required for this experiment.

In addition to the velocity measurements, the flow pattern around the cube was also of interests. The visualisation of flow pattern was made by using mythelated spirit to dissolve the powder-like particles into a mixed paint and then applying the paint on the board which the cube was mounted on. As the mythelated spirit is easy to vaporise so that the particles can stay on the board as soon as the paint is dried. The picture of the dried liquid (paint) on the board consequently exhibits the flow pattern. Two cases of flow pattern were observed – cube orientated 0° and 45°. The flow visualisation was done in another wind tunnel. The tunnel is of a close-circuit type in which the approaching wind is fully developed, i.e. typical channel flow with low turbulence. One advantage of using this tunnel was that the flow speed could be built up rapidly. This was desirable because if the wind speed could not be accelerated quickly, the mixed paint would have been dried already before reaching a steady wind speed. It was an alternative solution since using the large BLWT was not appropriate for this flow visualisation technique.

5.2 CFD Simulations

Since there are some differences between the large BLWT and the close-circuit wind tunnel, the CFD simulations therefore comprise two different sets of computation – one for the comparison of velocity field and the other one for the flow pattern comparison.

5.2.1 Simulations for Comparison of Velocity Field

The computing domain was 3.0 m × 3.0 m × 0.7 m (length × width × height), which was slightly smaller than the working section of the wind tunnel but it was large enough to secure the correct boundary conditions because a larger domain was checked and it did not affect the calculated flow field. The cube was placed on the centre of the bottom (floor) of the domain. Wall conditions were specified at the surfaces of the cube and the

floor. The velocity profile of the approaching wind need to be defined with a power-law or log-law model but none of them was available in the CFD code. Since the power-law profile (figure 5.2) was already a good approximation of the mean wind velocity profile in this BLWT, it was therefore selected for the required coding. There are three options available for user-defined subroutine in this code:

- writing FORTRAN code directly into the GROUND – a subroutine of PHOENICS;
- using PLANT, the built-in FORTRAN code generator and,
- exploiting the PHOENICS Input Language (PIL)

The first two options need a FORTRAN compiler to build a new executable solver, whereas the last option can directly translate the formulae into the solver. The option of using PLANT was selected for this computation because it was simpler and the user-defined subroutine generated by PLANT was immediately acceptable by the solver. The mean velocity profile was created by inputting the mathematical expressions of the power-law model and the relationships between each variable were defined using the syntax of PLANT. In addition to the mean velocity profile, the profiles of k and ε were also required by the turbulence model. The profile of turbulent kinetic energy (k) was estimated by

$$k(z) = (U(z) \times I(z))^2 \tag{5.2}$$

where $I(z)$ is the profile of turbulence intensity. The $I(z)$ was obtained by using an polynomial function of 2nd order to approximate the scattered values measured in the wind tunnel (figure 5.2) instead of using equation (2.6), since the turbulence intensity was available from the wind tunnel experiment. The profile of the dissipation rate (ε) can be derived based on a local equilibrium assumption since the approaching wind is neutrally stable (Lumley and Panofsky, 1964). Therefore the production of turbulence energy is approximately equal to its dissipation rate, i.e.

$$\varepsilon(z) = \frac{u_*^3}{\kappa z} \tag{5.3}$$

where u_* is the friction velocity and κ is the von Kámán constant (= 0.41 in this computation). The friction velocity in equation (5.3) can be determined by

$$k = \frac{u_*^2}{\sqrt{C_\mu}} \tag{5.4}$$

with a known value of k. Therefore the profile of ε can be rewritten as

$$\varepsilon(z) = \frac{k(z)^{3/2} \times C_\mu^{3/4}}{\kappa z} \tag{5.5}$$

Inlet	$U(z) = U_G \left(\frac{z}{z_G} \right)^{0.15}$ $k(z) = (U(z) \times I(z))^2$ $\varepsilon(z) = k(z)^{3/2} \times C_\mu^{3/4} / \kappa z,\ \kappa = 0.41,\ C_\mu = 0.09$
Outlet	Fixed pressure, $P = 0$
Cube	Smooth wall condition
Bottom	Smooth wall condition
Top	Free slip, flux normal to the boundary is zero
Sides	Free slip, flux normal to the boundary is zero

Table 5.1 The boundary conditions of the computing domain.

Table 5.1 summarises all the boundary conditions defined in the computing domain. The two-layer k-ε turbulence model was used and the non-linear higher-order scheme SMART was applied to velocities (u, v, w), k and ε. The initial values of velocities, k and ε were also programmed into PHOENICS using the inlet profile to accelerate the rate of convergence, since these values were "better guess" during the first iteration, whereas the default initial values were 10^{-10} for all the variables. The conjugate-gradient solver was used to solve the algebraic equations and the convergence criteria were set when the maximum residual became less than 10^{-5}. After a prescribed number of iterations, the "result" file, a file generated by PHOENICS to summarise the result of each run, indicated that the residual for the mass was smaller than 10^{-6} and the monitored values (pressure, velocities, k and ε) were steady; therefore the calculation was convinced to be sufficiently converged, i.e.

$$(\text{mass of air})_{\text{in}} = (\text{mass of air})_{\text{out}} \tag{5.6}$$

The velocity sources (u, v, w) were not expected to be in balance because the presence of obstacle would generally cause momentum loss due to friction (energy dissipation)

and therefore the momentum given by the inlet would be not necessarily equal to the momentum obtained in the outlet.

The grids were refined in the vicinity of solid walls (cube and the floor) in order to place the first node near the wall in the range $y^+ < 10$, since the two-layer turbulence model would require the node to resolve the viscous sub-layer when calculating the local Reynolds number (Re_y). As the eddy viscosity in the near wall-layer is calculated from the damping function f_μ proposed by Norris (1975) as follows:

$$\nu_t = C_M \times k^{1/2} \times f_\mu \times l_m \tag{5.7}$$

$$f_\mu = (1.0 - e^{(-0.0198 \times \mathrm{Re}_y)}) \tag{5.8}$$

$$l_m = \kappa \times y_n \tag{5.9}$$

$$\mathrm{Re}_y = k^{1/2} \times y_n \times \nu^{-1} \tag{5.10}$$

where ν_t is the eddy viscosity, $C_M = 0.5478$, $\kappa = 0.41$ and y_n is the distance normal to the nearest wall. As a result, the model is a function of Re_y. The two-layer model uses Re_y to calculate the distribution of the length scale near the wall and subsequently the outer layer using the standard k-ε model will match the inner layer at the regions where Re_y = 350. If the first node is not placed very near the wall, i.e. y_n is moderately large, thus Re_y will be large and subsequently the damping function expressed by equation (5.8) will be close to 1.0, which effectively eliminates the viscous effects of the wall. Therefore the two-layer model is sensitive to the near-wall nodes and the first node near the wall has to be placed in the viscous layer.

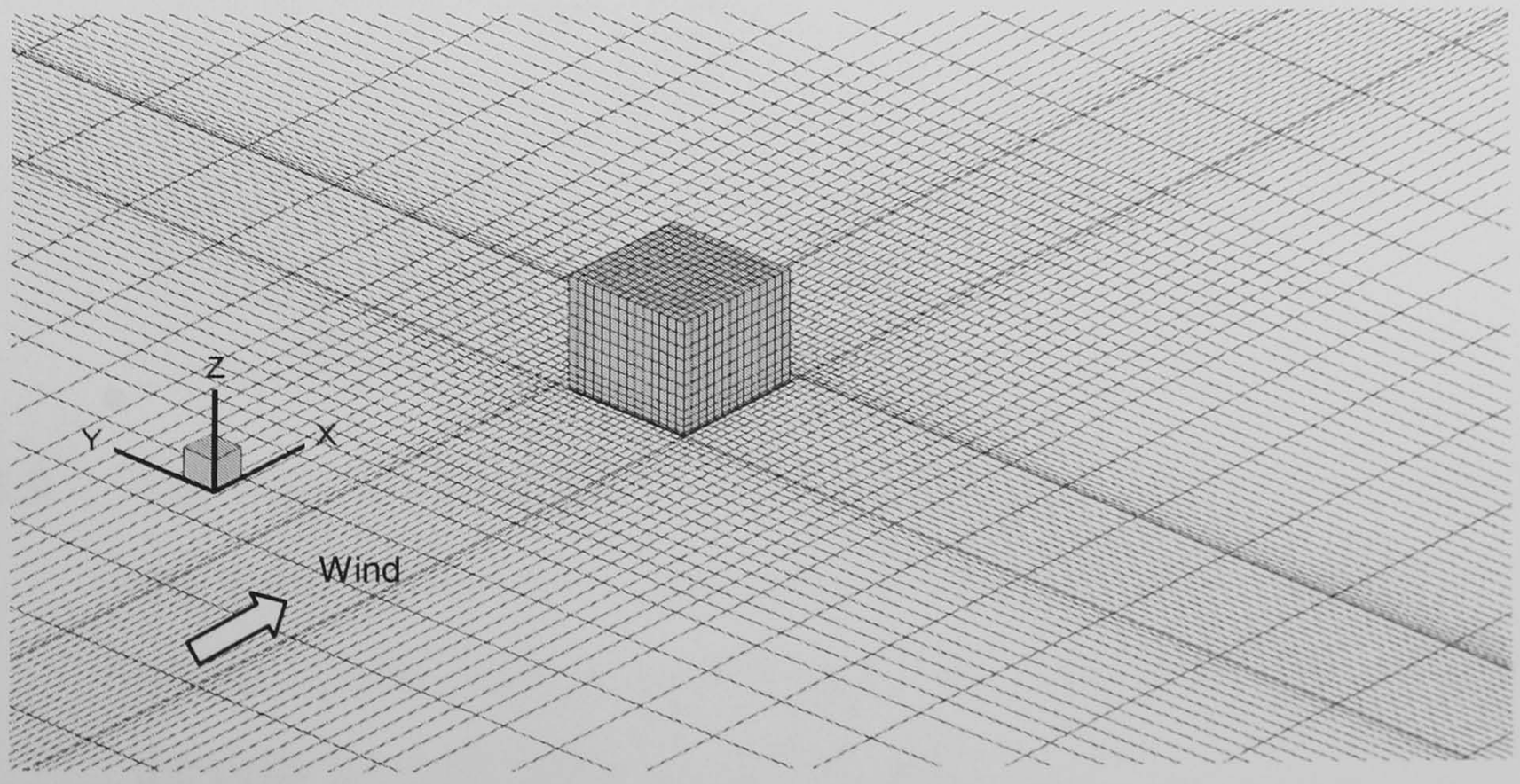

Figure 5.7 The computational grids. Wind direction is normal to the cube.

The number of grids was $85 \times 71 \times 30$ and the minimum spacing was 0.01H (H is the cube height) for the CFD simulation of wind direction normal to the cube (figure 5.7). The grids for the cube orientated 45^{o} to the approaching wind were still of Cartesian type but using two different treatments with regard to the boundary conditions.

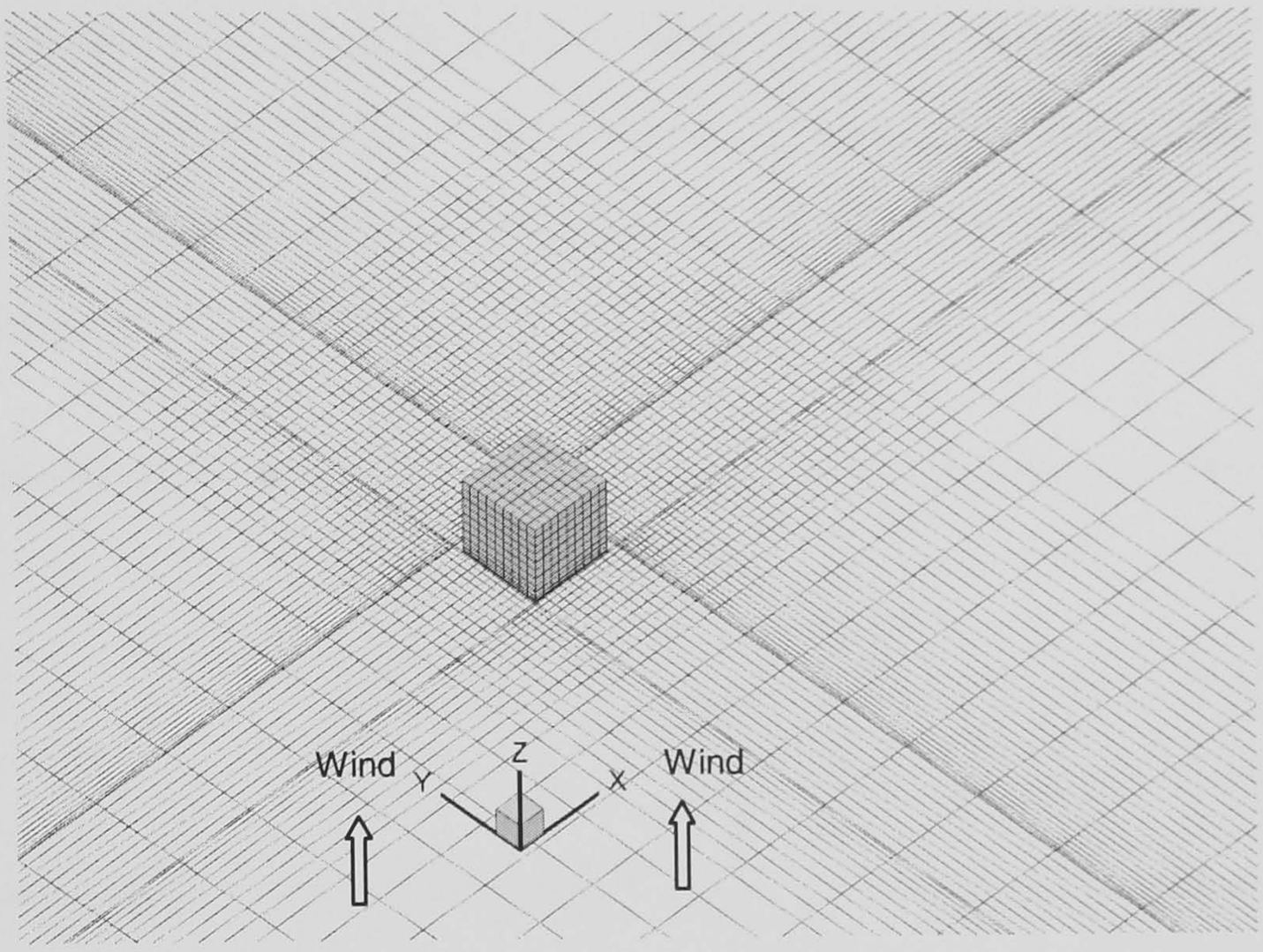

Figure 5.8 The computational grids (CFD1). The approaching wind has been decomposed into X-Y components and the resulting wind angle is 45^{o} to the cube.

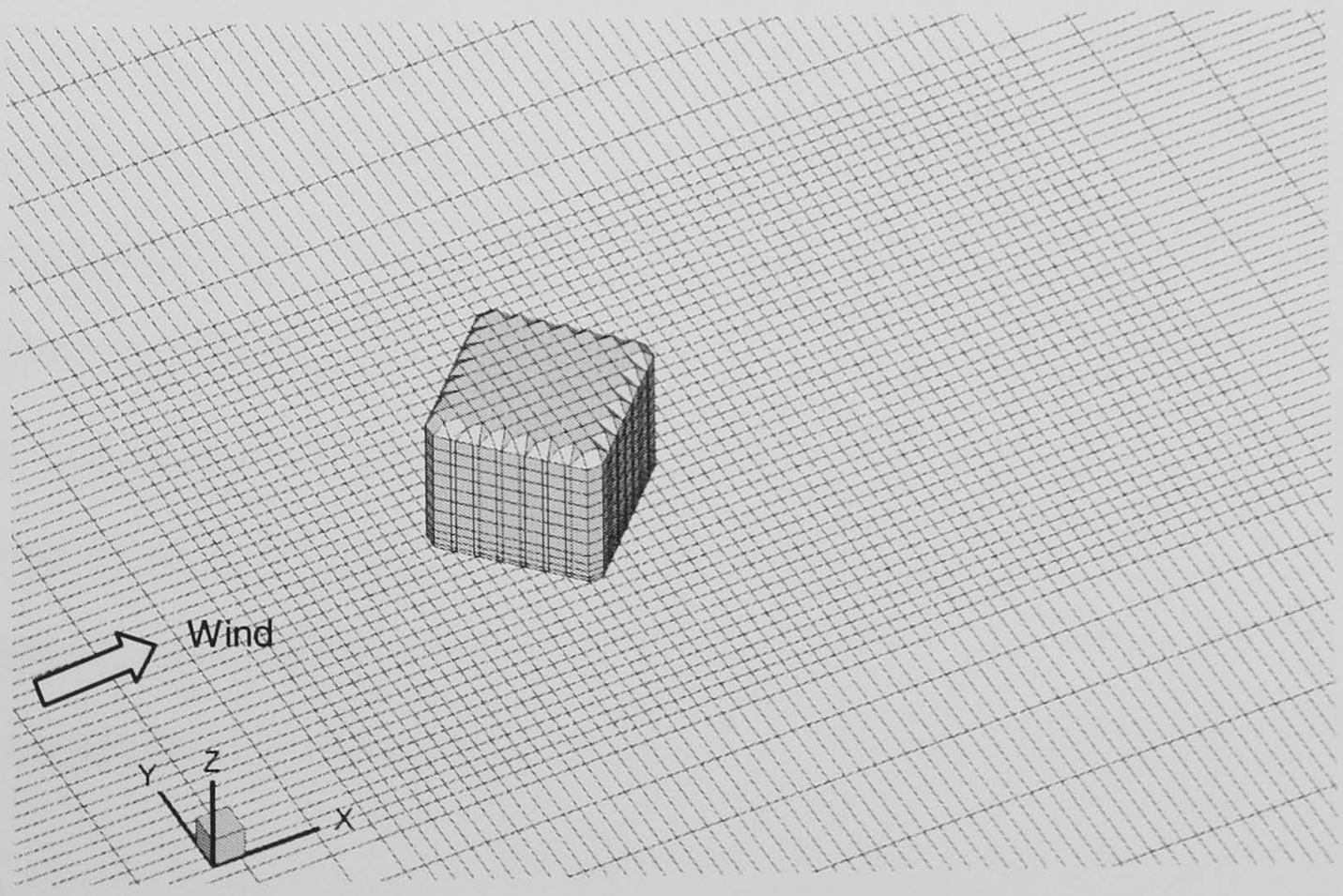

Figure 5.9 The cube is 45^{o} oblique to the approaching wind (CFD2). The edges of the cube can only be approximated by "staircase" grids, i.e. the cells whose centres happen to fall within the cube will be blocked, otherwise the cells are fully open.

One approach (CFD1) was to change the wind angle to 45° by decomposing the wind into X and Y components (U and V), where the boundary conditions for the inlets were modified accordingly (table 5.2). The second approach (CFD2) was to directly rotate the cube by 45°. The former treatment aligned the grids with the edges of the cube (figure 5.8), whereas the later approach simplified the task of grid generation but the geometry of the cube composed by the grids was an approximation (figure 5.9). The number of grids in the first case was $76 \times 76 \times 30$ and the minimum spacing was also 0.01H, whilst the grids employed were $84 \times 66 \times 30$ in the second case. All the CFD simulations were grid-independent.

Inlet X and Y	$U(z) = U_G (z/z_G)^{0.15} / \cos 45^o$
	$V(z) = V_G (z/z_G)^{0.15} / \sin 45^o$
	$k_U(z) = (U(z) \times I(z))^2 \quad \varepsilon_U(z) = k_U(z)^{3/2} \times C_\mu^{3/4} / \kappa z$
	$k_V(z) = (V(z) \times I(z))^2 \quad \varepsilon_V(z) = k_V(z)^{3/2} \times C_\mu^{3/4} / \kappa z$
	$\kappa = 0.41,\ C_\mu = 0.09$

Table 5.2 The modified boundary conditions for wind angle = 45°.

5.2.2 Simulations for Comparison of Flow Pattern

The simulations were modified to suit the boundary conditions of the close-circuit tunnel. The computing domain was 1.0 m × 1.0 m × 0.5 m (length × width × height), which was similar to the dimensions of the test section of this tunnel. One major difference was the boundary conditions of the approaching wind. The approaching wind was defined using a uniform (in terms of bulk velocity) profile with low turbulence at the inlet. The Reynolds number, based on the cube height, was 6.6×10^4. The turbulence intensity was 5%, based on a typical value for fully developed channel flows. The other computational parameters – turbulence model, differencing scheme, grids and the boundary conditions of the solid walls were the same as described in the previous section.

5.3 Results

The experimental data and numerical simulations were compared in terms of flow pattern and velocity fields. The flow pattern obtained from the experiment in the close-

circuit tunnel was firstly compared, followed by the comparison of the velocity fields measured in the large BLWT.

5.3.1 Flow Pattern Comparison

The cube is a bluff body, the flows immediately separate at the sharp edges of the cube and, the interactions between pressure gradients and the flows in the freestream force the flow to change its behaviour near the walls intermittently; therefore various flow phenomena, including recirculation, vortex sheet, separation and reattachment can be observed (figure 5.10). The flow pattern exhibited by the dried paint was "skin friction lines", which were similar to the conventional oil streaks. The skin friction lines are also called "limiting streamlines" and the skin friction lines are not necessarily akin to the streamlines, especially when the flows are turbulent. The flow pattern displayed by the dried paint was somewhat like a drawing sketched by the mean flows. The mean flows represented the "general trend" of fluid motion, whereas the computed streamlines were obtained from a steady-state simulation in which the mean flow equations (RANS equations) were solved. From this point of view, the skin friction lines and the streamlines were comparable.

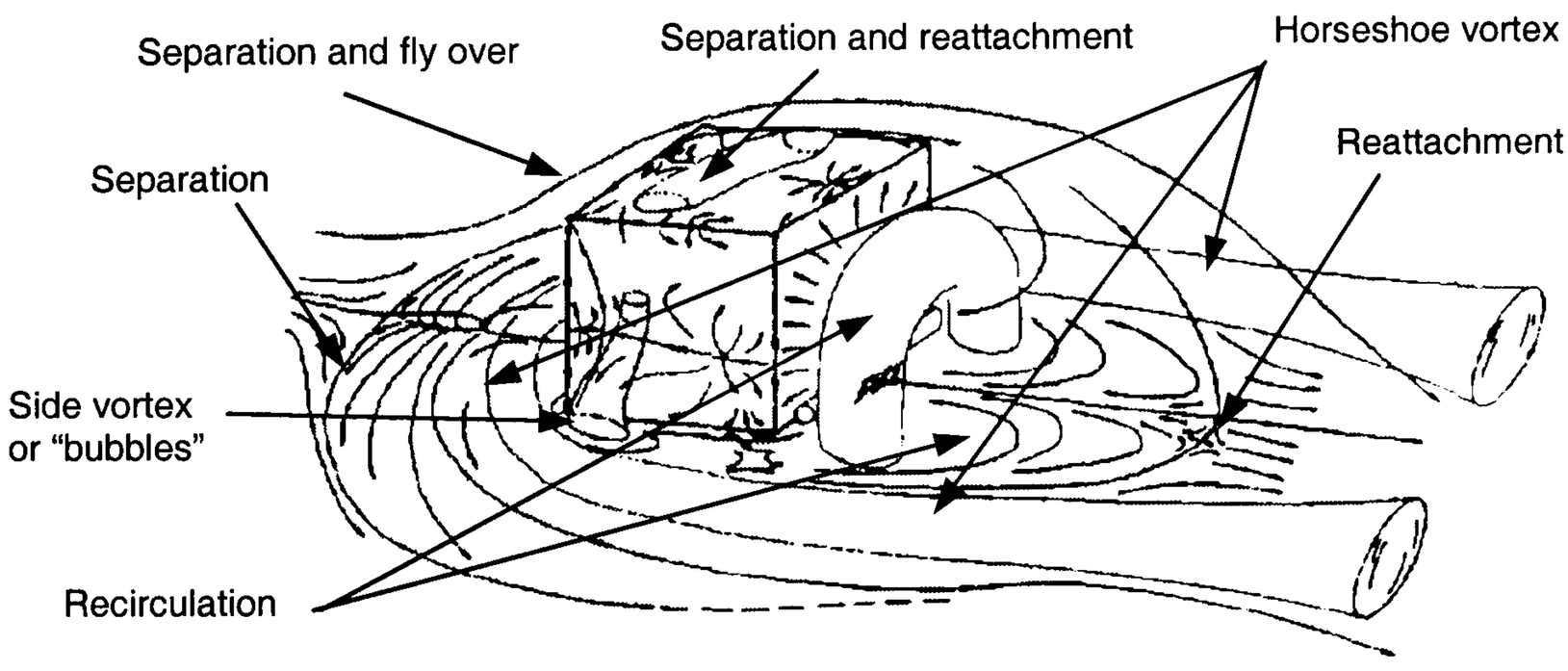

Figure 5.10 The schematic representation of the flow field around a cube [From: Martinuzzi and Tropea (1993)].

Figure 5.11 shows the computed streamlines in which the flow separations, eddies, vortex sheets and reattachment can be observed. In figures 5.11-12, line "A" corresponds to the primary upstream separation line and line "B" corresponds to the approximate centre line of the horseshoe vortex around the cube. Line "B" presents a typical diverging-converging behaviour of the vortex sheet. The points "C" and "D" are the vortex cores of two major large eddies in the wake and "K" is another pair of vortex

cores formed by flow separations at the front corners of the cube. The region "R" is the location of flow reattachment in the wake. The observed flow pattern from this experiment was similar with that of Martinuzzi and Tropea (1993), where the flow field around a cube was visualised by oil film (figure 4.12).

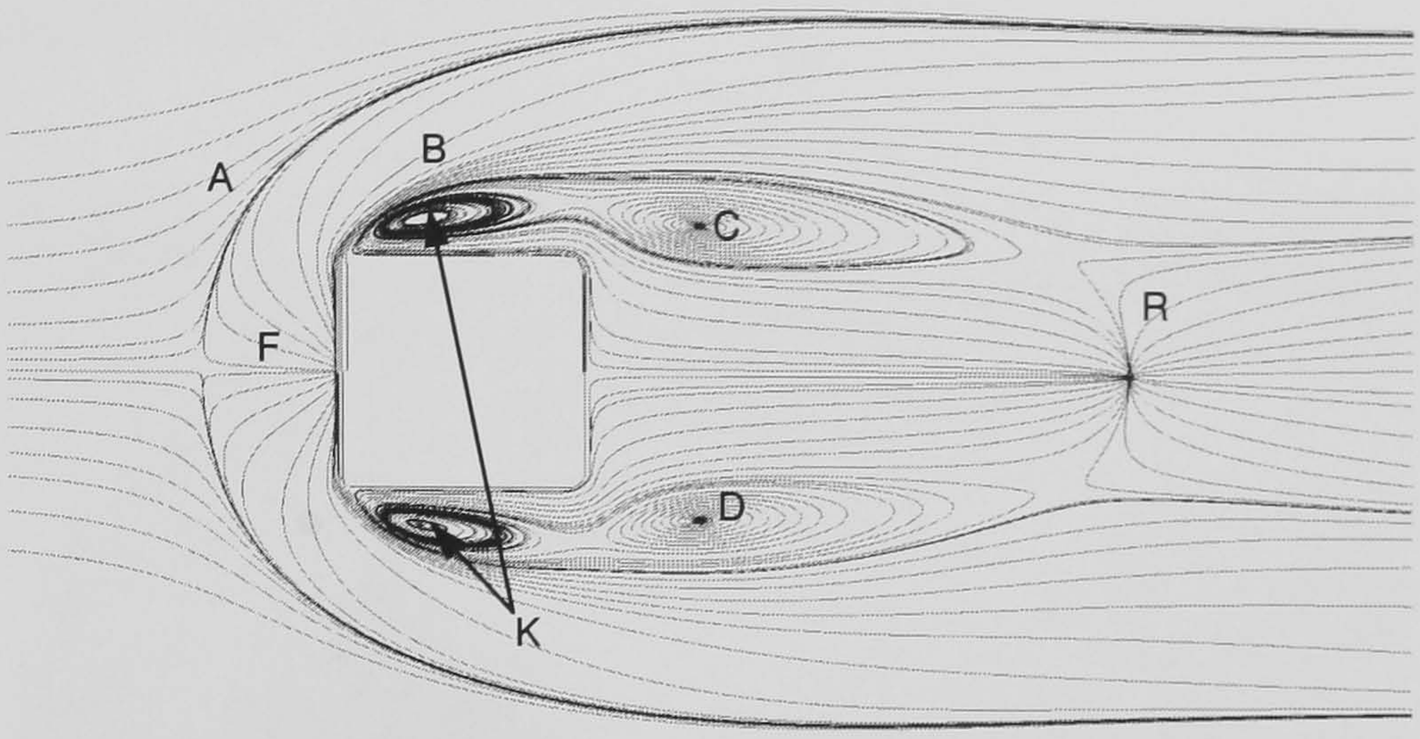

Fig 5.11 The computed streamlines when wind direction is normal to cube.

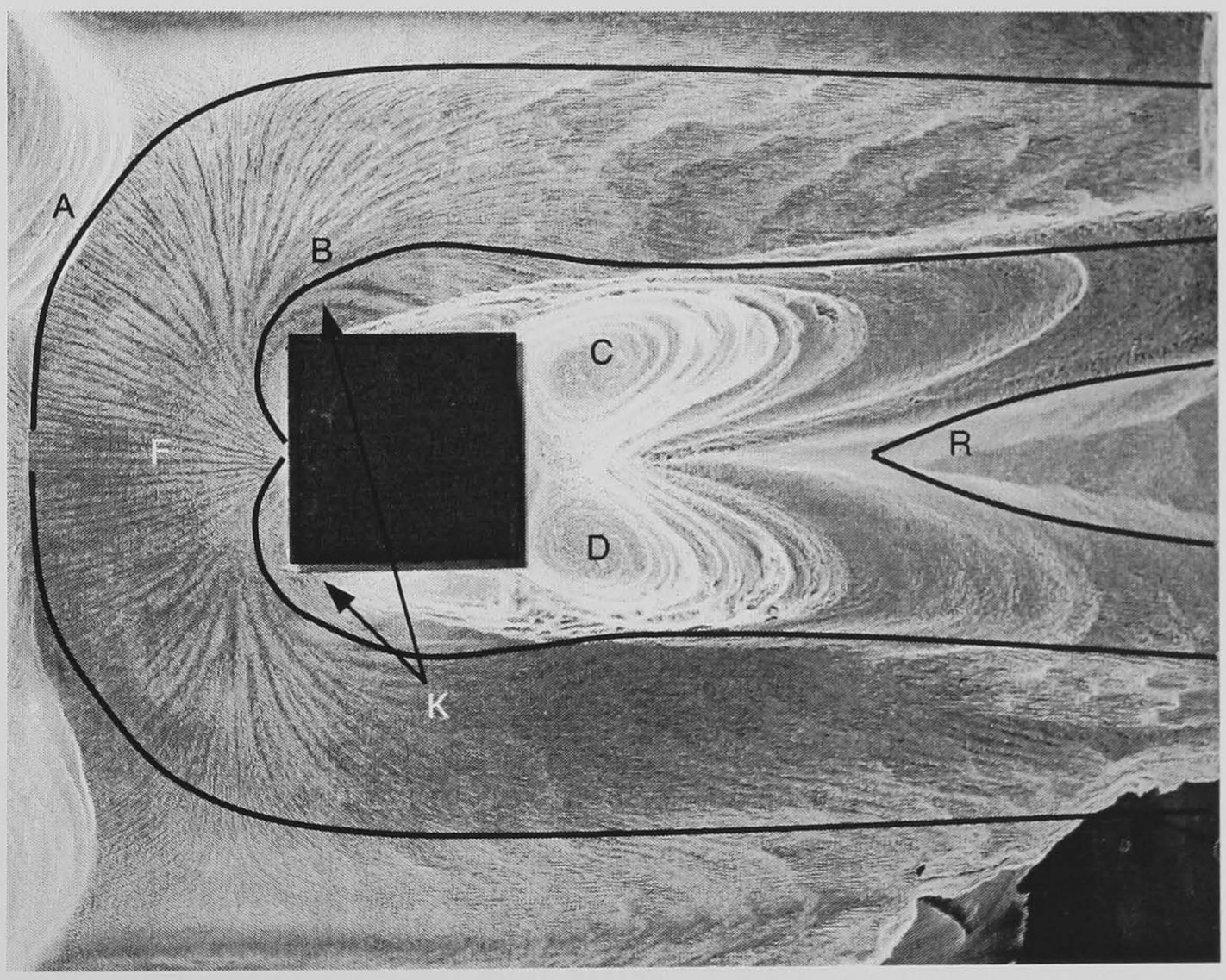

Fig 5.12 Flow pattern visualised by the dried paint.

Comparing figure 5.11 with figure 5.12, one significant difference is the size of the standing vortex in front of the cube, denoted by "F" in both figures. The width of the region between line "A" and the front face of the cube was about 1.0H (H is the cube height) observed from the experiment, whereas the width of "F" presented by computation was approximately 0.6H. The location of "R" was at about 2.0H from the rear face of the cube in the computed streamlines whilst the experimental result

indicated that the corresponding reattachment length was about 1.7H. The locations of "C" and "D" were closer to the cube in the picture of the experiment compared to the computed streamlines. The shape and orientation of the two large eddies presented in the wake flows were slightly different between the experiment and the computation. The other flow features such as the locations of vortex cores "K" and the behaviour of line "A" and line "B" were similar.

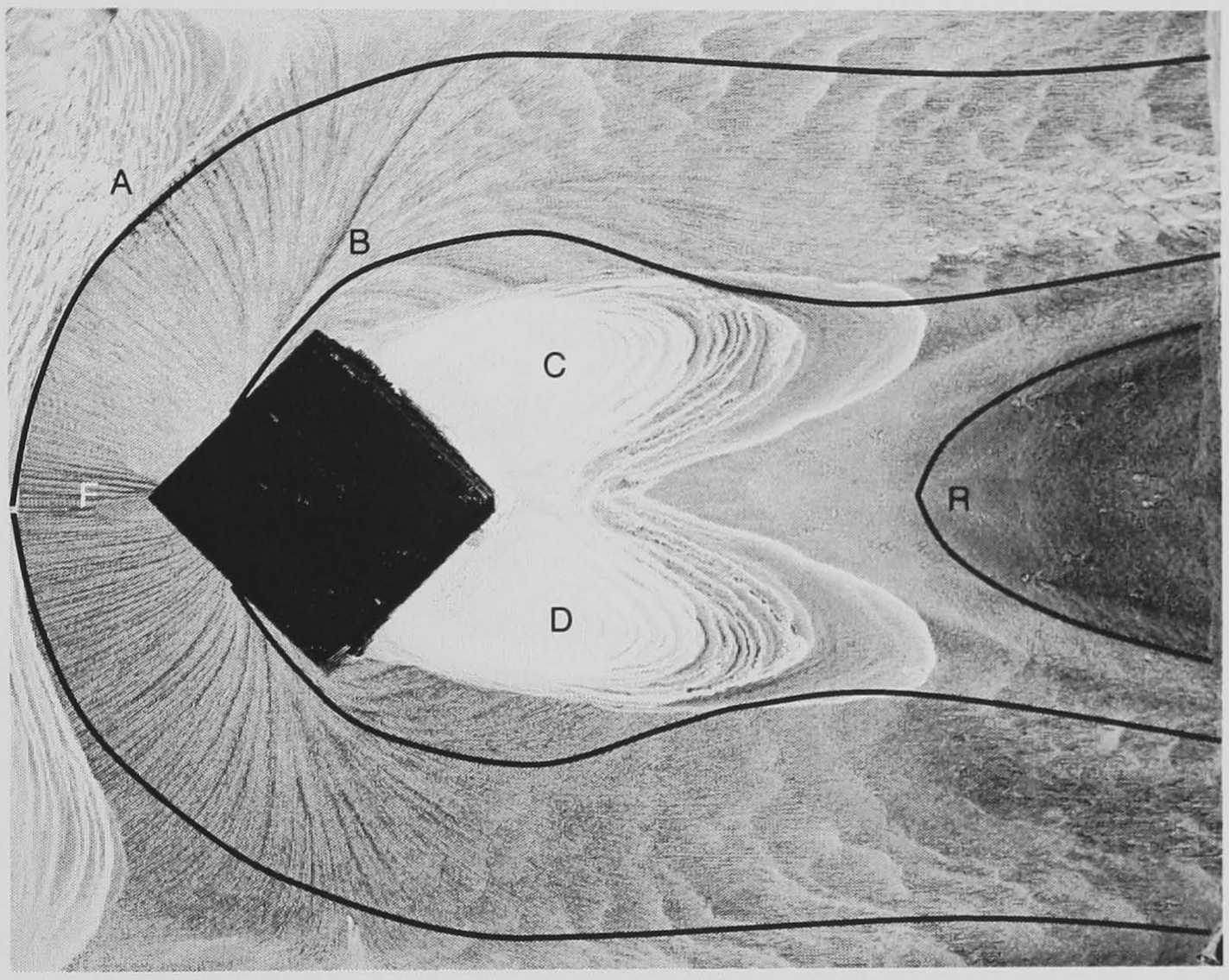

Figure 5.13 Flow pattern exhibited by the dried paint.

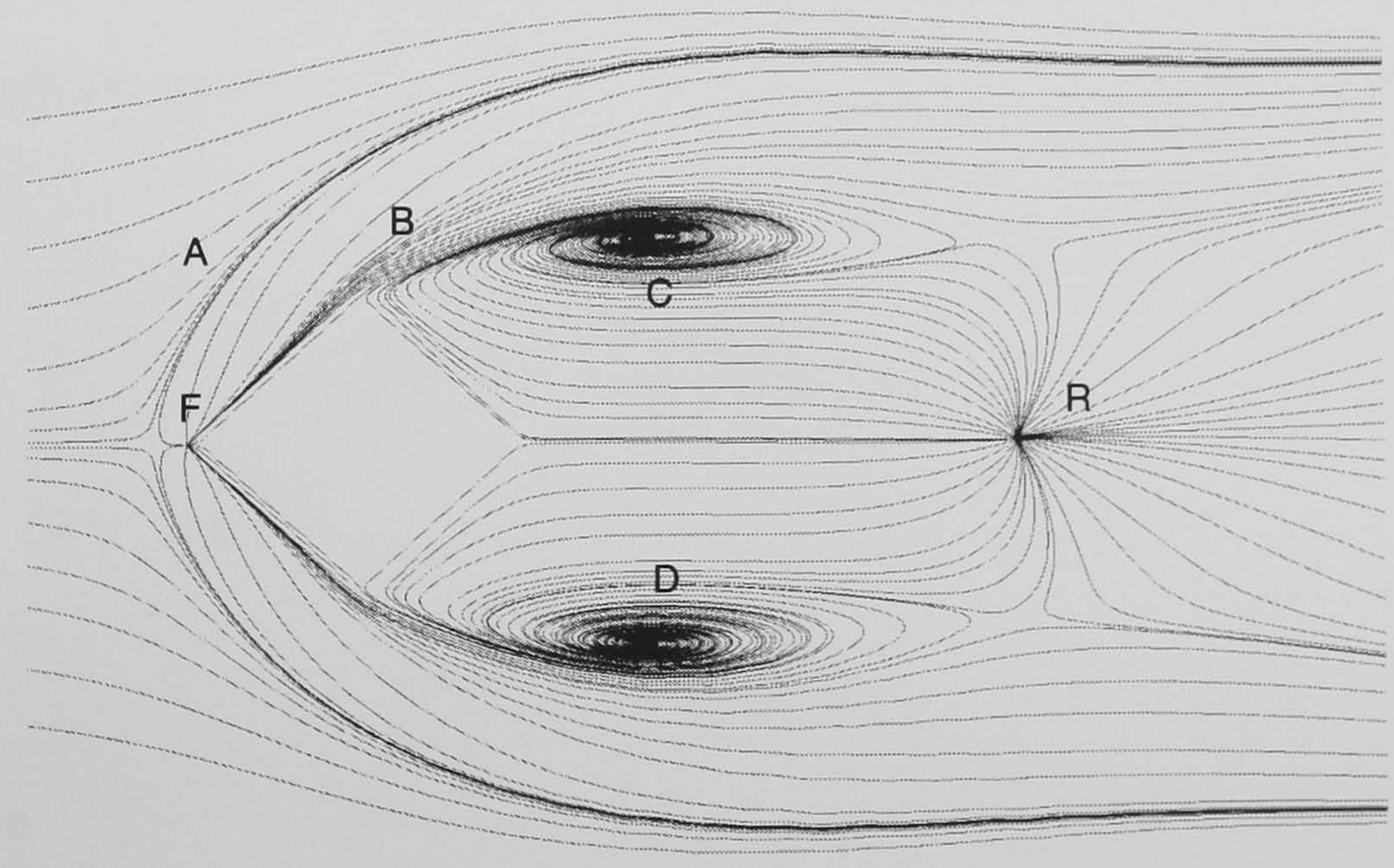

Figure 5.14 The computed streamlines when wind direction is 45° to cube.

The flow pattern around a cube orientated 45° to the approaching wind was compared using the same symbols – A, B, C, D, F, R (figures 5.13-14). One noticeable difference between the experiment and computation was the separation zone denoted by "F". The

experiment indicated that there were significant reverse flows in front of the cube (figure 5.13), whereas the computation did not present similar phenomena in this region. Though, there were a few streamlines showing some reverse flows near the plane of symmetry (figure 5.14). The diverging-converging behaviour sketched by line "B" was more obvious in this case. The behaviour of upstream flow separation marked by line "A" and the trend of line "B" agreed well between the computation and the experiment. The location of flow reattachment "R" was at about 2.1H from the rear corner of the cube (5.14), whilst the distance between the rear corner and "R" was about 1.9H, observed from the experiment (figure 5.13). The other features such the locations of the two vortex cores "C" and "D" were slightly different between the computation and experiment. Apart from the significant difference in the prediction of the standing vortex "F", the flow pattern obtained from the computation agreed fairly well with the experiment.

The second computation using the Cartesian grids (figure 5.9) for the cube rotated 45^{o} is shown in figure 5.15. The computed streamlines were fairly different from the previous case (figure 5.14). No reverse flows were present in the front of the cube and the separation region depicted by line "A" and line "B" were thin, indicating the vortex sheet in that region was not clear. The location of reattachment "R" was at about 1.9H and the distance between the two vortex cores ("C" and "D") was narrower. Both of the flow features in the wake computed by this grid arrangement were closer to the experimental observation.

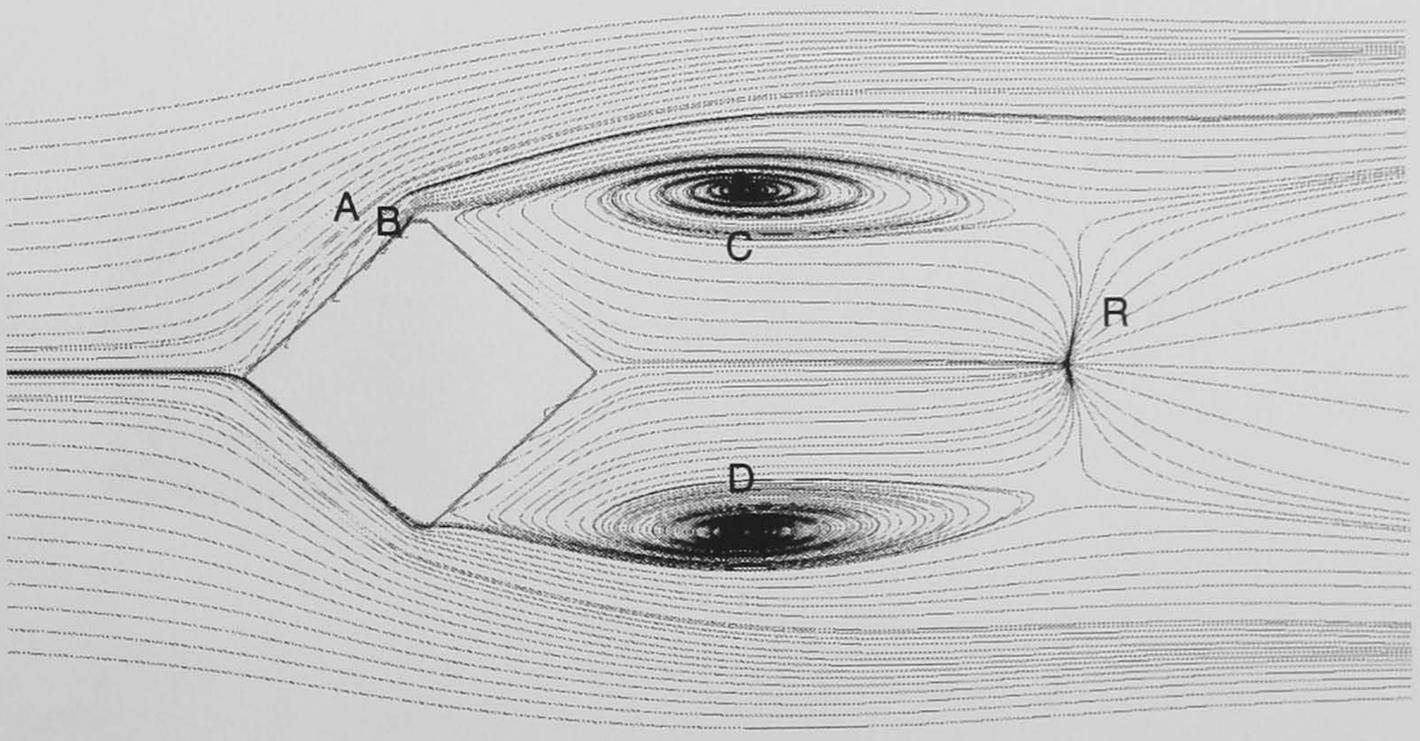

Figure 5.15 The computed streamlines when cube is orientated 45^{o} to the wind, i.e. the grids do not align with the edges of the cube.

From the observation, the "staircase" approximation of geometry was likely to reduce the effects of flow separation; therefore there was no significant vortex sheet around the

cube. This grids arrangement accidentally "streamlined" the bluff body; it prevented the flows from separation and consequently the wake was narrower. The comparison indicated that the simulated flow field was another flow problem, which was slightly different from the intended flow simulation if using this grid arrangement.

5.3.2 Investigation of the Velocity Field

The mean wind velocities were selected for comparison since the velocities acquired from the experiment were mean values. The CFD simulations were different from the previous ones, since the measurements were done in the large BLWT; therefore the computations were modified using different boundary conditions (tables 5.1-2). All measured values in this experiment were normalised by the reference velocity, which was the measured velocity at each point when the cube was absent. A ratio greater than unity (1.0) indicates that the velocity at the corresponding point is accelerated by the presence of the cube, whereas a value less than 1.0 implies that the velocity is reduced. Figure 5.16 shows the results of computer simulation and the measured values in the case when the wind direction is normal to the cube. Each point in the figure corresponds to its relative location to the cube. The CFD results are shown in the upper half plane and the measured values are in the lower half.

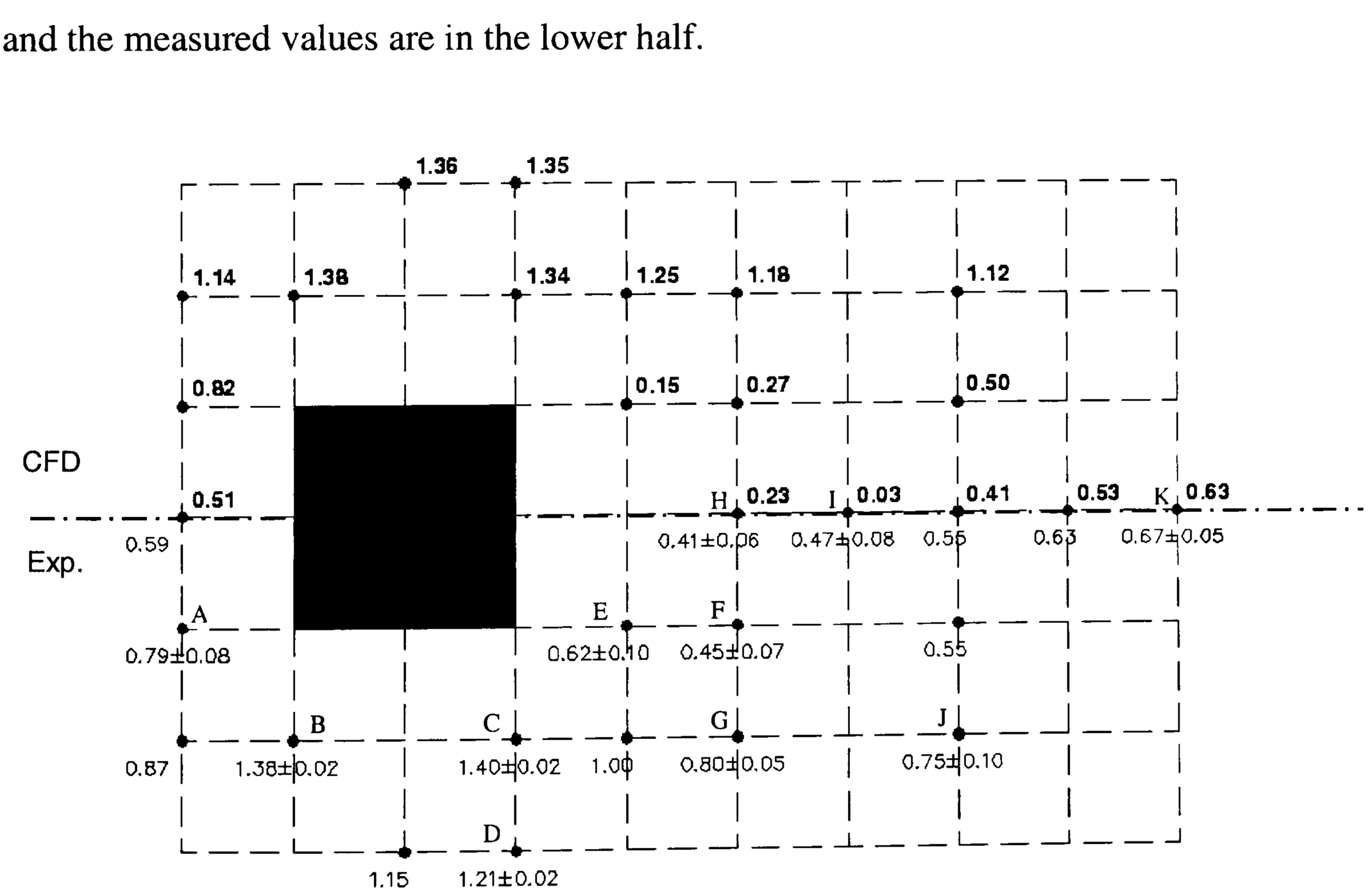

Figure 5.16 The measured velocity ratios vs. CFD computation

The minimum scale of the manometer was 2 mm (manometer fluid); therefore the readings could be accurate to the order of 2 mm. An estimate in the order of 1 mm was also possible to be made by eyes. Since the velocity field around the cube was unsteady, the readings observed were also fluctuating. The averaged value was obtained from the mean between the maximum value and the minimum value. The range of fluctuation was expressed by the sign of "±". Some measured values without "±" indicated that the fluctuations of the manometer readings were not discernible by eyes. At point "A", the magnitude of fluctuation was 10% of the mean, indicating the unsteadiness of the flow field near the sharp edge of the cube was noticeable. Same phenomena were also observed at points "B", "C" and "D" but the flow field was less unsteady. The maximum scale of fluctuation was 17% of the mean at point "I" and the flow field was also very unsteady in the wake near the cube, indicated by the values measured at points "E", "F", "G" and "H". Farther away from the cube, the unsteadiness of the flow field was not discernible except at points "J" and "K". The unsteady phenomena were mainly due to vortex shedding and the complicated mechanism between flow separation and reattachment, as depicted in figure 5.10. In addition, some possible errors caused by instrumentation were:

- Tubing: the length and the quality of the tube connecting the Irwin sensor and the manometer was likely to affect the pressure difference detected. The length of the tube was controlled between 2 m and 2.5 m and each tube was checked before the experiment but there might be undetectable flaws.
- Manometer: the sensitivity of the multi-tube manometer was low and the minimum scale was not precise enough to acquire more accurate readings.

The velocity ratios calculated by CFD were in good agreement with the measured values except some points in the wake. The error percentage was in a range between 1% and 20% except some discrepancies found in the wake. The computed values at the locations corresponding to "E", "F" and "H" were significant lower than the measured values, indicating the computed velocities in those locations were much weaker than the actual velocity field. Though, at the locations corresponding to "G" and "J", the computed velocities were higher than the measured values. Nevertheless, the computed velocity field in the wake was correct in terms of its trend. These points were all located in the unsteady wake flows and the unsteadiness might impair the accuracy of measurement (Stathopoulos and Baskaran, 1996; Stathopoulos, 1997); therefore, the

discrepancies between the experiment and the computation were relatively large in this region. The worst prediction made by CFD was at point "I", where the computed value was 0.03 but the measured value was in the range between 0.39 and 0.55. The computed streamlines (figure 5.17) suggested that the vortex core "C" or "D" behind the cube was approximately at the location corresponding to point "E" in figure 5.16 and the location of flow reattachment was also at about the location of "I". Therefore the computed values at these two points were very low. In contrast to the flow pattern compared in the previous section, the streamlines presented in figure 5.17 were fairly different from figure 5.11. The distance of reattachment was shorter ("R" was at approximately 1.5H from the leeward side of the cube) and "F" was thinner as well as the two vortex cores – "C" and "D" were closer to the cube. The change of upstream wind conditions resulted in significant alterations to the flow behaviour around the cube.

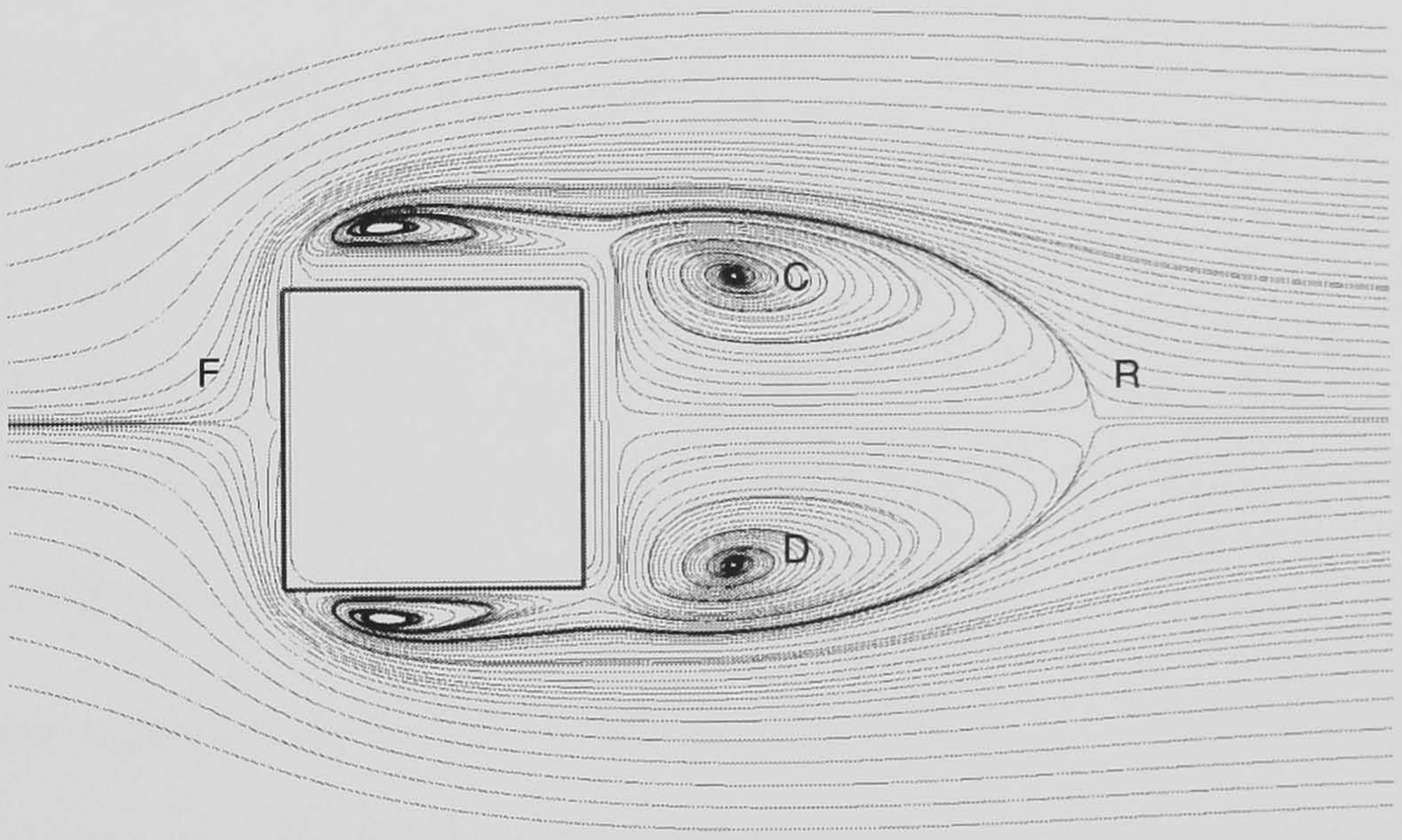

Figure 5.17 The computed streamlines at 5 mm above ground.

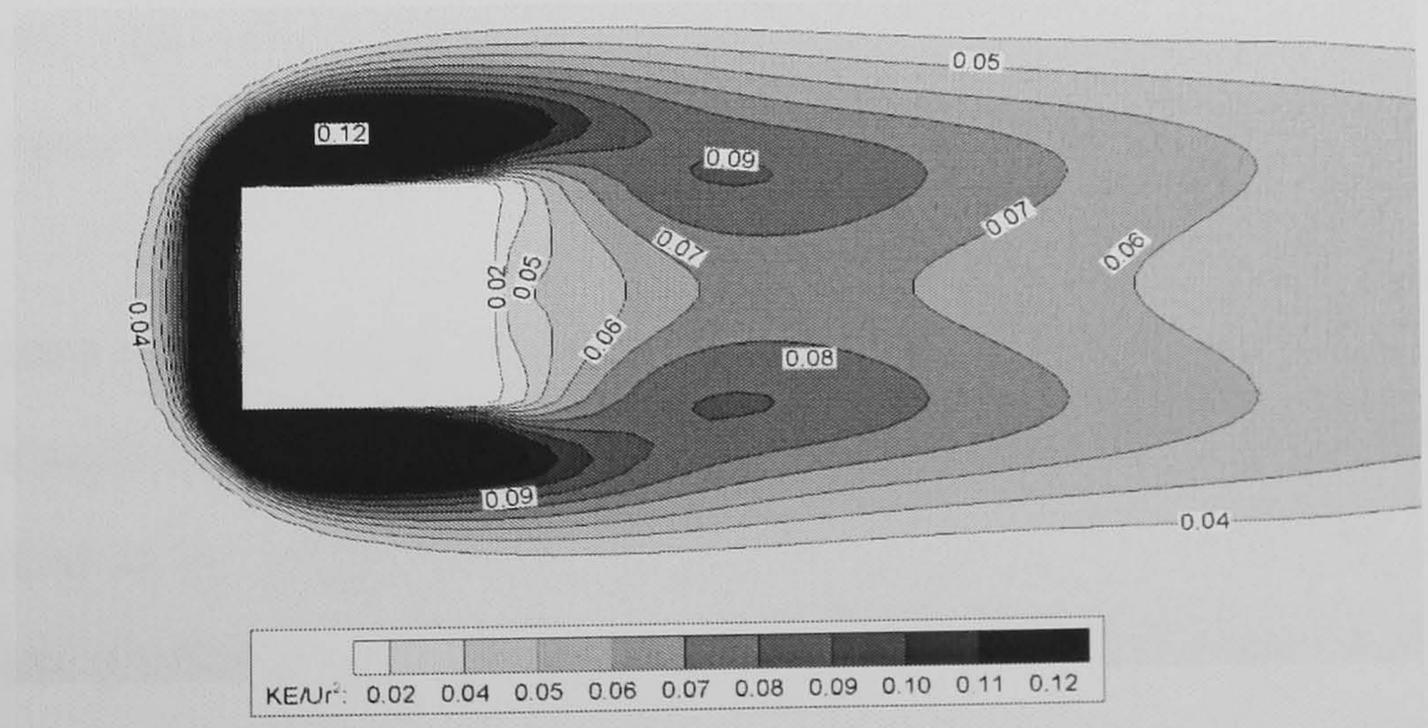

Figure 5.18 The computed turbulence energy (in ratios) around the cube.

The computed turbulence energy (KE) is shown on figure 5.18. The values have been non-dimensionalised by the square of the reference velocity (U_r), which is the same reference velocity when the cube is absent from the flow simulation. The values shown in figure 5.18 were the scales of turbulence. The most noticeable area of the KE production was within the black "horseshoe" shape where the scale of turbulence was 0.12, indicating there were stronger fluctuating velocities in that region. This region was characterised by flow separation, generated by the interactions between pressure gradient ($\partial p / \partial x$) and velocity gradient ($\partial u / \partial x$). Since the positive pressure gradient ($\partial p / \partial x > 0$) may retard the fluid motion and it may appear when the fluid is approaching an obstacle (e.g. wall). On the other hand, the momentum transfer from other higher velocity regions (e.g. free stream) tends to accelerate the fluid motion. As a result, if the velocity gradient is sufficiently large in magnitude, there will be a reversal of the direction of flow near the wall (Guyon *et al.*, 2001). The velocity profile near the wall therefore becomes negative due to excessive pressure gradient. The phenomenon is called "adverse pressure gradient". The adverse pressure gradient is the onset of flow separation in general. Within the layer of flow separation, some complicated flow behaviours like flow stretching and swirling is apparently possible. The highly complicated flow phenomena consequently generate a very unsteady flow field and the fluctuating velocity components ($u_i^{'}$) can vary drastically. Therefore the production of turbulent stresses ($\rho\overline{u_i^{'}u_j^{'}}$) in the layer of flow separation was high. The KE productions in the wake flows were relatively lower and the turbulence energy in the recirculation zone was not as high as speculated. It was due to the eddy viscosity hypothesis employed by the turbulence model was not ideal in this area. Apart from the highly turbulent region, the other areas of the flow field were relatively steady as the turbulence energies were dissipated by wall friction and fluid viscosity.

Figure 5.19 shows the computed and observed velocity field around the cube orientated 45° to the approaching wind. CFD1 combined two velocity components to create the approaching wind at an angle of 45° to the cube (figure 5.8), whereas CFD2 used the normal Cartesian grids but the cube was placed with an orientation of 45° (figure 5.9). The results of both computations are shown in the upper half plane in figure 5.19. In the experiment, the fluctuations of the velocity field were observed at points "A", "B", "C", "D", "E", "F", "G" and "I". The maximum scale of fluctuation was 12% of the mean at point "H". In comparison with figure 5.16, the velocity field in figure 5.19 was less

unsteady as the scales of fluctuations were slightly smaller. The velocities at points "B" (U/U_r = 1.35) and "C" (U/U_r = 1.68) were largely accelerated due to the corner effects by the presence of the cube.

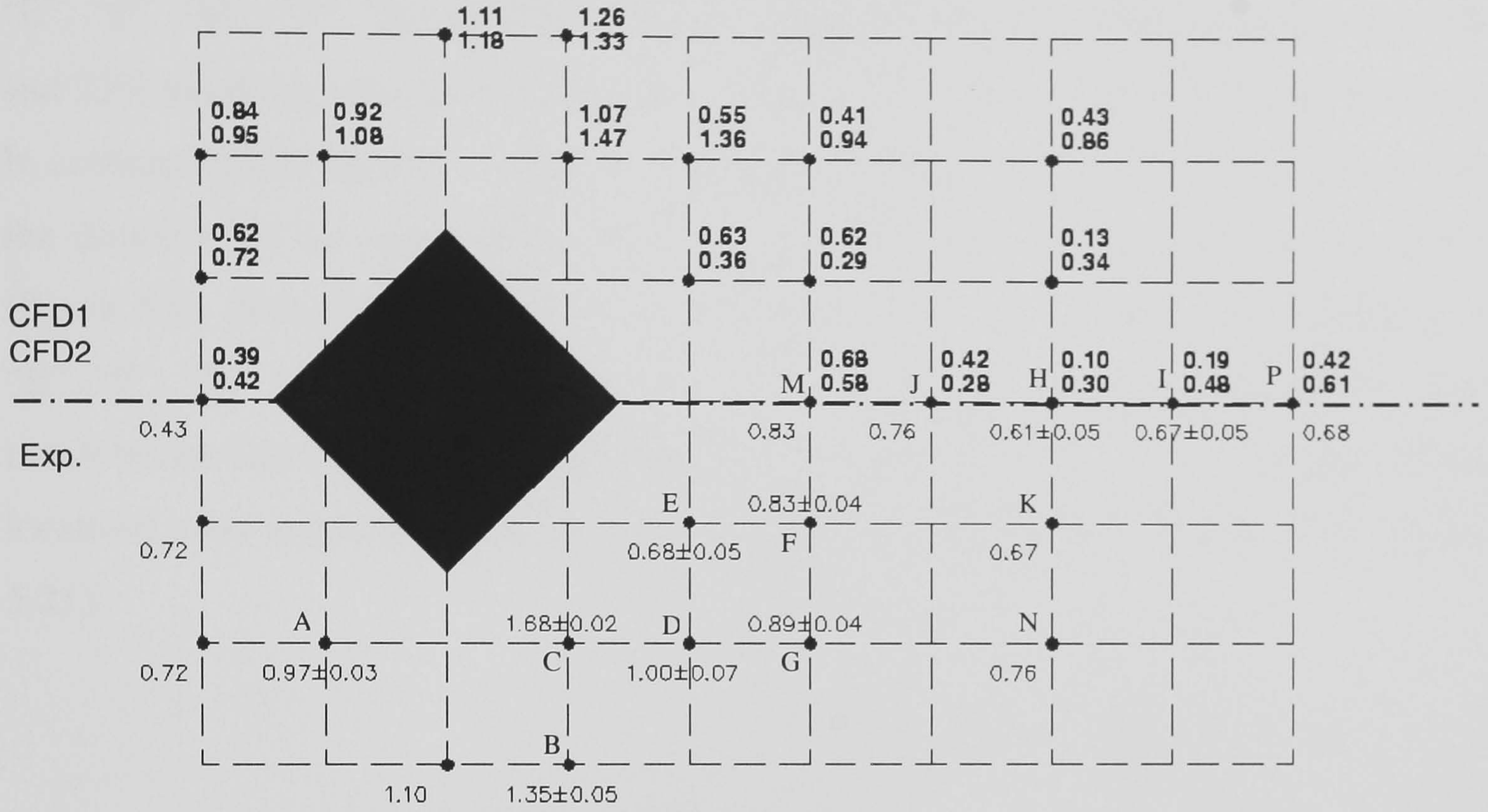

Figure 5.19 The measured values vs. computed velocity field.

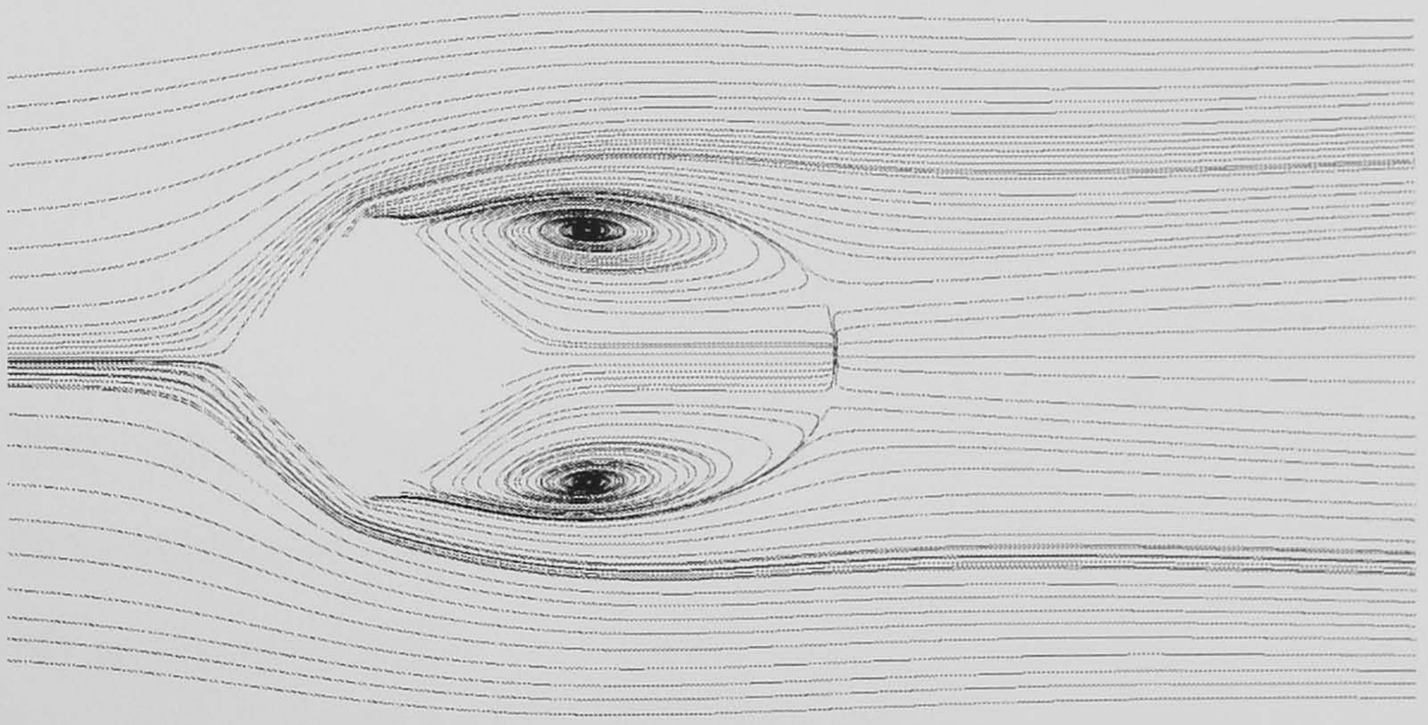

Figure 5.20 The streamlines computed by CFD2. The locations of vortex cores and the flow reattachment in the wake are close to the locations corresponding to "E", "F", "M" and "J" in figure 5.19.

The computed values at the location corresponding to "C" were 1.07 by CFD1 and 1.47 by CFD2 in which the predicted value was closer to the experimental observation. Most of the computed values made by CFD2 were higher than CFD1 except at the locations corresponding to "E", "F", "M" and "J". It was due to that the velocity field computed by CFD2 was a slightly different but "streamlined" flow field, as discussed in the

previous section; therefore the momentum loss in the wake was recovered at a faster rate, except at the locations near "E", "F", "M" and "J", where the vortex cores and flow reattachment were present (figure 5.20). The velocity field predicted was also in fairly good agreement with the experimental values except at the locations corresponding to "E", "F", "M", "J", "H" and "K". The error percentage was in the range between 1% and 25% except at those points near the locations of vortex cores and flow reattachment. In contrast, CFD1 obtained a weaker velocity field in general. It was mainly due to that the direction of the approaching flow was not orthogonal to the grid lines in CFD1 (figure 5.8). Nonetheless, it made better predictions at the locations corresponding to "E", "F", "M" and "J" if compared with CFD2. The values calculated by CFD1 were much lower than the measured values at "D", "G", "H", "K", "N" and "I" because these locations were adjacent to the vortex cores and flow reattachment in the wake (figure 5.21).

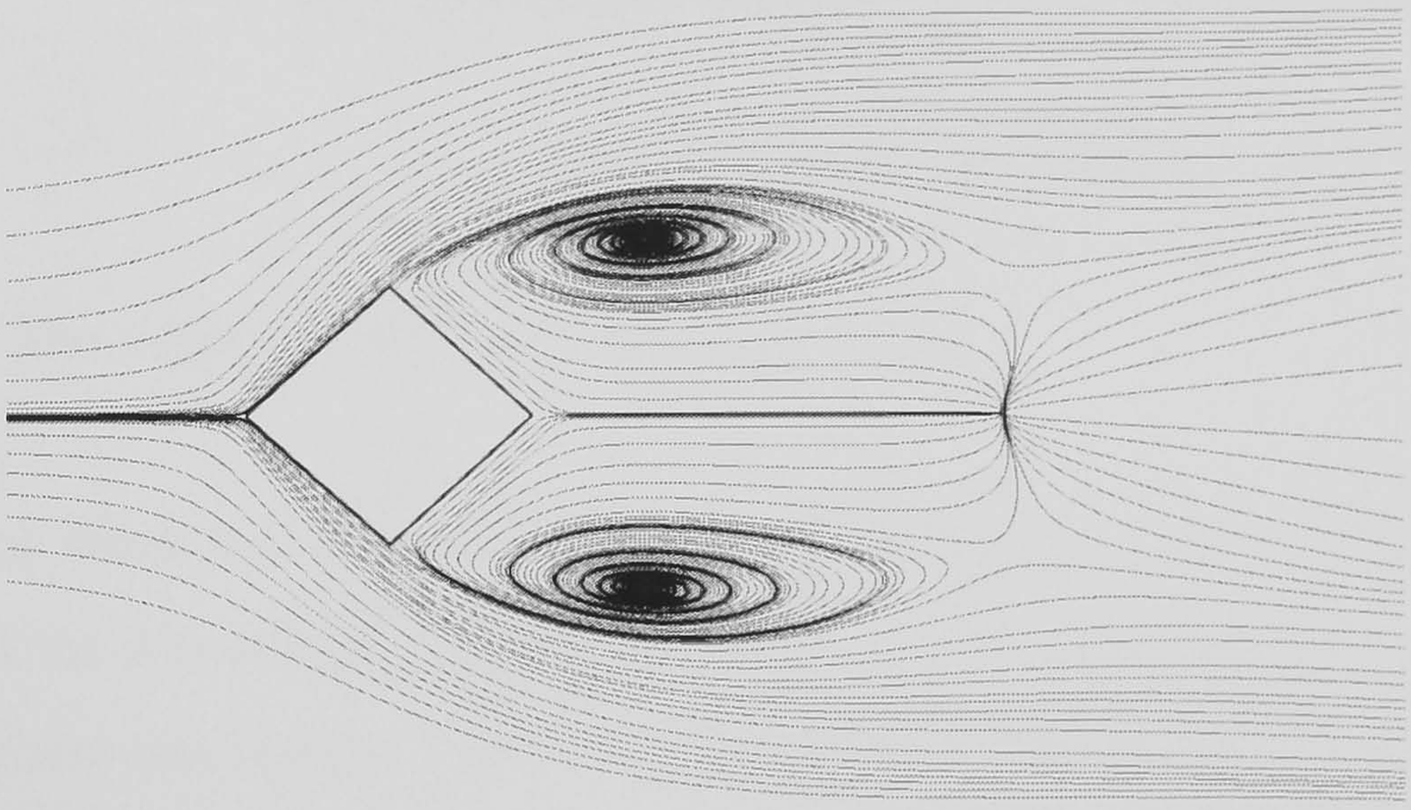

Figure 5.21 The computed streamlines by CFD1. The locations vortex cores and the flow reattachment in the wake are close to "D", "G", "H", "K", "N" and "I" in figure 5.19.

The trend of velocity field predicted by both computations was analogous to the experimental observation, though the computed velocity field in the wake was less satisfactory in both cases. The computed KE fields by CFD1 and CFD2 are shown as figure 5.22 and 5.23 respectively. As it was observed from the computed streamlines (figures 5.20-21), the layer of flow separation in front of the cube was thin in both computations; therefore the computed turbulence energies were low, denoted by the contour line with a value 0.03.

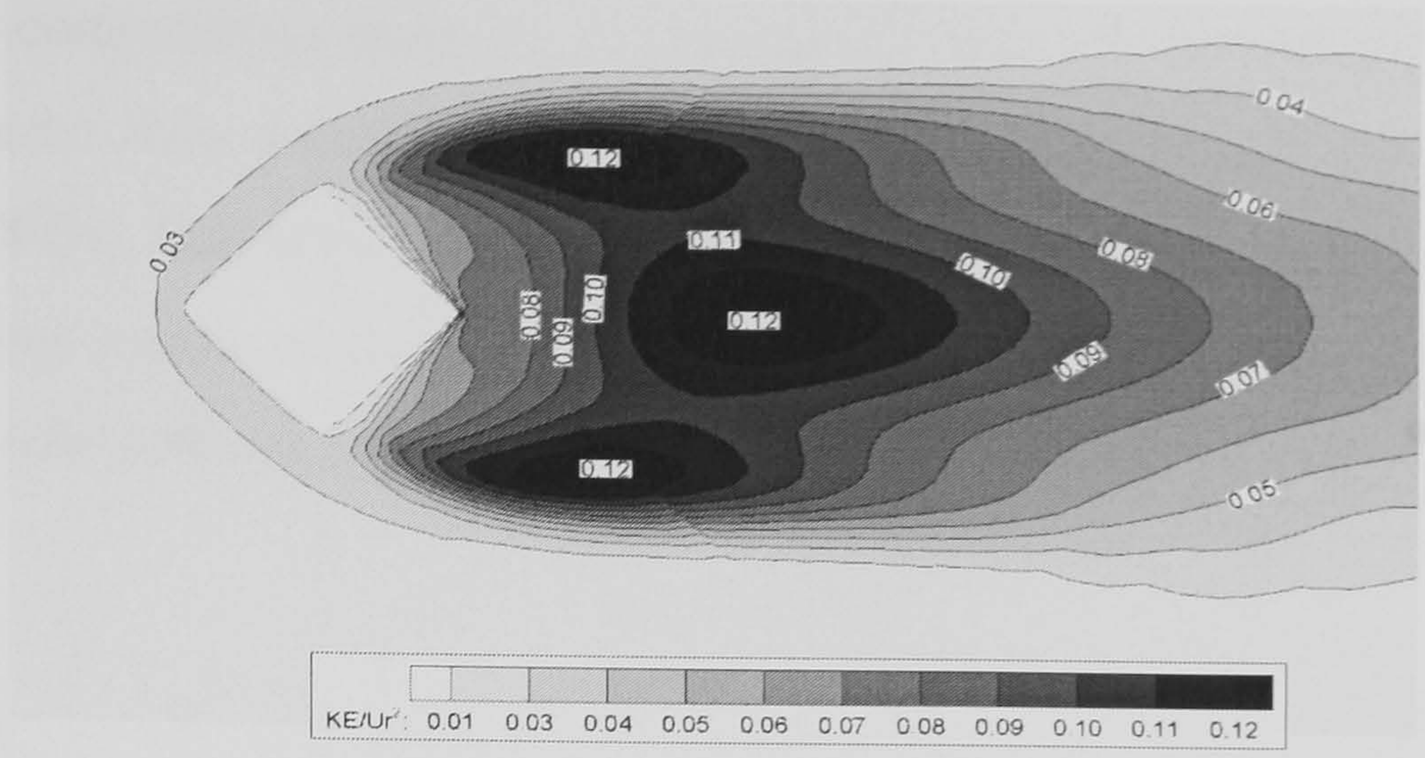

Figure 5.22 The computed KE distribution by CFD1.

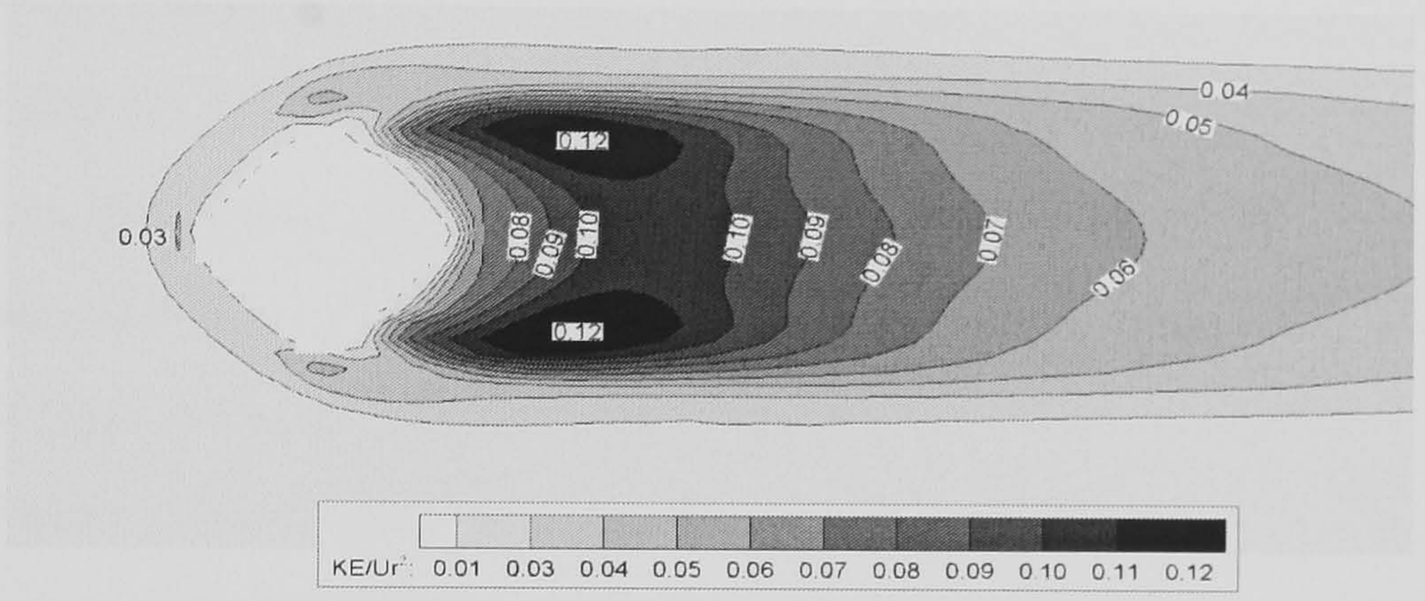

Figure 5.23 The computed KE distribution by CFD2.

The observation from the experiment also indicated that the velocity fluctuations were less discernible in that region. The higher values of KE in this case were found in the wake flows, where the highest value 0.12 was present near the vortex cores and in the region of flow reattachment (figure 5.22). The computed results by CFD1 agreed favourably with the experimental observation, where the larger scales of velocity fluctuations were observed at "D", "E", "F", "G" and "H" (figure 5.19). Noticeably, the computation by CFD2 did not yield high KE values in the region of flow reattachment (figure 5.23). It indicated that the velocity field predicted by CFD2 in the wake near the location of flow reattachment was less unsteady.

Overall, the computation made by CFD1 obtained good agreement with the experimental observation but the calculated velocities were likely to be lower because the direction of approaching flow was not normal to the grid lines. The effects are called "numerical diffusion". It may limit the accuracy of CFD computation if the flow direction is highly skewed to the grid lines (e.g. recirculating or swirling flows). It can also explain why the flow field behind a cube is usually very difficult to be predicted

correctly. The computation made by CFD2 was actually a "streamlined" flow field. It was not the same flow simulation as intended but it somewhat "complemented" the weakness of CFD1. The velocity field calculated by CFD2 was stronger in the wake and it obtained better results in the prediction of wake flows, though the overall flow field predicted was still different from the experimental observation.

5.4 Summary

This chapter presents the experimental investigation and numerical simulations of the flow field around a cube. Though the agreement between the experiment and CFD simulation may be unsatisfactory in the wake behind a cube, the general trend of flow behaviour computed by the proposed method is likely to be correct. For a flow simulation where the grid lines do not align with the edges of a cube, the predicted flow field in the wake is likely to be stronger yet closer to the experimental observation. If the flow details near walls are not of primary concerns, using this simplified approach is adequate. The next chapter is applying the proposed methods to investigate the street-level winds in some more complicated cases.

Chapter 6 Numerical Simulations of Street-Level Winds within a Passage and in a Built-up Area

Street-level winds are one of the primary concerns in environmental design. Architects and urban planners need to mitigate unfavourable or dangerous winds that may occur in the areas accessible to pedestrians, since "wind nuisance" may impair some desired functions of the outdoor spaces. Studies regarding the issues of wind comfort have been mostly done in wind tunnel laboratories. These facilities are, however, not generally available to architects or building professionals due to high construction and maintenance costs associated with those tunnels and instrumentations. As a result, for design purposes, using CFD to simulate the wind environments around buildings becomes an option for the design team.

This chapter is to apply the previous validated methods in the simulations of street-level winds in a built-up area. The winds in a passage between two buildings and the winds around a group of buildings will be simulated. The results will be compared with experimental data for further validations.

6.1 Method

The winds in a passage between two buildings have been studied by Stathopoulos and Storms (1986) using a BLWT. The first case is a corresponding numerical simulation of their study. Another wind tunnel study of the street-level winds around a group of buildings has also been conducted by Stathopoulos and Wu (1995). Their model will be simulated in the second case. Both studies use simple rectangular objects to represent typical building blocks along streets and their wind tunnel models are ideal for Cartesian grids. Therefore their experimental data are selected.

6.1.1 CFD Simulation of Ground-Level Wind in a Passage

For the first case, the computing domain was 1.8 m ×1.8 m ×1.0 m, according to the dimensions of the test section in the wind tunnel where they conducted the experiment.

The model buildings were located at the centre, mounted on the floor of the domain. All the buildings were scaled and the scale was 1: 400. The floor (ground) was modelled with a smooth wall. Since they investigated the winds in the passage under different wind directions, the various wind incidents were also simulated. They changed the orientation of their model in the wind tunnel by rotating the turntable but the CFD simulation employed another approach. The wind directions simulated were 0°, 15°, 30°, 45°, 60° and 90° by decomposing the wind into two horizontal components (U and V). Figure 6.1 illustrates the geometry of the buildings and passage.

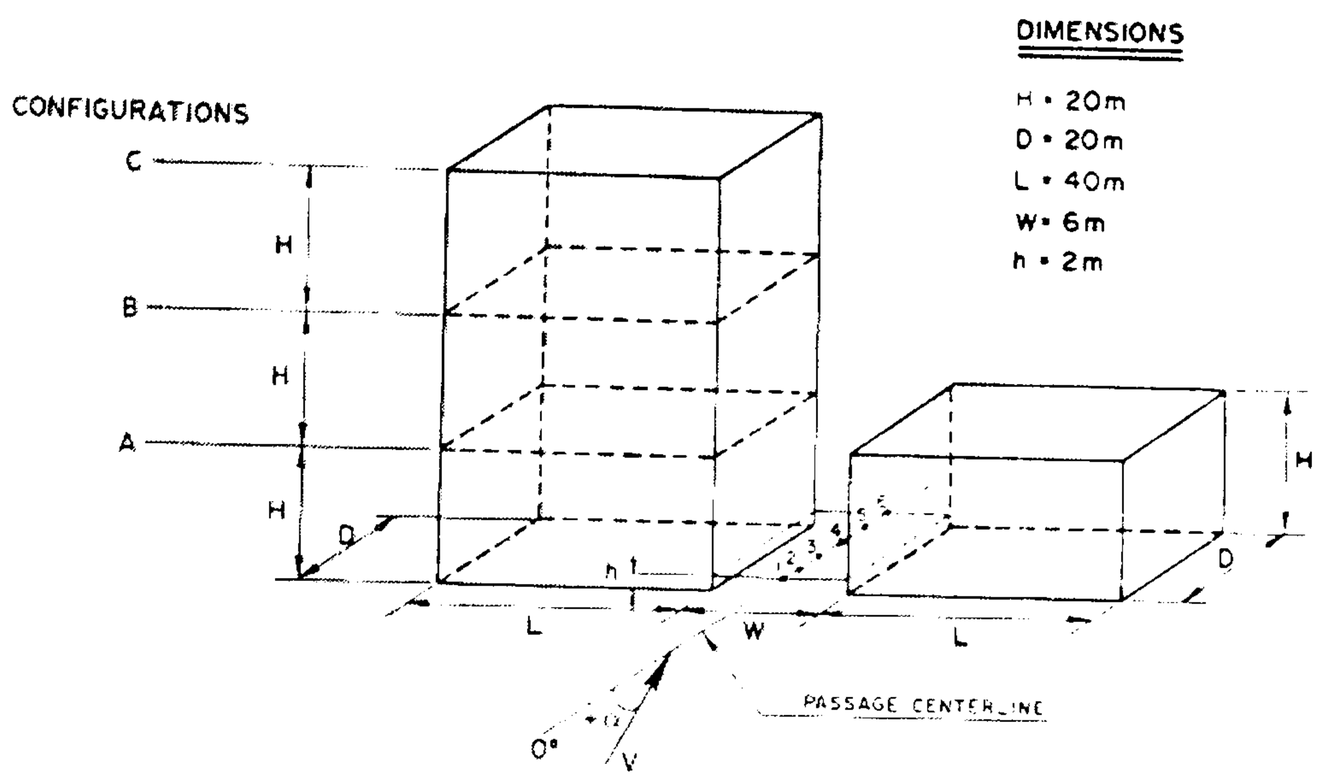

Figure 6.1 The geometry and building layout. Dimensions shown are in full scale whilst the model used is scaled. The investigation is to be made along the passage centre line [From: Stathopoulos and Storms (1986)].

The mean velocity profile (U) was fitted by a power-law model with an exponent 0.15 and the intensity of turbulence (U_{rms} / U) was about 20% near the ground, whereas it was about 5% at the gradient level. The wind speed at the gradient height was 13 m/s. The two-layer k-ε turbulence model and the non-linear higher-order differencing scheme "SMART" were applied in the simulation. The conjugate-gradient solver was used to solve the linear equations. Two different sets of computations for this case were carried out. The first set of simulations was to investigate the winds along the passage when the two buildings were in the same height (20 m in full scale). The second set of computations was to investigate the wind field in the passage when one of the buildings was three times taller than the other building.

For a good resolution of the flow field, to define an area in which the velocity gradient was likely to change significantly was necessary.

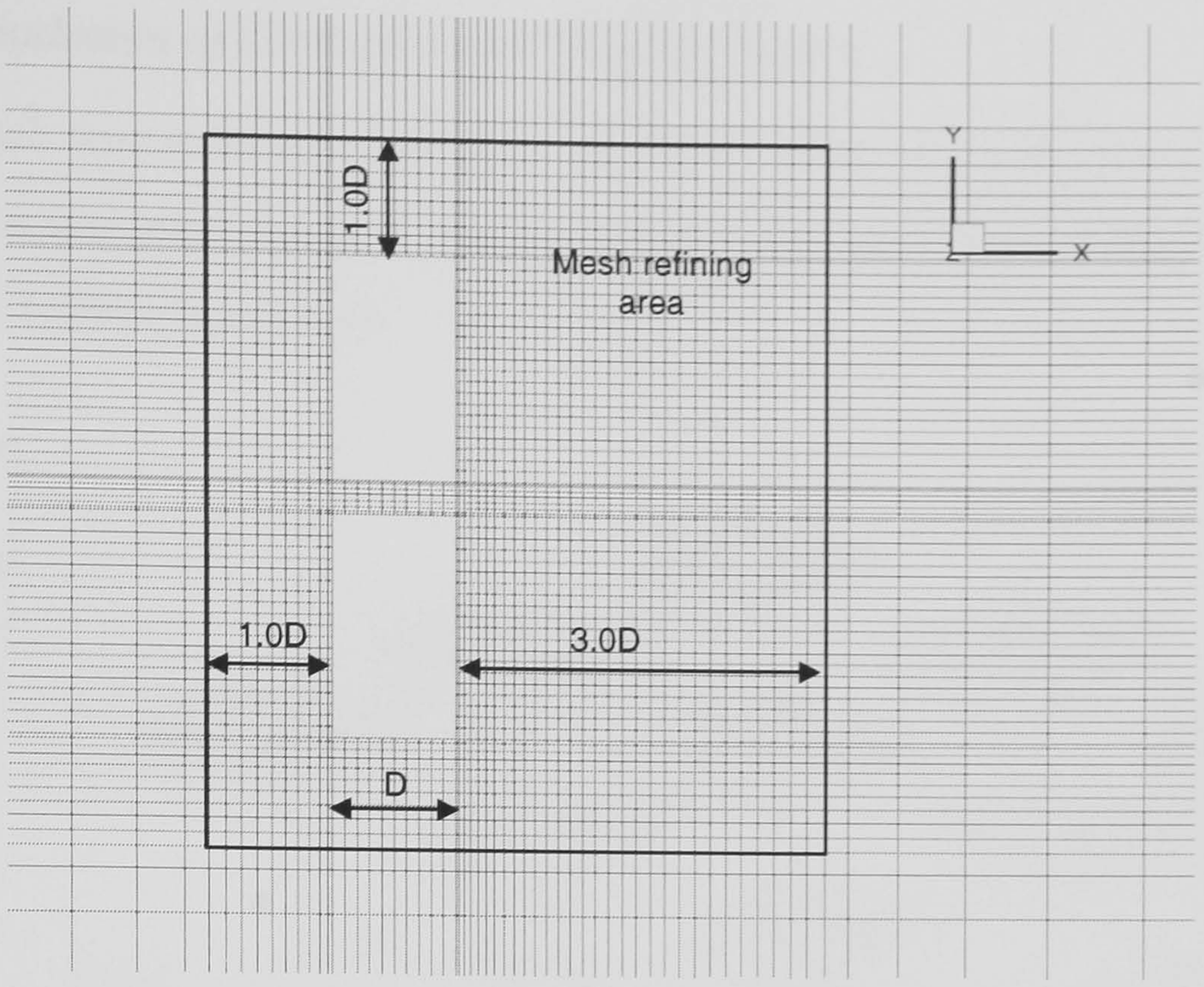

Figure 6.2 Horizontal mesh. The mesh refining area is shown on the figure.

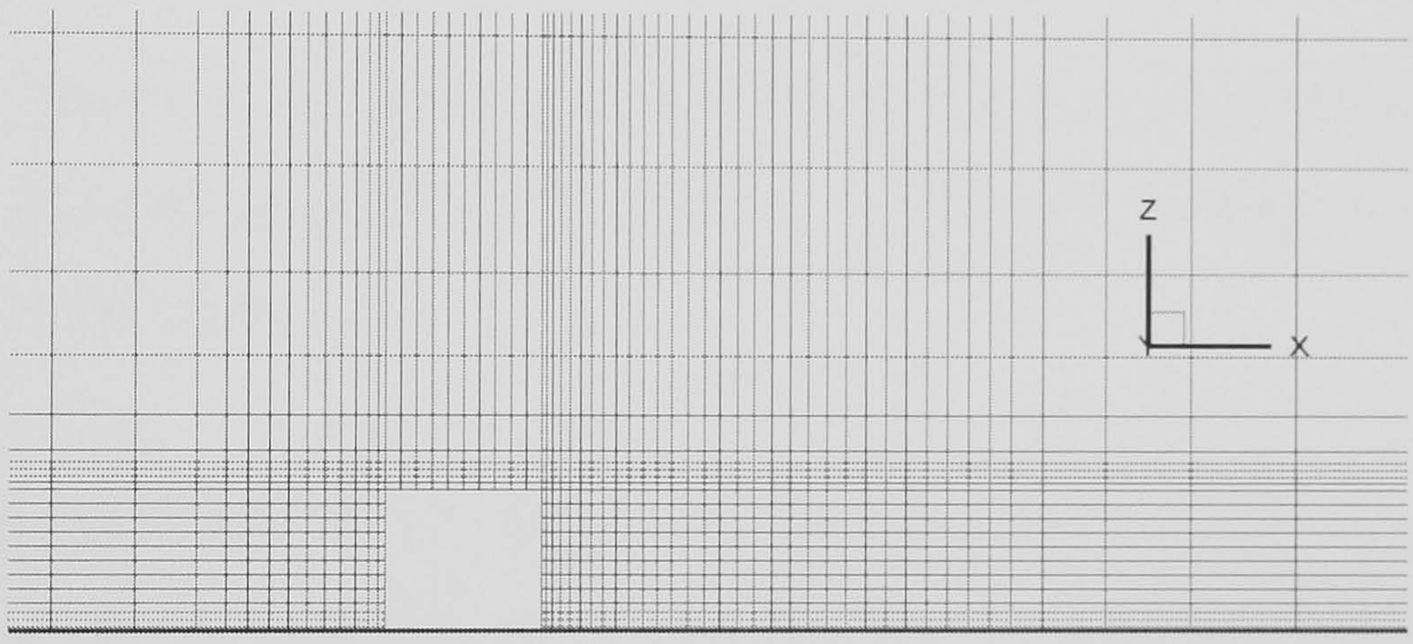

Figure 6.3 Vertical mesh. The mesh is refined at the ground level.

Since the wind velocity may drop sharply when it approaches the buildings due to the adverse pressure gradient and, the variations of velocity in the wake flow are also large due to the mixing effects of momentum transfer. Therefore refining the mesh in this area is of help to increase the resolution of the velocity field and it can also minimise the discretisation error accordingly. From previous investigations (chapter 5), the area was within a distance of 1.0D (D is the depth of the building block, shown as figure 6.1) in front of the windward side and a distance of 3.0D from the leeward side, as illustrated in figure 6.2. Another dimension, the vertical mesh was also refined at the ground level to capture the sharp velocity variations near ground (figure 6.3). In addition, although the velocity field at the top of buildings was not one of the primary interests, the grid density near the top of buildings was still increased in order to capture the flow separation and to minimise possible errors due to inadequate grid resolutions.

6.1.2 CFD Simulation of Ground-Level Wind in Streets

The second case was to investigate the street-level winds around a group of buildings. As the same as the previous case, the buildings were modelled by rectangular objects with a scale of 1/500 (figure 6.4).

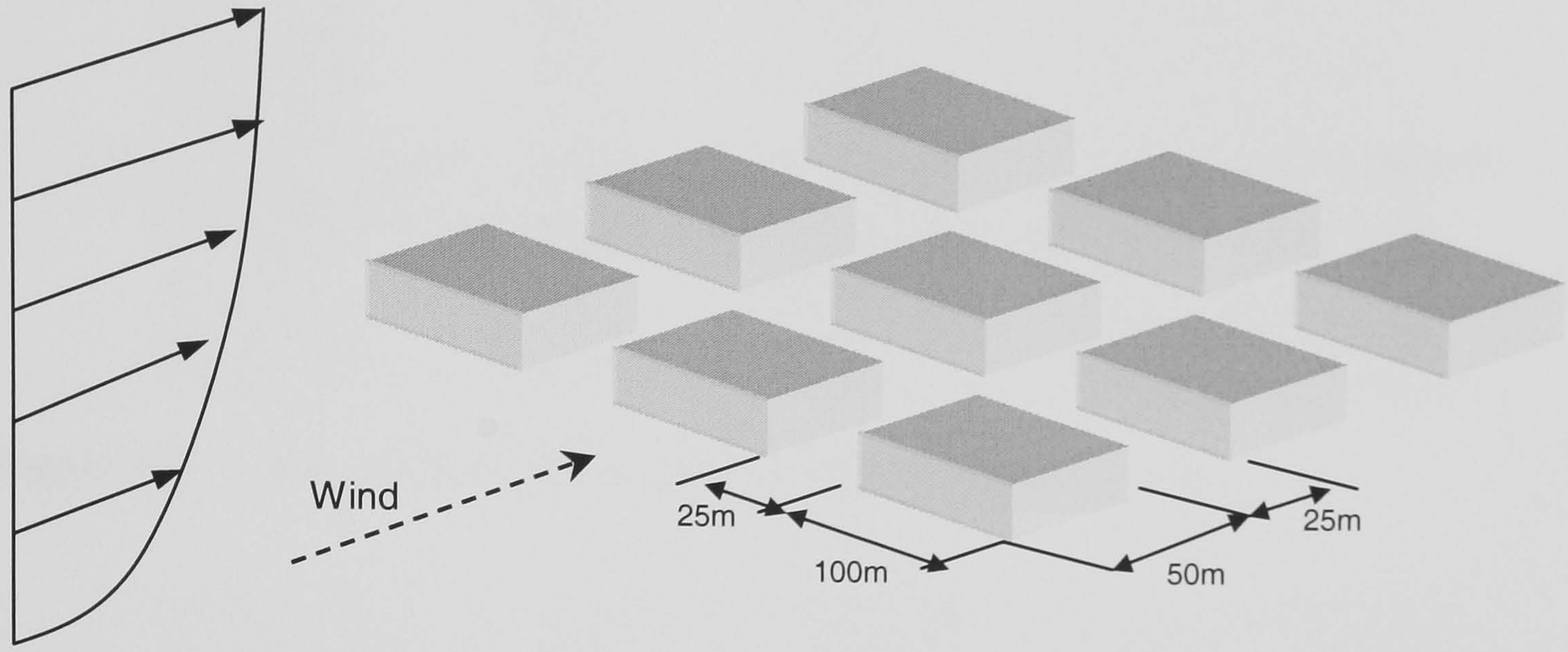

Figure 6.4 The geometry and layout of the model. The street width is 25 m and the dimensions of a block is 100 m × 50 m × 19 m (length × depth × height) in full scale.

The computing domain for the second case was 1.8 m × 0.9 m × 1.0 m (length × width × height) as the direction of approaching wind was normal to the buildings and therefore the horizontal dimension could be reduced to a half by taking advantage of geometric symmetry. The symmetric boundary conditions were applied at the plane of symmetry. It was a favourable approach because the geometry was much more complex and the number of grids could be very large if the full model was simulated. The approaching wind was simulated using a suburban wind profile as described in their paper. The mean wind speed profile was simulated with a power-law model but the exponent was changed to 0.25. The turbulence intensity near the ground was about 25% and it decreased to about 5% at the gradient level. The number of computational grids was 106 × 59 × 35 (streamwise × spanwise × vertical) and the meshing strategy was as the same as aforementioned. The grids and the geometry layout of buildings are shown in figures 6.5-6. The other computational parameters (turbulence model, differencing scheme, linear equation solver) were set as the same as the previous case.

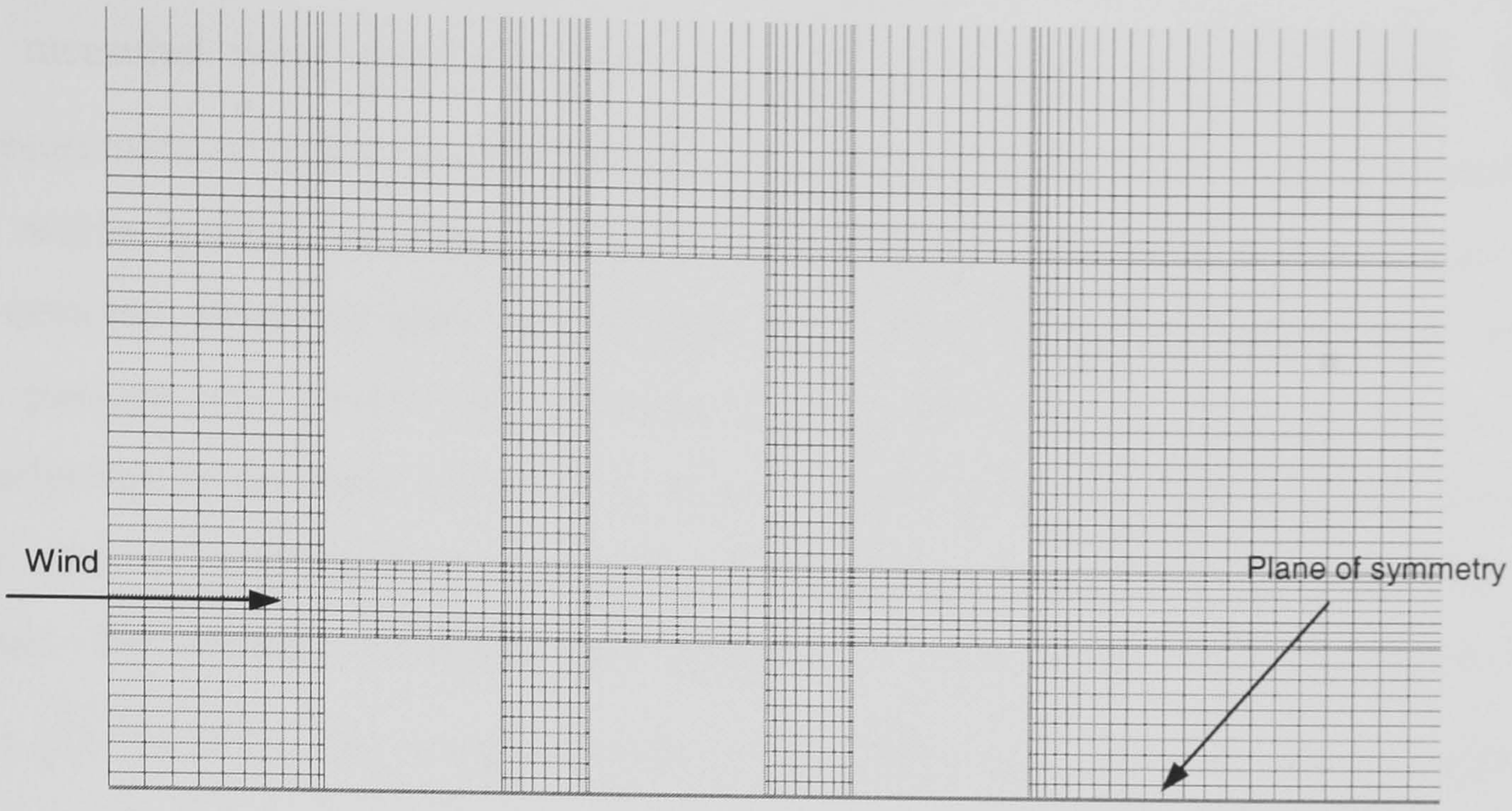

Figure 6.5 The mesh on the horizontal plane for the second case.

Figure 6.6 The mesh on the vertical plane for the second case.

6.2 Results – Pedestrian-level winds in the Passage between Buildings

Since there are two sets of CFD simulations (H : H and H : 3H) for the first case, the results will be presented and discussed separately.

6.2.1 Computation vs. Experiment in the Case of H : H

Stathopoulos and Storms (1986) have measured the wind velocities along the passage at 5 mm (2 m in full scale) above the turntable with a hot-film probe. Since the hot-film probe is omni-directional, the magnitude of velocity measured is the resultant of two velocity components, i.e. U and V or U and W, depending on the orientation of the probe (Cook, 1990). If the probe is oriented vertically, the velocity acquired is the horizontal wind speed $Q_h = \sqrt{(U^2 + V^2)}$, whereas if the probe is horizontally oriented,

the measured wind speed is effectively equal to a speed $Q = \sqrt{(U^2 + W^2)}$. In the measurement of pedestrian-level winds, the common practice is to mount the probe on the nearby building and place the probe vertically so that the horizontal wind speed can be detected. However, they used another approach in the original experiment because the passage was narrow and therefore placing the probe in that way would cause interference to the flow. The alternative was using a traverse to hold the probe and place it at desired locations. In that situation, the probe had to be horizontally oriented. As a result, the velocity measured and presented in their paper was the wind speed $Q = \sqrt{(U^2 + W^2)}$. The wind velocities in the CFD simulation were also calculated in the same manner for comparison. All the values were normalised by a reference wind velocity (V_r), which was the wind velocity at the corresponding locations when the buildings were absent. Figure 6.7 shows the comparison between computation and wind tunnel experiment when the wind direction is parallel with and when the wind angle is 15^o to the centreline of the passage.

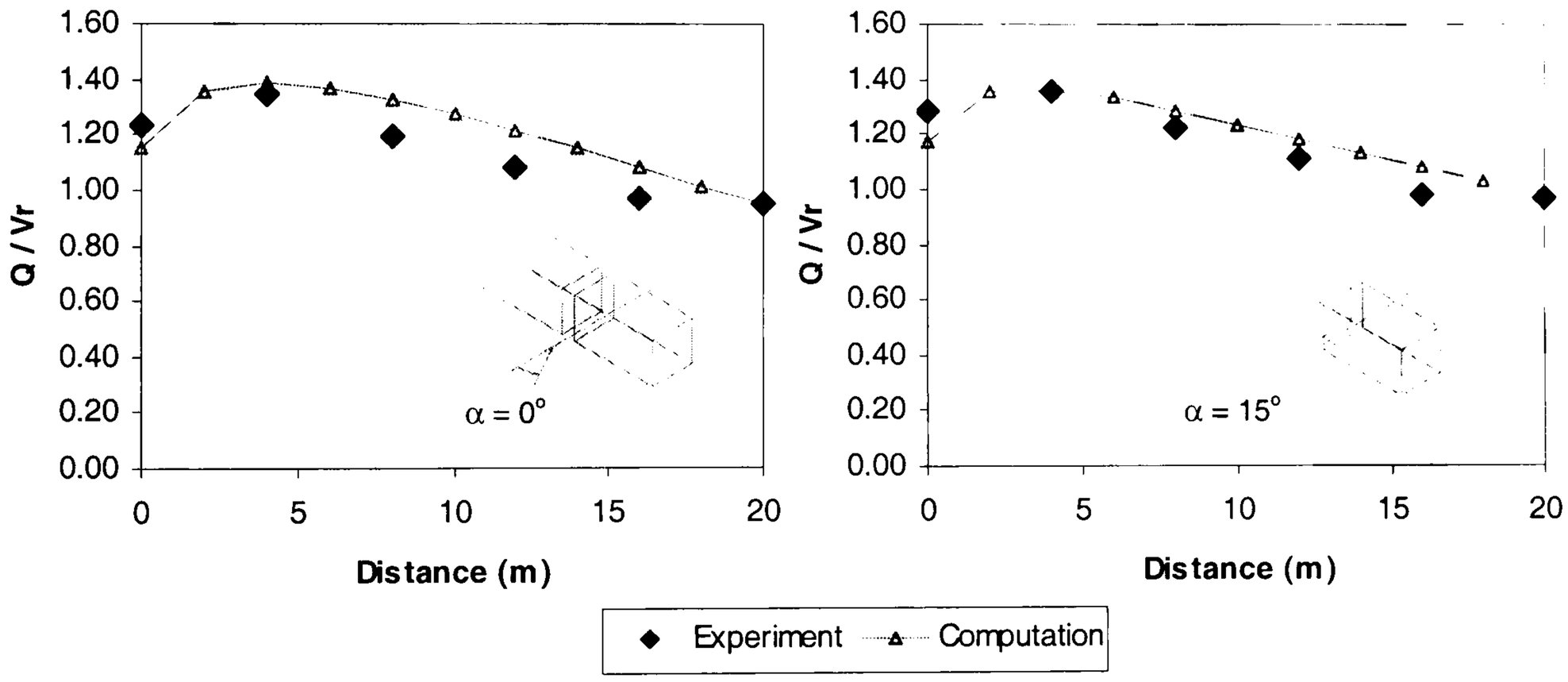

Figure 6.7 The comparison of velocity ratios when the wind angle is 0^o and 15^o; α is the azimuth; Vr is the reference wind velocity and Q is the resultant of velocity components (U and W).

In their experiment, the measured locations are at 0 m, 4 m, 8 m, 12 m, 16 m and 20 m from the entrance and along the centreline of the passage. The experimental data indicate that the wind speed is accelerated near the entrance and gradually decreases till the exit in the two occasions ($\alpha = 0^o$ and 15^o). The amplification of wind speed is about 40% at the location around 4 m and it decreases steadily to approximately equal to the reference wind speed at the exit. The computed values depicted the same trend and the

velocity ratios were very close to the measured values with a discrepancy in a range within 10%.

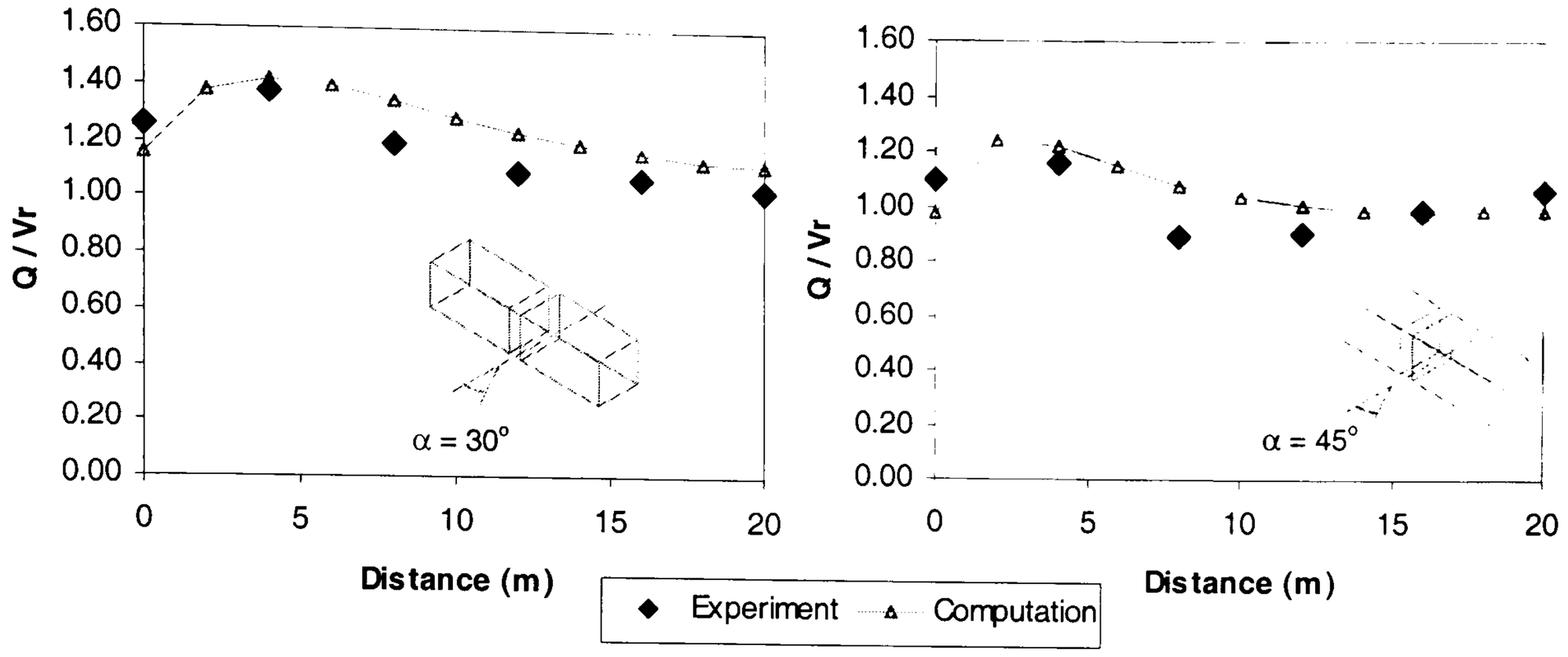

Figure 6.8 The comparison of velocity ratios when the wind angle is 30° and 45°.

When the wind angle is 30°, the maximum amplification of the wind speed indicated by the experimental data is also about 40% and the location where the wind is most likely to be accelerated is still around 4 m from the entrance (figure 6.8). In figure 6.8, it also shows that in the case when the wind angle is 45°, a rather different trend of the wind velocity is present. The experimental data indicate that the wind velocities are slightly lower than 1.0 around the halfway of the passage and the maximum amplification of the wind speed decreases to about 20%. The computed values were still in good agreement with the experimental data but the agreement was slightly less satisfactory when the wind angle was 45°, in which case the maximum discrepancy was 20%.

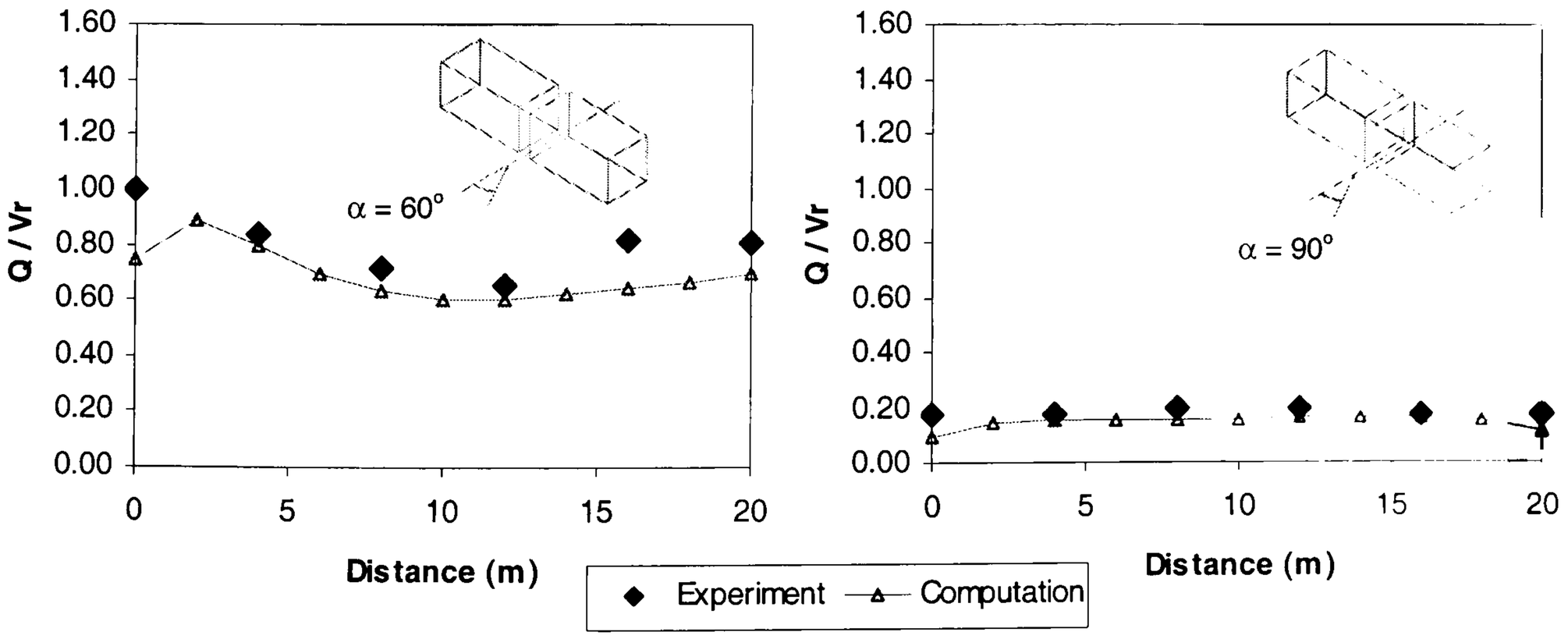

Figure 6.9 The comparison of velocity ratios when the wind angle is 60° and 90°.

With the increment of azimuth, the shelter effects become more evident when the wind angle is highly oblique to the passage. When the wind angle increases to 60°, the experimental data shows that most of the velocity ratios are lower than 1.0 except the measured value at the entrance (figure 6.9). The computed values agreed well with the data in most of the locations though, the agreement was less satisfactory at the entrance of the passage. The maximum discrepancy was 25% in this occasion. However, the velocity ratio at the entrance under this wind condition was likely to be lower than 1.0 because of the wake effects. Increasing the azimuth to 90°, the wind angle becomes orthogonal to the passage. The measured values indicate that the maximum velocity ratio is about 20% of the undisturbed wind speed. The computed values predicted the same trend and the agreement between computation and experiment was satisfactory.

6.2.2 Computation vs. Experiment in the Case of H : 3H

Another investigation of the pedestrian-level wind in the passage was made when one of the two buildings was three times taller than its neighbouring block. Figure 6.10 shows the velocity ratios in the passage when the azimuth is 0° and 15°.

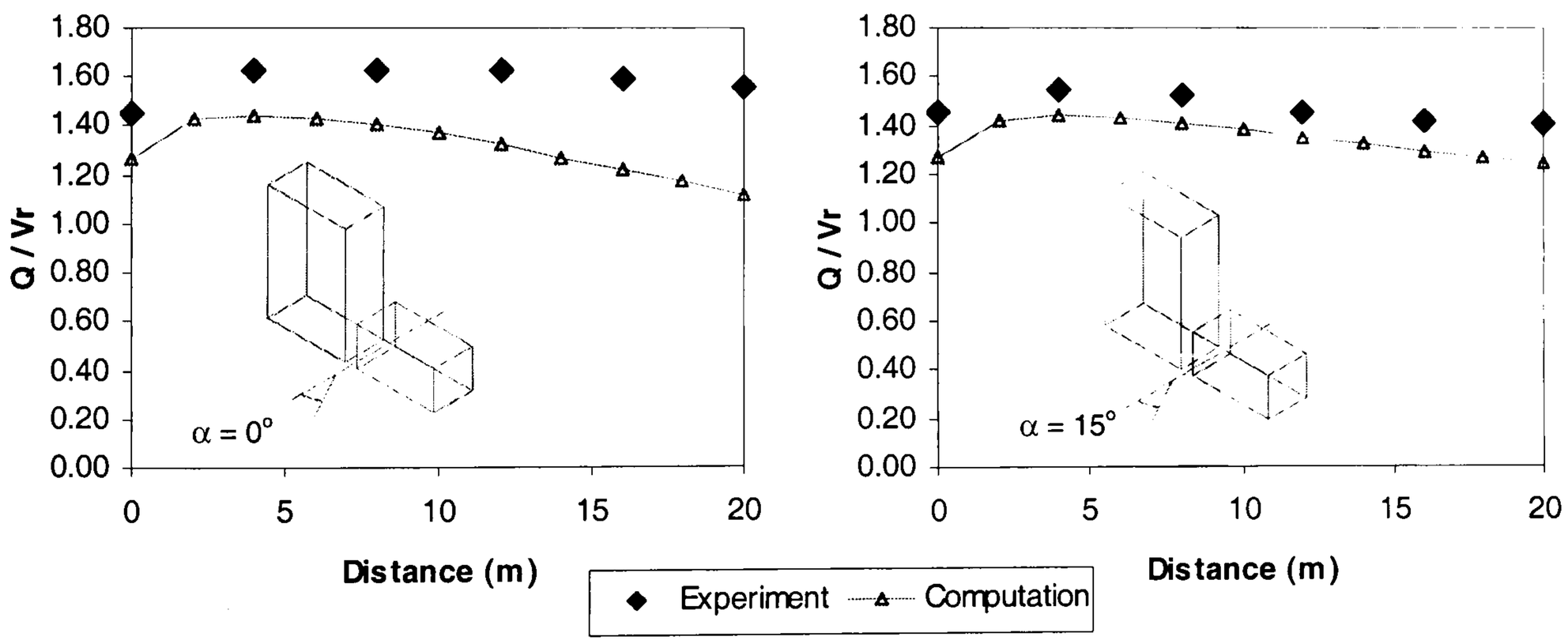

Figure 6.10 The comparison of velocity ratios when the wind angle is 0° and 15°.

The experimental data shows that the wind velocities have been largely accelerated due to the height difference and the maximum amplification of wind speed is 60% when the wind direction is parallel with the passage. The computed values were lower than the experimental data and the error percentage was between 11% and 26%. The discrepancies were larger in the locations between 10 m and 20 m from the entrance. A possible explanation was that there might be stronger downwash and reverse or

recirculating flows in that area because the hot-film probe was likely to report a higher velocity if the reverse flows were strong enough to make contributions. When the azimuth = 15°, the experimental data shows that the maximum amplification of wind speed is 55% at a distance around 5 m from the entrance. The computation predicted a similar trend with small discrepancies. The error percentage was in a range between 7% and 14%. The predicted values agreed favourably with the measurement.

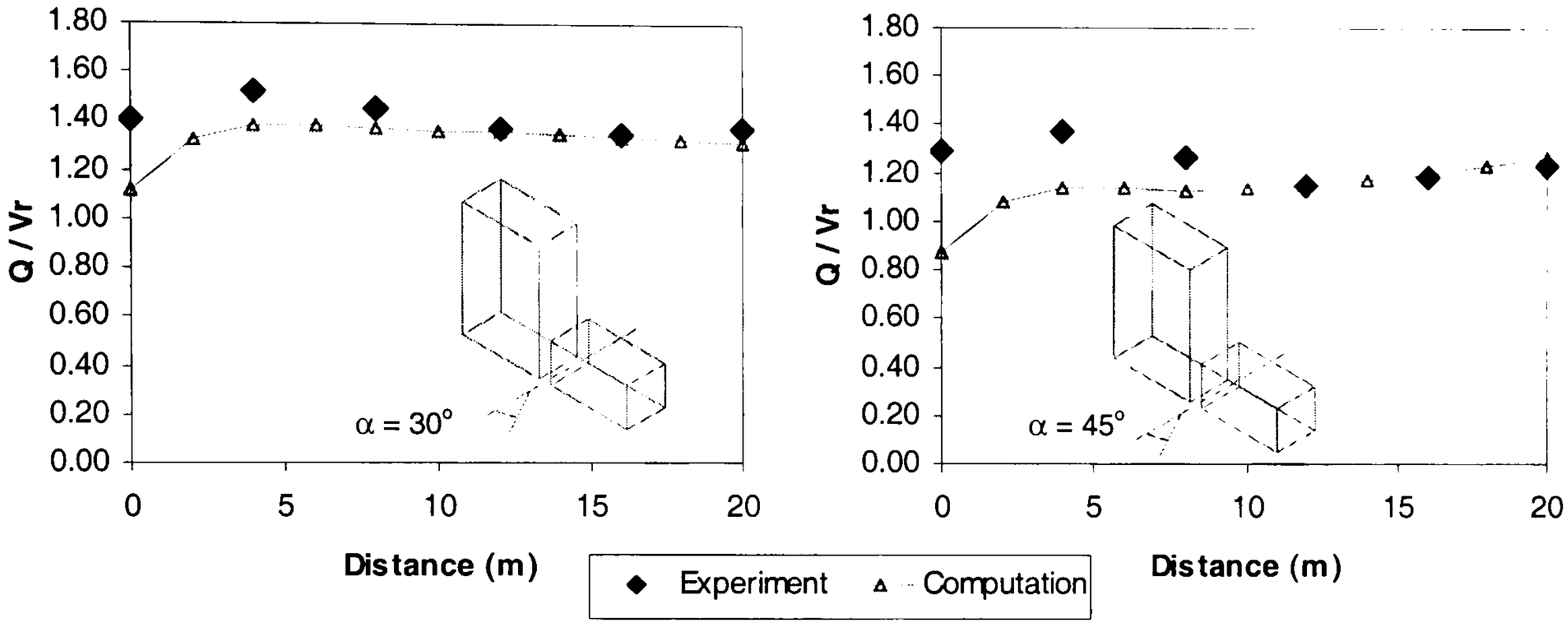

Figure 6.11 The comparison of velocity ratios when the wind angle is 30° and 45°.

In the cases when the azimuth = 30° and 45° (figure 6.11), the experimental data indicate that most of the velocity ratios are still greater than 1.0, implying the tall building can still cause acceleration of wind speed even when the wind direction is relatively oblique to the passage. The amplifications of wind speeds became lower due to the weakened flows in the wake but the strength of the downwash flows from the tall building was likely to increase. The computations predicted similar trends in both cases but the agreement was less satisfactory in the range between 0 m and 10 m from the entrance of the passage. The maximum discrepancy was 20% in the case when the wind angle was 30° and it increased to 32% when the wind direction was 45° obliquely to the passage. Apart from that, the agreement between the computation and experiment was good.

When the wind angle becomes 60°, the experimental data indicate that the wind velocity is as strong as the reference wind speed and it decreases gradually and reaches a lowest value at the location around 8 m from the entrance and, subsequently the wind velocity increases more rapidly till the exit of the passage (figure 6.12). The computation depicted the same trend except at the location near the entrance. The maximum

discrepancy was 46% in this case. It was also possible that the velocity detected by the probe was higher than actual wind speed in the vicinity of the entrance due to recirculating flows. When the wind direction is orthogonal to the passage, the experimental data indicate that the wind speed is about 50% of the reference wind velocity in the middle of the passage and the velocity ratio increases to 1.08 at the locations near the entrance and the exit. The computation predicted the same trend with an error percentage between 12% and 41%. The large discrepancy found in this case was also likely due to that the strong downwash flows "overlapped" the response of the probe; therefore the value detected by the probe was likely to be higher.

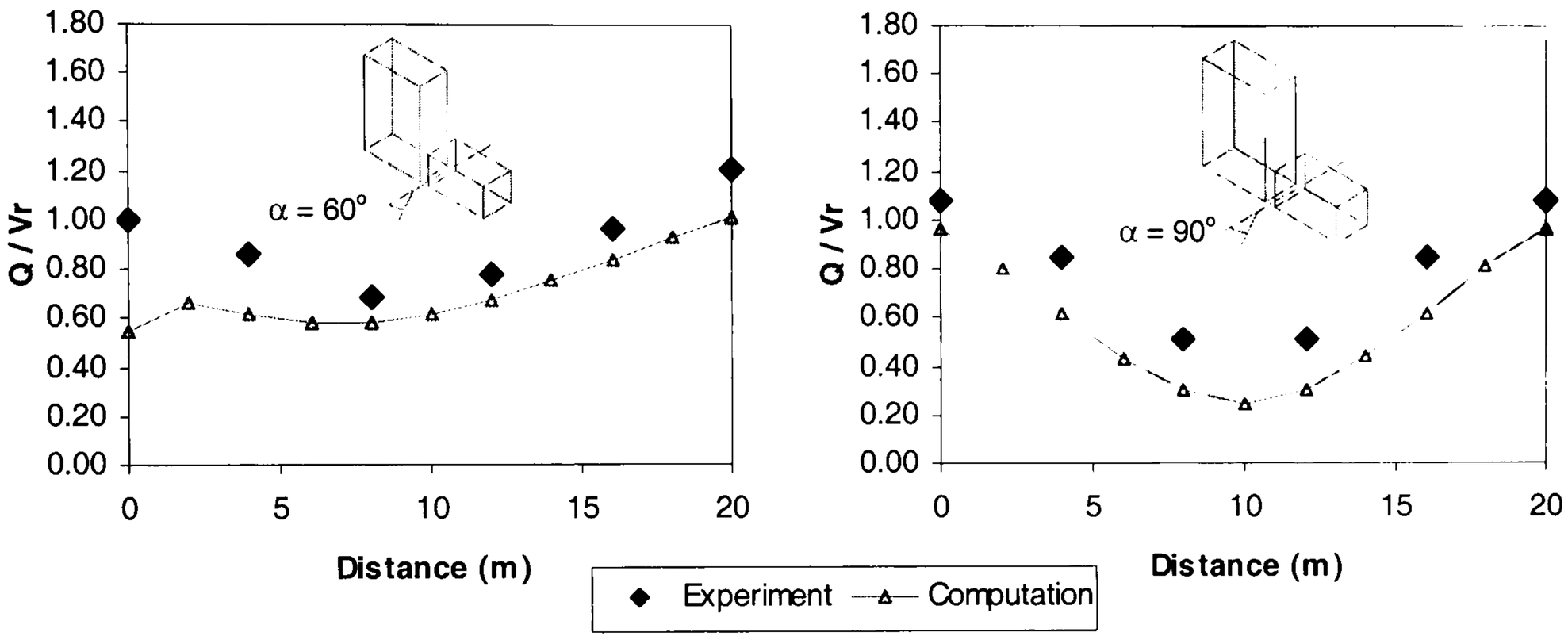

Figure 6.12 The comparison of velocity ratios when the wind angle is 60^{o} and 90^{o}.

As a conclusion, in the case when there is a height difference between two buildings, the results of computation and experiment agreed less satisfactory but the general trend of the wind speed predicted by CFD was correct.

7.2.3 Comparison of Turbulence Intensities

The turbulence intensity is another key factor affecting pedestrian comfort in the evaluation of street-level winds. Since the computation was a steady-state numerical simulation and the turbulence model used was a RANS model, the turbulence statistics obtained from this approach was also a time-independent value. The turbulence energy (KE) is the product of averaged fluctuating velocities, i.e. root-mean-square (r.m.s.) value. The turbulence energy (per unit mass) is defined as

$$KE = \frac{1}{2}(\overline{u'^2} + \overline{v'^2} + \overline{w'^2}) \tag{6.1}$$

It is a scalar and it measures the kinetic energy contributed by the fluctuating components. The r.m.s. value can be estimated by

$$V_{rms} = \sqrt{KE} \tag{6.2}$$

where V_{rms} is the r.m.s wind speed. With the V_{rms} determined, the turbulence intensity can be calculated from

$$T.I. = \frac{V_{rms}}{V} \tag{6.3}$$

where V is the mean wind speed at a specific location. $T.I.$ is a dimensionless quantity indicating the scale of turbulence. Figure 6.13 shows the variations of the turbulence intensities in the passage due to the change of wind directions.

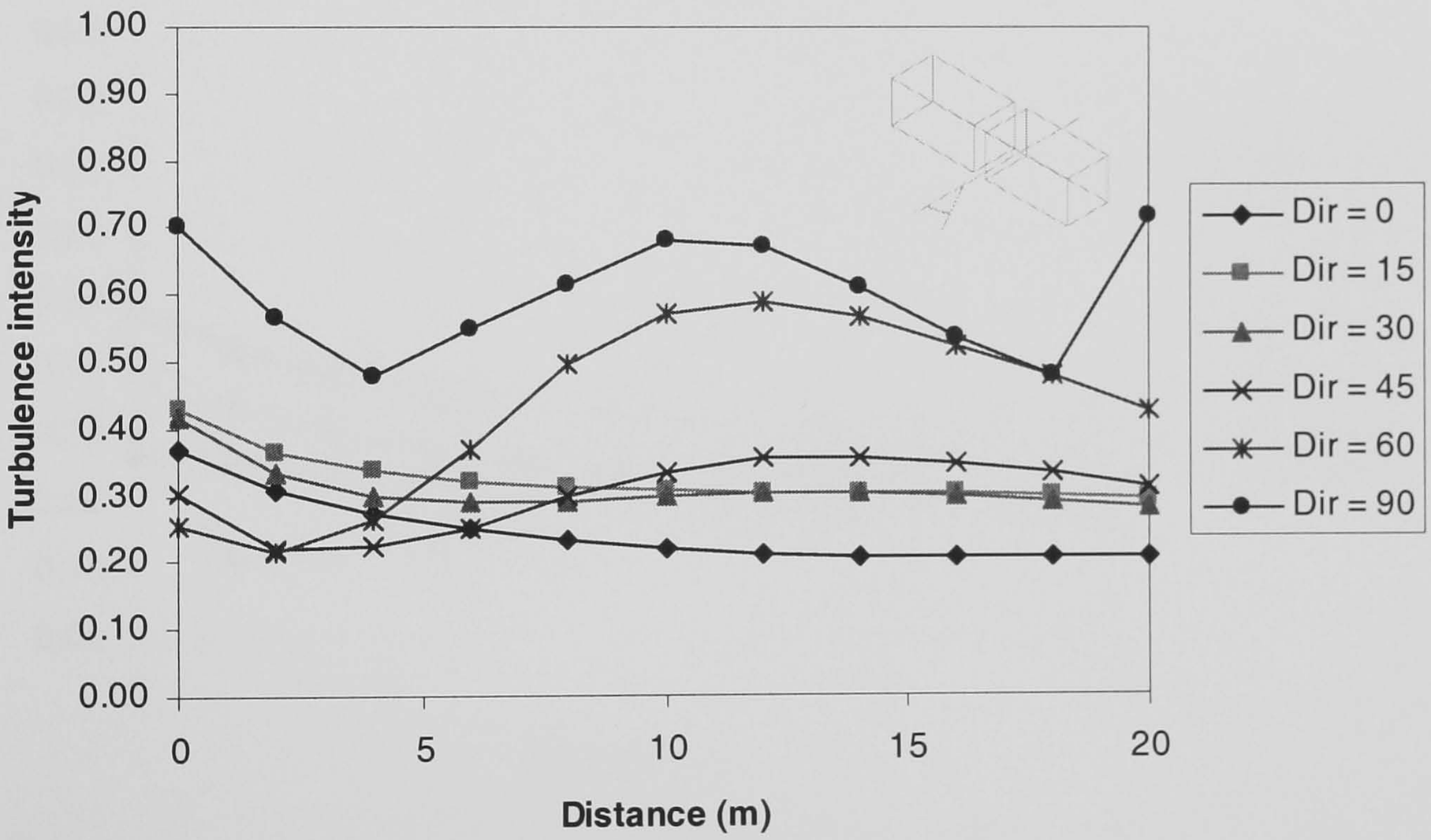

Figure 6.13 The comparison of turbulence intensities under different wind directions when the two buildings are with the same height.

In the case when the wind direction was parallel to the passage, the maximum intensity of turbulence was 37% at the entrance. The intensity of turbulence gradually decreased till the exit where the value was about 20%. The variation of the turbulence intensity was smooth. When the azimuth = 15°, the turbulence intensity was higher than the case of azimuth = 0° throughout the passage. The maximum value was 43% at the entrance and it slowly decreased to 28% at the exit. The variation of the turbulence intensity in the case when azimuth = 30° was very similar to the trend delineated by the curve for

the case when the wind angle = 15° whilst the turbulence intensity was slightly lower in the locations between 0 m and 8 m from the entrance. Increasing the azimuth to 45°, a different trend was observed; the value was 30% at the entrance and subsequently it decreased to 21% at a distance 2 m from the entrance and, the value increased again afterwards to 35% at 12 m and it decreased again slowly till the exit. A similar trend but with more noticeable variations, was delineated by the curve for the case when the azimuth = 60°, where the peak value was 59% at a distance 12 m from the entrance. In the case when the wind direction was orthogonal to the passage, the curve of turbulence intensity delineated a trend like "W". Three peak points were found – at the entrance, the middle and the exit. The values of those peak points were all about 70%. Though the mean wind velocities in the passage were low in the passage (figure 6.9), the scale of turbulence was likely to be very significant in this case.

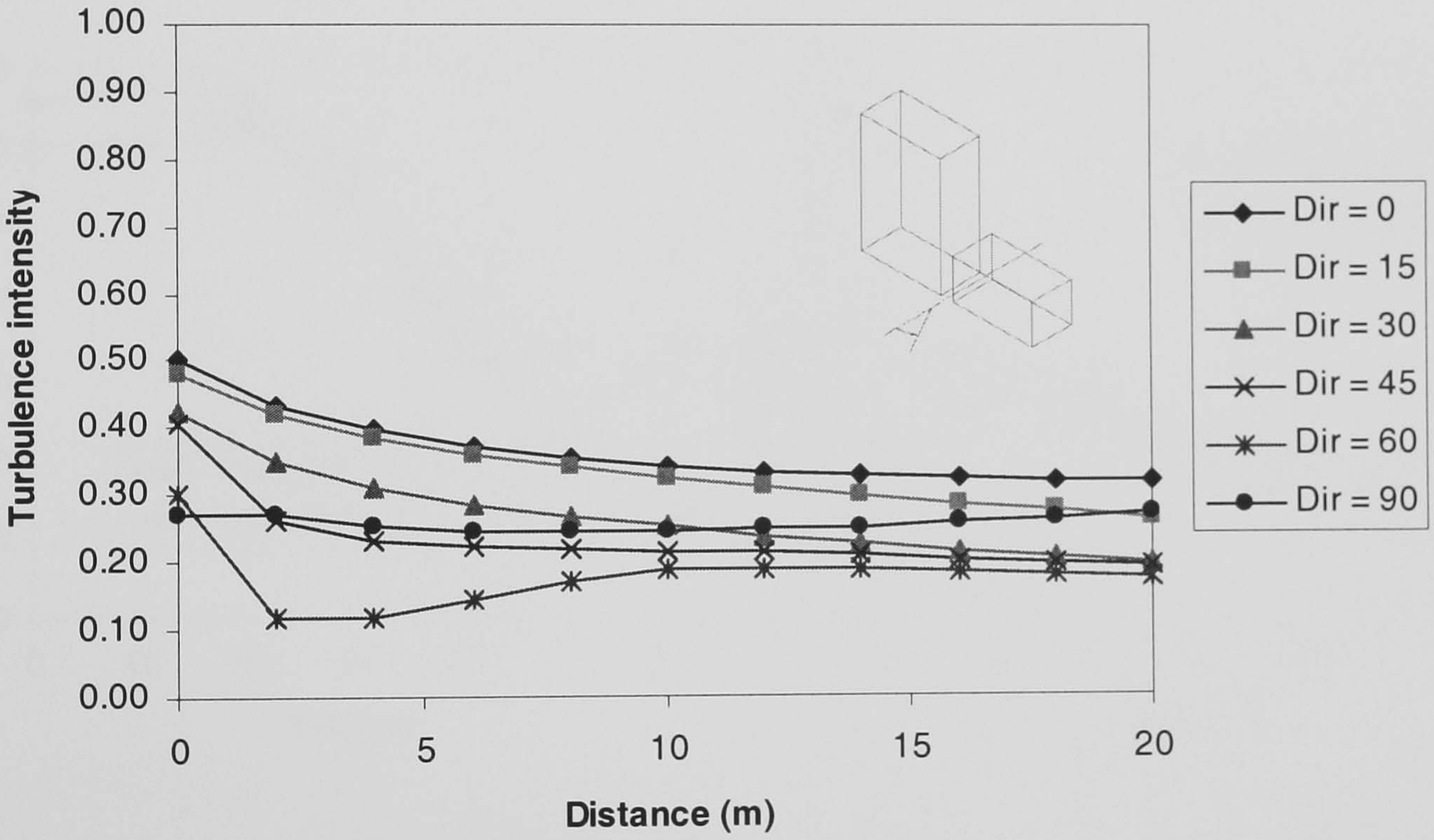

Figure 6.14 The comparison of turbulence intensities under different wind directions when there is a height difference (H : 3H) between two buildings.

Figure 6.14 shows the curves of turbulence intensity obtained from the computation for the case of H : 3H under various wind incidents. These curves were somewhat different from the previous case and, interestingly the highest value of the turbulence intensity was present when the wind angle was 0°. The overall turbulence intensity was the highest in all of the wind incidents simulated. The maximum value was 50% at the entrance and it slowly decreased to 32% at the exit. The curve for azimuth = 15° was very close to the curve for azimuth = 0° but the intensity of turbulence was slightly lower, which was about 26% at the exit. In the case when azimuth = 30°, the curve of

turbulence intensity departed significantly from the previous two curves; it was 40% at the entrance and 20% at the exit, though its slope and curvature was still analogous to the curve for azimuth = 15°. When the wind angle was 45°, the curve of turbulence intensity indicated a different trend; it was 40% at the entrance but it dropped sharply to 26% within 2 m and subsequently the turbulence intensity decreased smoothly till the exit where it became 19%. The trend of turbulence intensity changed more drastically when the wind angle became 60°. The turbulence intensity was 30% at the entrance but it dropped quickly to 12% within 2 m and subsequently it increased to 19% at a distance of 10 m, then the value steadily decreased to 17% at the exit. In the case when the wind direction was orthogonal to the passage, the curve of turbulence intensity presented a very different trend. It was very smooth without noticeable variations. The turbulence intensity was about 27% in average throughout the passage.

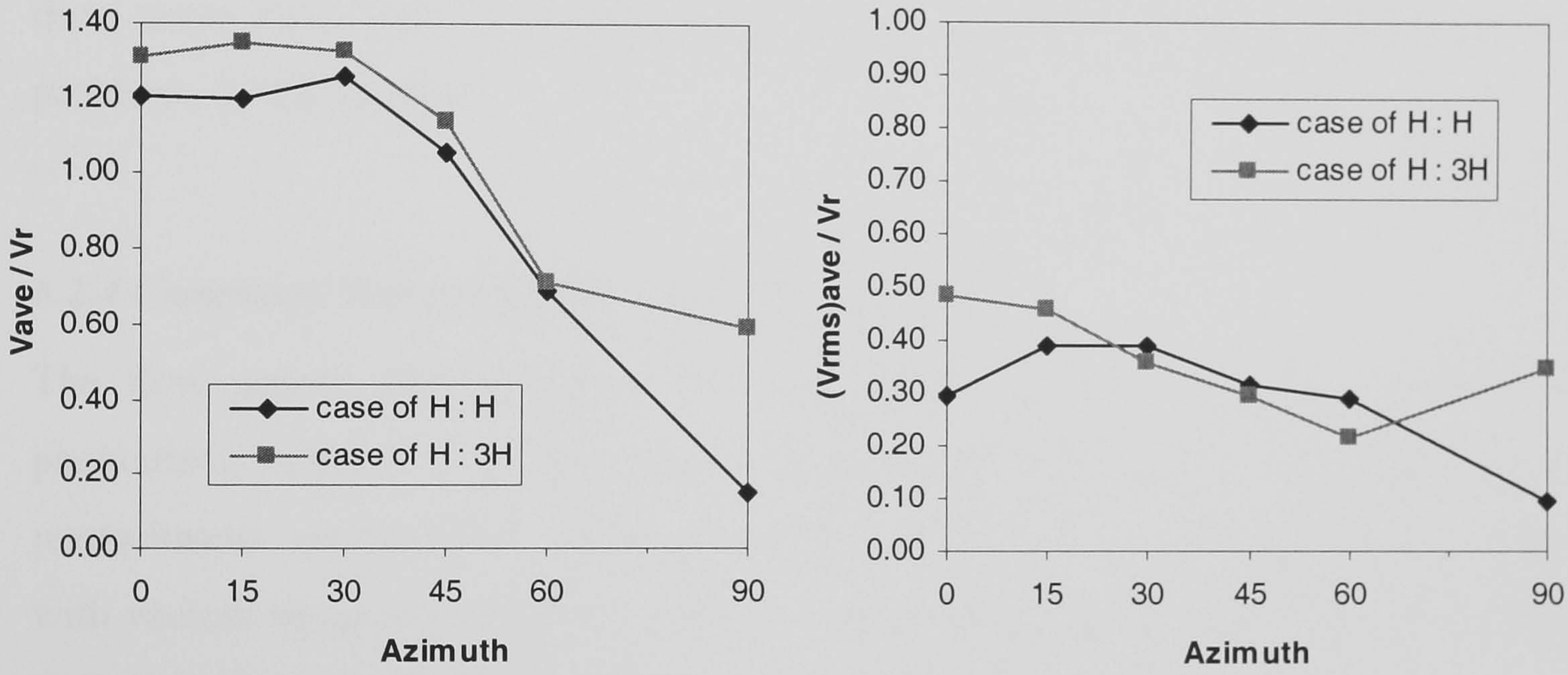

Figure 6.15 The amplification of averaged mean wind velocities and the averaged scale of turbulence under different wind angles.

The implications of changing wind angles and building height to the street-level wind in the passage were further examined by comparing the averaged amplification ratios and turbulence scales. The averaged wind velocity (V_{ave}) was normalised with the same reference wind velocity (V_r) and the $(V_{rms})_{ave}$ was also expressed as a ratio of the reference wind velocity (figure 6.15). The meaning of the ratio $(V_{rms})_{ave}$ / V_r was analogous to turbulence intensity. As V_r was a constant when the buildings were absent, the ratio $(V_{rms})_{ave}$ / V_r implied a scale of turbulence that was only affected by the magnitude of V_{rms}.

Results indicated that increasing the height of a building to three times taller than its neighbouring building also magnified the mean wind speed in the passage under all the wind incidents tested. The amplification of wind speed was very significant when the wind direction was orthogonal to the centreline of the passage. In the case of azimuth = 90^{o}, the mean wind speed was 320% stronger and the amplification of turbulence scale was 270%. The second noticeable case was when the wind direction was parallel with the passage in which the averaged mean wind speed was 10% higher and the scale of turbulence was 65% stronger. In the case when wind angle = 15^{o}, the mean wind speed was 13% higher but the amplification of turbulence scale was reduced to 25%. In other cases (azimuth = 30^{o}, 45^{o}, 60^{o}), the accelerations of mean wind speeds were not considerably large and the scales of turbulence decreased slightly. From figure 6.15 and the comparison, the investigation concluded an interesting finding: if the prevailing wind direction was oblique to the passage within the range $30^{o} - 60^{o}$, erecting a building three times taller than its neighbouring building was less likely to cause severe wind problems in this passage.

6.2.4 Computed Vector Field for the Case of H : H

The flow pattern obtained from the computation revealed a number of interesting phenomena (figures 6.16-21). These phenomena comprised flow separation and reattachment, recirculation, acceleration and deceleration. The flow pattern is plotted with vectors because the vector field also contains the information about wind velocity, as the length of vector implies the relative magnitude of wind speed.

Figure 6.16 shows the vector fields for the cases of wind angles equal to 0^{o} and 15^{0}, respectively. The vectors were "squeezed" into the passage and the lengths of vectors in the passage were longer compared to the vector in freestream, indicating the wind velocity was accelerated in close proximity to the entrance. Eddies formed by swirling flows (A, B, C, D) were found near the corners of buildings and flow separations (E, F) were observed in the case when wind direction was parallel with the passage. Reverse flows were found at the windward sides of two buildings and two stagnation points (S1, S2) were observed. The flow pattern was symmetric in this case. When the wind angle was 15^{o}, the eddy "A" and the flow separation "F" were disappeared. Eddy "B" moved and changed its orientation and eddy "C" became smaller with an orientation akin to eddy "B". The stagnation points "S1" and "S2" moved and the flow separation "E"

started to form a vortex in the wake. The vectors in the passage were slightly twisted by the oblique wind and the wind velocities were still relatively strong in this case.

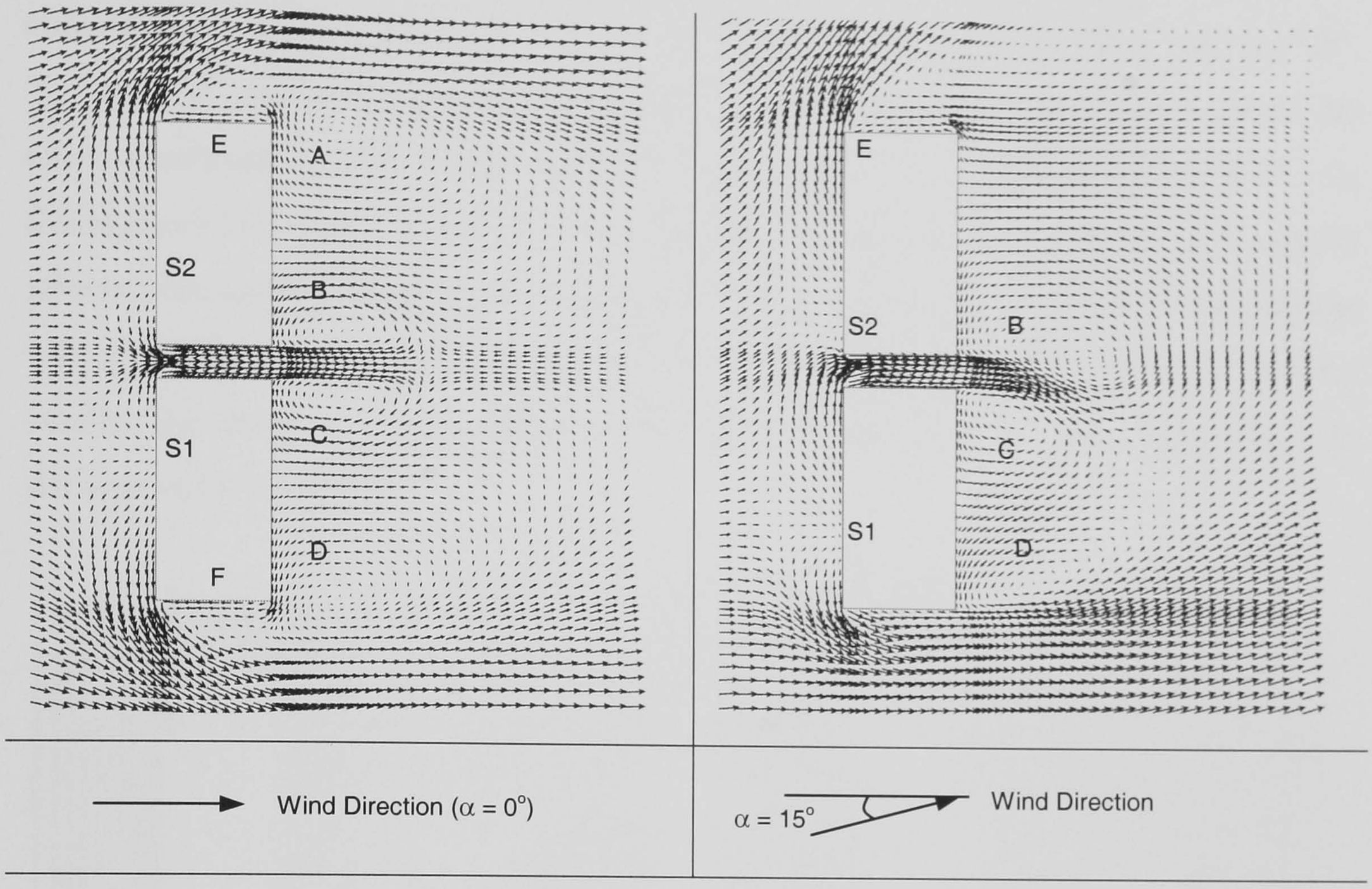

Figure 6.16 Vector fields – azimuth = 0° and 15° (H : H)

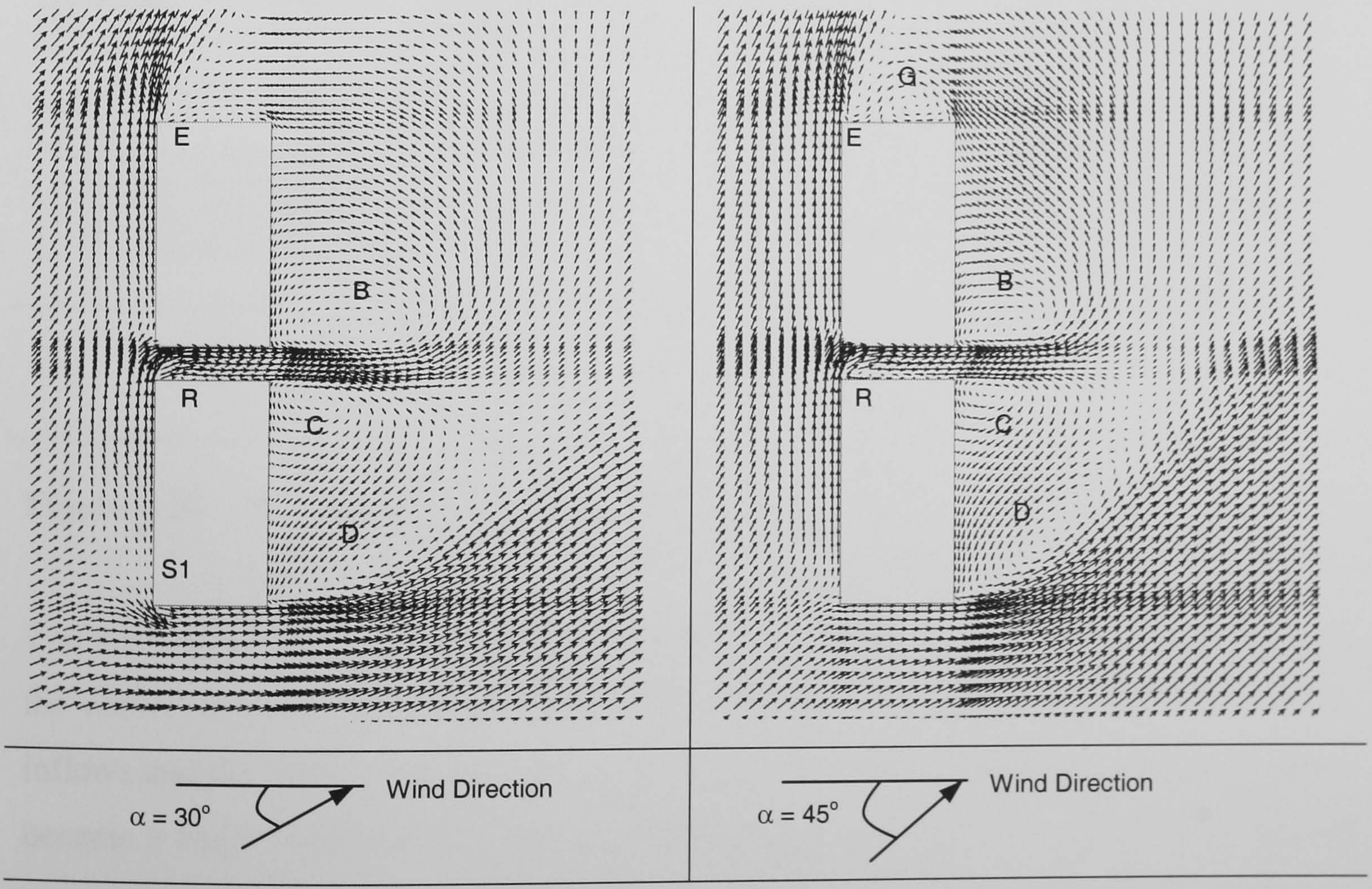

Figure 6.17 Vector fields – azimuth = 30° and 45° (H : H)

In the case when the azimuth became 30°, the stagnation point "S2" was gone but "S1" was still visible and the vortex "E" was formed. Some reverse flows "R" were found in the passage and the interaction between the inward flows and the reverse flows at the entrance inclined to generate a new vortex (figure 6.17). The other flow features "B", "C" and "D" did not present very dissimilar trends if compared with figure 6.16 (in the case of azimuth = 15°). When the wind angle = 45°, the stagnation point "S1" was disappeared but a new vortex "G" was formed. The formation of vortex "G" slightly affected the size and orientation of vortex "E". The vortex at the entrance of the passage was gradually formed with the reverse flows "R". Eddy "B" and Eddy "C" became smaller but they were still visible. Eddy "D" became a larger vortex surrounded by stronger velocity vectors.

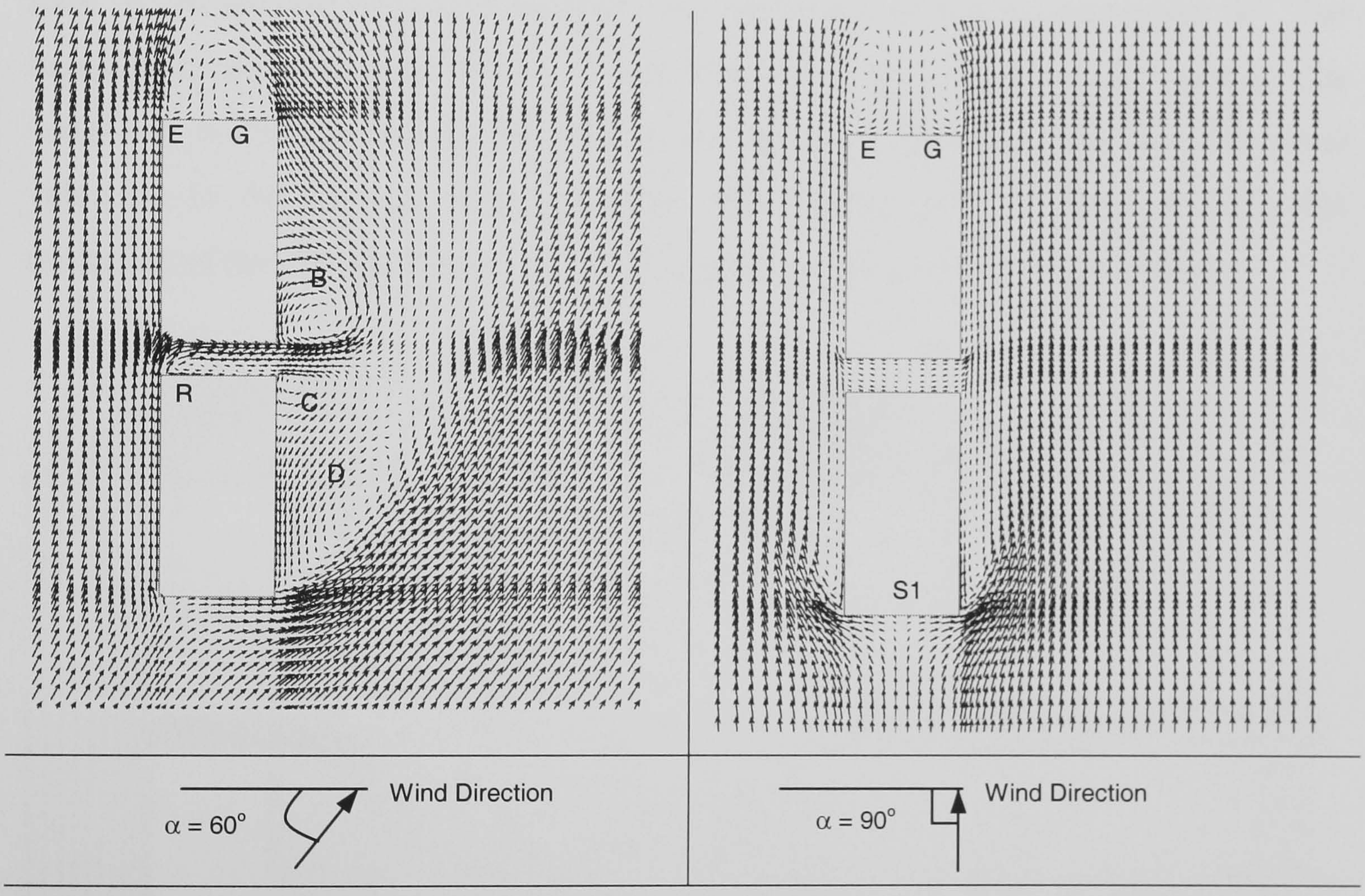

Figure 6.18 Vector fields – azimuth = 60° and 90° (H : H)

The velocity vectors were weaker in the passage when the wind angle became 60° and the vortex "R" near the entrance was formed (figure 6.18). The interaction between the inflows and the vortex weakened the velocity field in the passage. Eddy "G" in the wake became a major vortex and its size was nearly two times of eddy "E". Vortex "B" and vortex "D" increased their strength but vortex "C" became very small and it was hardly discernible. When the wind direction was orthogonal to the passage, the wind velocities in the passage was very low, implied by the weak vectors. The eddies "B", "C" and "D"

were all vanished in this wind incident. A stagnation point "S1" was found at the windward side of the building. Vortex "E" and vortex "G" became a pair of symmetric eddies in the wake.

6.2.5 Computed Vector Field for the Case of H : 3H

The flow patterns for the case of H : 3H under various wind incidents exhibit very different pictures (figure 6.19-21). Since there was a height difference between two buildings, the flow pattern was irregular and no longer symmetric, even when the wind direction was parallel with the passage. Three eddies – "B", "C" and "D" were found in the wake of low-rise building when the wind angle was 0^{o} (figure 6.19). There was one stagnation point – "S1" at the windward side of the tall building. The flow separation zone "E" on the side of the tall building was slightly larger than its counterpart "F". The flow separation zone generated by the tall buildings at the entrance of the passage was wider and it also affected the distribution of velocity vectors in the passage. The wind velocities in the passage were strong but the strongest vectors were not along the centreline of the passage but along the line slightly closer to the low-rise building.

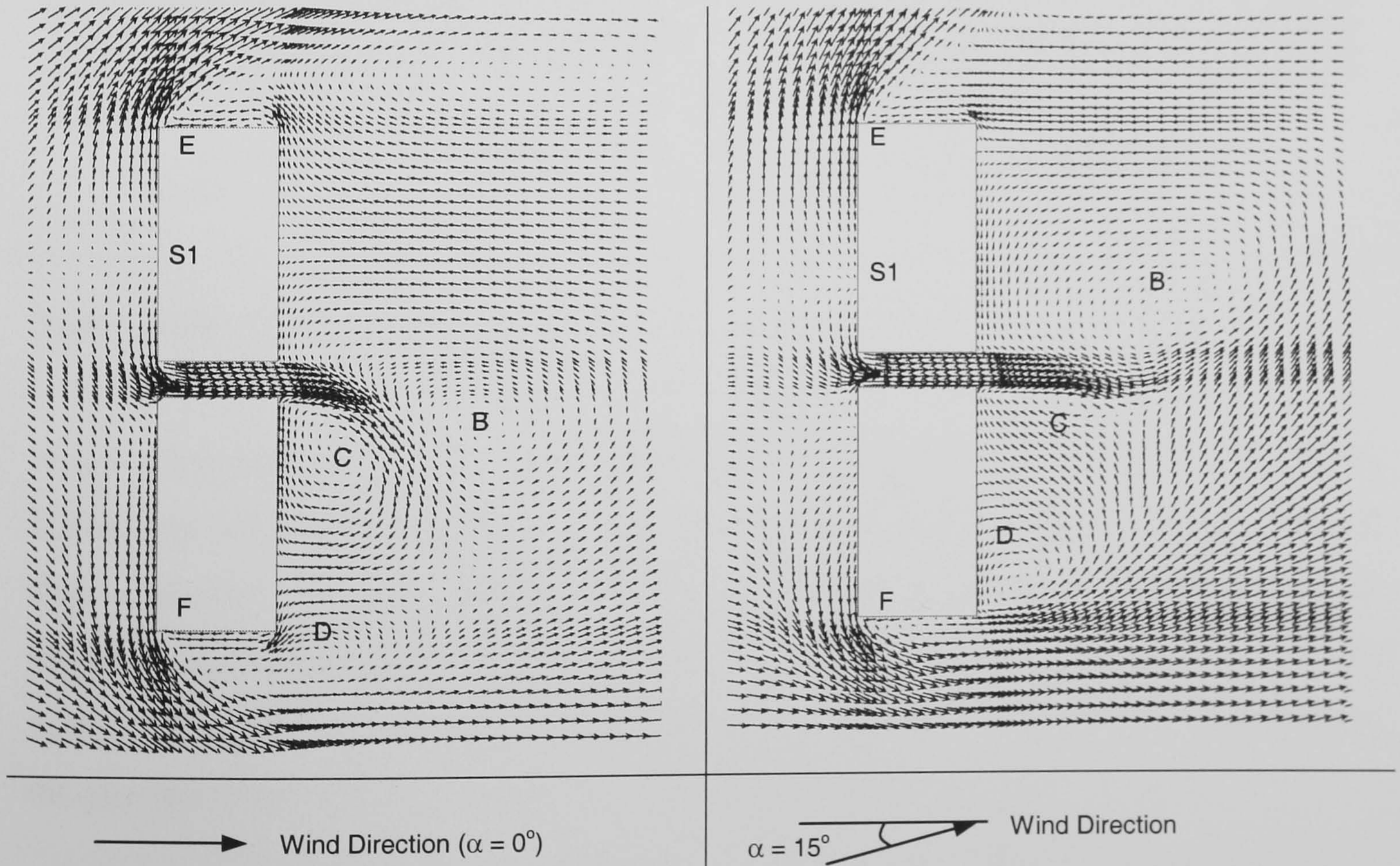

Figure 6.19 Vector fields – azimuth = 0^{o} and 15^{o} (H : 3H)

When the wind angle became 15°, the stagnation point "S1" moved slightly towards the passage and the eddy "C" became hardily discernible. The vortex "B" moved into the wake of the tall building and its size was larger and the vortex "D" changed its position and orientation. The flow separation zone "F" became smaller and a vortex at "E" started to appear. The vectors in the passage indicated the wind velocities were accelerated and the amplification was noticeable at the entrance. The overall wind velocities in the passage were relatively high in this case.

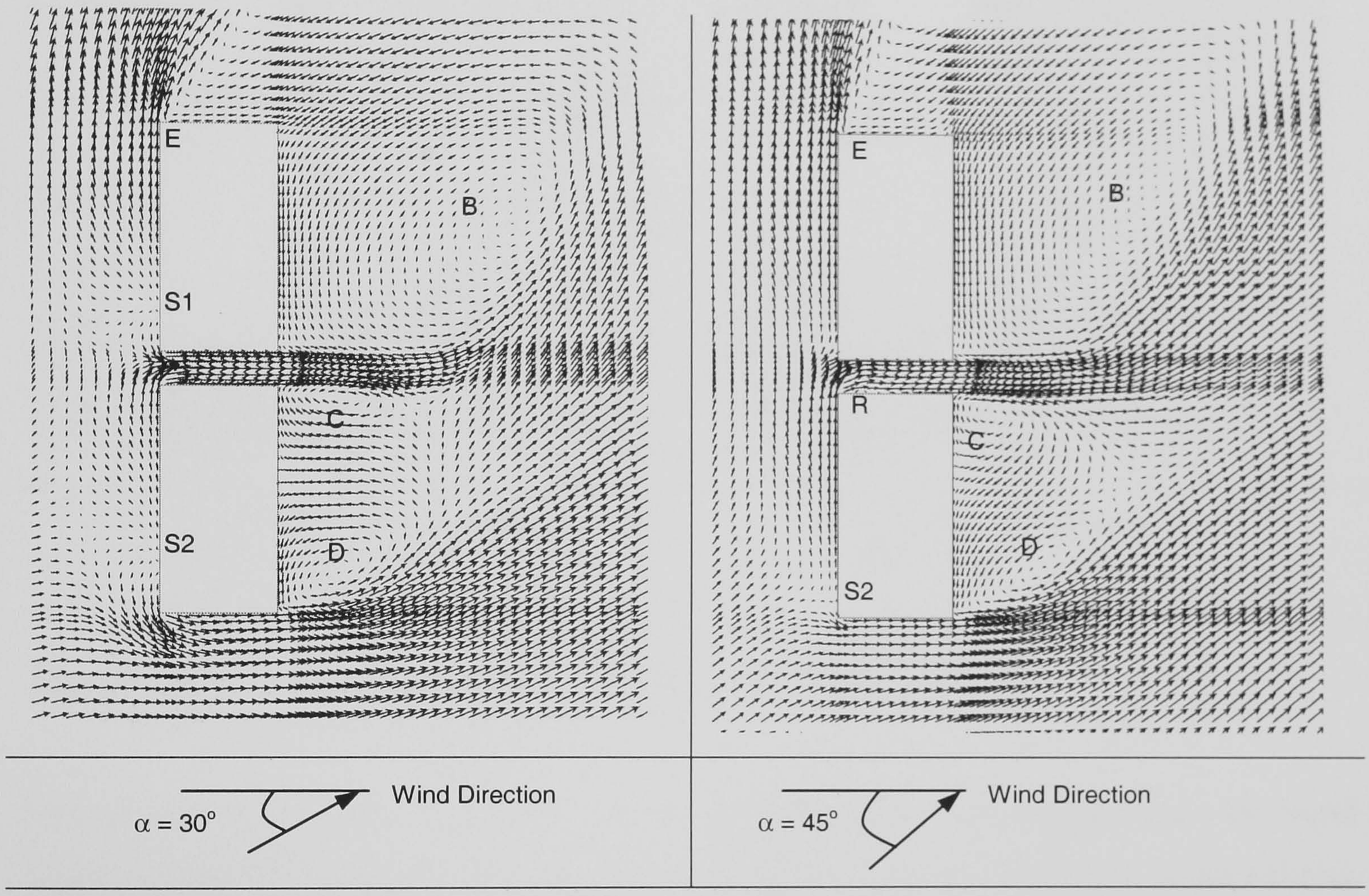

Figure 6.20 Vector fields – azimuth = 30° and 45° (H : 3H)

A new stagnation point "S2" was observed and the stagnation point "S1" moved slightly further towards the passage when the wind angle became 30° (figure 6.20). The zone of flow separation "F" was vanished in this wind incident. The core of vortex "B" moved slightly farther away but it was still in the wake of tall building. The vortex "C" and vortex "D" were more obvious and the vortex "E" was formed. The wind velocities in the passage were still amplified but the magnitudes were weaker.

The reverse flows "R" were present and a vortex was forming at the entrance of the passage when the azimuth = 45°. The stagnation point "S1" was disappeared and the point "S2" moved to the corner of the low-rise building. The vortex "E" became a large eddy at the corner of the tall building. The vortex "B" slightly changed its position but it

was still the only vortex in the wake of the tall building. The connection between vortex "C" and "D" became noticeable. The wind velocities in the passage were relatively weaker due to the interactions between the inflows and the reverse flows.

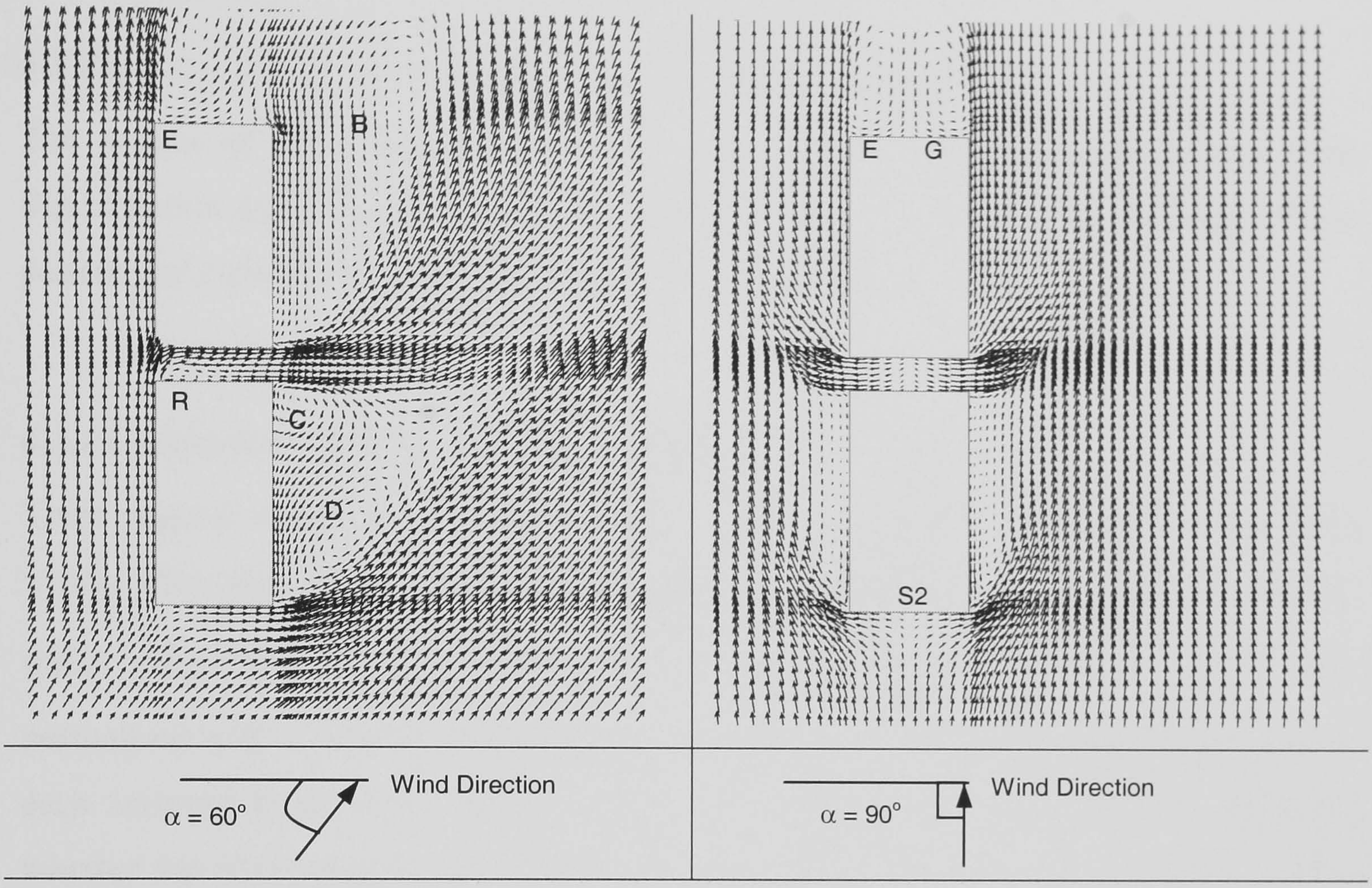

Figure 6.21 Vector fields – azimuth = 60° and 90° (H : 3H)

The reverse flows formed a vortex "R" at the entrance of the passage when the wind angle became 60° (figure 6.21). The vortex weakened the wind velocities in the vicinity of it and the overall wind speeds in the passage were lower. The vortex "B" became highly twisted in this wind incident. The vortex "D" suppressed the growth of vortex "C" ant the vortex "C" was vanishing. The vortex "E" became a major vortex at the leeward side of the tall building.

When the wind direction was orthogonal to the passage, the vortices – "B", "C" and "D" were gone and a pair of vortices – "E" and "G" was formed and, the stagnation point "S2" was present again. Large separation zones on the two sides of the low-rise building were observed. The wind velocities in the passage were strong at the entrance and the exit of the passage, since the tall building diverted the incoming flows into the passage and consequently the wind pressure in the middle of the passage was high (low wind speed) but the wind pressure near the two ends of the passage was low (high wind speed).

Observing figures 6.19-21, an interesting finding was that the larger eddies were likely associated with the tall building, whereas the smaller vortices were usually induced by the low-rise building under these wind incidents.

6.3 Results – Street Level Winds Around a Group of Buildings

The results of computation are to be compared with the experimental data from Stathopoulos and Wu (1995). In addition, some other computational outcomes (flow pattern and turbulence intensity) will be presented and discussed.

6.3.1 Comparison of Wind Speeds – Computation vs. Experiment

Their original wind tunnel test selected 37 points for the measurements of street-level winds. They used Irwin sensor to measure the wind velocity at a height of 2 m (in full scale) above ground level. The measured velocities $Q_h = \sqrt{(U^2 + V^2)}$ have been normalised with a reference velocity (V_r), which is the corresponding wind velocity at each selected point when all the buildings are absent. The velocity ratio indicates whether the wind speed is accelerated (greater than 1.0) or weakened (less than 1.0) by the presence of buildings. The relative locations of these points are shown as figure 6.22 in which all the points are classified with lines (L1 – L6) to assist the task of comparison.

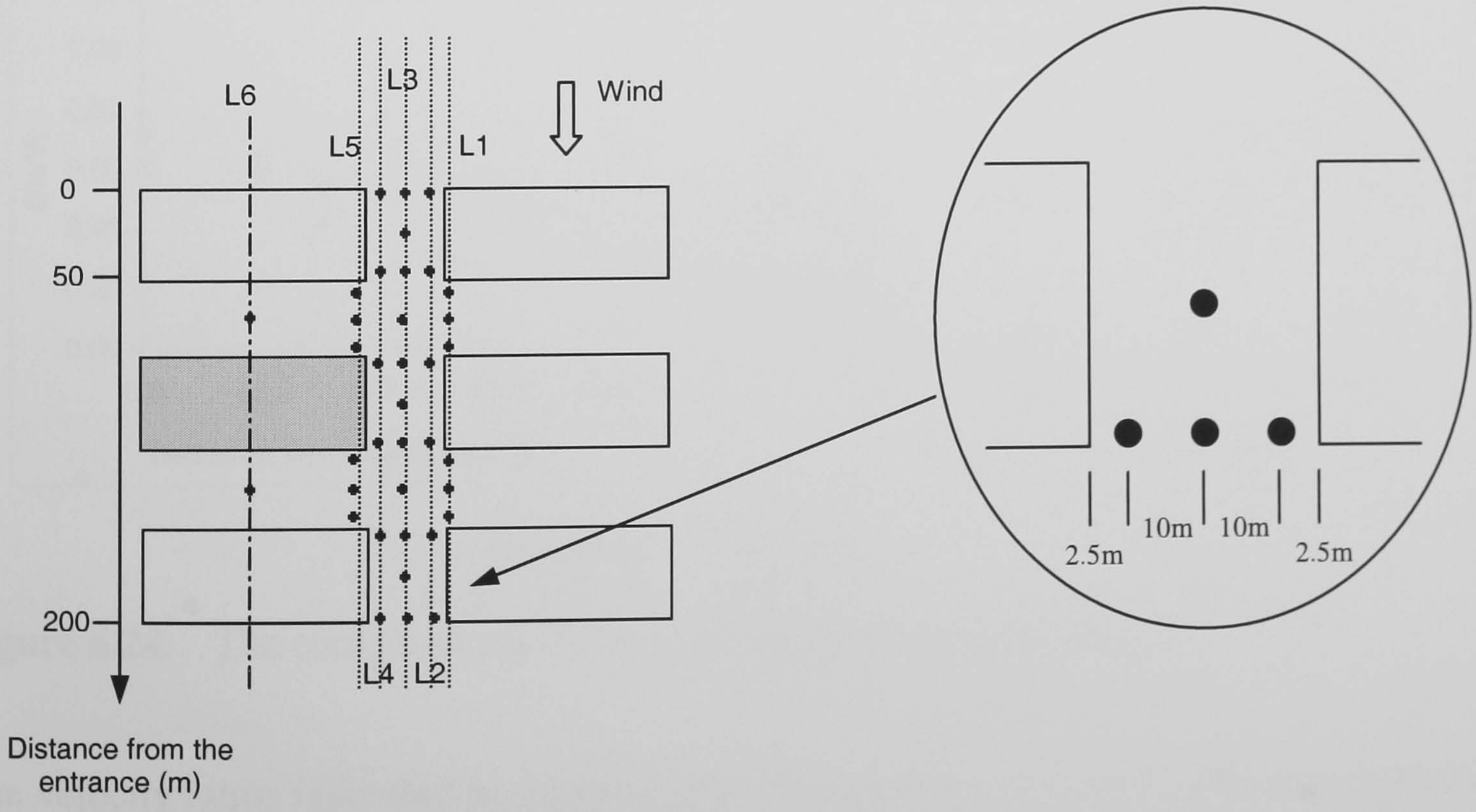

Figure 6.22 The locations of measured points. L6 is the line coinciding with the symmetric plane of the computing domain. Dimensions are in full scale.

The experimental data indicate the wind velocities measured at L1 and L5 are significantly lower than the reference wind velocities; the velocity ratios are between 0.25 and 0.41 (figure 6.23). The computed values were in the range between 0.16 and 0.36 but some predicted values were lower than the data at some locations. The large discrepancy was possibly due to the fact that the location evaluated was covered by a corner vortex, where the unsteady velocity field was difficult to be predicted correctly by the turbulence model. Some computed values at L1 and L5 were in good agreement with the experimental data.

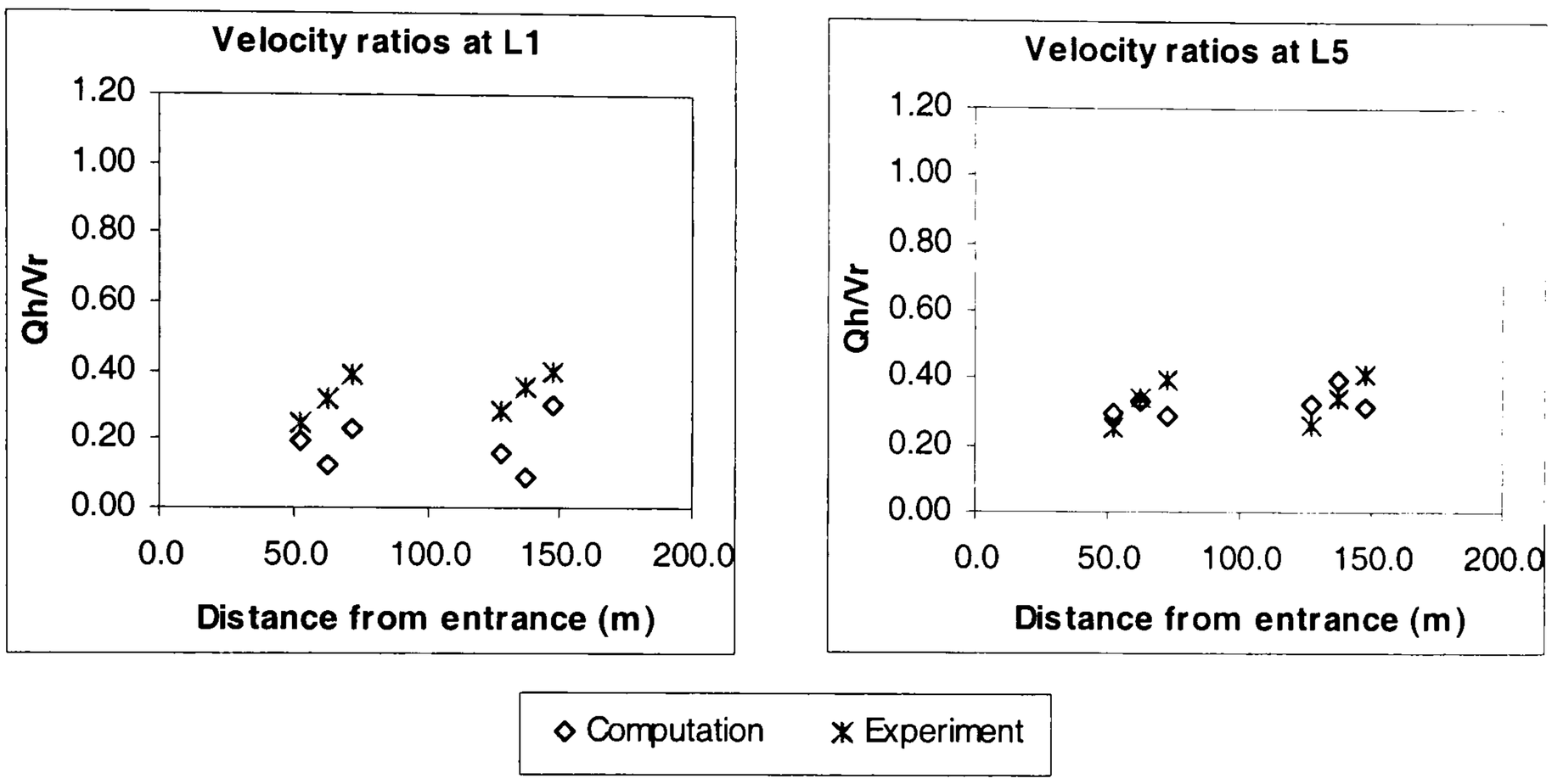

Figure 6.23 The computed values vs. experimental data at L1 and L5.

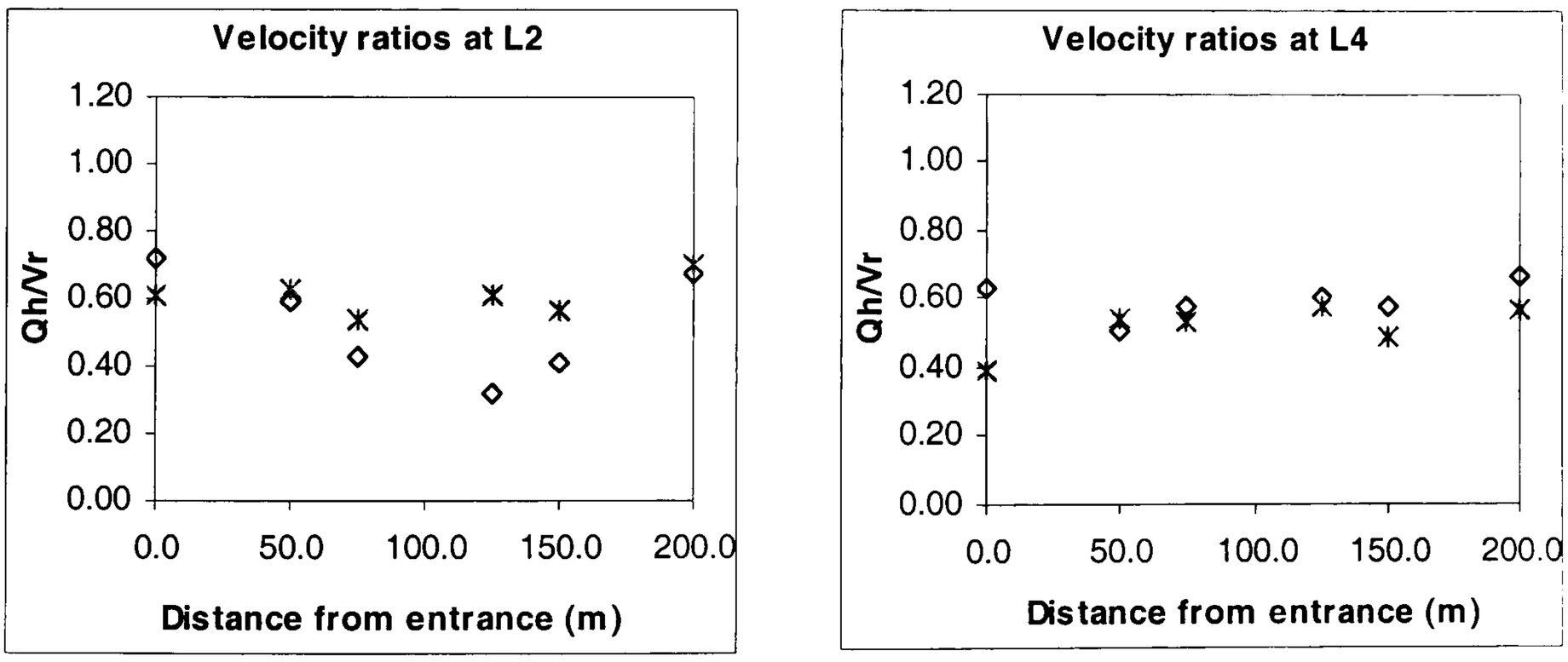

Figure 6.24 The computed values vs. experimental data at L2 and L4.

The velocity ratios indicated by experimental data are also lower than 1.0, ranging from 0.39 to 0.70 in L2 and L4 (figure 6.24). The computed values were between 0.31 and 0.72. The agreement between computation and measurement was satisfactory except one point at L2 and another point at L4. The point located at 122.5 m in L2 was likely to

be covered by locally separated flows, where the wind velocity was also difficult to be predicted correctly. The wind velocity at the point located at the entrance in L4 was retarded by the presence of buildings but the measured values seemed to be lower than expected (c.f. the corresponding point in L2), whereas the computed value was likely to be reasonable.

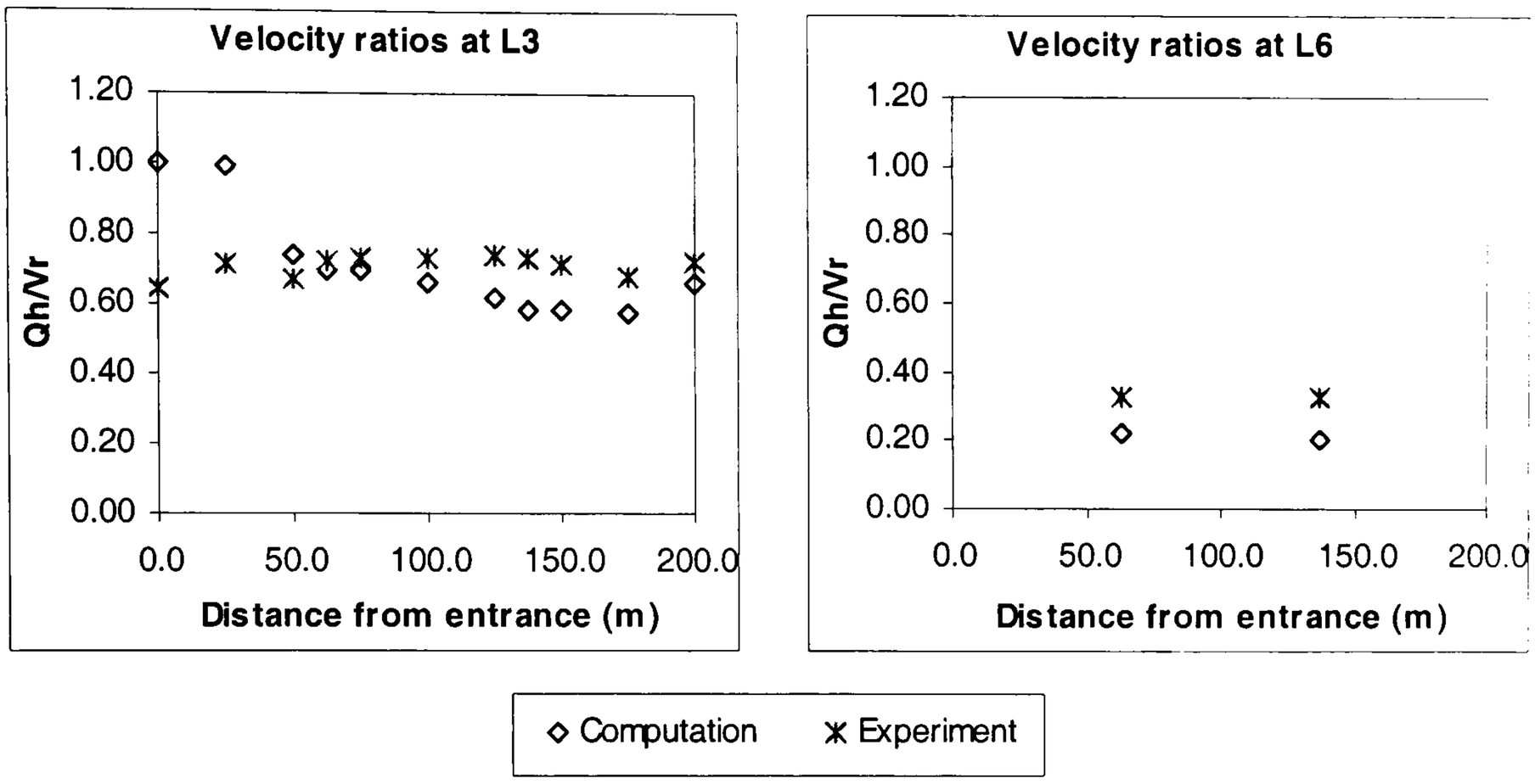

Figure 6.25 The computed values vs. experimental data at L3 and L6.

The measured values in L3 are in the range between 0.64 and 0.72 and the variations are smooth throughout the centreline of the street (figure 6.25). The computed values were ranging from 0.57 to 1.00. The values obtained from the computation depicted a different trend at the first two points but it was likely to be correct. Since the wind velocities at the centreline near the entrance are likely to be accelerated due to "channelling effect", as shown in figure 6.7 and figure 6.16; therefore the velocity ratios in the vicinity of the entrance are likely to be higher but the trend is not presented by the experimental data. Apart from the first two points, the computed values agreed favourably with the experiment. The points at L6 are located in a region characterised by standing vortex and swirling flows. The measured values are 0.33 for both points. The computed values were 0.22 and 0.20 for the first and second points respectively.

The discrepancies found in this comparison were mostly due to highly complicated flow structures, where the wind velocities were difficult to be measured and computed accurately. In fact, wind tunnel test is not an exact science (Simiu and Scanlan, 1996) and many factors may affect the accuracy of data acquisition. Numerical simulations also contain uncertainties in turbulence modelling and some possible errors in numerics. Therefore, Castro *et al.* (1999) argue that the best CFD simulation is not necessary to be

identical with wind tunnel experiment and Summers *et al.* (1986) suggest a 20% discrepancy for validation of a CFD model when studying bluff body aerodynamics, since a 20% discrepancy between wind tunnel test and full-scale measurement is not uncommon. Moreover, Ferziger (1990) proposes that a larger discrepancy of more than 25% between computation and experiment is acceptable and sufficient for wind engineering applications. Stathopoulos and Baskaran (1996) consider that an error percentage around 30% is applicable in CFD modelling of wind environments around buildings. In summary, according to the above arguments, for the study of street-level winds, a 30% discrepancy between computation and experiment can be considered satisfactory.

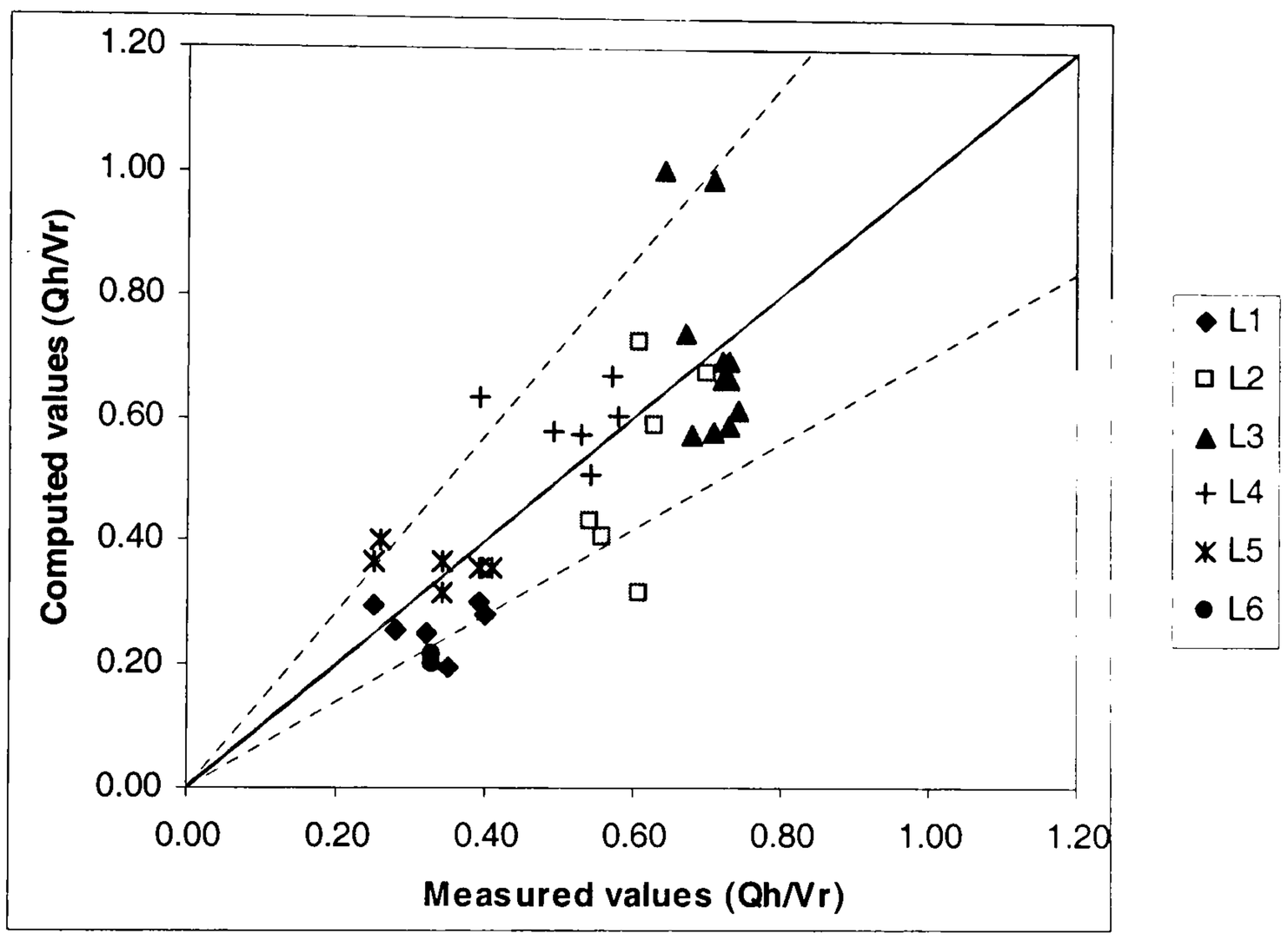

Figure 6.26 The computed values vs. experimental data. The area embraced by the dash lines is the range within 30% discrepancy between computation and experiment.

Figure 6.26 summaries the result of this comparison and shows the discrepancy range within 30%. Most of the points were located in this range; therefore the CFD simulation was satisfactory. In addition, if the averaged velocity ratio is of concern, from the experimental data, the averaged velocity ratio is 0.63 by taking the average of the sum of all velocity ratios in L2, L3 and L4. The ratio indicates the averaged wind velocity in the along-wind street and it is often of concern to urban planners and architects (Brown and Dekay, 2001). The corresponding value obtained from the CFD simulation was also 0.63, which agreed more satisfactorily with the experimental result.

6.3.2 Flow Pattern in the Streets

The vector field is plotted on the horizontal plane at 2 m (full scale) above ground level, as shown in figure 6.27. Very interesting flow phenomena were observed along and across the streets, including vortices, separation, recirculation and reverse flows. In the along-wind street, two small vortices were found at the corner – "A" and "B" and this explained the wind velocities were low in the corresponding locations. There were some vortices in the cross-wind streets, denoted by "C", "D", "E" and "F". The velocity ratios obtained in those locations were also low and the discrepancies between computation and measurement were large. The reverse flows (R1, R2, R3) were found at the leeward sides of buildings and in the cross-wind streets. The wind velocities in close proximity to the entrance of the along-wind street were apparently accelerated and this was also identical to the observation in the previous case (figure 6.16).

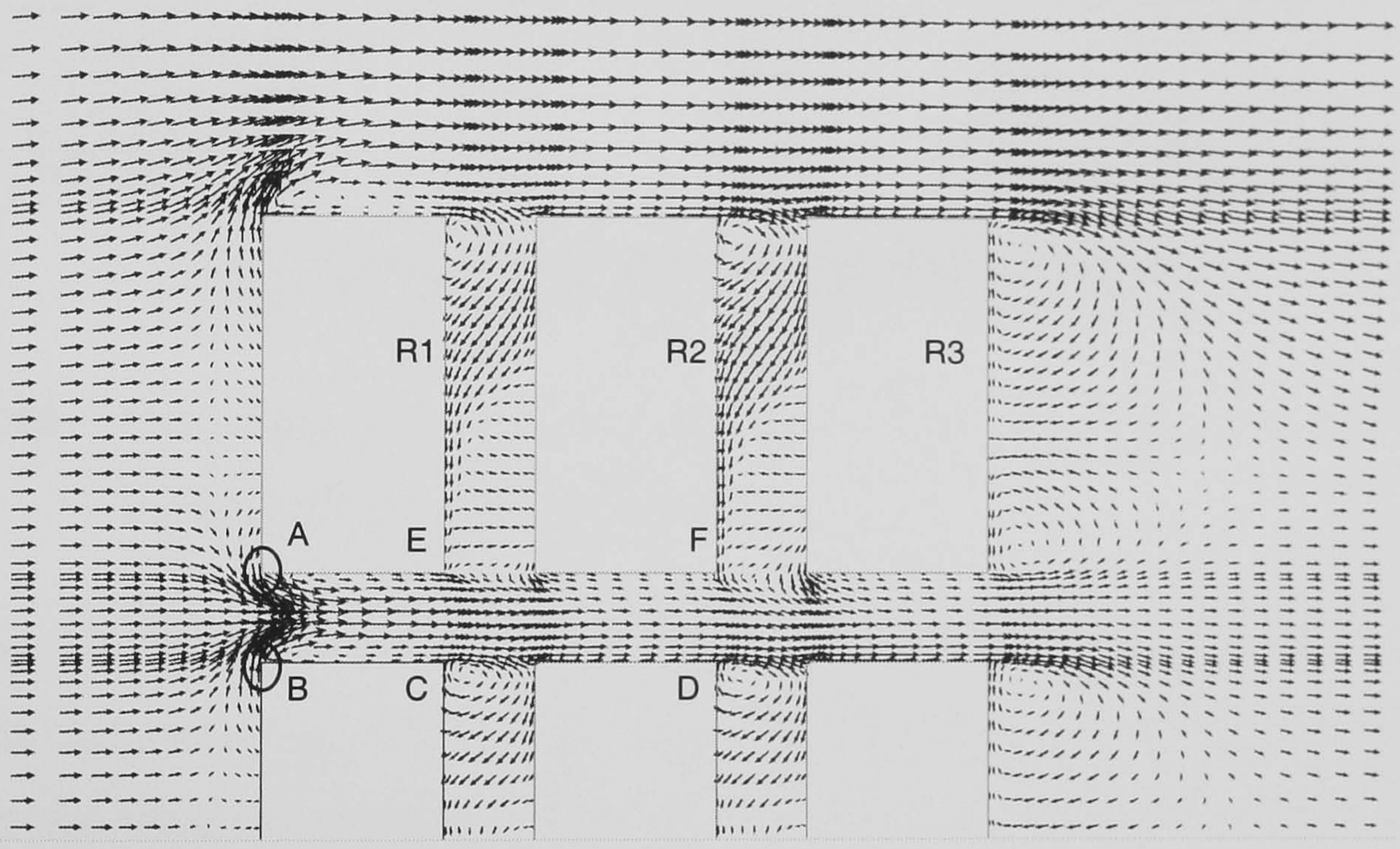

Figure 6.27 The vector field on the horizontal plane (2 m above ground level).

By observing the lengths of vectors in the streets, the wind velocities were weakened by the presence of buildings, except the wind velocities at the entrance of the along-wind street. It was unlikely to cause severe wind problems to pedestrian walking along the street in this occasion.

6.3.3 Distribution of Turbulence Intensities

The turbulence intensity needs to be taken into account when considering pedestrian comfort (c.f. chapter 2), since "gustiness" can affect the balance of walking. The scale

of gustiness is associated with turbulent winds. Therefore the most commonly used formula defining the "effective gust" is:

$$V_{eff} = V\,(1 + 3.0\ T.I.) \tag{6.4}$$

where V_{eff} is the effective gust, V is the mean velocity and $T.I.$ is the turbulence intensity as defined by equation (6.3). The distribution of turbulence intensities in the streets is shown as contours in figure 6.28.

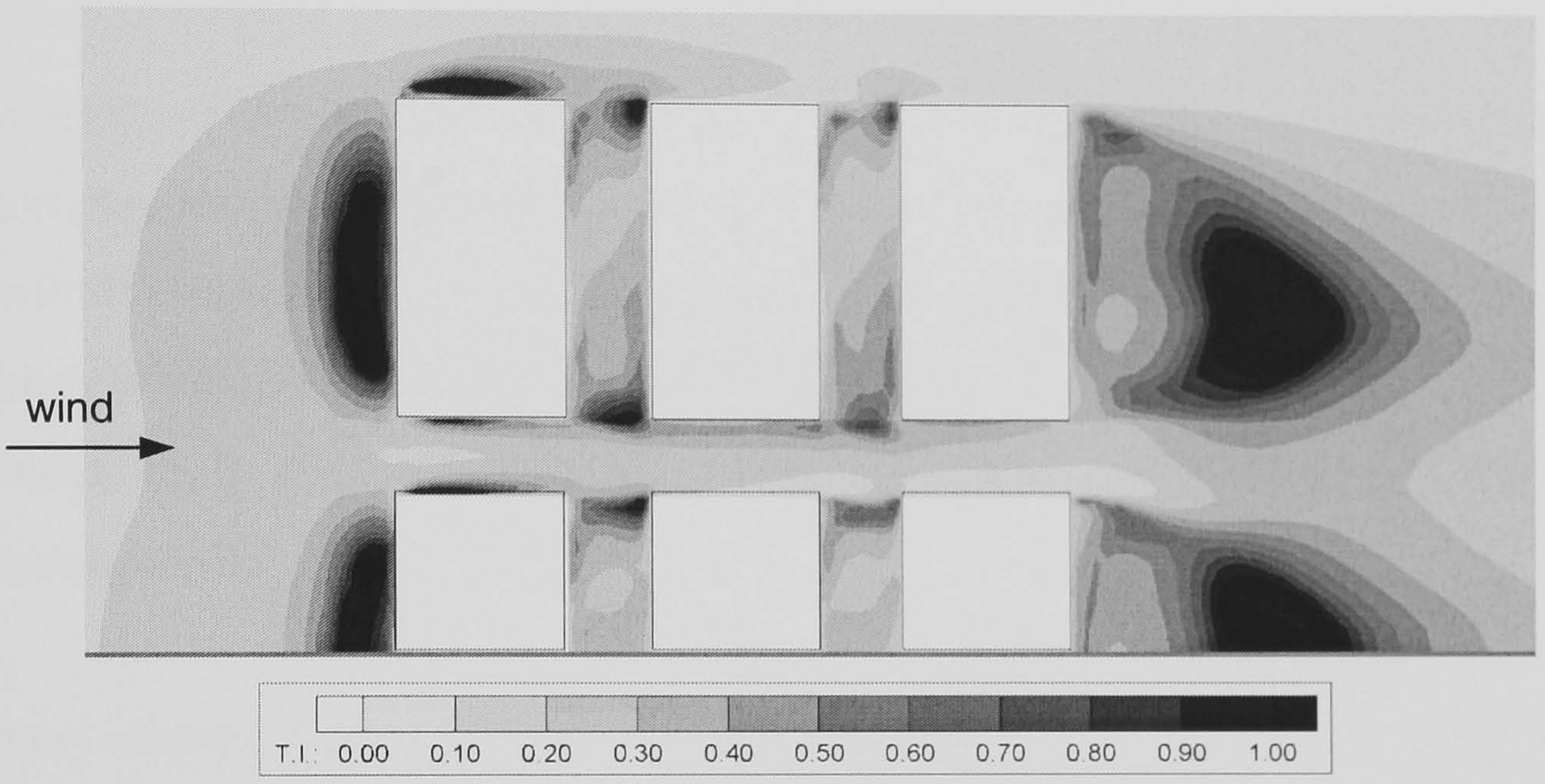

Figure 6.28 The contours of turbulence intensities. The turbulence intensity is calculated from equations (6.1-3).

The scales of turbulence were strong at the corners, the separation layer and in the wake. The turbulence intensity in the along-wind street was about 20-30% but a few areas near the entrance exhibited higher levels of turbulence (70-80%). High turbulence intensities (70-90%) were also found in some corners of these buildings. The highly turbulent areas were commonly associated with vortices and flow separation, where the mean velocities were low but their turbulent kinetic energies were high. The variation of turbulence intensity in the cross-wind streets was more noticeable, ranging from as low as 10% to as high as 90%. By investigating the along-wind street, the turbulence intensities were moderate (20-50%) in most of the areas and the corresponding mean velocities ratios were also lower than 1.0; therefore the effective gust was unlikely to be high. Though large scales of turbulence were present in some regions of the street, the corresponding mean velocities were low; consequently the effective gust was also relatively weaker. This concluded and further proved that this building layout was unlikely to cause severe wind problems to pedestrian walking along the street under this wind direction.

6.4 Summary

The study of street-level winds in a number of building layouts with various wind incidents has been presented. The comparison shows the CFD simulation using the proposed method is satisfactory when investigating the velocity field in the passage between two buildings. The influences of wind directions and the height differences have been examined. Raising the height of an adjacent building may accelerate the wind speed in the passage but the effects may be less significant if the wind direction is within the range $30^{o} - 60^{o}$.

In the study of street-level winds around a group of buildings, the agreement between the computation and experiment is less satisfactory but most of the discrepancies are still within a range 30%. However, the averaged velocity ratio in the along-wind street has been predicted satisfactorily. The flow pattern and the distribution of turbulence intensities have been also examined and discussed with respect to evaluation of pedestrian comfort.

The next chapter is an application of the proposed numerical methods to an industrial case in which the wind effects will be simulated as a further study of the wind effects around buildings.

Chapter 7 An Industrial Case Study of Wind Comfort and Windchill Using the Proposed CFD Approach

The environmental quality of open spaces has great impacts on outdoor activities. Building form and layout can significantly affect the quality of public space by inducing or diverting wind into streets and open spaces. It has been a priority in architectural design and urban planning. Undoubtedly, the study of wind effects on people is one of the focuses in the assessment of environmental quality of open spaces.

Since the proposed methods have been sufficiently validated in previous chapters, this chapter is to apply the numerical approach in an industrial case study for the evaluation of pedestrian-level winds in open spaces. There are two scheme designs in this project – layout A and layout B. Both options will be simulated with the CFD approach. The results will be presented for comparison to decide a better option in this project.

7.1 Project Background

The client's brief was to develop a design with both excellent environmental quality and strong financial viability. The architects made two proposals of building design to the client for a newly developed land. The design consisted of eight four-storey rectangular buildings and a central pedestrian space, which was the spotlight of the environmental assessment. As the environmental conditions were one of the client's primary concerns, a study of the environmental wind around the buildings was therefore carried out. Various preliminary configurations of the site were assessed and considerable importance was given to the wind environment as an indispensable part of the overall strategy in environmental design. People were the important focus in the design strategy as the comfort of occupants together with maximising the ambient energies was a prime consideration. The objectives were to shelter the designated space, primarily the centre yard in the centre, from the cold prevailing south-westerly wind in winter and also allowed the central open space to access sunlight during the day. This central yard was designed to provide a community space during the lunchtime for the occupants of the buildings. Two scheme designs – layout A and layout B, as illustrated in figure 7.1,

were proposed for comparison. Layout A is composed of a series of staggered rectangular blocks arranged along a central pedestrian walking area. Individual buildings are orientated along an east-west axis to maximise solar access. Layout B employs a different strategy in which the buildings are linked together at each side and the central pedestrian area is embraced by the "wings". Both schemes have similar total floor areas.

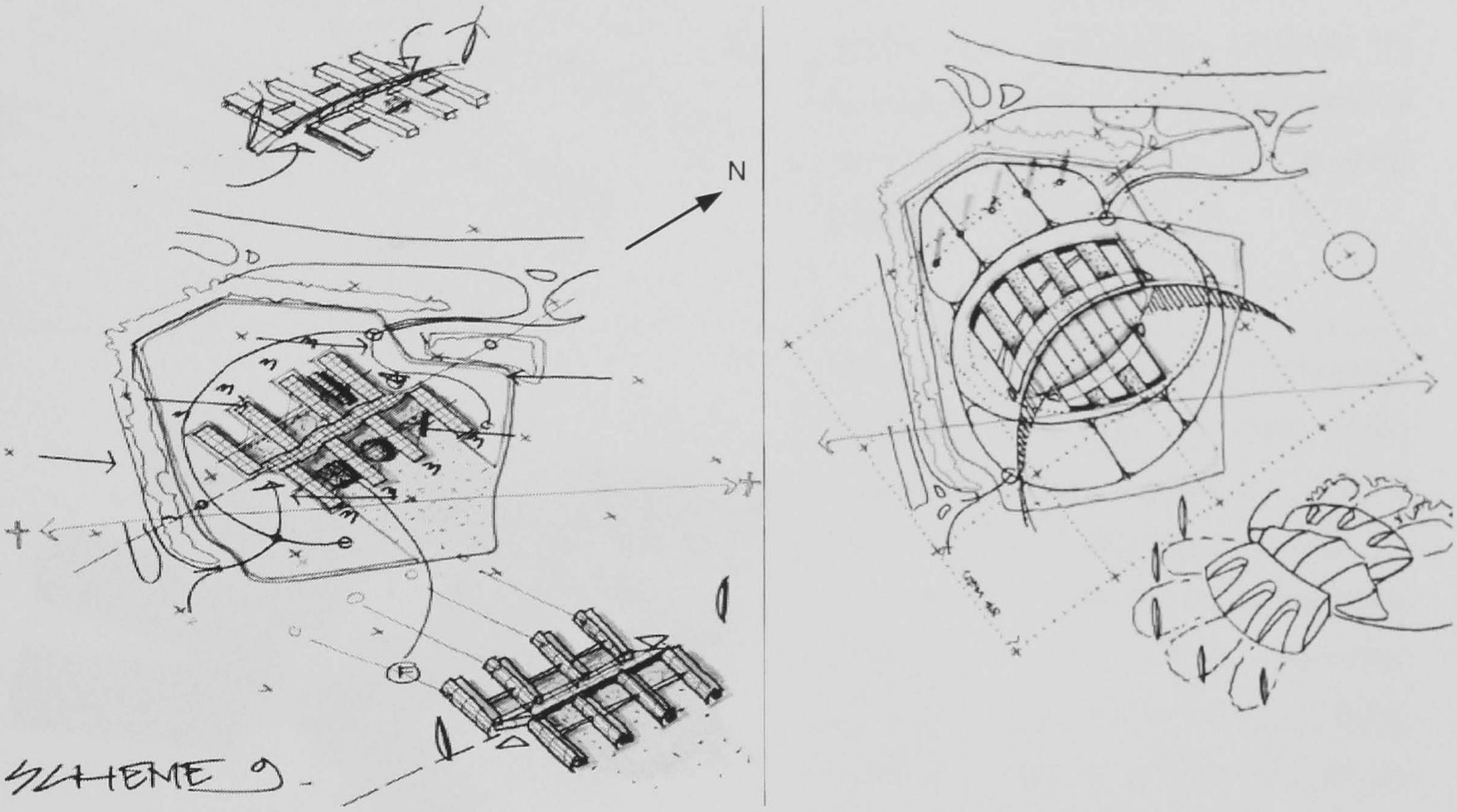

Figure 7.1 Scheme design – layout A (left) and layout B (right) [Courtesy of Battle McCarthy Consulting Engineers].

The schemes will be modelled with CFD to determine a better option that may improve the microclimate in the outdoor space.

7.2 CFD Modelling

The modelling procedure was firstly to extract the buildings from the original CAD drawings and subsequently converted it into a model that was accessible to the CFD code. The process of conversion was complicated, since the original CAD drawing was not created specifically for mechanical analysis, where a solid model was required. However, the CFD code necessitates a solid model and the geometric characteristics – 2D surfaces and 3D volumes must be properly defined. In order to simplify the geometric model, some details of the buildings such as the cladding and glazing of exterior walls were omitted but the principal geometries were retained. Landscaping and

vegetation were also omitted when creating the CFD model because the information given was inadequate in the CAD drawing and therefore some required aerodynamic parameters required for a CFD simulation was not available. The process of conversion is illustrated in figure 7.2.

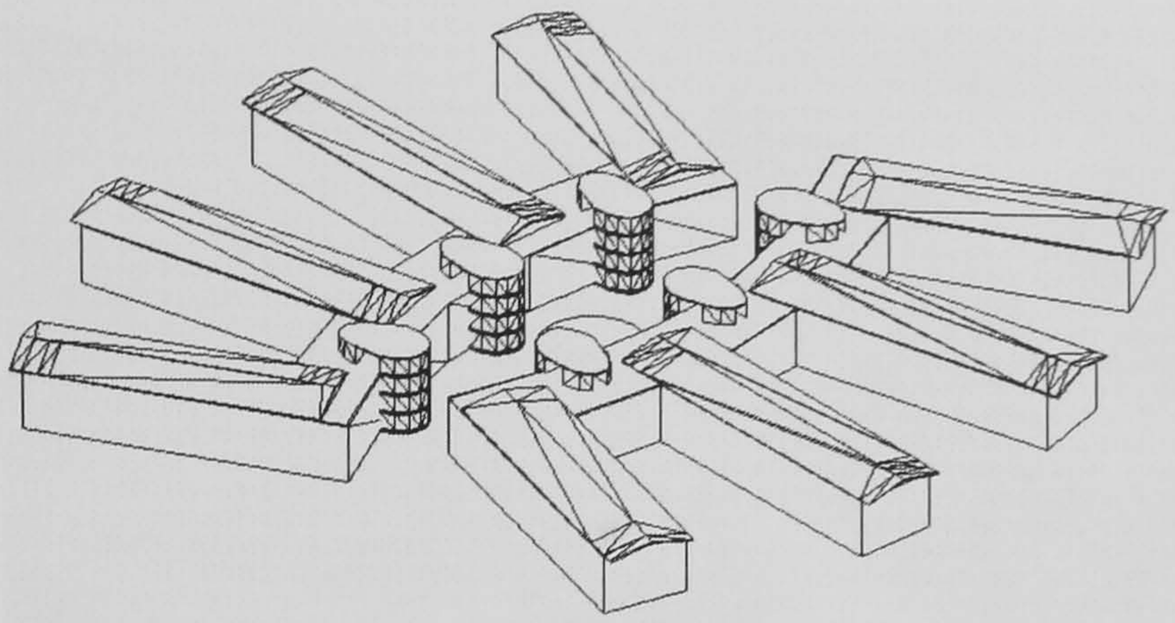

Original CAD drawing in which many details are particularly created for architectural design but the attributes of drawing elements are not properly defined as a 3D model.

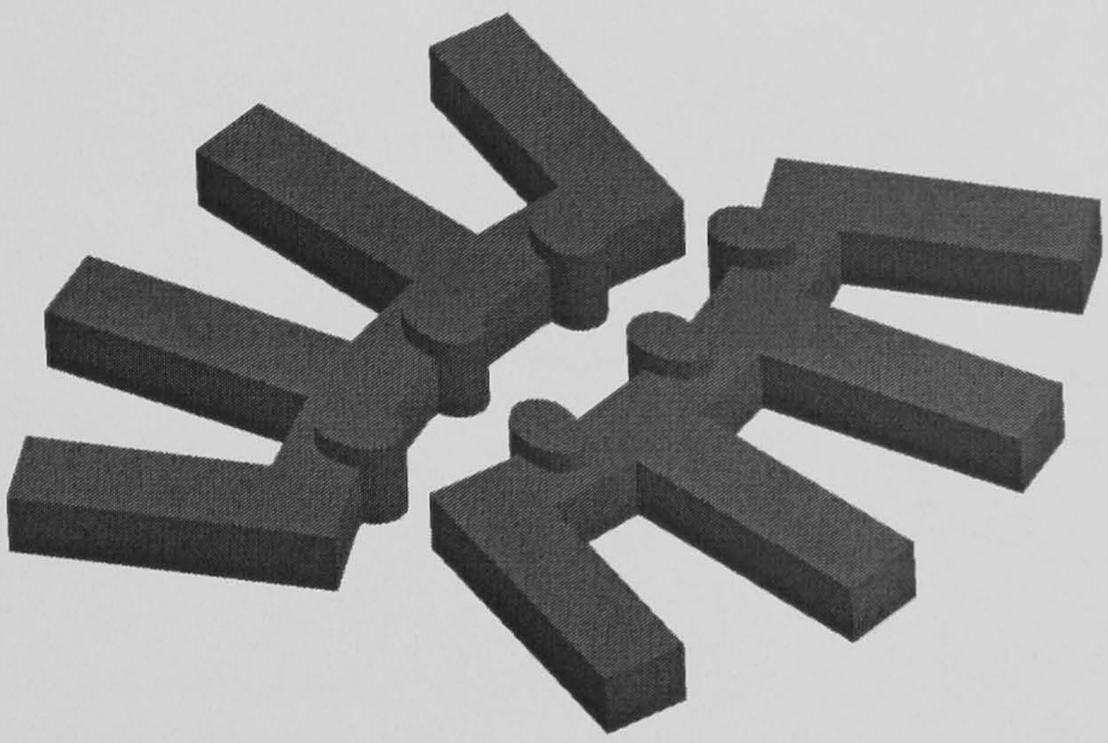

Since CFD or other mechanical analysis codes need to know which element is a line, surface or a volume when creating a geometric model, the CAD model is therefore required to be converted. The most important geometry is the lines of exterior walls, from which the 3D solid model can be created for CFD analysis.

Figure 7.2 Model conversion – from CAD to CFD

7.2.1 Choice of Grids

The geometries in both schemes were highly complicated, which resulted in some difficulties in the design of grids. Two options were considered – Cartesian and unstructured. The option of structured and body-fitted grids was excluded, as it was too difficult to create that type of grids in a very complicated geometry. The simulation using Cartesian grids was created with PHOENICS, whereas the computation using unstructured grids was done by CFX 5. Both CFD simulations were tentative in order to compare the flow pattern obtained from the experiment. The model selected was "layout B" since its geometry was relatively more complicated.

For flow visualisation, one option considered in this experiment was to employ the technique of particle image velocimetry (PIV). PIV is a quantitative technique of flow

measurement, which uses the laser sheet to illuminate the flow field in which the motion of seeding particles can be captured by synchronising the multi-exposure cameras (Grant, 1997). The image subsequently will be analysed by the PIV software to depict the flow field with velocity vectors.

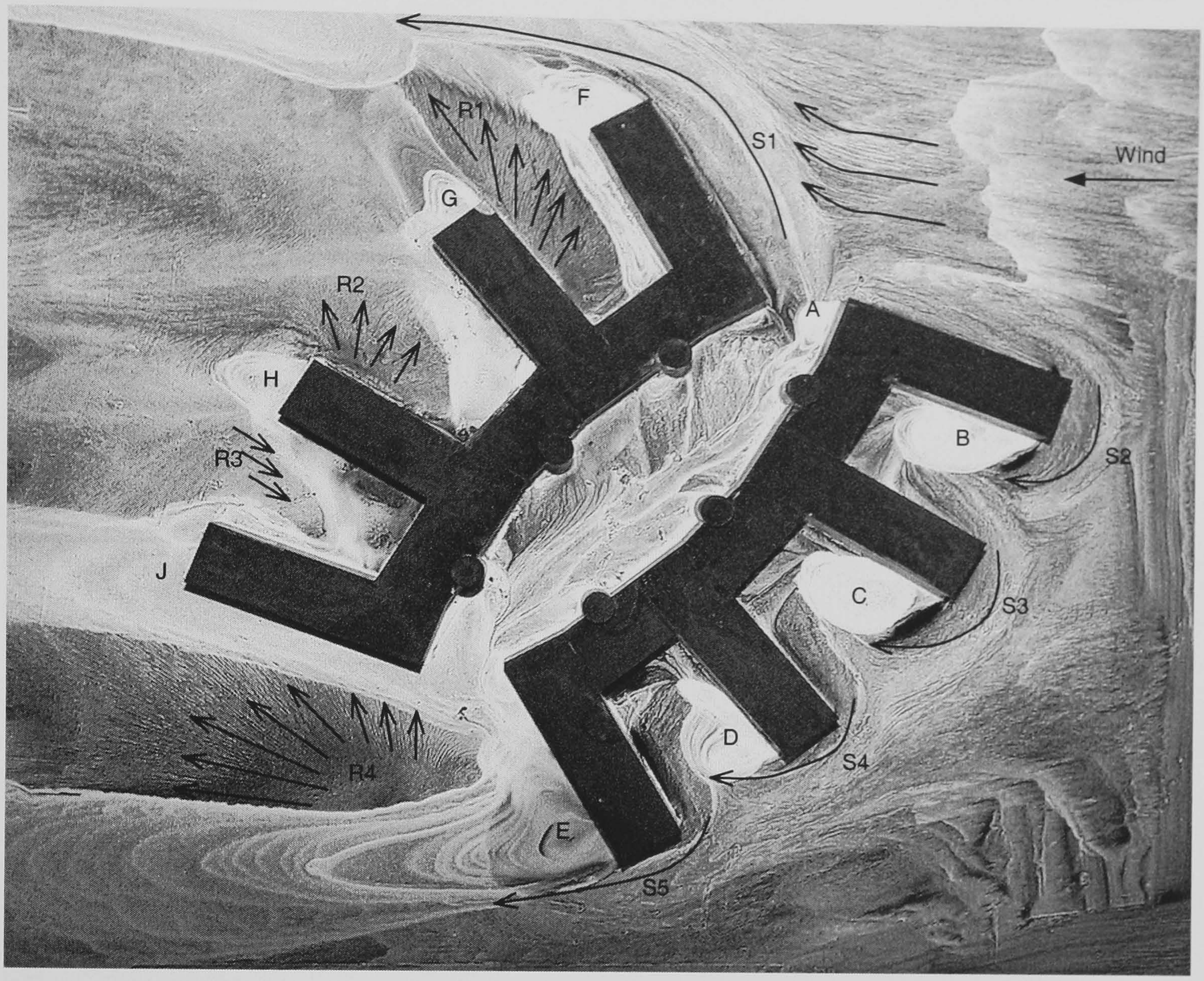

Figure 7.3 The flow pattern of the building model – layout B. The wind direction is from right to left. "S" denotes flow separation; "R" represents reverse flows and reattachment; "A" – "J" indicate eddies or vortices.

It was thought using PIV would be able to get a more accurate vector field for comparison with the CFD simulation if successful. However, the resolution of captured images was not high enough for the PIV software to calculate the correlations of exposed particles and the model created some "shadows" which impaired the quality of the image, though it was made of transparent materials. Many remedial actions were attempted, for example, increasing the density of particles, raising the power of laser, maximising the aperture of the lens, increasing the focal length, changing the frequency of impulse of the laser beam, applying a black background to the model, etc. These methods still failed to improve the quality of the raw images. As a result, the

correlations of "particle pairs" could not be analysed correctly and the output of vector field by the PIV software was not very meaningful. Therefore the flow pattern was still visualised by the same technique depicted in chapter 5.

Figure 7.3 shows a very complicated flow field, characterised by a number of features – separation, vortex, reverse flows and reattachment. The flows separated at the windward sides of the buildings and the vortices were formed and attached to the leeward sides of buildings. Five separation lines (S1 – S5), nine eddies (A – J) and four regions of reverse flows or reattachment (R1 – R4) were observed. The flow pattern in the central space between two buildings was too complicated to be classified. The experimental observation indicated the flow speeds within the space were low but the velocities near the corner in the vicinity of eddy "A" were slightly higher.

Figure 7.4 shows the flow pattern predicted by CFX 5. The density of vectors was higher in close proximity to the buildings, as the grids were refined in those regions.

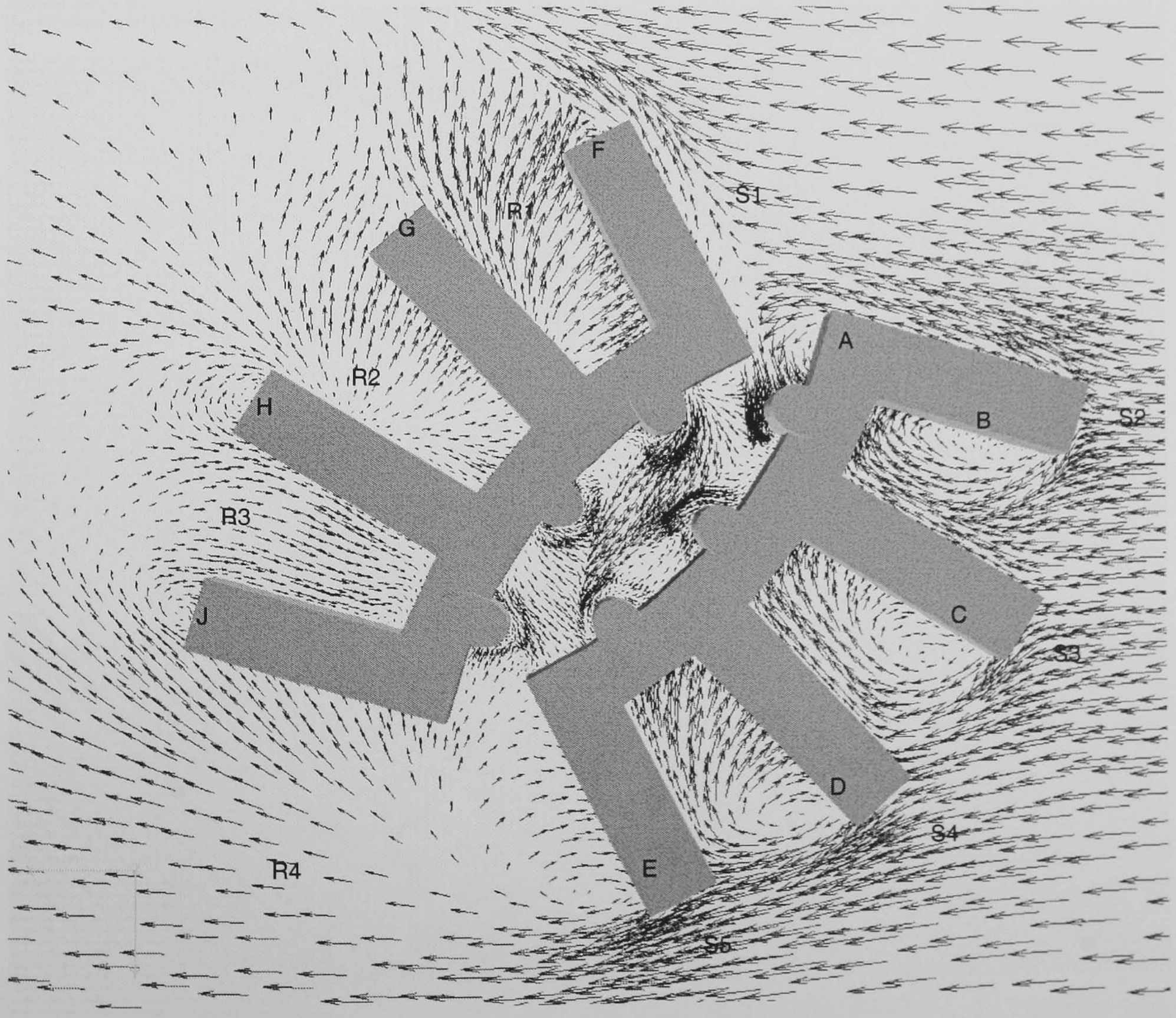

Figure 7.4 Computed flow pattern using unstructured grids.

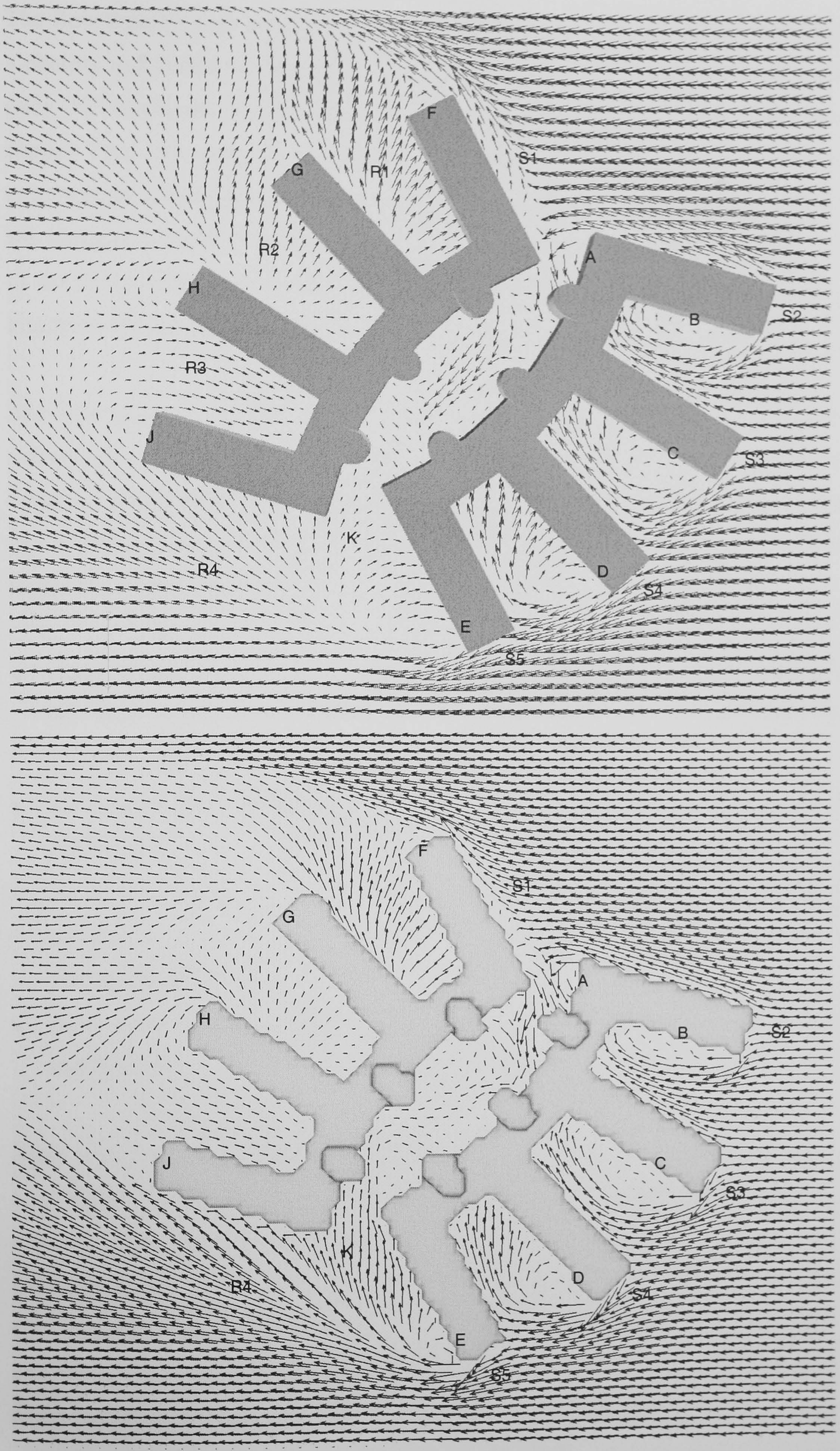

Figure 7.5 Vector fields calculated by CFX (upper half) and PHOENICS (lower half).

The flow features corresponding to the experimental result were denoted with the same alphabets and numbers. The eddies – "B", "C" and "D" were relatively smaller and the eddy "G" was hardly discernible but the flow separation line "S1" was clearly depicted (figure 7.4). The flow behaviours at "S2", "S3", "S4" and "S5" were akin to the experimental observation and there were flow accelerations at the corners, indicated by the elongated vectors. The reverse flows at the regions – "R1", "R2" and "R3" as well as the flows in the reattachment area "R4" were clearly predicted and their trends were similar to the experimental result.

The flow pattern predicted by PHOENICS using the Cartesian grids and the vector field calculated by CFX are shown in figure 7.5. The vector field depicted by CFX was the same as figure 7.4 but the vectors had been redrawn with uniform sampling. Comparing the uniformly sampled vector field with the flow field calculated by PHOENICS, the noticeable differences were:

- some swirling flows were found in the central space between two buildings, whereas the flow pattern predicted by CFX did not show the similar trend in the corresponding location,
- the zone of flow separation at "S1" was slightly smaller in the picture depicted by PHOENICS,
- the flow velocities at the region "R4" were stronger compared to the freestream velocity but the calculation made by CFX presented a weaker velocity field in the that region and,
- there were stronger flows in the region "K" presented by the calculation of PHOENICS.

Apart from these, the general flow patterns predicted by the two computations were in a very similar trend. Therefore, although the geometric model in PHOENICS was an approximation, the flow field depicted was not very different from the approach using the unstructured grids. The geometry of the building model was correctly represented in CFX but the costs of computation using the unstructured grids were also higher; the computing time was nearly two times longer. However, the flow field predicted by using unstructured grids was not significantly more accurate than that of Cartesian grids. As a result, using Cartesian grids was considered sufficient to study the flow field around buildings in this occasion.

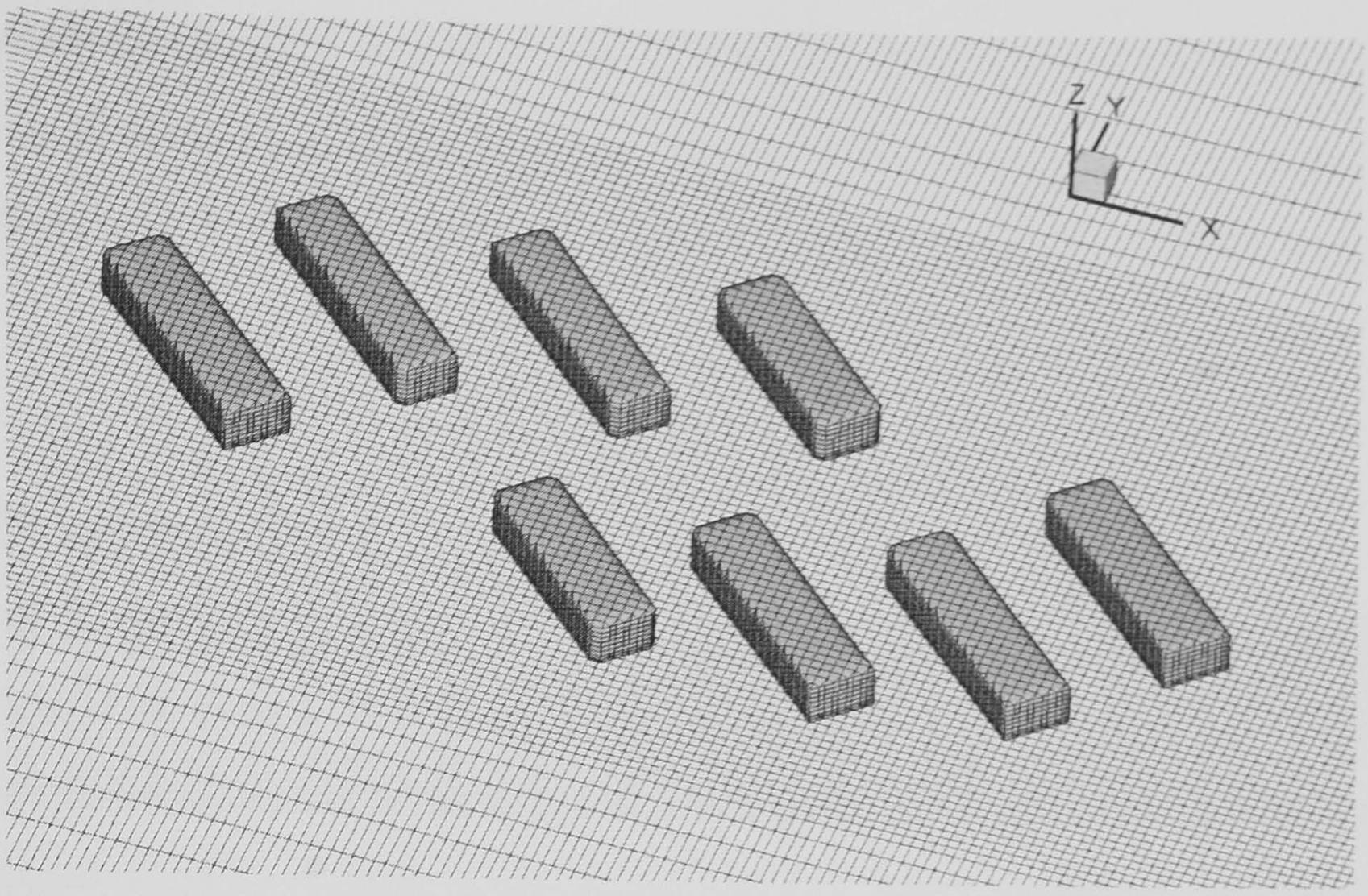

Figure 7.6 The computational grids – layout A.

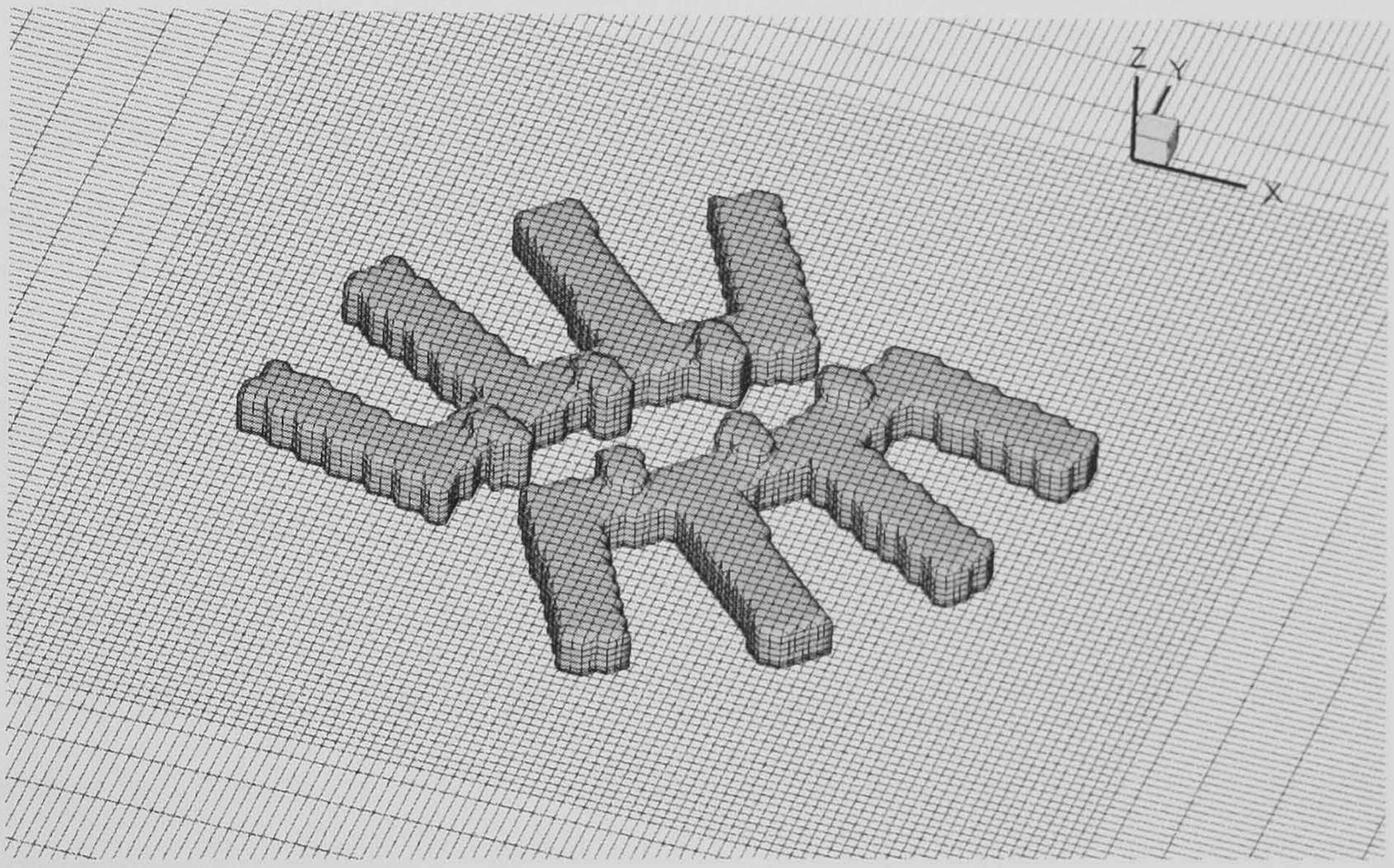

Figure 7.7 The computational grids – layout B.

Since the Cartesian grids were able to capture the flow characteristics concerned, the Cartesian grids were therefore applied in subsequent CFD simulations. The grids for "layout A" and "layout B" are illustrated in figure 7.6 and figure 7.7 respectively. The grids were refined near the ground but the edges of buildings were represented by the "staircase" approximation. The CFD models were created in a scale of 1/400 and the mesh density in the vicinity of buildings was the same in both CFD models so that the two different layouts were computed with the same level of numerical resolution. This ensured that both of the CFD models were calculated at the same basis in terms of spatial discretisation.

7.2.2 Turbulence Model

The two-layer turbulence model was used in this study, as the previous chapters using the two-layer k-ε model obtained satisfactory results compared with the experimental data.

7.2.3 Differencing Scheme

The SMART scheme applied in the previous chapters shows good performance in the simulations of flow field around bluff bodies. Nevertheless, one drawback of this non-linear higher-order scheme is that the rate of convergence is slow and it becomes worse if the number of grids is large. Since the geometries were complicated and the number of grids were $169 \times 112 \times 25$ and $120 \times 120 \times 25$ for "layout A" and "layout B" respectively, the convergence rate became relatively sluggish when using the SMART scheme. The alternative – VANL2 scheme was considered. It is a 2^{nd} order accurate discretisation scheme and its performance is very competitive to the SMART scheme (cf. chapter 4). Therefore, the VANL2 scheme was applied in this study.

7.2.4 Calculation of Windchill

Windchill is not calculated by CFD but it is an extension of the post-processing of the computed flow field. The calculation of windchill combines the wind velocity and ambient temperature to determine the chilling effect on exposed skin. The wind velocities can be obtained from the CFD simulation, whereas the ambient temperature can be assumed with reference to the weather report. Soligo *et al.* (1998) suggest that the areas subject to seasonal temperatures less than 10 °C should include a windchill component when assessing pedestrian comfort. Steadman (1971) has reviewed some commonly used windchill formulae and the widely accepted are:

$$T_{eqv}(^{\circ}\mathrm{C}) = -0.04544 \times q + 33 \tag{7.1}$$

$$q(kcal/m^2/hr) = (10.45 + 10\sqrt{V} - V) \times (33 - T_a) \tag{7.2}$$

where T_{eqv} is the equivalent temperature; V is the mean wind speed and T_a is the ambient temperature (≤ 10 °C). The above equations assume a person is properly clothed for the local season. Equation (7.2) calculates the heat loss of exposed skin due to the wind. The wind velocity considered is the mean wind speed only in equation (7.2). This may

be slightly optimistic since the effects of turbulent wind are not included. Therefore the calculation of heat loss of exposed skin may be suggested by

$$q(kcal/m^2/hr) = (10.45 + 10\sqrt{V_{eff}} - V_{eff}) \times (33 - T_a) \qquad (7.3)$$

$$V_{eff}(m/s) = V(1 + 3.0\sqrt{k}) \qquad (7.4)$$

where V_{eff} is the effective gust and k is the turbulent kinetic energy. The equations (7.3-4) apply to $V_{eff} \geq 1.79$ m/s since there will be no chilling effect if the wind velocity is less than 1.79 m/s.

7.3 Results

The two layouts are to be compared in respects of streamlines, comfort parameter and windchill. The streamlines will be shown in another style – 3D ribbons. All the streamlines are 3D volume lines and the seeding points are at 2 m (full scale) above ground (figures 7.8-9).

7.3.1 Comparison of streamlines

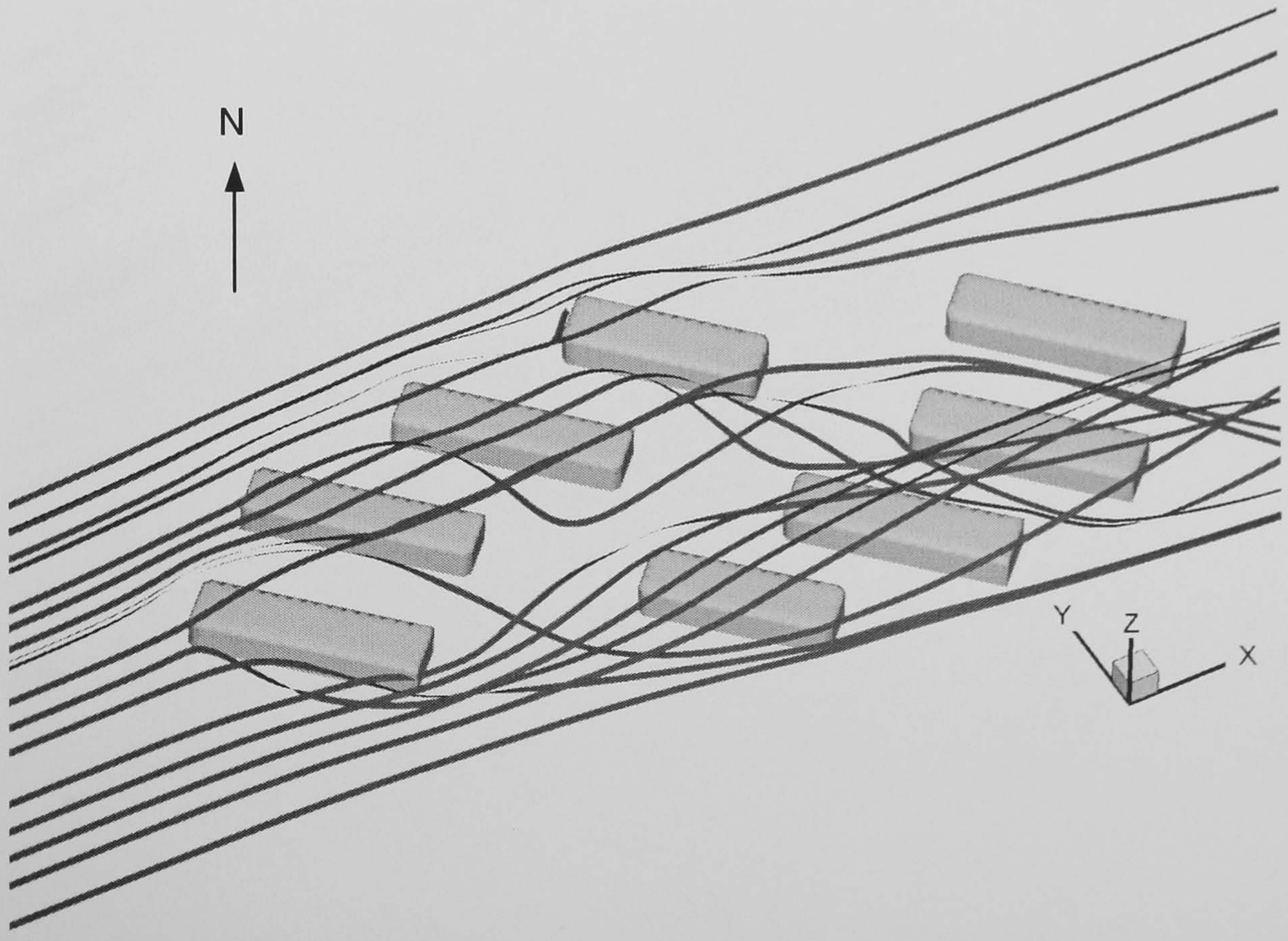

Figure 7.8 The streamlines for layout A. Twisted ribbons illustrate swirling flows or vortex sheets. The wind is from southwest direction.

In figure 7.8, the buildings (layout A) deflected the flows in various ways – some flows flew over the buildings and some streamlines were twisted and displaced. The local flow pattern was irregular but the shelter effects appeared to be weak. The designated space for pedestrians was still likely to receive relatively stronger winds, which was possible to cause discomfort to people walking or sitting in this area.

Another scheme design – layout B created a more complicated flow field around buildings (figure 7.9). Highly twisted and irregular ribbons were observed. Some ribbons were present with a spiral shape, indicating that the flow field was very unstable in those areas. The layout B was likely to create a more complicated flow field than the previous layout but the designated space for pedestrians was unlikely to receive stronger winds in this wind incident. As the buildings were linked at each side and the distance between the two blocks (wings) was narrow, the winds inclined to fly over the buildings instead of visiting the space amidst the wings.

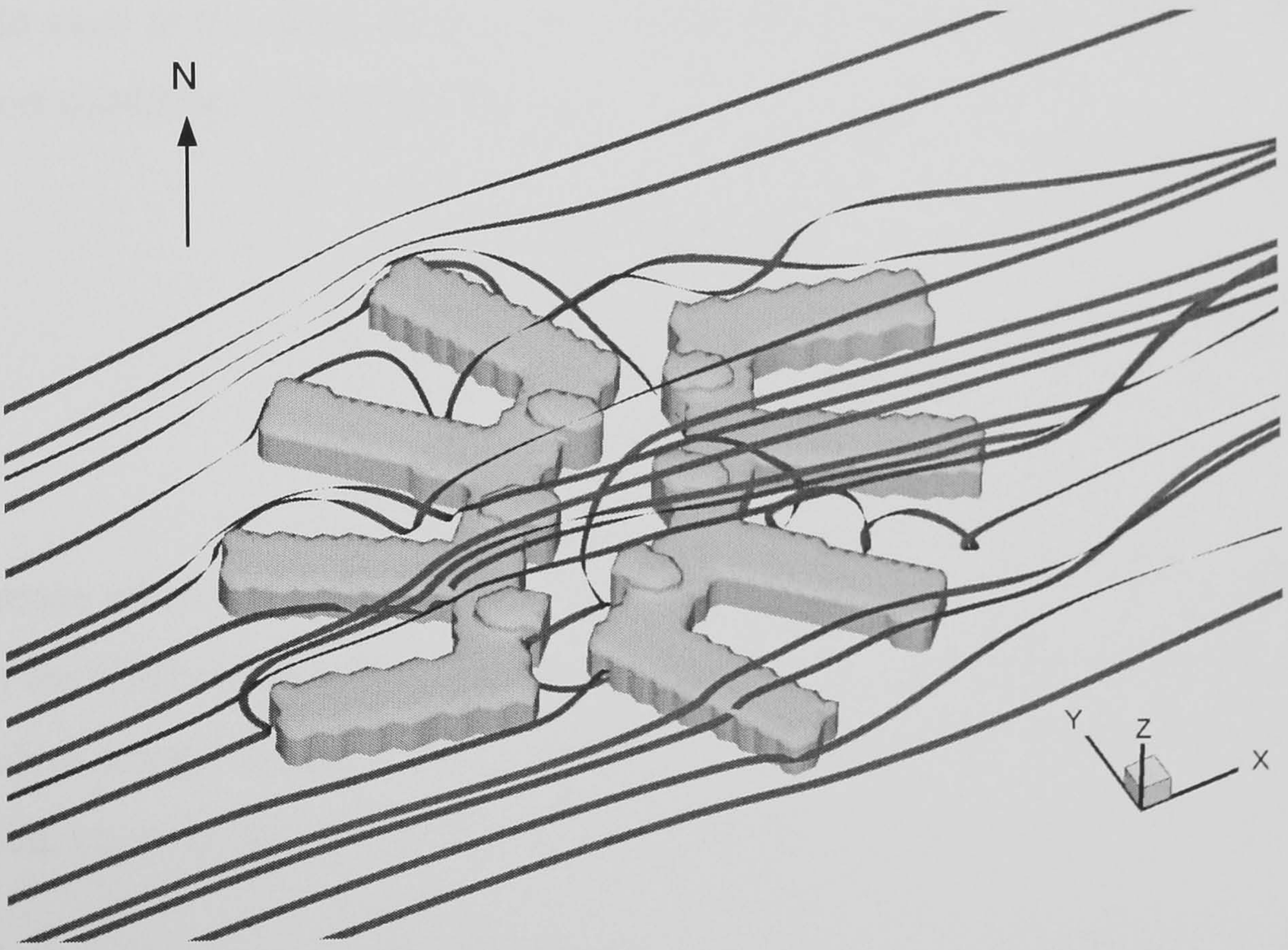

Figure 7.9 The streamlines for layout B. Twisted ribbons illustrate swirling flows or vortex sheets. The wind is from southwest direction.

7.3.2 Comparison of Wind Speeds Using Comfort Parameter

The comparison was based on the comfort parameter suggested by Gandemer (1978). The comfort parameter is defined as

$$\psi = \frac{(V + \gamma\sigma)}{(V_r + \gamma\sigma_r)} \tag{7.5}$$

where V_r and σ_r are the mean wind speed and the standard deviation (r.m.s. value) at the reference height (about 2 m in full size) without the presence of the layout plan under investigation. The constant γ may be 1.0, 1.5, 3.0 or 3.5 according to different authors. A value of 3.5 indicates that the wind speed $V + \gamma\sigma$ is approximately equal to 2 or 3 second peak gust (c.f. chapter 2) if the gusts distribution is Gaussian. However, as it has been studied by Stathopoulos and Storms (1986), the various values of γ present little difference when it is applied to calculating the non-dimensional parameter ψ. In this study, a relatively common value 3.0 was used for the constant γ.

With respect to the threshold of discomfort, a commonly assumed value $V_r \leq 5$ m/s was taken, associated with a standard deviation $\sigma_r = 1$ m/s corresponding to the turbulence that would exist at the same speed above the ground level (in open country). Therefore the comfort condition to be observed was:

$$V + \gamma\sigma < 5 + \gamma \tag{7.6}$$

or

$$\psi = \frac{(V + \gamma\sigma)}{5 + \gamma} < 1.0 \tag{7.7}$$

The reference wind speed at 2 m above ground level was 5 m/s using open country wind profile in the CFD computation and the value of σ was obtained from the square root of the turbulent kinetic energy. The mean wind velocity considered was the horizontal wind speed, i.e. only the horizontal components (U and V) were taken into account.

The values of ψ from the CFD simulation for layout A are shown as figure 7.10. The designated community area for pedestrians in the centre was likely to exceed the discomfort threshold in the incident when the approaching wind speed was 5 m/s from the southwest direction. The minimum value was 0.6 and the maximum value was 2.0, which had been considerably larger than the favourable value (1.0 or less). This was likely due to the density of buildings in this scheme was loose, thus the spaces amidst the buildings allowed more winds to flow through. The shelter effects provided by the

buildings were weak and pedestrians walking or sitting in the designated space were likely to be disturbed by slightly stronger winds.

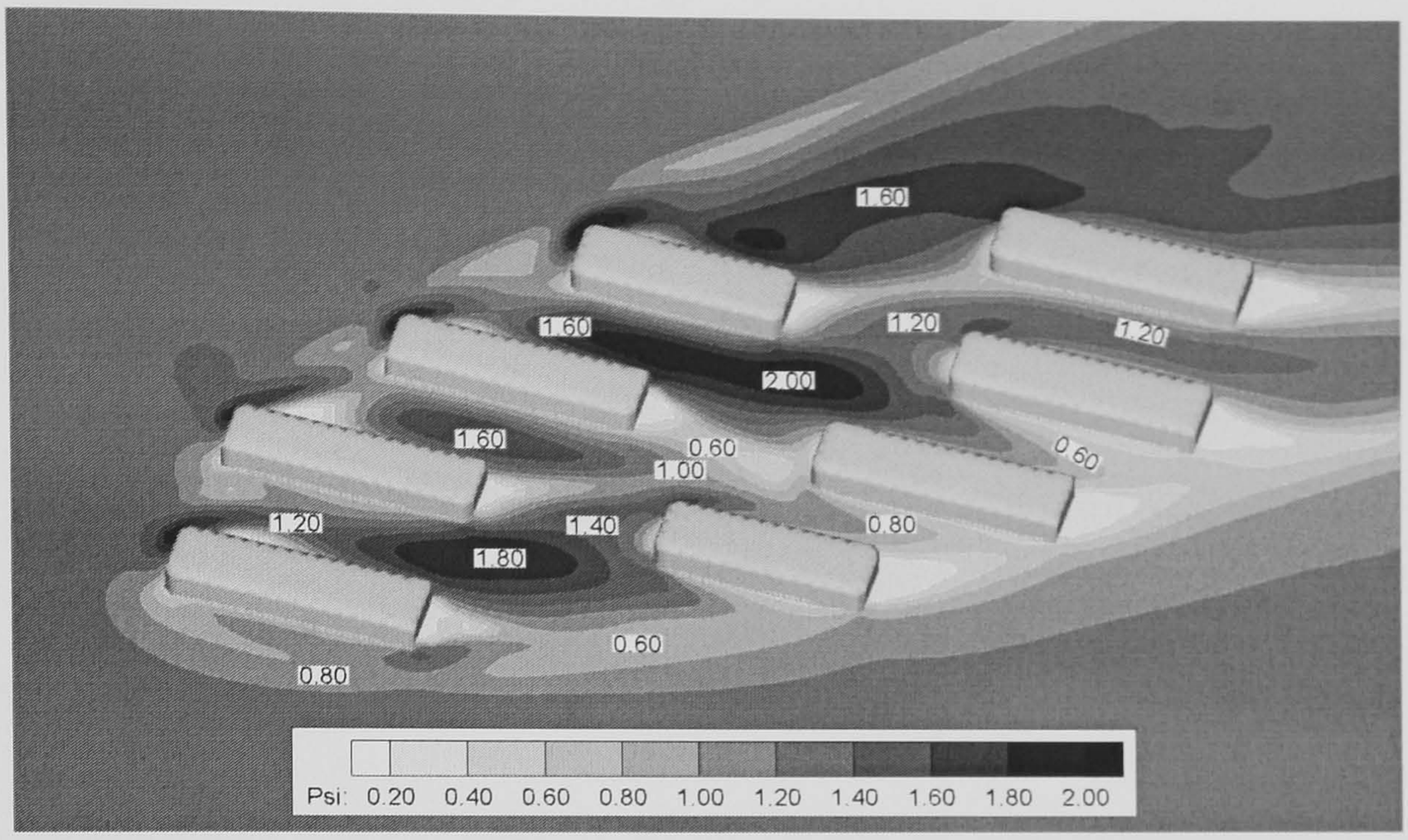

Figure 7.10 The distribution of ψ for layout A.

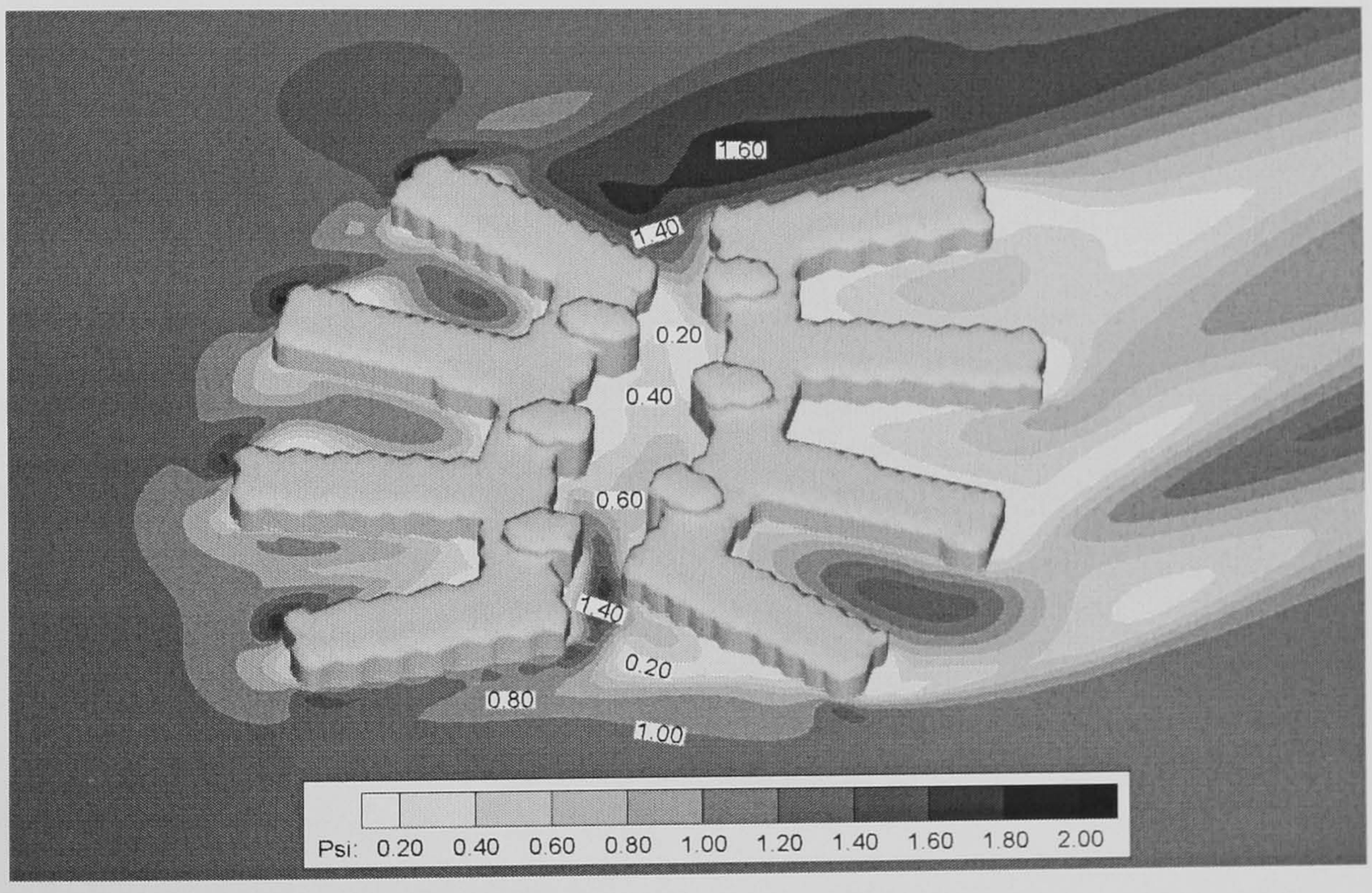

Figure 7.11 The distribution of ψ for layout B.

Figure 7.11 shows the distribution of ψ calculated for layout B. The values of ψ in the central space were significantly lower than the previous layout. The maximum value was 0.6 and the minimum value was 0.2 but the values of ψ at the two ends of the pedestrian walk were still considerably high. The central part of the community space was well sheltered and the pedestrians were likely to receive mild and pleasant winds in the designated space. To mitigate the wind problems that were likely to occur at the

entrance and the exit of the central space, some remedial approaches such as planting trees or creating windbreaks could be suggested as a part of the design for this layout.

When considering the comfort or discomfort due to the mechanical wind, another important information required is the frequency of occurrence. The probability distribution of wind speed, independent of direction, is usually modelled with a Weibull distribution given as

$$P(v > V) = \exp\left[-\left(\frac{V}{C}\right)^{k}\right] \tag{7.8}$$

where $P(v > V)$ is the probability that the wind speed v is greater than V, and C as well as k are the Weibull distribution parameters. The parameters – C and k are obtained by fitting the wind speed data using standard methods, including method of maximum likelihood, method of least squares, methods of moments and some other statistical techniques (ASCE, 1999). The analysis requires the wind speed data, which may be obtained from the weather station nearest the site concerned, since the parameters vary from place to place. CIBSE (1999) supplies the values of C and k for major cities and meteorological sites in the UK.

Usually the Weibull distribution of wind speed is presented in the form of a chart in which the horizontal axis corresponds to wind speeds (V) and the vertical axis shows the probability of exceeding a wind speed V. By observing the wind speed concerned can obtain the probability of exceeding that wind speed in question.

Since this study assumed the prevailing wind was from southwest and the approaching wind speed was 5 m/s (which was identical to the threshold of discomfort) at 2 m above ground level, figure 7.10 and figure 7.11 therefore contained the information regarding which areas were likely to cause discomfort under this wind direction. If the probability $P(V > 5$ m/s) is 50% a year at the reference height (2 m), a value 1.0 of ψ indicates that the probability of exceeding the discomfort threshold is also 50% a year. A lower value of ψ, for example, 0.5 indicates that the approaching wind speed needs to be increased to 10 m/s in order to reach the threshold (5 m/s) at that region. If the probability $P(V >$ 10 m/s) is 20% a year, it shows that the likelihood of discomfort caused by the wind is only 20% a year at those regions where $\psi = 0.5$. Therefore, as a conclusion, higher

values of ψ imply higher frequencies of discomfort; lower values of ψ represent better wind conditions and the frequencies of discomfort caused by the wind are lower.

7.3.3 Comparison of Windchill

The windchill need be considered when the ambient temperature is lower than 10 °C and when the local wind speed is greater than 1.79 m/s. This kind of environmental condition is not uncommon during a year in the UK; therefore the study of windchill for the two layouts is no less important. To evaluate the seriousness of windchill, the ambient temperature was assumed to be 10 °C and the approaching wind speed was still 5 m/s in the CFD computation.

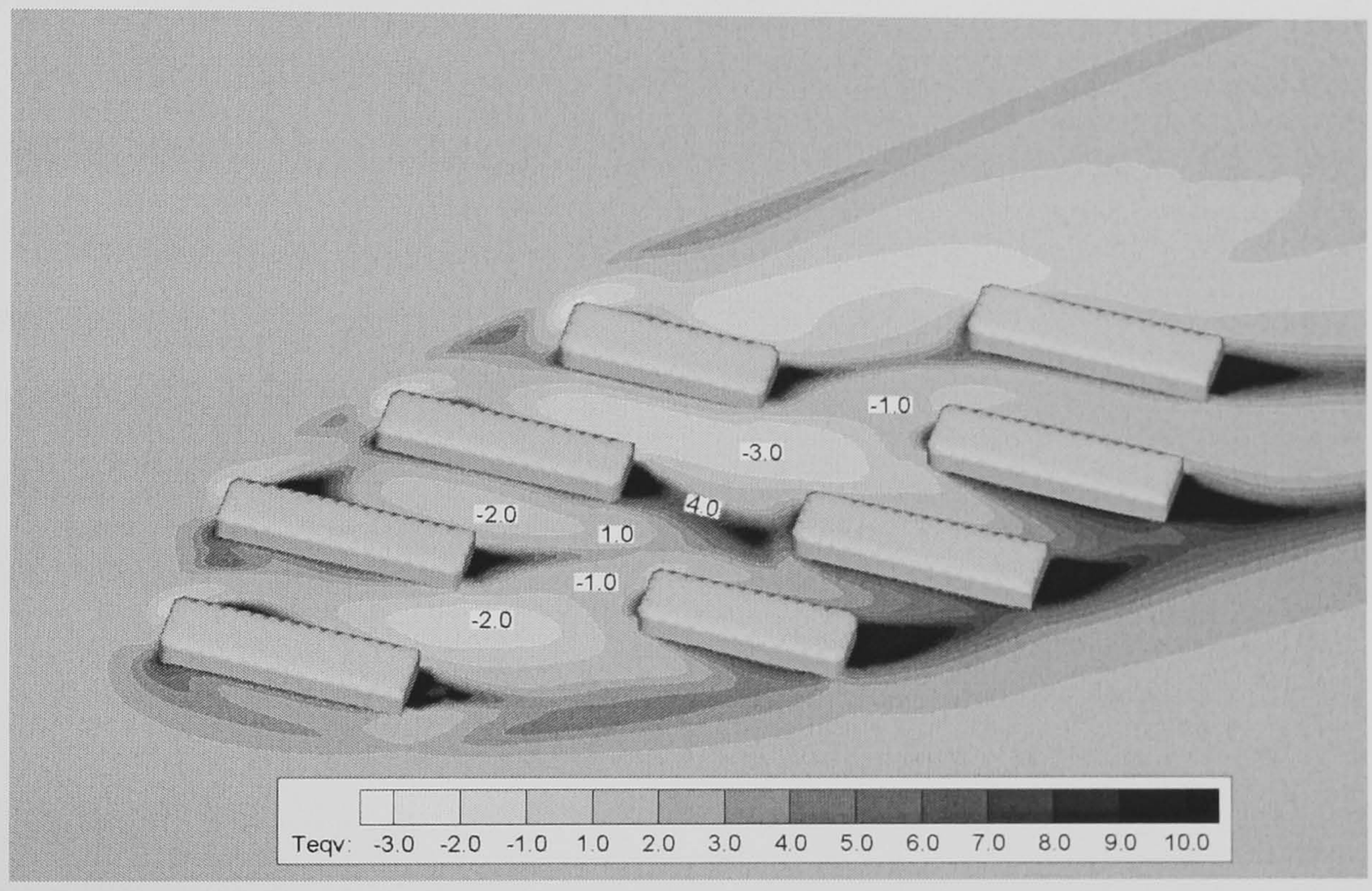

Figure 7.12 The contours of equivalent temperatures for layout A.

The windchill was expressed as the equivalent temperature T_{eqv} defined by equation (7.1) and all the equivalent temperatures were presented as contours. The shelter effects provided by layout A was somewhat insufficient, the chilling effects were significant in this occasion (figure 7.12). The warmest T_{eqv} was 4 °C and the lowest equivalent temperature -3 °C was found in the central space. Some warmer T_{eqv} were observed but they were not in the areas concerned. In a mild season, unless there is ample sunshine, people are unlikely to undertake outdoor activities in the designated space in layout A.

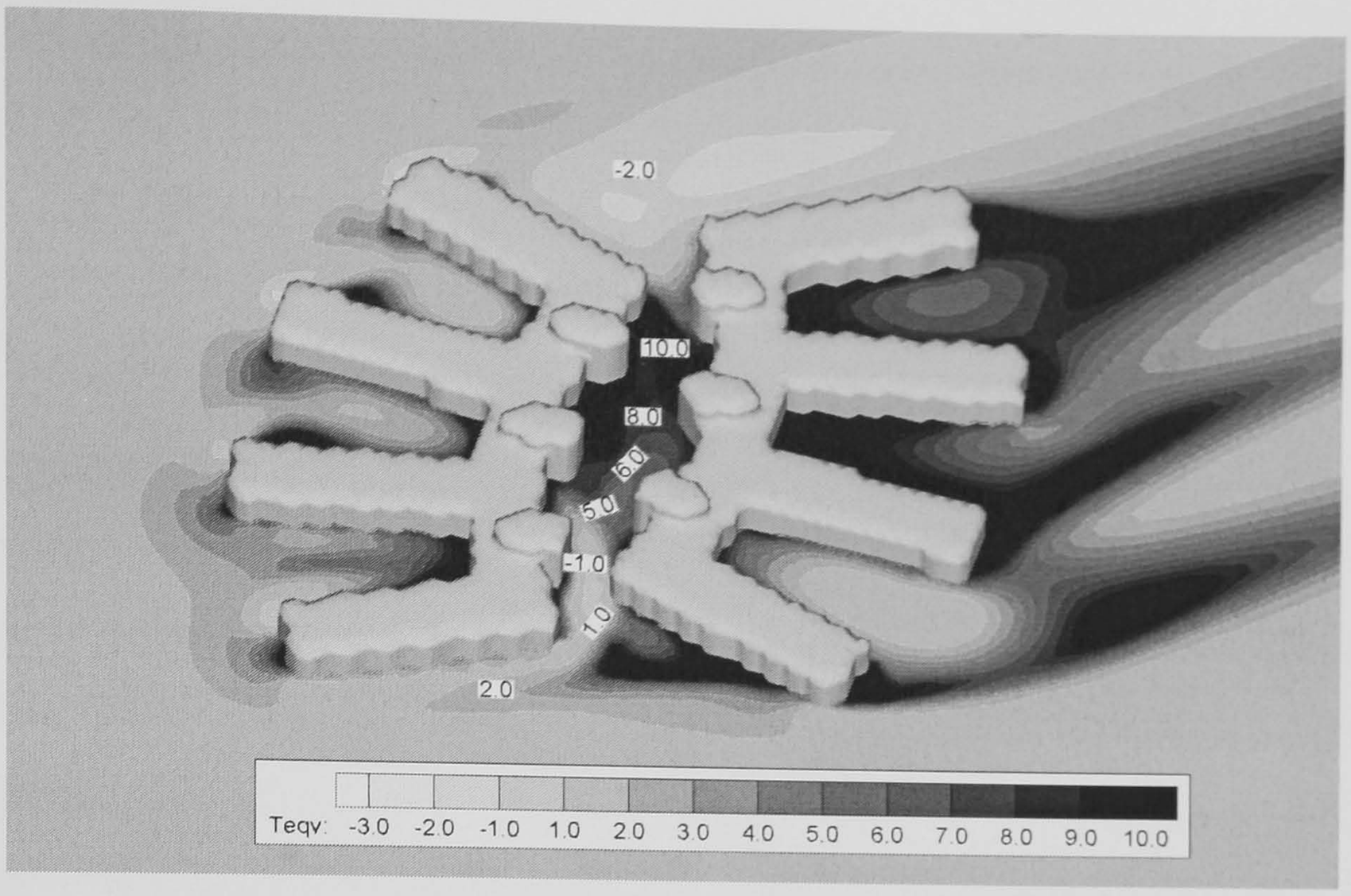

Figure 7.13 The contours of equivalent temperatures for layout B.

In contrast to layout A, the layout B created a warmer climate in the central space (figure 7.13). The equivalent temperatures were ranging from 5° C to 10° C, although there were low temperatures found at the two ends of the pedestrian walk. The low temperatures were mainly due to turbulent winds induced by the buildings. Apart from a few locations that were likely to receive unfavourable winds, the majority of the designated space for pedestrians was relatively ideal for outdoor activities in a mild season.

Overall, through the comparisons of flow pattern, comfort parameter and windchill, layout B created a better wind environment; therefore the scheme design – layout B was a better option in this project.

7.4 Summary

This chapter has presented an industrial case study of environmental design. Various environmental conditions – flow pattern, comfort parameter and windchill have been simulated by the proposed CFD methods. The comfort parameter is useful when it is associated with the frequency of occurrence. Through the comparisons and discussions, the scheme design – layout B becomes a better option in this project. The next chapter is a summary of using CFD to simulate the airflow around buildings. All the important findings obtained from the case studies in the previous chapters will be presented as guidelines to conclude this research.

Chapter 8 General Guidelines and Discussions

Using a commercial CFD package may have the advantages in the evaluation of environmental winds and the accuracy is acceptable in the validation studies. Nevertheless, to harness CFD necessitates solid mathematical background and sufficient expertise in fluid dynamics. Although many CFD commercial packages declare that their codes are user-friendly and easy to use, the danger still exists if there is no proper training provided. However, the code vendors usually can only provide limited training to their users and sometimes the programmes provided are of little help to modelling the complicated flow problems, such as the wind. Therefore the quality of a CFD model and the reliability of its predictions are greatly dependent on users' experience and their insights into the problems concerned.

This chapter summarises the findings from previous chapters and also cast out some issues for discussion with regard to modelling the wind environment around buildings using a CFD package.

8.1 The Components of CFD

Chapter 3 has dedicated considerable paragraphs to delineate the structure of CFD but some key elements can still be extracted for discussion in the following sections. CFD is principally devised to solve the unsteady and intricately coupled Navier-Stokes (N-S) equations since the analytical solutions that are generally applicable to the primitive N-S equations have not been known yet. In order to solve the N-S equations numerically, a number of techniques such as finite-difference, finite-volume and finite element methods have been widely employed. The most common one is the finite-volume method, as it is the simplest way to depict the conservation laws of mass, momentum and energy in a finite volume of fluid. The finite-volume method needs a finite number of "cells" to constitute a computational domain in which the boundary conditions need be properly defined. Each cell possesses the required physical properties such as the flux of mass, momentum and energy that are to be determined by the corresponding differential equations. The primitive N-S equations are subsequently to be integrated

and discretised into a large number of algebraic equations that can be calculated by computer. The procedure to determine the unknowns is iterative and the solution is usually a compromise between accuracy and available computing resources. In addition, if the flows are turbulent, another element – turbulence model, is required. The turbulence model is a set of algebraic or differential equations devised to solve the additional unknowns – turbulent stresses or subgrid stresses, which are the products of time-averaged N-S equations and space-filtered N-S equations, respectively. Selecting an appropriate turbulence model requires the understanding of turbulent flows and the knowledge of what phenomena have been translated into the modelled equations and its limitations. In order to create a reliable CFD simulation of the wind flows around buildings, attentions need be given to the following key elements:

- Computing domain
- Boundary conditions
- Grids or mesh
- Discretisation scheme
- Turbulence model
- Convergence criteria and numerical accuracy

Their implications to modelling the winds around buildings will be discussed individually.

8.2 Guidelines on Computing Domain and Boundary Conditions

Most of the subsonic flow problems, especially the flows around bluff bodies, are elliptic. The term "elliptic" refers to the formulation of the partial differential equations. If the partial differential equations are said to be elliptic, the solution domain must be closed. A closed domain requires its boundary conditions (BC) to be defined everywhere along its boundaries. The domain can be regarded as the test section of a wind tunnel, in which there are inlet, outlet, sidewalls, ceiling and floor. All the elements are the boundary conditions constituting the domain where the flows are to be simulated. However, sometimes a user may be careless and forget to set required boundary conditions for his CFD simulation. It might be working because sometimes a CFD code might have its default values (e.g. symmetric BC in PHOENICS) for an undefined boundary but the default values may be sometimes inappropriate for the

intended flow simulation. This also raises another question – "where are the appropriate boundaries?" or "how large is the domain size that can be considered appropriate?"

To answer these questions, one should be aware of the boundary conditions that have been defined in the CFD code. There are a number of boundary conditions, which are commonly employed by commercial CFD codes; for example, inlet, outlet, wall (moving or stationary), plane of symmetry, etc. Since all the flow simulations considered in this thesis are without heat source, i.e. all the flow simulations are adiabatic, therefore the following discussions focus on mass flows only.

Inlet: The magnitude of the inlet velocity is specified and the direction is taken to be normal to the boundary. The inlet velocity is given as

$$\mathbf{V}_{inlet} = U_{spec}\mathbf{i} + V_{spec}\mathbf{j} + W_{spec}\mathbf{k} \tag{8.1}$$

where U_{spec}, V_{spec} and W_{spec} are the velocity components in Cartesian space (x, y, z) and **i**, **j**, **k** are unit vectors. The velocity components need to be specified by the user. With the velocity specified, the total pressure is automatically calculated from

$$P_{total} = P_{static} + \frac{1}{2}\rho V^2 \tag{8.2}$$

where V is the magnitude of **V** defined in equation (8.1); ρ is the density of fluid and P_{static} is the static pressure, which may be taken from the value of reference pressure. Also, the required mass flux is given by ρV per unit area. If the flow is turbulent, additional properties need be specified. The additional values are subject to the turbulence model employed in the flow simulation. The k-ε family models require the values of k and ε, whereas other more sophisticated model such as LES necessitates that the inlet velocity is a function of time. The value of k dictates a velocity scale and the value of ε implies the corresponding length scale of turbulence. If the user does not specify the values of k and ε, the intensity of turbulence is required for the CFD code to calculate the values of k and ε. The auto-computed values are given by

$$k = (UI)^2 \qquad \varepsilon = C_\mu^{3/4} k^{3/2} / l_m \qquad l_m \approx 0.1H \tag{8.3}$$

where I is the turbulence intensity ($0.01 < I < 0.05$) and l_m is a length scale taken from a characteristic length H of the inlet. The connections defined in equation (8.3) are derived from internal pipe flows; therefore the turbulence intensity and length scale may be unsuitable if it is applied to external flows. It is recommended to specify k and ε in the external flow simulations if they are known. The appropriate values for k and ε have been suggested by Richards and Hoxey (1993) and the practices have been illustrated in the chapters 5 and 6.

The velocity specified by the user will create a velocity profile that represents the approaching flows. A distance between the object (e.g. building) and the inlet is required in order to keep the profile correct. This can be further illustrated in figure 8.1.

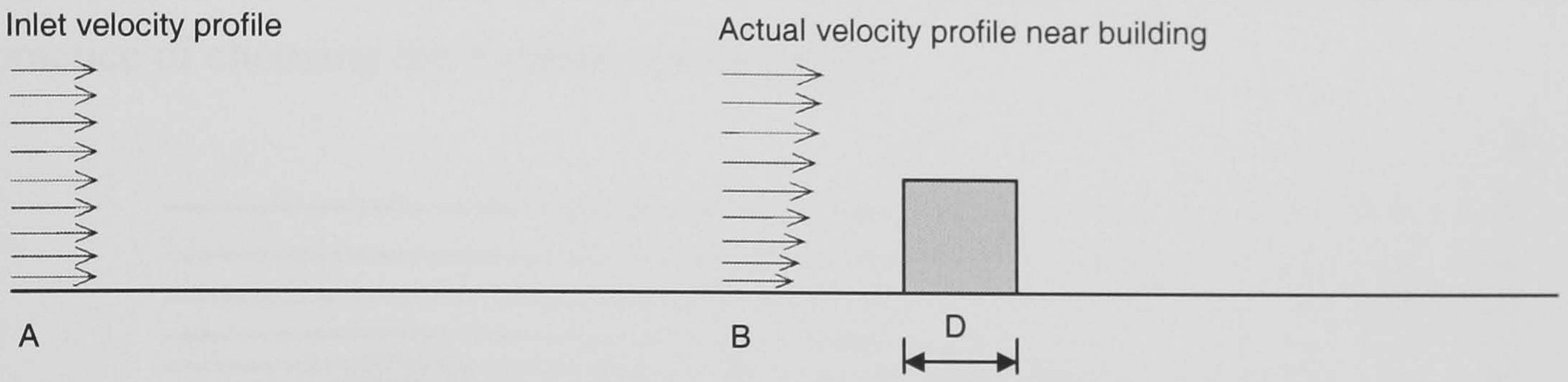

Figure 8.1 The implication of the inlet location. If the inlet is placed at location "B" but using a velocity as it is at location "A", the velocity profile is incorrect and it need be redefined using profile "B".

In figure 8.1, if the distance between the inlet and the building is small, say 1.0D, and if the inlet profile is defined as uniform flow, it is not correct because the actual velocity profile near the object is affected by shear, i.e. velocity gradient can be present. Therefore if the inlet is to be set very close to the object, the velocity profile must be redefined. It may be difficult unless the velocity profile is known by measurement. Another danger is that if the flow separation exists in front of the object, the flow field will be unstable and very complicated, which renders a simple velocity profile invalid. As a result, it may be safer to put the inlet farther from the building and the recommended distance is 3.0D – 5.0D to avoid unwanted flow conditions. The upstream velocity profile must be specified at an appropriate location where reasonable estimates are available.

Outlet: The required condition is usually a fixed pressure (static). The fixed pressure is uniformly distributed on the surface normal to the stream. It is specified by

$$P_{static,\ outlet} = P_{spec} \tag{8.4}$$

The specified pressure is usually a relative pressure and the value is zero. It is also possible to specify a velocity profile at the outlet but it is of use only if the outlet velocity profile is known and if it may have significant influence to the upstream flow field of concerns.

A proper distance between the outlet and the object is also required since the boundary condition – zero static pressure must be satisfied. It implies that the pressure gradient in the nearby flow field must be a favourable gradient, i.e. $\partial p/\partial x < 0$, which also stipulates that flow recirculation is not allowed. Figure 8.2 shows the good practice and bad practice of choosing the location for the outlet.

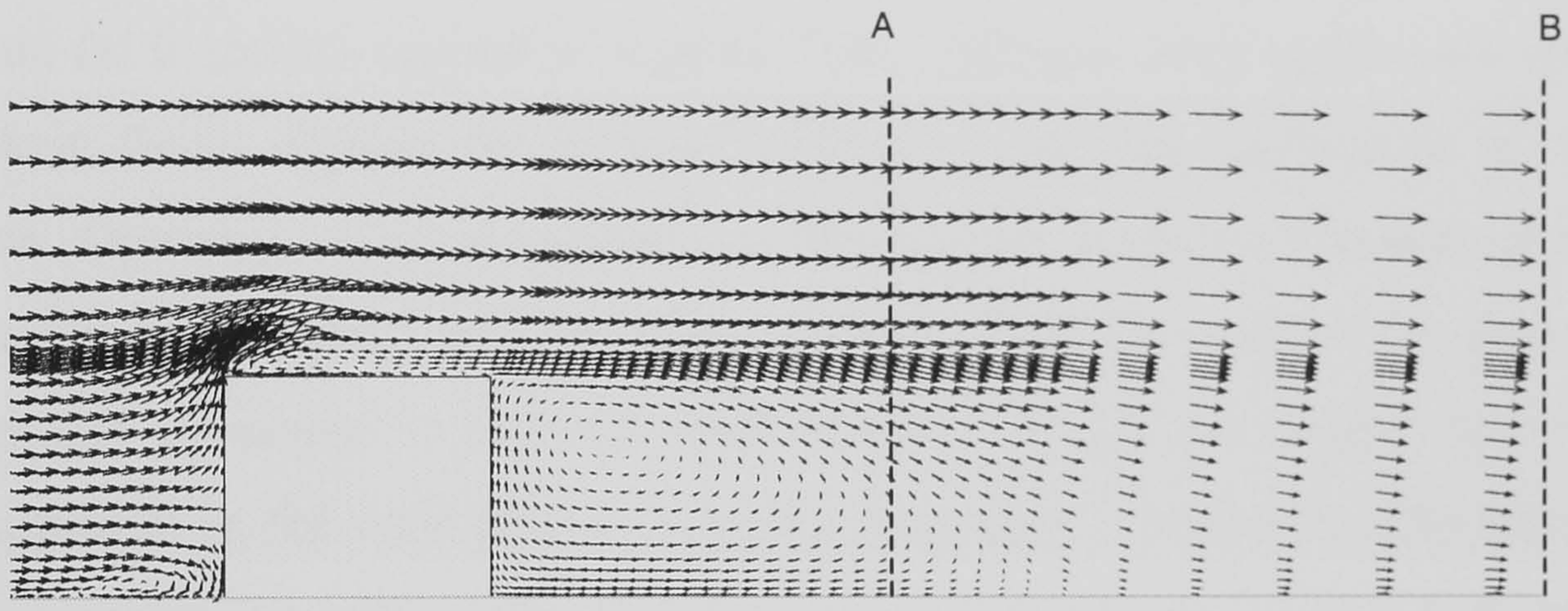

Figure 8.2 The choice of outlet location. Location "A" is a bad choice because there are some flow recirculation over a part of it. Location "B" is a better choice as it has avoided the unwanted "inflow" across the outflow boundary.

As the wake flows may affect the location of a suitable outflow boundary, the same question is "how far can it be suitable?" According to Castro and Robins (1977), a distance of 8.5H (H is the cube height) makes no discernible deviation of the mean velocity profile from the upstream velocity profile and even at a distance of 4.5H, the differences are only a few percent. Their measurement gives a good reference value but they have also observed that the velocity profile of the wake is also dependent on the upstream shear, turbulence intensity and the orientation of the cube. Therefore an appropriate distance between the object and the outlet boundary is problem-dependent. If a distance needs to be recommended, a minimum value of 5.0H (H is a characteristic height, say, the height of the tallest building) probably is a safer choice.

Wall: There are moving walls and stationary walls. The discussion presented here is mainly concerned with stationary walls as the moving walls are rarely applied in the bluff-body flow simulations. To specify a wall as a boundary condition is straightforward in most of the CFD codes but the function of a wall may be sometimes perplexing since there are a variety of wall functions available as options. For instance, PHOENICS has four wall functions that may be selected for a specific wall. The available options are:

(a) Blasius law (power law or 1/7 law)

(b) Equilibrium logarithmic law

(c) Non-equilibrium logarithmic law of Launder and Spalding (1974)

(d) Fully rough logarithmic law

The option (a) is mostly applied in laminar flows, whereas other options are applicable to turbulent flows. Option (b) is ideal if there is no flow separation in the flow simulation. Option (c) is recommended to calculate the turbulent transport of heat and species at a reattachment point. The final option – option (d) is similar to option (b) but the roughness parameter is defined as an effective roughness height (z_0), which is mostly appeared in the atmospheric boundary layers (c.f. chapter 2). The default wall function is option (b) with a smooth wall. User can specify the roughness by means of equivalent "sand-grain" roughness height (c.f. Schlichting, 1968) or alternatively, use option (d) when a rough wall is needed for the flow simulation.

The use of wall function is not arbitrary and it needs to be considered with turbulence model. Usually the high-Reynolds-number models (e.g. standard k-ε model) need the wall function to account for the wall-affected viscous layer in which the boundary conditions are determined with the empirical formulae supplied by a specific wall function. Some models require fine grids implementation near the walls, e.g. low-Reynolds number models in which the wall functions are not applicable. These will be discussed together with the guidelines on grid generation in section 8.3.

Symmetry Plane: This boundary condition imposes constraints which "mirror" the flow on either side of it. The plane is impervious to flows and the velocity component normal to that plane is set to zero:

$$\mathbf{V}_n = 0 \tag{8.5}$$

The gradients of scalars (p, k, ε, etc.) normal to the plane is also set to zero:

$$\frac{\partial \phi}{\partial n} = 0 \qquad \phi = p, k, \varepsilon, \text{etc.} \tag{8.6}$$

The plane of symmetry is a default boundary condition in PHOENICS if no user input is set for that boundary. It is frictionless and adiabatic in addition to the conditions specified in equations (8.5-6).

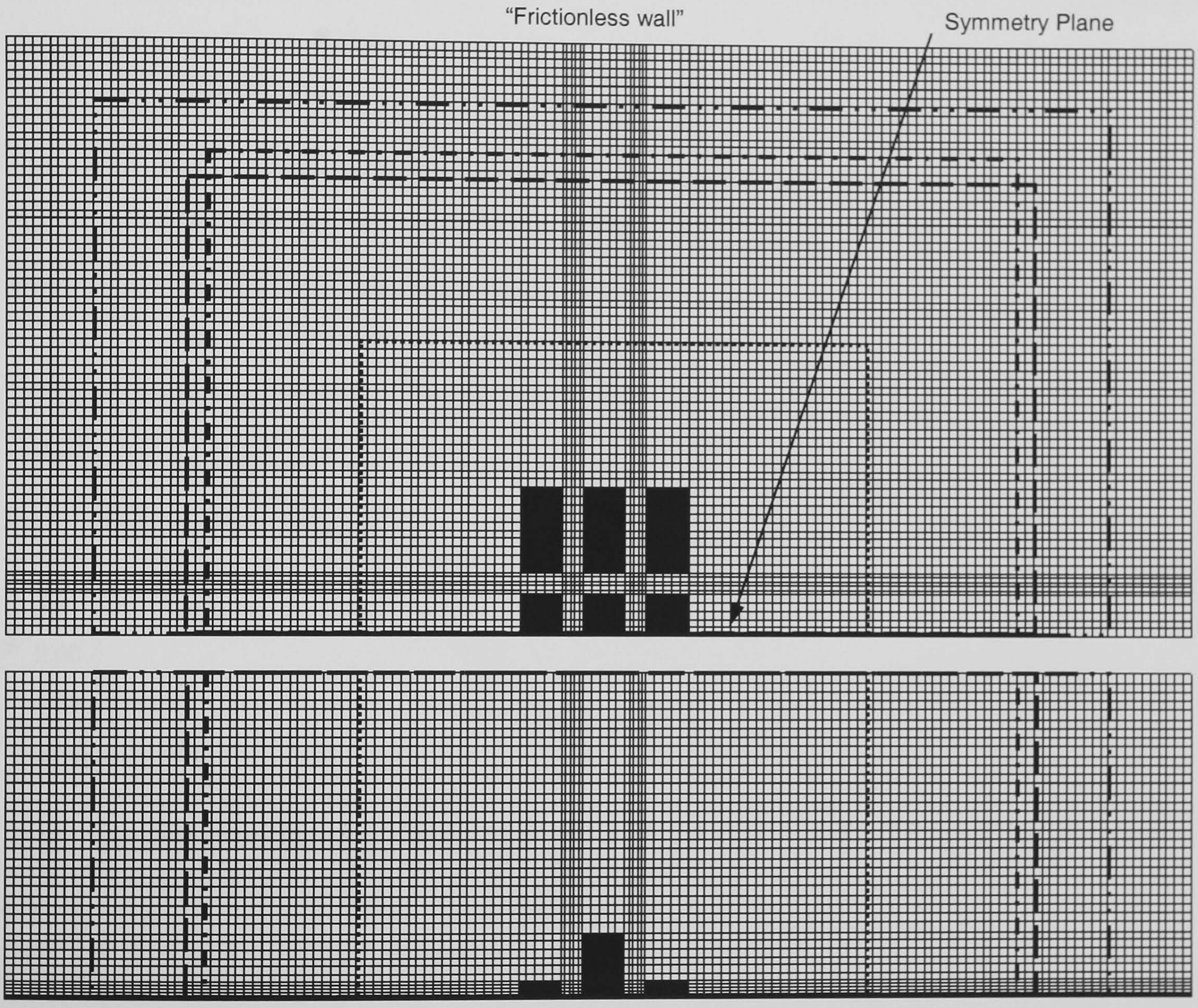

Domain size	Legend	Number of Grids (x, y, z)
600m × 350m × 380m (Domain 1)	.....	65×37×40
960m × 555m × 380m (Domain 2)	– · – · – ·	101×58×40
1000m × 525m × 380m (Domain 3)	— — —	105×55×40
1200m × 625m × 380m (Domain 4)	— · · —	125×65×40
1400m × 700m × 380m (Domain 5)	———	145×72×40

Figure 8.3 Domain size testing. The upper drawing is the horizontal plane and the lower one is the vertical plane of the computing domain. The sides and the top of domain are symmetry planes or "frictionless walls".

The plane of symmetry can also be seen as a "frictionless wall" since it is impervious to flows. Care still need be taken when it is used as a frictionless wall. A minimum distance of 5.0H between any building and the "frictionless wall" probably is recommended. Or, more scientifically, the appropriate locations of the frictionless wall can be determined by a sensitivity test (figure 8.3-4). In the test, the boundaries of the domain were composed of a symmetry plane, smooth wall (as the ground) and the frictionless walls (as other boundaries). The grids were uniformly distributed but the density of the grids in the streets was slightly higher. The height of the domain was fixed because the thickness of atmospheric boundary layer was known. Since it was to test the sensitivity of the velocity field in the streets by varying the size (horizontally) of the domain, no local refinement of grids was done in this testing. The main purpose was to determine the location of the "frictionless wall". The results of the test are shown in figure 8.4, the velocity variations between different domains become insignificant when the size of domain is larger than "Domain 3". Therefore "Domain 3" can be an appropriate selection in this case.

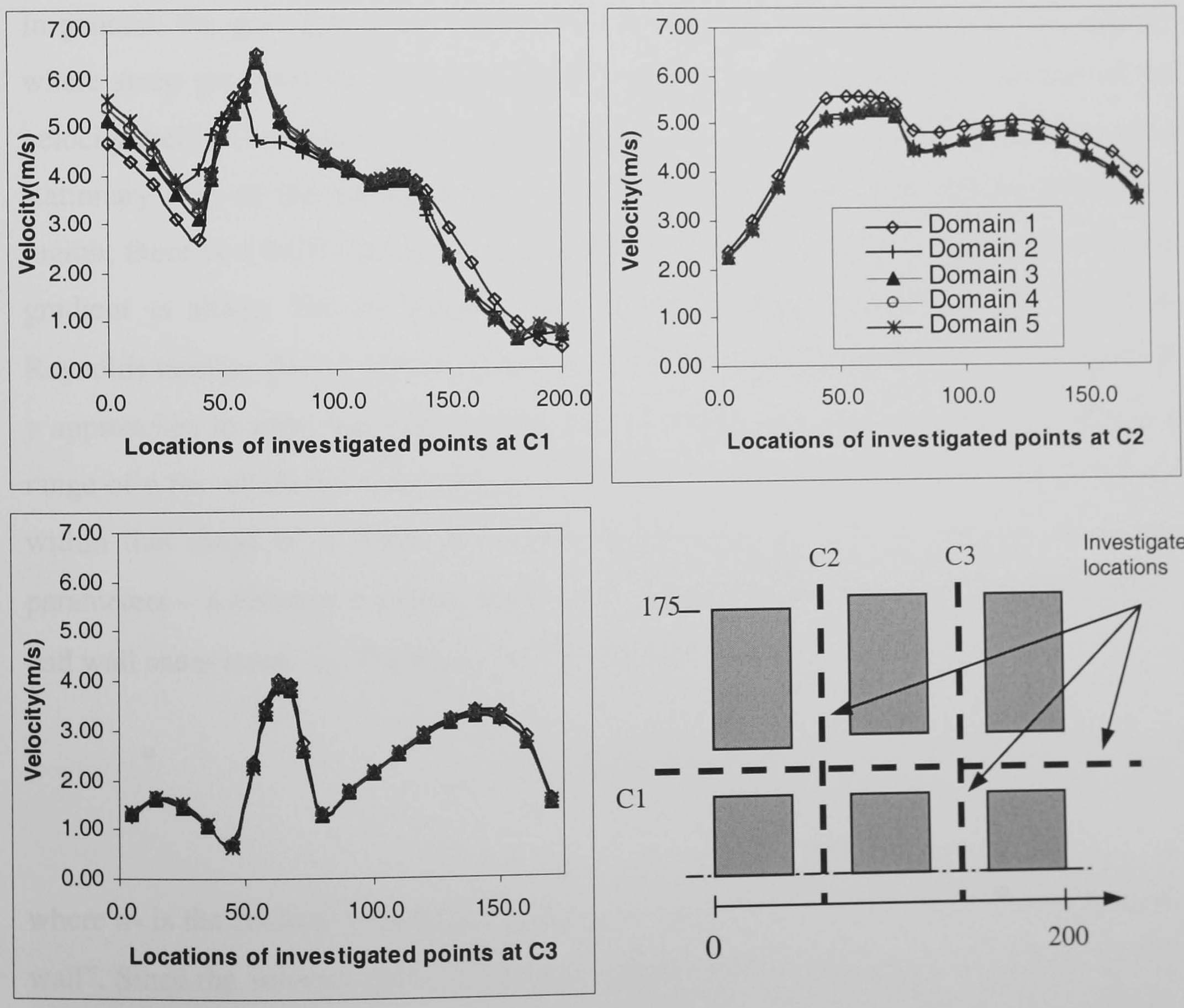

Figure 8.4 The results of the domain size testing.

An experienced user may use his "rule of thumb" to determine the domain size. Either way, the basic principles are to ensure that the specified boundaries are compatible with their mathematical definitions. This is one requirement of a reliable flow simulation.

8.3 Guidelines on Grid Generation

The computational grid is crucial to the CFD computation. The grid generation is not only in close connection with the geometry but also the resolution of flow field and the efficiency of computation. Better grids usually can yield better flow simulation in which some flow features such as flow separation and reattachment can be captured as desired. However, the number of grids also affects the efficiency of computation. Coarse grids require fewer CPU time and storage but finer grids need more computing resources and sometimes using very fine grids may cause difficulties in computation, i.e. sluggish convergence or even worse. It is fairly adequate to say that the quality of grids is almost equal to the quality of a CFD simulation.

In general, the grid density is closely related to the velocity gradients, i.e. the regions where steep gradients exist would need fine grids to resolve the rapid variation of the velocity field. The velocity components parallel to a wall is zero at the surface of a stationary wall as the no-slip condition applies. Between the wall and the freestream region, there is a buffer layer or, more generally, boundary layer in which the velocity gradient is sharp. The thickness of the boundary layer is dependent on the local Reynolds number ($\mathrm{Re}_y = Uy / \nu$), which is based on a distance (y) away from the wall. If y approaches to zero, the value of Re_y will also approach to zero and there will be a range of y for which the value of Re_y is on the order of 1. The viscous effects dominate within that range of y. Since the mean velocity near the wall is affected by several parameters – a distance y normal to the wall, fluid dynamic viscosity μ, fluid density ρ, and wall shear stress τ_w. Therefore, by dimensional analysis, it shows that

$$u^+ = \frac{U}{u_*} = f\left(\frac{u_* y}{\nu}\right) = f(y^+) \tag{8.7}$$

where u_* is the friction velocity ($u_* = (\tau_w / \rho)^{1/2}$). Equation (8.7) is termed as "law of the wall". Since the velocity profile $U(y)$ is no longer determined by the freestream velocity U_∞ only, the velocity profile within the boundary layer is represented by the "velocity-defect-law":

$$\frac{U_\infty - U(y)}{u_*} = g\left(\frac{y}{\delta}\right) \tag{8.8}$$

where δ is the thickness of the boundary layer. The turbulent boundary layer adjacent to a solid surface is composed of two regions:

- The inner region: about 10 – 20% of the total thickness of the boundary layer; the shear stress is (almost) a constant and it is equal to the wall stress τ_w. This region consists of two layers: *linear sub-layer* and *log-law layer*.

  - the linear sub-layer: it is a very thin layer in which the viscous stresses dominate the flow adjacent to the surface. The value of u^+ is equal to y^+ in this layer ($5 \le y^+ \le 10$).
  - the log-law layer: in this layer the viscous stresses and turbulent stresses are equally important. The well-known log-law formula is derived from this region. It is generally within the range of $30 \le y^+ \le 500$ but the upper limit of y^+ is dependent on the Reynolds number.

- The outer region: it is inertia-dominated region far from wall and it is free from direct viscous effects.

To account for the viscous effects at the wall and to resolve the rapid variation of flow variables which occurs within the boundary-layer region has been a very active research theme in the CFD community. Currently there are two approaches commonly employed by commercial CFD codes, one is the wall-function approach and the other one is the low-Reynolds-number method. Use of the low-Reynolds-number method may cost greater CPU time and storage because it requires more nodes placed in the near wall region. It is not recommended unless the flow features near the wall are crucial to the problem of concerns.

If the wall-function approach is employed, the recommended number of nodes placed in the boundary layer is at least 10 and the first node near the wall should be placed in the range $30 \le y^+ \le 130$. It may be difficult to estimate the value of y^+ since it requires the value of u_* but it remains unknown until the CFD simulation is done. An empirical

formula proposed by Schlichting (1968), which is derived from the velocity profile in a smooth pipe may be used as a reference value when the estimate need be made. The friction velocity is given by:

$$u_* = 0.150U^{\frac{7}{8}}\left(\frac{\nu}{y}\right)^{\frac{1}{8}} \tag{8.9}$$

where U is the freestream velocity, y is the physical distance away from the wall and ν is the kinetic viscosity of the fluid.

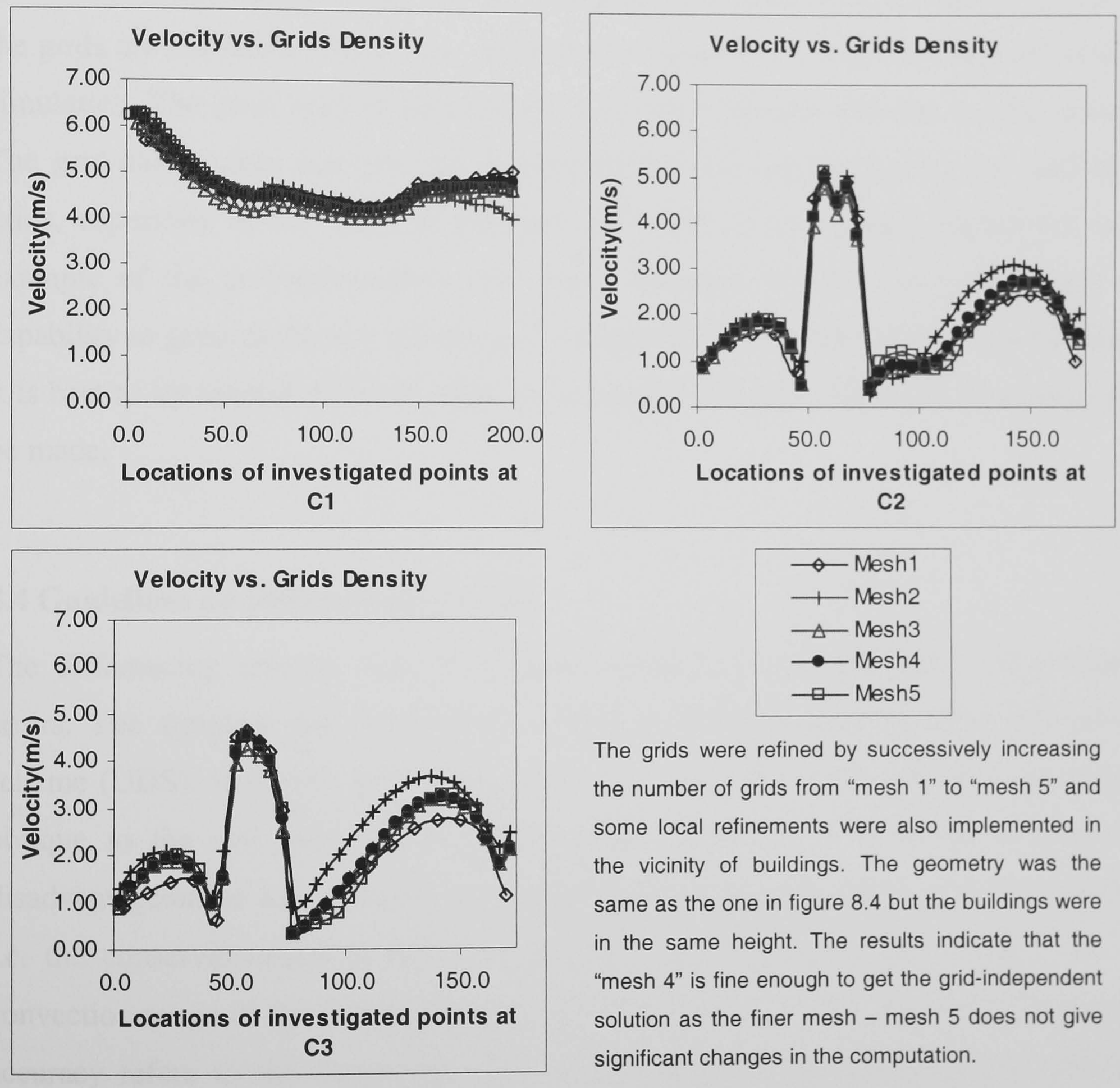

The grids were refined by successively increasing the number of grids from "mesh 1" to "mesh 5" and some local refinements were also implemented in the vicinity of buildings. The geometry was the same as the one in figure 8.4 but the buildings were in the same height. The results indicate that the "mesh 4" is fine enough to get the grid-independent solution as the finer mesh – mesh 5 does not give significant changes in the computation.

Figure 8.5 The sensitivity test of mesh refinement.

Another much simpler formula can be found in Bradshaw (1971) in which the value of u_* is given as $u_* \approx 0.04U$. The user may try both formulae and select a bigger value as a conservative estimate.

The main purpose of grids refinement is to enhance the resolution of the flow field. In addition, the knowledge of boundary layer is required when creating grids in the near-wall regions. Using an expansion ratio to control the distribution of grids near a wall is recommended because it can enhance the resolution in the region very close to the wall.

In addition, the performance of a turbulence model may also be dependent on the grids, as demonstrated by Thangam and Speziale (1992). They have concluded that the poor performance of a turbulence model is sometimes due to insufficient resolution. Richards (1989), Baskaran and Stathopoulos (1992), Baskaran and Kashef (1996) also have shown that some flow features like the separation and reattachment may be missing if the grids are too coarse. Therefore, refinement of grids is an important task in the CFD simulation. The grids need be refined until a grid-independent solution can be attained. The grid-independent solution can be obtained by refining (increasing the number of grids, especially in the areas of interests) the mesh in succession. Figure 8.5 is an example of the grid-independent test. Some commercial CFD codes may have the capability to generate locally refined grids automatically but care still need be taken and it is best to try several different densities of meshes before a final flow simulation is to be made.

8.4 Guidelines on Differencing Scheme

The differencing scheme (DS) is in close connection with the spatial discretisation errors. The simplest and most robust scheme is the first-order upwind differencing scheme (UDS). However, it has been found very diffusive when the flow direction is oblique to the cell face (Malin and Waterson, 1999). The numerical diffusion is disadvantageous to the transport of momentum or scalar flux during the computation, i.e. the conservativeness is not well secured. Using a higher-order scheme for the convection terms of the transport equations may improve the inadequacy. The order of accuracy refers to the truncation error of the scheme's exact formulation based on Taylor expansion series. For a function $\phi(x)$ the Taylor series development of $\phi(x + \Delta x)$ around the point i at x is

$$\phi(x+\Delta x) = \phi(x) + \left(\frac{\partial \phi}{\partial x}\right)_x \Delta x + \left(\frac{\partial^2 \phi}{\partial x^2}\right)_x \Delta x^2 + \ldots\ldots \tag{8.10}$$

therefore,

$$\left(\frac{\partial \phi}{\partial x}\right) = \frac{\phi(x+\Delta x) - \phi(x)}{\Delta x} + O(\Delta x) \tag{8.11}$$

The $O(\Delta x)$ represents the truncated terms. Equation (8.11) can also be written as

$$\left(\frac{\partial \phi}{\partial x}\right) = \frac{\phi(x+\Delta x) - \phi(x-\Delta x)}{2\Delta x} + O(\Delta x^2) \tag{8.12}$$

with a derived expression of $\phi(x - \Delta x)$ by replacing the $+\Delta x$ with $-\Delta x$ in equation (8.10). The order of accuracy in equation (8.12) is of second order, whereas the representation of $(\partial \phi / \partial x)$ in equation (8.11) is of first order by neglecting the truncated terms. The term Δx can be seen as the spacing between each node in the discretised computational domain and theoretically a smaller spacing can obtain a better approximation. The impact is greater if a higher-order scheme is employed.

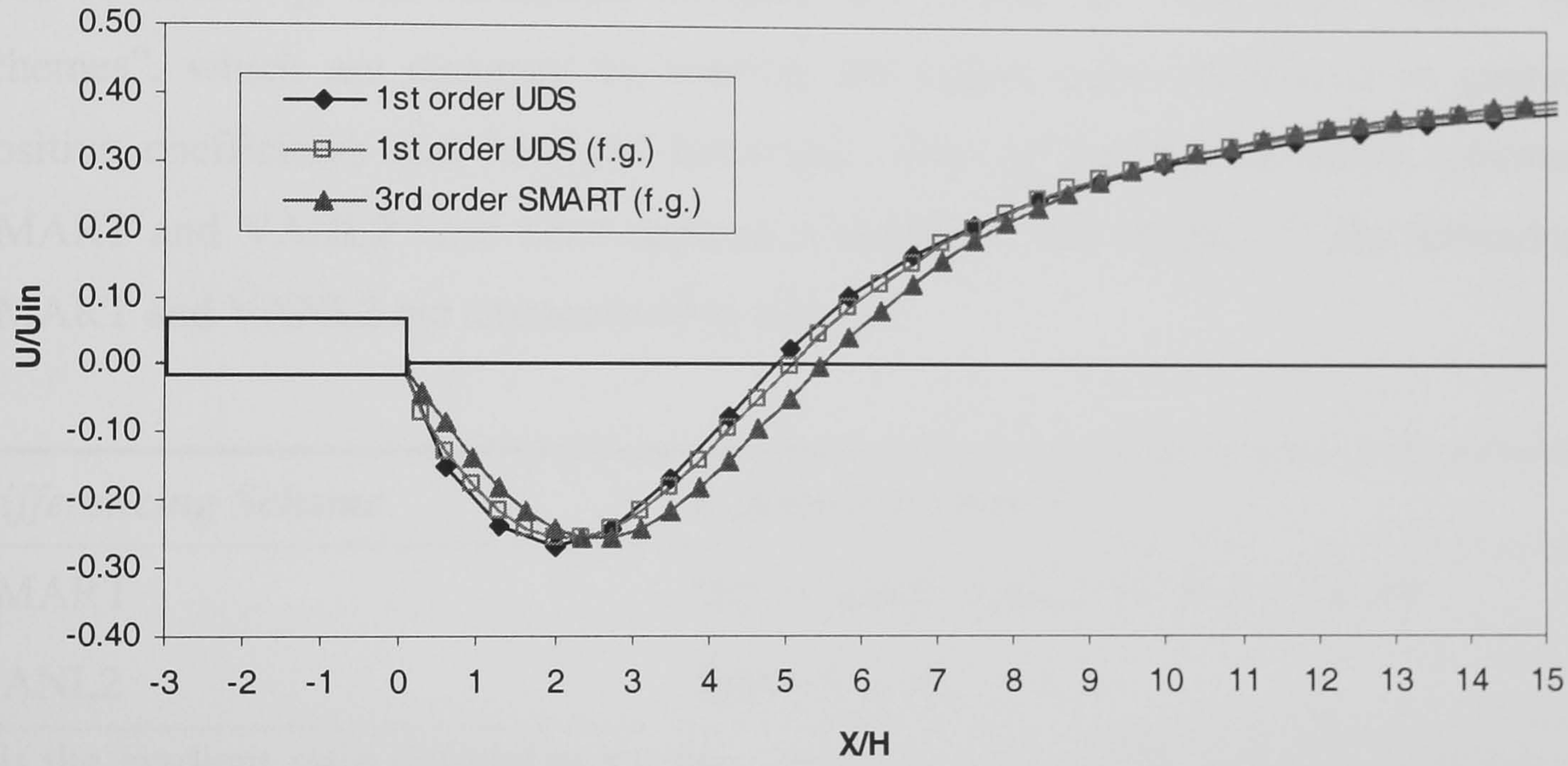

Figure 8.6 Turbulent flow past a backward-facing step using a first-order UDS and a third order SMART scheme.

For example, halving the cell size in all directions using a third-order scheme will reduce the numerical error by a factor of 8, while this factor is only 2 with a first-order scheme. In other words, the improvement of accuracy is slow if using a first-order scheme. Figure 8.6 illustrates this implication by a simulation of the turbulent flow past a backward-facing step. The reattachment length predicted by 1st order UDS was 4.87H (H is the step height) using coarse grids, whilst the reattachment length slightly increased to 5.08H using finer grids (by halving the cell sizes at the streamwise direction only). Nevertheless, using a 3rd order scheme – SMART significantly increased its length to 5.49H with the same cells. The measured value, supplied by

CHAM in the library case (T103) of PHOENICS is 5.66H. The comparison shows using a higher-order scheme does improve the resolution and accuracy faster than a 1st order scheme does in this case.

Another consideration of using high-resolution schemes is the requirement of boundedness. Some higher-order differencing schemes are unbounded, including the QUICK scheme of Leonard (1979). The QUICK scheme is of 3rd order and it has been a favourable choice for the momentum equations but it is inappropriate for the transport equations of turbulence energy k and its dissipation rate ε (Bosch and Rodi, 1998), since it is unbounded. This unboundedness behaviour usually arises in the regions where steep gradients are present and in the calculations of turbulence energies. The spurious oscillations are usually caused by the higher-order terms (Waterson, 1994). Therefore many researchers have attempted to improve the inadequacy of those schemes at some cost of accuracy. The modified schemes are termed as "non-linear higher order schemes", which are designed by limiting the higher-order corrections to guarantee positive coefficients and bounded behaviour. Two of the representative schemes – SMART and VANL2 have been applied in chapter 4 and chapter 7. The formulae of SMART and VANL2 are summarised in table 8.1.

Differencing Scheme	***Limiter Function*** B(r)
SMART	$B(r) = \max(0, \min(2r, 0.75r + 0.25, 4))$
VANL2	$B(r) = (r + \lvert r \rvert) / (r + 1)$

r is the gradient ratio defined as $r = (\phi_D - \phi_C) / (\phi_C - \phi_U)$, where ϕ_U is the upstream cell-centred value; ϕ_C is the centre cell-centred value and ϕ_D is the downstream cell-centred value (c.f. figure 3.12).

Table 8.1 The differencing schemes – SMART and VANL2 with their corresponding limiter functions.

The SMART scheme of Gaskell and Lau (1988) is a modified version of QUICK and it is a piecewise-linear scheme, which is most likely to give good accuracy as it can switch between linear schemes (e.g. QUICK) for higher accuracy where possible, controlled by the limiter function but the discontinuous nature may result in convergence problem. In contrast, the VANL2 scheme is a smooth scheme, which is operated by a smooth and continuous limiter function without discontinuous switching, thereby aiding the convergence with slightly less accuracy. The selection of a higher-order scheme is

dependent on the user's experience and preference, as different schemes need different treatments with regard to the relaxation factors. For example, the SMART scheme entails a very strong under-relaxation factor during the computation but a weaker value of the under-relaxation factor the VANL2 scheme may suffice.

Although the first-order scheme is not recommended for the flow simulations that require higher accuracy, it can still be used as a start of a computation. Since it is robust and stable, usually it can yield convergence within a few hundred times of iterations using a very weak under-relaxation factor. It is also good for the initial testing of domain size and grid-independent study. The results of the tentative computation can be subsequently used as the initial values for another run using the higher-order schemes to produce a fine-tuned numerical simulation.

8.5 Guidelines on Turbulence Model

A CFD simulation of airflow around buildings is inevitably associated with the turbulent flows. Theoretically, turbulent flows can be resolved without any "model" by Direct Numerical Simulation (DNS). The DNS approach is, however, limited by currently available computing power and it is not feasible yet to simulate general turbulent flows involving a wide range of time and length scales. The time scales need to be approximated by temporal discretisation and the length scales require spatial discretisation and both discretisations need to resolve the time and length scales from the smallest scales to the largest ones. The number of cells and time steps required is too huge to be computed using affordable computing resources. In other words, unless there is a great leap forward in computer technology so that the number of grids beyond 10^9 can be calculated in an acceptable amount of time (say, hours if not days), it is not realistic to apply DNS in general flow problems involving turbulence. Therefore, a particular "model" that may account for some important characteristics of turbulence is required for turbulent flow simulations. Since it is a "model", the solutions given by suchlike simulations are not exact and sometimes unsatisfactory due to the knowledge concerning the complicated flow phenomena is limited. Bradshaw (1997) made an interesting statement to describe the way of using a turbulence model to solve the turbulent flow problems as:

"*a cheap answer to expensive problems*"

Apparently, any turbulence model has its limitations and there is no "universal model" that can be applicable to any turbulent flow. Therefore, the discussion in this section is limited to the turbulence models that have been used in this study. It has been shown that two-equation models are the most widely employed turbulence models in the industry and among which the standard k-ε model with wall functions is most popular. Its limitations are also well documented, such as

(a) excessive production of turbulence energy (KE) in regions of flow impingement,
(b) poor performance in flow separation under the action of adverse pressure, and
(c) flow recovery after reattachment is poorly predicted.

The implications of (a) may lead to poor prediction of heat transfer and the development of boundary layer flow around leading edges and bluff bodies (Casey and Wintergerste, 2000). The most prominent example is that the flow separation around the leading edge may be less accurate or missing due to the excessive production of turbulence energy (figure 8.7).

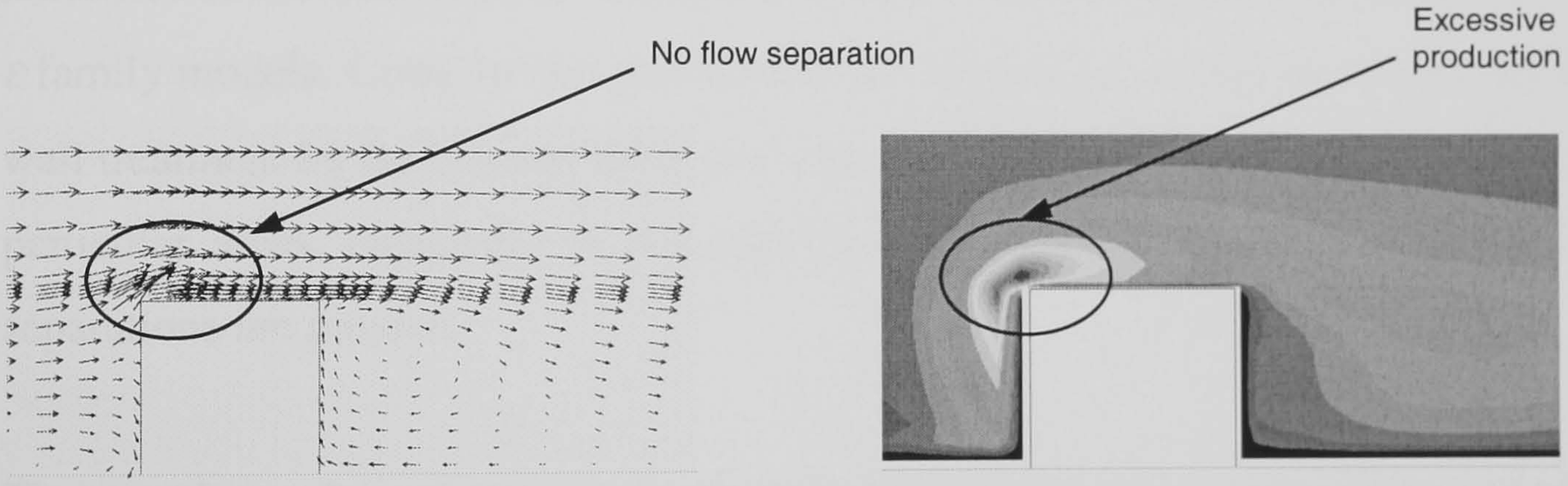

Figure 8.7 The implications of excessive production of KE.

The feature of flow separation is missing in figure 8.7. This may be improved by increasing the number of upstream grids but the feature may be still less accurate, as it has been compared in chapter 4. A modification made by Renormalization Group (RNG) to the standard k-ε model was an attempt to correct this problem. The model is known as RNG k-ε model in which some constants in the standard k-ε model are modified and a correction term is added to the ε equation. This has been successful to eliminate the excessive production of KE in the impinging areas but another problem is introduced – the worse prediction of flow reattachment in the wake. As has been shown in chapter 4, the calculated length of the recirculation zone behind the cylinder is longer than the prediction made by the standard k-ε model and the recovery of velocity in the

wake is also slower. Using the RNG model may be more suitable for other types of flow simulations but it is not recommended for the flow simulation around buildings, especially when the surrounding flow fields are the main concern.

The phenomena of (b) were observed in chapter 4 and 5, where the flow separation areas in front of the cube were inevitably smaller compared to the experiments. The results made by the two-layer k-ε model were slightly better than the standard k-ε model. One explanation to the inadequacy of the model is that the flow field within the separation region is highly unstable and therefore the actual turbulent stresses generated within this region cannot be simply approximated with the isotropic eddy viscosity hypothesis and wall functions. The improvement presented by the two-layer k-ε model is probably because it employs a one-equation model involving the length scale prescription near the wall.

Regarding the phenomena (c), as it has been observed in chapter 4, the computed velocity profile after reattachment is weaker than the measured values. This may be also attributed to the drawback of the isotropic eddy viscosity hypothesis employed by the k-ε family models. Consider the phenomena (a), (b) and (c), it may conclude that the near wall treatment by the conventional wall function approach seems unsatisfactory in some particular areas, especially in the regions where adverse pressure gradients or flow separations are present.

The two-layer k-ε model improves the deficiencies by employing a length scale prescription to avoid the use of wall functions. It is a variant of low-Reynolds-number k-ε model but it has been designed to limit the use of intensive mesh near the wall by a modelled equation of ε. Since the conventional low-Reynolds-number k-ε models involve a transport equation of ε and the gradient of ε is very steep near the wall, hence very fine grids are needed to resolve the steep gradient of ε. The complete set of the two-layer k-ε model built in PHOENICS is given as following equations.

Outer layer:

$$\nu_t = C_\mu \frac{k^2}{\varepsilon} \tag{8.13}$$

$$\underbrace{\frac{\partial k}{\partial t}+U_i\frac{\partial k}{\partial x_i}}_{\text{transport of } k}=\underbrace{\frac{\partial}{\partial x_i}\left(\frac{\nu_t}{\sigma_k}\frac{\partial k}{\partial x_i}\right)}_{\text{transport of } k \text{ by diffusion}}+\underbrace{\nu_t\left(\frac{\partial U_i}{\partial x_j}+\frac{\partial U_j}{\partial x_i}\right)\frac{\partial U_i}{\partial x_j}-\varepsilon}_{\text{rate of production of } k \text{ - rate of destruction of } k} \tag{8.14}$$

$$\underbrace{\frac{\partial \varepsilon}{\partial t}+U_i\frac{\partial \varepsilon}{\partial x_i}}_{\text{transport of } \varepsilon}=\underbrace{\frac{\partial}{\partial x_i}\left(\frac{\nu_t}{\sigma_\varepsilon}\frac{\partial \varepsilon}{\partial x_i}\right)}_{\text{transport of } \varepsilon \text{ by diffusion}}+\underbrace{C_{1\varepsilon}\frac{\varepsilon}{k}\left(\frac{\partial U_i}{\partial x_j}+\frac{\partial U_j}{\partial x_i}\right)\frac{\partial U_i}{\partial x_j}-C_{2\varepsilon}\frac{\varepsilon^2}{k}}_{\text{rate of production of } \varepsilon \text{ - destruction of } \varepsilon} \tag{8.15}$$

$$C_\mu=0.09,\sigma_k=1.00,\sigma_\varepsilon=1.30,C_{1\varepsilon}=1.44,\text{ and } C_{2\varepsilon}=1.92 \tag{8.16}$$

Inner layer:

$$\nu_t=C_M\times k^{1/2}\times f_u\times l_m \tag{8.17}$$

$$\varepsilon=C_D\times\frac{k^{3/2}}{l_\varepsilon} \tag{8.18}$$

$$l_\varepsilon=\frac{l_m}{1+5.3/\mathrm{Re}_y} \tag{8.19}$$

$$f_\mu=(1.0-e^{(-0.0198\times \mathrm{Re}_y)}) \tag{8.20}$$

$$\mathrm{Re}_y=\frac{k^{1/2}y}{\nu} \tag{8.21}$$

$$l_m=\kappa\times y \tag{8.22}$$

where κ is the von Kármán's constant (= 0.41), C_M = 0.5478, C_D = 0.1643, l_ε is the length scale and y is the distance normal from the wall. The inner layer and the outer layer are matched at the regions where Re_y = 350. A noticeable difference of the treatment with respect to ε is that its value is determined by the transport equations (8.14-15) in the outer layer but it is determined by a length scale prescription (8.18) in the inner layer. In addition, since the velocity scale employed in equation (8.21) is obtained from the turbulence energy, which is not associated with a friction velocity ($u*$) – that is usually appeared in the wall functions, the treatment in equation (8.21) and the related equations has been considered also suitable for separated flows (Rodi, 1991). The turbulence energy (k) at the wall is fixed to zero as a boundary condition and it is calculated with equation (8.14) in the inner layer. The near wall treatment made by the two-layer model also imposes a condition that the number of grids near the wall must be sufficient in order to resolve the boundary layer correctly.

It is recommended to create at least 15 nodes in the boundary layer and the first node is best to be placed in the regions where $y^+ < 10$. Using the expansion ratio to increase the density near the wall is very beneficial, as illustrated in figure 8.8. It shows that if the grids are uniformly distributed near the wall, as shown as the lower graph in figure 8.8, the feature of flow separation and vortex formation is disappeared, though the grid density is adequately high.

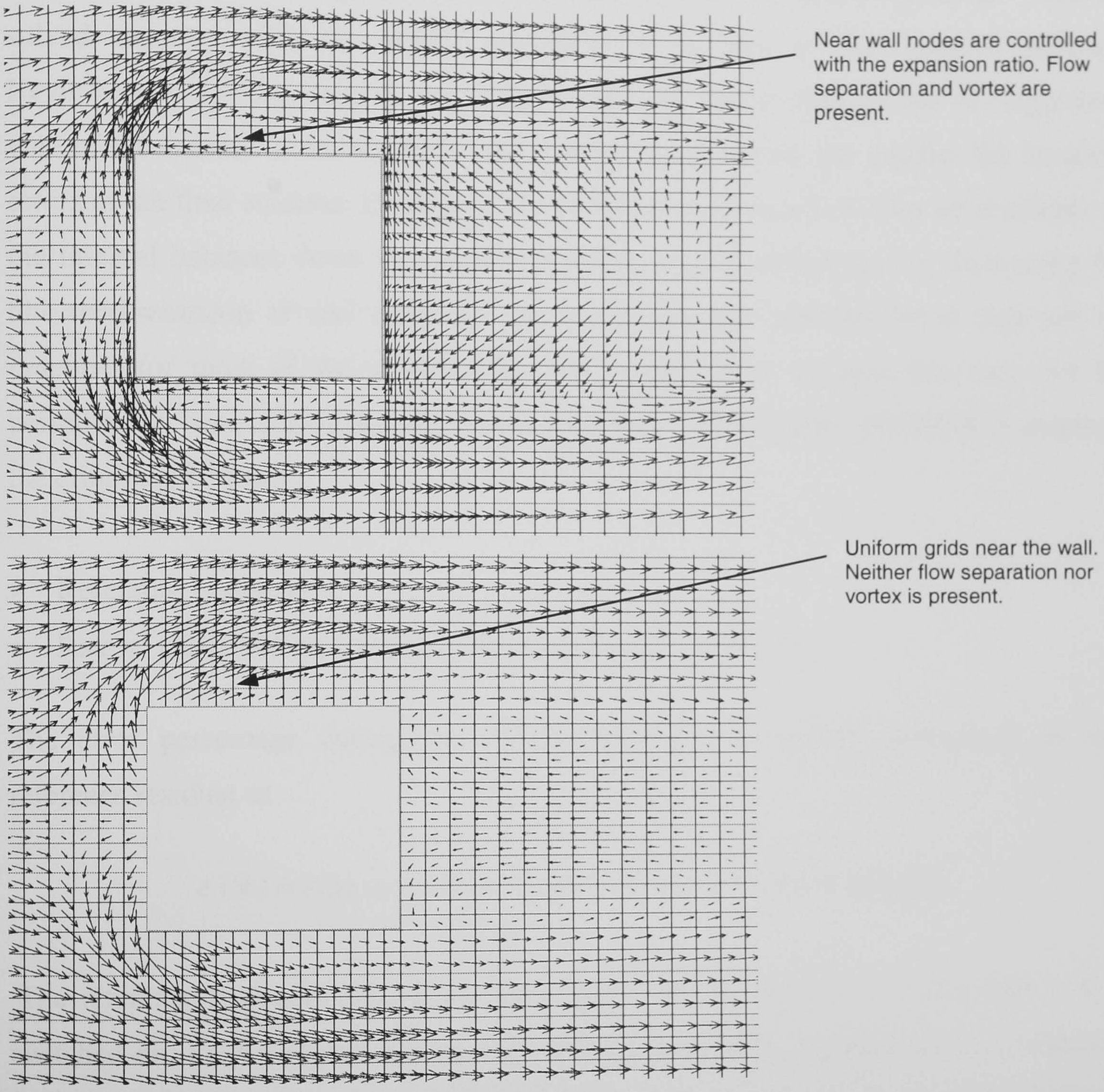

Figure 8.8 The implications of the treatment of near wall nodes.

Therefore, it is evident that the location of the first node near the wall is crucial to the performance of the two-layer k-ε model. The recommended value is between 1.4 and 1.6 if the power-law distribution is to be applied to the expansion ratio. Higher value (> 1.6) gives more nodes close to the wall but the distribution of grids becomes very uneven. The highly uneven distribution of grids may be sometimes required but the best value can be determined only from a user's experiences.

8.6 Guidelines on Convergence

A numerical simulation is considered converging when the residuals (or errors) in the equations decrease as the iterative solution proceeds. The iterative process is usually long and it is not uncommon that thousands of iteration may be required to reach the target of convergence in a 3D flow simulation. Currently there is no convergence theory for the solution of the discrete RANS equations (Casey and Wintergerste, 2000). Probably because it is highly coupled and the required "modelled equations" need be solved together with the RANS equations as a part of the iterative process. Nevertheless, the convergence can be observed and certain criteria can be suggested. One of the indices is the residual – the smaller the residuals, the smaller the iteration errors of the final solution. Driving all the residuals in all equations plus the residuals of the integral balances down to machine accuracy (e.g. double-precision float using 64 bits representation of real numbers) can be an absolute criterion but it may not be practical for most of the engineering flow computations because this may not be permitted by time constraints. Therefore, practically, for example, PHOENICS employs the criteria as follows.

- Reference residuals
- Rate of change of each variable between successive iterates

The error percentage during the solving procedure is usually normalised by the reference residual as

$$e\ (\%) = \text{sum of residuals of the variable / reference residual}$$

The reference residuals can be calculated internally by the solver if SELREF = T is switched on. Each variable has its corresponding reference residual and it is obtained from a typical flow rate of the variable times a reference factor. The reference factor is 0.001 by default but it can be changed by the user. Using the default reference factor for each variable is usually a crude estimate and therefore sometimes the error percentage appeared to be higher than it should be because the auto-calculated reference residual is too small. Conversely, it may also be lower than it should be if the auto-calculated value is too large. An alternative way is to set SELREF = F, which disables the auto-calculation of reference residuals. In practice, to set a reference residual with a value in the range from 10^{-4} to 10^{-5} for the velocities (U, V, W) and k as well as ε may suffice to

ensure that the physical property of a variable is well conserved if the sum of residuals for the variable is less than the reference value.

Another parameter that needs to be observed is the rate of change of the variable. If the residual of a variable is in diminution but the rate of change of the variable is still considerable, it signals that the convergence has not yet been reached. Only if both of the criteria are achieved – small residuals and diminutive rate of change of each variable, can the computation be considered converged. Figure 8.9 is an example in which the rate of change of each variable is hardly discernible at the left-hand-side diagram as the computation proceeds and the residuals are also diminishing shown by the right-hand-side graph. Though some error percentages were greater in the example, they were actually the consequences of smaller reference residuals determined by the solver. Since the reference residuals calculated by the solver were P1 = 2.949E-05, U1 = 3.891E-04, V1 = 5.797E-07, W1 = 8.147E-07, KE = 2.566E-05 and EP= 6.763E-05, extracted from the "result" file produced by the solver for inspection.

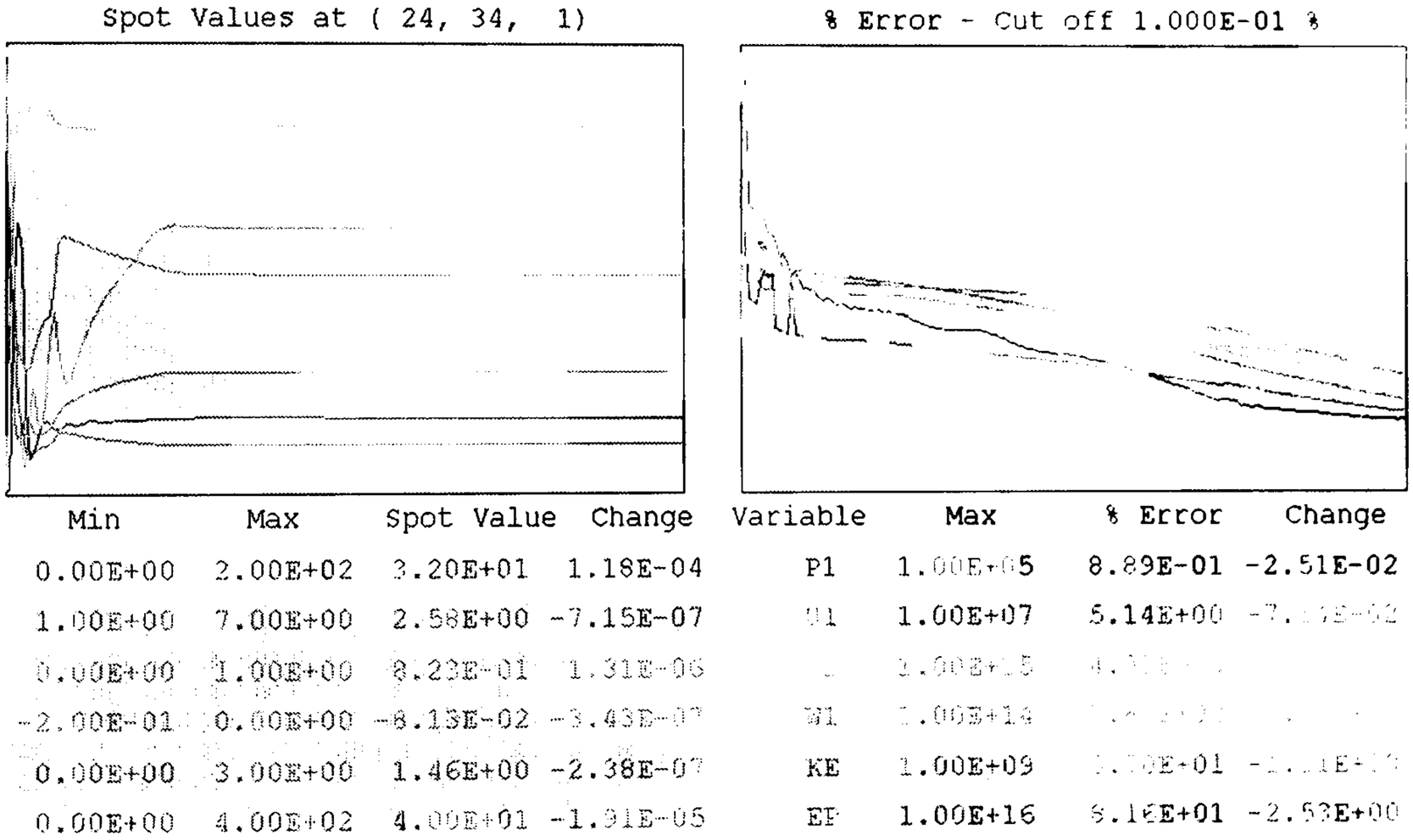

Figure 8.9 An illustration of converged computation.

Generally, the rate of change can be considered slow if the change of value of a variable is of the magnitude between 10^{-4} and 10^{-5}. Sometimes the residuals may stop decreasing after a certain number of iterations and proceed with small amplitude of oscillations; this can also be a signal of convergence, provided that the rate of change of every variable is small, as the oscillation of residuals is normally caused by the binary representation of a floating number that may be rounded off by the computer.

It also often occurs that convergence proceeds smoothly, but not fast enough. The possible reasons of slow convergence may be among the following points.

- *Possibly too much under-relaxation is being applied*: the function of under-relaxation is to limit the rate of change of a variable in a successive iterate. Using a strong (small) value may limit the change efficiently but it may also slow down the process of convergence. Some variables may rarely require the use of under-relaxation in certain solvers, such as the pressure in SIMPLEST. Velocity variables often use the "false time step" to limit their changes and the suggested values have been given in chapter 3. The turbulence quantities (k and ε) may use the linear relaxation, which is the default, or the aforementioned false time step method if the k-ε family models are used.
- *Possibly a lower-than-needed value of reference residual is specified*: it is usually difficult to set an appropriate reference residual and users incline to let the solver decide the reference residuals. It is convenient but sometimes it may also result in slow convergence.
- *Use of higher-order differencing schemes*: it is a common cause in slow convergence as higher-order differencing schemes need stronger values of under-relaxation.
- *Poor quality of grids*: this may also affect the rate of convergence. If the quality of grids is poor, sometimes the calculated flux in cells may not balance in an efficient manner and the required number of corrections is consequently higher in the computation.

Users may look into their computations with reference to the points listed above if slow convergence occurs. The choice of solver may also affect the rate of convergence because different solvers have their specific approaches to reduce the residuals. In addition, if a flow problem is inherently unsteady, the calculation probably will be neither converged nor diverged if using a steady-state simulation. Therefore to promote convergence still depends on a user's experience and the nature of his flow simulation.

8.7 Estimation of Numerical Accuracy

A study of flow problems using CFD involves many issues concerning fluid dynamics and numerical algorithm. Undoubtedly, there are numerical uncertainties and errors.

Freitas (2002) has quoted a statement from Albert Einstein to emphasis the existence of numerical uncertainties in mathematical methods:

> "*As far as the laws of mathematics refer to reality, they are not certain, and as far as they are certain, they do not refer to reality*"

It is certainly applicable to CFD. The term "uncertainty" refers to limited knowledge of physical phenomena and "error" is attributed to a recognisable deficiency that is not due to lack of knowledge. Uncertainties probably can only be reduced by improving the understanding of physical and numerical phenomena but the errors are usually identifiable and they may be corrected or minimised. From previous discussions, the identified errors appeared in a CFD simulation can be summarised in table 8.2.

Source	***Possible errors***
Grids	Spatial discretisation error; insufficient resolution
Differencing scheme	Truncation error
Turbulence model	Modelling errors by simplified assumptions
Boundary conditions	Incorrect physical representation
Linear equation solver	Convergence error; residuals
User	Lack of experience

Table 8.2 Identifiable sources of errors

Variable	**Resref**	**Residual sum / Resref**	**Residual sums**
P1	1.00E-05	5.06E-01	5.06E-06
U1	1.00E-05	7.69E+00	7.69E-05
V1	1.00E-05	3.25E+00	3.25E-05
KE	1.00E-05	1.02E+00	1.02E-05
EP	1.00E-05	9.86E+01	9.86E-04

Table 8.3 The residuals reported from the "result" file generated by PHOENICS.

These errors can be minimised and a CFD analyst has a reasonable chance to estimate the likely magnitude of the errors in his or her computation. It is possible to tell if the solution is grid-independent and whether the boundary conditions are correct. The task of estimation of errors is somewhat like the "quality assurance" of a CFD simulation. Since any numerical simulation contains errors, whereas the important thing is to know how large the errors are and whether they are within an acceptable range in the particular application.

Ferziger and Peric (1999) suggest that a CFD analyst should begin by estimating the iteration error (i.e. convergence error), then the discretisation error and, finally, the modelling error. The convergence errors can be clearly shown by the magnitude of residuals and a commercial CFD package can generate a report that contains the information of the history of computation in which the summations of residuals can be located. One may investigate the report generated by the code to get the sums of residuals for each variable (table 8.3).

As a commercial CFD code can generate the information about residuals, the user's task is to ensure that the computation is sufficiently converged, i.e. the sums of residuals are small. Subsequently, the discretisation errors need be minimised. The estimation of discretisation errors needs at least two computations since it involves refinement of grids and using higher-order schemes. To reduce the discretisation error can be achieved with a systematic test of grid density. Sometimes it may be difficult for a very complicated geometry because the number of grids is large. However, since the quality of grids is crucial to a CFD computation, it is recommended that at least two or three successive grids refinement using higher-order schemes can be performed.

Thirdly, the user may embark on minimising the modelling error. The modelling errors are the most difficult part of error estimation because the uncertainties of physical laws are involved. This necessitates the task of validation. It is even more difficult for the simulations of turbulent flows since sometimes the data of turbulence quantities are unavailable. The most noticeable errors in a turbulent flow simulation are the incorrect implementations of boundary conditions such as the inappropriate turbulence quantities specified in the inlet. Also, the turbulence models have their limitations and they cannot perform better than the physics embedded in the models. Using the two-equation models to simulate the wind has been criticised because the accuracy is not enough for dynamic structural analysis in which the peak value is important. Even so, the performance of conventional k-ε family models probably is still adequate to simulate the wind environment around buildings for the evaluation of pedestrian comfort, provided the long-term averaged values and the flow pattern are the main concern. Ideally, the user can try different models to compare the results but it is impossible to create a "model-independent" turbulent flow simulation, except using DNS. What is important is that users can acknowledge the limitations of a turbulence model appropriately and they know how to interpret the results obtained from their CFD simulations.

Last but not least are user errors, which mainly arise from mistakes and careless of a user, cannot be quantified and the errors probably can only be reduced through the learning curve. Hall (1996) and Cowan *et al.* (1997) have illustrated that different groups of users can generate very different CFD simulations with regard to one single flow problem using the same commercial code. This is also the most uncertain part of error estimation.

In summary, the errors in a CFD computation are interrelated and the significant errors are the discretisation errors, i.e. the quality of grids. The grids affect a number of key issues – spatial resolution, turbulence modelling and the efficiency of differencing scheme. The largest error can be minimised by using finer grids and this also requires the knowledge of which flow feature is important in ones CFD simulation. The convergence error probably is the easiest one to be inspected. Therefore, a CFD simulation is said to be "numerically correct" only if the identifiable errors have been minimised.

8.8 Summary

This chapter has discussed some common issues that appear in a CFD simulation of airflow around buildings. It is challenging because the flow behaviour is complicated and the computational parameters are interconnected. If the transport of pollutants and thermal effects (e.g. buoyancy) are involved, it will be surely more difficult and uncertain. Though the guidelines and discussions presented here concentrate on adiabatic and mechanical flow simulations, they can be a foundation for further studies of flow simulations involving transport of scalars and thermal effects. Finally, it is fairly adequate to conclude that the quality of a CFD simulation is highly dependent on the quality of a CFD user's expertise.

Chapter 9 Conclusions and Recommendations

The various aspects of CFD simulations of wind flows around buildings and the proposed guidelines are presented. It has been shown that using CFD is a viable way to predict the wind environments in the open spaces and streets if the mean values and the flow pattern are the main concern. However, care needs to be taken when a commercial CFD code is being used and the users also require sufficient expertise in fluid dynamics and numerical methods to get the best out of their codes. The present study has discussed a number of key computational parameters in a CFD simulation of wind flows through a number of cases. The flow field around a bluff body is characterised by separation and reattachment, recirculation as well as vortex shedding, which are very challenging to turbulence modelling. The deficiencies of a CFD simulation of turbulent flows need be properly comprehended. In other words, CFD users or analysts need to understand the limitations of a turbulence model and their interpretations of results shall be made with professional insights.

From this study, the recommended computational parameters – the two-layer k-ε turbulence model and the non-linear higher-order differencing scheme presented good results in the simulations of wind flows around buildings, provided

- sufficient grid density was deployed near walls and
- the grid-independent solution was obtained.

This is an economical computational approach when using CFD to study the wind environments around buildings and the information obtained is useful to the design team at the stages of environmental design and masterplanning.

It is recommended to carry out a series of validation studies, as has been presented in the thesis, before actually applying their CFD codes to simulate more complicated industrial cases. The selected cases for validation in the thesis can be used to test their CFD models. Most of the papers in the academic journals concentrate on the studies of flow field around a *single* building but the validation cases selected in this thesis include

the flow fields around *two* buildings and *a group* of building blocks, which are more practical to the studies of pedestrian-level winds. The validation studies can unveil some weakness of a numerical method but the result cannot be worse if the other sources of errors can be controlled and minimised, as suggested in chapter 8. The practice is to achieve a "numerically correct" modelling approach that can be applied in the studies of wind environments around buildings. Since a best numerical simulation – which is entirely free from any numerical error will not be necessary identical with the experimental results because an experiment itself also contains certain levels of instrumental inadequacies and errors (Castrol *et al.* 1999); therefore the more important thing to be kept in mind is to ensure that the right *methods* are employed with the right *tools* in one's CFD simulations.

The geometries used throughout this thesis were all in model scales since all the data were available from wind tunnels. In an industrial project, however, it is not uncommon that a full-scale numerical simulation is required. Using CFD to simulate the winds around buildings in full size need more validations because turbulence modelling is one of the biggest issues. Since most of the turbulence models are derived from experiments and the experiments are conducted in laboratories, some parameters may be dependent on the scaling and therefore the model performance is best when the flow conditions are similar to the experimental conditions. However, the experimental conditions can hardly exist in a full-scale environment and one immediate question is that where is the upper limit of $y+$, which is required for modelling the flows near walls. Certain types of flows are independent from the Reynolds number (cf. chapter 2) and this is a theoretical basis that the results of wind tunnel experiments are comparable to the full-scale measurements. Nevertheless, it may be a different story if using CFD because there are some parameters that *do* depend on the Reynolds number (e.g. the upper limit of $y+$). Therefore the viability of using CFD to simulate the winds in full size needs more scrutiny. This can be suggested for further research. Some other issues like the constants in the turbulence models, inspection of atmospheric dispersion using CFD, prescription of the inlet velocity profiles in the LES approach and the meshing strategy in LES are all possible research areas in the studies of modelling airflow around buildings.

References

Abbott M. B. and Basco D. R. (1989). Computational fluid dynamics: an introduction for engineers. Longman.

Anderson D. J. (1995). *Computational Fluid Dynamics – The basics with applications*. McGraw-Hill Inc, New York.

Arens E. (1982). On considering pedestrian winds during building design. In: *Proceedings of the international workshop on wind tunnel modelling criteria and techniques in civil engineering applications*, Gaitherburg, Maryland, USA. Cambridge University Press, New York, pp. 8-26.

Arens E., Ballant D., Bennett C. Guldman S. and White B. (1989). Developing the San Francisco wind ordinance and its guidelines for compliance. *Building and Environment*, Vol. 24, No. 4, pp. 297-303.

Arya S. P. (1982). Atmospheric boundary layers over homogeneous terrain. In: *Engineering Meteorology*. Plate E. J. ed. Elsevier, Amsterdam.

Aynsley R. M. (1989). Politics of pedestrian level urban wind control. *Building and Environment*, Vol. 24, No. 4, pp. 291-295.

ASCE (1999). *Wind tunnels studies of buildings and structures*. American Society of Civil Engineers, Virginia.

Baskaran A. and Stathopoulos T. (1992). Influence of computational parameters on the evaluation of wind effects on the building envelope. *Building and Environment*. Vol. 27, No. 1, pp. 39-49.

Baskaran A and Kashef A (1996). Investigation of airflow around buildings using computational fluid dynamics techniques. *Engineering Structure*, Vol. 18, No. 11, pp. 861-875.

Bottema M. (2000). A method for optimisation of wind discomfort criteria. *Building and Environment*, Vol. 35, pp. 1-18.

Bosch G. and Rodi G. (1998). Simulation of vortex shedding past a square cylinder with different turbulence models. *Int. J. Num. Meth. Fluids*, Vol. 28, pp. 601-616.

Bradshaw P. (1971). *An introduction to turbulence and its measurement*. Pergamon Press.

Bradshaw P., Cebeci T. and Whitelaw J. H. (1981). *Engineering calculation methods for turbulent flows*. Academic Press, London.

Bradshaw P. (1997). Understanding and prediction of turbulent flow – 1996. *Int. J. Heat and Fluid Flow*, Vol. 18, pp. 45-54.

Brown G. Z. and Dekay M. (2001). *Sun, Wind & Light – Architectural design strategies*. 2nd ed. John Wiley & Sons, New York.

Casey M. and Wintergerste T. (2000). ERCOFTAC Special interest group on "*Quality and Trust in Industrial CFD*" – *Best practice guidelines*. Fluid Dynamics Laboratory, Sulzer Innotec.

Castro I. P. and Graham J. M. R. (1999). Numerical wind engineering: the way ahead? In: *Proc. Instn Civ Engrs Structs & Bldgs*. Vol. 134, pp. 275-277.

Castro I. P. and Robins A. G. (1977). The flow around a surface-mounted cube in uniform and turbulent streams. *J. Fluid Mech*. Vol. 79, part 2, pp. 307-305.

Castro, I. P., Cowan, I. R. and Robins, A. G. (1999). Simulations of flow and dispersion around buildings, *J. Aerospace Engineering*. Vol. 12, No. 4, pp. 145-160, 1999.

Cermak J. E. (1970). Laboratory simulation of the atmospheric boundary layer. *AIAA Journal*, Vol. 9, No. 9, pp. 1746-1754.

Cermak J. E. (1975). Applications of fluid mechanics to wind engineering – a Freeman scholar lecture. *Journal of Fluid Engineering*, March, pp. 9-38.

Cermak J. E. (1977). Wind-tunnel testing of structures. *Journal of the Engineering Mechanics Division*, ASCE, December 1977, pp. 1125-1140.

Cermak J. E. (1979). Applications of wind tunnels to investigation of wind-engineering problems. *AIAA Journal*, Vol. 17, No. 7, pp. 679-690.

Cermak J. E. (1981). Wind tunnel design for physical modelling of atmospheric boundary layers. *Journal of Engineering Mechanics Division*, ASCE, Vol.107, No. EM3, pp.623-642.

Cermak J. E. (1982). Physical modelling of the atmospheric boundary layer (ABL) in long boundary-layer wind tunnels (BLWT). In: *Proceedings of the international workshop on wind tunnel modelling criteria and techniques in civil engineering applications*, Gaitherburg, Maryland, USA. Cambridge University Press, New York, pp. 97-125.

Cermak J. E. (1984). Wind-simulation criteria for wind-effects tests. *Journal of Structural Engineering*, ASCE, Vol. 110, No. 2, pp. 328-339.

Cermak J. E. (1987). Advances in physical modelling for wind engineering. Journal of Engineering Mechanics, Vol. 113, No. 5, pp. 737-756.

Cermak J. E., Cochran L. S. and Leffler R. D. (1995). Wind-tunnel modelling of the atmospheric surface layer. *J. Wind Engng. Indus. Aerodyn*. Vol. 54/55, pp. 505-513.

CHAM (2001). PHOENICS Documentation. CHAM Ltd. London.

CIBSE (1999). *CIBSE Guide A: environmental design*. 6th ed. Chartered Institution of Building Services Engineers.

Ciofalo M. (1994). Large eddy simulation: a critical survey of models and applications. *Advances in Heat Transfer*, Vol. 25. Academic Press.

Ciofalo M. (1996). Large eddy simulations of turbulent flow with heat transfer in simple and complex geometries using Harwell-Flow3D. *Appl. Math. Modelling*, Vol. 20, pp. 262-271.

Cook N. J. (1973). On simulating the lower third of the urban adiabatic boundary layer in a wind tunnel. *Atmospheric Environment*, Vol. 7, pp. 691-705.

Cook N. J. (1978). Wind tunnel simulation of the adiabatic atmospheric boundary layer by roughness, barriers and mixing device methods. *Journal of Industrial Aerodynamics*, Vol. 3, pp. 157-176.

Cook N. J. (1982). Simulation techniques for short test-section wind tunnels: roughness, barriers and mixing-device methods. In: *Proceedings of the international workshop on wind tunnel modelling criteria and techniques in civil engineering applications*, Gaitherburg, Maryland, USA. Cambridge University Press, New York, pp. 126-136.

Cook N. J. (1985). The designer's guide to wind loading of building structures, Part 1: Background, damage survey, wind data and structure classification. Butterworths, London.

Cook N. J. (1990). The designer's guide to wind loading of building structures, Part 2: Static structure and measurement. Butterworths, London.

Counihan J. (1969). An improved method of simulating an atmospheric boundary layer in a wind tunnel. *Atmospheric Environment*, Vol. 3, pp. 197-214.

Cowan I. R., Castro I. P. and Robins A. G. (1997). Numerical considerations for simulations of flow and dispersion around buildings. *J. Wind Engng. Indus. Aerodyn.* Vol. 67&68, pp. 535-545.

Counihan J. (1975). Adiabatic atmospheric boundary layers: a review and analysis of data from the period 1880-1972. *Atmospheric Environment*, Vol. 9, pp. 871-905.

Cowlin F and Westbury P. (2002). Testing times for buildings. *Building Services Journal*. Vol. 24, No. 3, pp. 53-57.

Dalgliesh A. W. (1982). Comparison of model and full scale tests of the commerce court building in Toronto. In: *Proceedings of the international workshop on wind tunnel modelling criteria and techniques in civil engineering applications*, Gaitherburg, Maryland, USA. Cambridge University Press, New York, pp. 575-589.

Davenport A. G. (1965). The relationship of wind structure to wind loading. Paper No. 2, *Proceedings of the Conference held at the National Physical Laboratory* on 26-28 June 1963. HMSO.

Durgin F. H. and Chock A. W. (1982). Pedestrian level winds: A brief review. *Journal of Structural Division, Proceedings of ASCE*, Vol. 108, No. ST8, pp.1751-1767.

Durgin F. H. (1989). Proposed guidelines for pedestrian level wind studies for Boston – comprison of results from 12 studies. *Building and Environment*, Vol. 24, No. 4, pp. 305-314.

ESDU (1974). Characteristics of atmospheric turbulence near the ground. Part 1: definitions and general information. *ESDU data Item 74030*. Engineering Science Data Unit, London.

Farell C. and Iyengar A. K. S. (1999). Experiments on the wind tunnel simulation of atmospheric boundary layers. *J. Wind Engng. Indus. Aerodyn.* Vol. 79, pp. 11-35.

Flay R. G. J. and Andrews R. J. (1995). A wind tunnel/full-scale comparison of the wind flow over Auckland City. *J. Wind Engng. Indus. Aerodyn.* Vol. 54/55, pp. 151-161.

Ferziger J. H. (1977). Large eddy simulation of turbulent flows. *AIAA Journal*, Vol. 15, No. 9, pp. 1261-1267.

Ferziger J. H. (1990). Approaches to turbulent flow computation: Applications to flow over obstacles. *J. Wind Engng. Indus. Aerodyn.*, Vol. 35, pp. 1-19.

Ferziger J. H. and Peric M. (1999). *Computational Methods for Fluid Dynamics*. 2nd ed. Springer, Germany.

Flow Science Ltd. (2002). Environmental boundary layer wind tunnel – further details. Available from: http://www.flowscience.co.uk/etdetail.htm.

Frank W. (1995). Large eddy simulation of the three-dimensional flow around buildings. In: *Wind Climate in Cities*. J. E. Cermak *et al.* eds. Kluwer Academic Publishers, pp. 669-679.

Freitas C. J. (2002). The issue of numerical uncertainty. *Appl. Math. Modelling*. Vol. 26, pp. 237-248.

Gandemer J. (1978). Aerodynamic studies of built-up areas made by C.S.T.B. at Nantes, France. *J. Wind Engng. Indus. Aerodyn.* Vol. 3, pp. 227-240.

Gaskell P. H. and Lau A. K. (1988). Curvature-compensated convective transport: SMART, a new boundedness-preserving transport algorithm. *Int. J. Num. Metho. Fluids*, Vol. 8, pp. 617-641.

Gosman A D. (1999). Developments in CFD for industrial and environmental applications in wind engineering. *J. Wind Engng. Indus. Aerodyn.* Vol. 81. pp. 21-39.

Grant I. (1997). Particle image velocimetry: a review. *Proc. Instn. Mech. Engrs.* Vol. 211 Part C, pp. 55-76.

Guyon E., Hulin J., Petit L. and Mitescu C. (2001). *Physical Hydrodynamics*. Oxford University Press. New York.

Hall R. C. (1996). *Evaluation of modelling uncertainty – CFD modelling of near-field atmospheric dispersion*, Project EMU final report, WS Atkins Consultants Ltd.

Harris R. I. (1970). The nature of the wind. In: *The modern design of wind-sensitive structures* – Proceedings of the seminar held on 18 June 1970 at ICE. Construction Industry Reseasrch and Information Association, London.

Harris R. I. and Deaves D. M. (1981). The structure of strong winds. *Paper 4 of CIRIA Conf. On Wind Engineering in the Eighties*. Construction Industry Reseasrch and Information Association, London.

He J. and Song C. C. S. (1999). Evaluation of pedestrian winds in urban area by numerical approach. *J. Wind Engng. Indus. Aerodyn.*, 81, pp. 295-309.

Hirsch C. (1988). *Numerical computation of internal and external flows, vol. 1 – fundamentals of numerical discretisation*. John Wiley & Sons, New York.

Hirsch C. (1990). *Numerical computation of internal and external flows, vol. 2 – Computational methods for inviscid and viscous flows*. John Wiley & Sons, New York.

Holms J. D. (1982). Comparison of model and full-scale tests of the Aylesbury house. In: *Proceedings of the international workshop on wind tunnel modelling criteria and techniques in civil engineering applications*, Gaitherburg, Maryland, USA. Cambridge University Press, New York, pp. 605-617.

Houghton E. L. and Carruthers N. B. (1976). *Wind forces on buildings and structures: an introduction*. Wiley, New York.

Hoxey R. P. and Richards P. J. (1993). Flow patterns and pressure field around a full-scale building. *J. Wind Engng. Indus. Aerodyn.* Vol. 50, pp. 203-212.

Hunt J. C. R., Poulton E. C. and Mumford J. C. (1976). The effects of wind on people: new criteria based on wind tunnel experiments. *Building and Environment*, Vol. 11, pp. 15-28.

IMechE (1991). *Computational fluid dynamics for the environmental and building services engineer – tool or toy*? Papers presented at a seminar organised by the

Environmental Engineering Group of the Institution of Mechanical Engineers and held at the Institution of Mechanical Engineers on 26 November 1991. IMechE seminar publication.

Irwin H. P. A. H. (1981). A simple omnidirectional sensor for wind-tunnel studies of pedestrial-level winds. *J. Wind Engng. Indus. Aerodyn.* Vol. 7, pp. 219-239.

Isyumov N and Davenport A. G. (1977). The ground level wind environment in built-up areas. In: *Proceedings of the fourth international conference on wind effects on buildings and structures*, Heathrow, 1975. Cambridge University Press, New York, pp. 403-422.

Isyumov N. (1978). Studies of the pedestrian level wind environment at the boundary layer wind tunnel laboratory of the University of Western Ontario. *Journal of Industrial Aerodynamics*. Vol. 3, pp. 187-200.

Lakehal D. and Rodi W. (1997). Calculation of flow past a surface-mounted cube with two-layer turbulence models. *J. Wind Engng. Indus. Aerodyn.*, Vol. 67&68, pp. 65-78.

Lauder B. E. and Spalding D. B. (1974). The numerical computation of turbulent flows. *Comp. Meth. in Applied Mechanics and Engng*. Vol. 3, pp. 269-289.

Lawson T.V. and Penwarden A. D. (1977). The effects of wind on people in the vicinity of buildings. In: *Proceedings of the fourth international conference on wind effects on buildings and structures*, *Heathrow*, 1975. Cambridge University Press, New York, pp. 605-622.

Lawson T. V. (1980). *Wind effects on buildings*, Volume 1, chapter 2, pp. 5-14. Applied Science, London.

Lee B. E. (1982). Model and full scale tests of the Arts Tower at Sheffield University. In: *Proceedings of the international workshop on wind tunnel modelling criteria and techniques in civil engineering applications*, Gaitherburg, Maryland, USA. Cambridge University Press, New York, pp. 590-604.

Leonard B. P. (1979). A stable and accurate convective modelling procedure based on quadratic upstream interpolation. *Comput. Methods Appl. Mech. Engrg.*, Vol. 19, pp.55-98.

Lumley J. L. and Panofsky H. A. (1964). *The Structure of Atmospheric Turbulence*. Wiley, New York.

Lyn D. A., Einav S., Rodi W., Park J-H. (1995). A laser-Doppler velocimetry study of ensemble-averaged characteristics of the turbulent near wake of a square cylinder. *J. Fluid Mech.*, Vol. 34, pp. 285-319.

Malin M. and Waterson N. P. (1999). Schemes for convection discretisation in PHOENICS. PHOENICS Journal, Vol.12, No.2. pp. 173-201.

Marshall R. D. (1984) Wind tunnels applied to wind engineering in Japan. *Journal of Structural Engineering*, ASCE, Vol. 110, No. 6, pp. 1203-1221.

Martinuzzi R. and Tropea C. (1993). The flow around surface-mounted prismatic obstacle placed in a fully developed channel flow. *J. Fluid Engineering*. Vol. 115, pp. 85-92.

Melbourne W. H. (1978). Wind environment studies in Australia. *Journal of Industrial Aerodynamics*. Vol. 3, pp. 201-214.

Mohammadi B. and Medic G. (1996). A critical evaluation of the classical k-ε model and wall- laws for unsteady flows over bluff bodies. *INRIA Report*, No. 3056, ISSN 0249-6399.

Munson B. R., Young D. F. and Okiishi T. H. (1998). *Fundamentals of Fluid Dynamics*, 3rd ed. John&Wiley, New York.

Murakami S., Uehara K. and Deguchi K. (1980). Wind effects on pedestrians: new criteria based on outdoor observation of over 2000 persons. In: *Proceedings of 5th International Conference on Wind Engineering*. Pergamon, pp. 277-288.

Murakami S. and Mochida A. (1989). Three-dimensional numerical simulation of turbulent flow around buildings using the k-ε turbulence model. *Building and Environment*, Vol. 24, No. 1, pp. 51-64.

Murakami S., Mochida A. and Hayashi Y. (1990). Examining the k-ε model by means of a wind tunnel test and large eddy simulation of the turbulence structure around a cube. *J. Wind Engng. Indus. Aerodyn.* Vol. 35, pp. 87-100.

Murakami S. (1993). Comparison of various turbulence models applied to a bluff body. *J. Wind Engng. Indus. Aerodyn.* Vol. 46&47, pp. 21-36.

Murakami S. and Mochida A. (1995). On turbulent vortex shedding flow past 2D square cylinder predicted by CFD. *J. Wind Engng. Indus. Aerodyn.* Vol. 54-55, pp. 191-211.

Murakami S. (1998). Overview of turbulence models applied in CWE-1997. *J. Wind Engng. Indus. Aerodyn.* Vol. 74-76, pp. 1-24.

Nishi A., Kikugawa H., Matsuda Y. and Tashiro D. (1999). Active control of turbulence for an atmospheric boundary layer model in a wind tunnel. *J. Wind Engng. Indus. Aerodyn.* Vol. 83, pp. 409-419.

Norris H. L. (1975). *Turbulent channel flow with a moving wavy boundary*. PhD thesis, Mech. Dept., Stanford University.

Ogawa Y., Diosey P. G., Uehara K. and Ueda H. (1981). A wind tunnel for studying the effects of thermal stratification in the atmosphere. *Atmospheric Environment*. Vol.15, No. 5, pp. 807-821.

Panofsky H. A. and Dutton J. A. (1983). *Atmospheric Turbulence*: *Models and Methods for Engineering Applications*. Wiley, New York.

Patankar S. V. (1980). *Numerical heat transfer and fluid flow*. Hemisphere Publishing Corp., London.

Paterson D. A. and Apelt C. J. (1986). Computation of wind flows over three-dimensional buildings. *J. Wind Engng. Indus. Aerodyn*. Vol. 24, pp. 193-213.

Penwarden A. D. and Wise A. F. E. (1975). *Wind environment around buildings*. Building Research Establishment, London, HMSO.

Plate E. J. (1999). Methods of investigating urban wind fields – physical models. *Atmospheric Environment*, Vol. 33, pp.3981-3989.

Rhie C. M. and Chow W. L. (1983). Numerical Study of the Turbulent Flow Past an Airfoil with Trailing Edge Separation. *AIAA Journal*, 21(11):1525-1532.

Richards P. J. (1989). *Computational modelling of wind flow around buildings using PHOENICS*. Div. Note DN1508, AFRC Inst. Engng. Res., Silsoe.

Richards P. J. and Hoxey R. P. (1993). Appropriate boundary conditions for computational wind engineering models using k-ε turbulence model. *J. Wind Engng. Indus. Aerodyn.*, Vol. 46&47, pp. 145-153.

Richards P. J. and Wanigaratne B. S. (1993). A comparison of computer and wind-tunnel models of turbulence around the Silsoe structures building. *J. Wind Engng. Indus. Aerodyn*. Vol. 46-47, pp. 439-447.

Rodi W. (1991). Experience with two-layer models combining the k-ε model with a one-equation model near the wall. *AIAA-91-0216*.

Rodi W. (1993). *Turbulence models and their application in hydraulics – A state-of-art review*. 3rd ed. A. A. Balkema, Rotterdam.

Rodi W. (1995). Introduction to the numerical simulation approaches in wind engineering. In: *Wind Climate in Cities*. J. E. Cermak *et al*. eds. Kluwer Academic Publishers, pp. 633-647.

Rodi W. (1997). Comparison of LES and RANS calculations of the flow around bluff bodies. *J. Wind Engng. Indus. Aerodyn*. Vol. 69-71, pp. 55-75.

Saeid S. A. (1991). *Initial calibration of Heriot-Watt University wind-tunnel*. MSc. dissertation, Heriot-Watt University.

Schlichting H. (1968). *Boundary Layer Theory*. 6th ed. McGraw-Hill.

Schumann U. (1975). Subgrid scale model for finite difference simulations of turbulent flows in plane channels and annuli. *J. Comp. Phys.* Vol. 18, pp. 376-404.

Shah K. B. and Ferziger J. H. (1997). A fluid mechanician's view of wind engineering: Large eddy simulation of flow past a cubic obstacle. *J. Wind Engng. Indus. Aerodyn.* Vol. 67&68, pp. 211-224.

Simiu E. and Scanlan R. H. (1996). *Wind Effects on Structures – Fundamentals and Applications to Design*. 3rd ed. Wiley, New York.

Smagorinsky J. (1963). General circulation experiments with primitive equations: Part I. The basic experiment. *Monthly Weather Review*, Vol. 91, pp.99-164.

Soligo J. M., Irwin A. P., Williams J. C., Schuyler D. G. (1998). A comprehensive assessment of pedestrian comfort including thermal effects. *J. Wind Engng. Indus. Aerodyn.* Vol. 77&78, pp.753-766.

Spalding D. B. (1972). A novel finite difference formulation for differential expressions involving both first and second derivatives. *Int. J. Num. Methods in Engineering*, Vol. 4, pp. 551-559.

Spalding D. B. (1981). A general purpose computer program for multi-dimensional one-and-two-phase flow. *Math. and Comp. in. Simul.* Vol. 23, No. 3, pp. 267-276.

Stathopoulos T. and Storms R. (1986). Wind environmental conditions in passage between buildings. *J. Wind Engng. Indus. Aerodyn.* Vol. 24, pp. 19-31.

Stathopoulos T. and Wu H. (1995). Generic models for pedestrian-level winds in built-up regions. *J. Wind Engng. Indus. Aerodyn.* Vol. 54/55, pp. 515-525.

Stathopoulos T. and Baskaran B. A. (1996). Computer simulation of wind environmental conditions around buildings. *Engineering Structures*, Vol. 18, No. 11, pp. 876-885.

Stathopoulos T. (1997). Computational wind engineering: Past achievements and future challenges. *J. Wind Engng. Indus. Aerodyn.* Vol. 67&68, pp. 509-532.

Steadman R. G. (1971). Indices of windchill of clothed persons. *J. Applied Meteorology*, Vol.10, pp. 674-683.

Summers, D. M., Hanson, and Wilson, C. B. (1986). Validation of a computer simulation of wind flow over a building model. *Building and Environment*, Vol. 21, No. 2, pp. 97-111.

Tennekes H. and Lumley J. L. (1972). *A first course in turbulence*. MIT press.

Thangam S. and Speziale C. G. (1992). Turbulent flow past a backward-facing step: a critical evaluation of two-equation models. *AIAA Journal*. Vol. 30, N0. 5, pp. 1314-1320.

Thomas T. G. and Williams J. J. R. (1999). Generating a wind environment for large eddy simulation of bluff body flows. *J. Wind Engng. Indus. Aerodyn.* Vol. 82, pp. 189-208.

Thompson J. F., Warsi Z. U. A. and Mastin C. W. (1985). *Numerical grid generation – foundations and applications*. Elsevier Science.

Tieleman H. W. (1982). Simulation criteria based on meteorological or theoretical consideration. In: *Proceedings of the international workshop on wind tunnel modelling criteria and techniques in civil engineering applications*, Gaitherburg, Maryland, USA. Cambridge University Press, New York, pp. 73-96.

Versteeg H. K., Malalasekera W. (1995). *An introduction to computational fluid dynamics*, Longman.

Visser G. T. and Cleijine J. W. (1994). Wind comfort predictions by wind tunnel tests: comparison with full-scale data. *J. Wind Engng. Indus. Aerodyn.* Vol. 52, pp. 385-402.

Waterson N. P. (1994). Development of a bounded higher-order convection scheme for general industrial applications. *VKI Report 1994-33*, Belgium.

White F. M. (1999). *Fluid Mechanics*. 4th ed. McGraw-Hill.

Welty J. R., Wicks C. E. and Wilson R. E. (1969). *Fundamentals of momentum, heat and mass transfer*. John Wiley & Sons, New York.

Wener H. and Wengle H. (1991). Large eddy simulation of turbulent flow over and around a cube in a plate channel. In: *Eighth symposium on turbulent shear flows*. Technical University of Munich, Sep. 9-11, 1991.

Wu H. and Stathopoulos T. (1993). Wind-tunnel techniques for assessment of pedestrian-level winds. *Journal of Engineering Mechanics*, ASCE: Vol. 119, No. 10, pp. 1920-1936.

Wu H. and Stathopoulos T. (1994). Further experiments on Irwin's surface sensor. *J. Wind Engng. Indus. Aerodyn.* Vol. 53, pp. 441-452.

Yakhot V and Smith L.M. (1992). The Renormalisation group, the eps-expansion and derivation of turbulence models. *J. Sci. Computing*. Vol. 7, No. 1.

Yu D. and Kareem A. (1997). Numerical simulation of flow around rectangular prism. *J. Wind Engng. Indus. Aerodyn.* Vol. 67&68, pp. 195-208.

Yu D. and Kareem A. (1998). Parametric study of flow around rectangular prisms using LES. *J. Wind Engng. Indus. Aerodyn.* Vol. 77&78, pp. 653-662.

Zhou Y. and Stathopoulos T. (1997). A new technique for the numerical simulation of wind flow around buildings. *J. Wind Engng. Indus. Aerodyn.* Vol. 72, pp. 137-147.